

Characteristics, Influence, and Sensitivity of Ice Cover on the Great Lakes

A Dissertation  
SUBMITTED TO THE FACULTY OF  
UNIVERSITY OF MINNESOTA  
BY

Daniel James Titze

IN PARTIAL FULFILLMENT OF THE REQUIREMENTS  
FOR THE DEGREE OF  
DOCTOR OF PHILOSOPHY

Jay Austin

November 2016

© Daniel James Titze 2016

## Acknowledgements

I would like to acknowledge:

- My PhD adviser: Dr. Jay Austin
- My PhD committee members: Dr. Sergei Katsev, Dr. Sam Kelly, Dr. Katsumi Matsumoto, and Dr. Byron Steinman
- Kathy Tokos for her technical support in getting started with the ROMS Lake Superior Model
- Faculty and staff at the Large Lakes Observatory and Water Resources Science Program
- The crew of the Blue Heron for their assistance collecting field observations
- The National Science Foundation for funding the mooring observations and my work on the cold 2013-2014 Lake Superior winter
- The NASA Jet Propulsion Laboratory for funding my work on ice sensitivity
- Friends and fellow students for helping to make grad school an enjoyable several years
- My family for their support

## Abstract

Three distinct aspects of ice cover on the Great Lakes are examined, including the influence of ice cover on water column processes, the characteristics of ice cover on Lake Superior during a high-ice year, and the sensitivity of ice on the Great Lakes to climate. Three subsurface moorings were deployed in Lakes Superior during the record-high ice year of 2013-2014, and datasets from these moorings are analyzed alongside remotely-sensed ice cover data and regional meteorological observations. Ice cover on Lake Superior is shown to be predominately free-drifting, behaving more like ice on the oceans than ice on smaller lakes. Pressure sensors on the moorings directly measured deep ice keels, which frequently occurred at depths of more than 6m and occasionally occurred at depths greater than 11m. Late-season ice on Lake Superior during the 2013-2014 winter delayed spring warming, which is a mechanism that has previously been identified, but not directly observed. Ice cover is shown to influence surface currents on Lake Superior, resulting in a large-scale redistribution of heat in the western basin of the lake. Ice cover on the Great Lakes shows a linear sensitivity to air temperature, both empirically and through three-dimensional hydrodynamic modeling. Small variations in seasonal air temperature, on the order of 1 to 2°C, can be the difference between a moderate to high ice year and a very low ice year. Air temperatures during the time of ice formation have a significant influence on the amount of seasonal-average ice cover, while air temperatures during the remainder of the year do not greatly affect the amount of ice that forms. Shallow regions of the Great Lakes (<10m) exhibit similar sensitivity to air temperature as do smaller inland lakes, but the absolute amount of ice that forms on each of these different systems varies.

## Table of Contents

<b>List of Tables .....</b>	<b>v</b>
<b>List of Figures .....</b>	<b>vi</b>
<b>1.0 Introduction .....</b>	<b>1</b>
<b>2.0 Methods and Data Sources .....</b>	<b>3</b>
2.1 Lake Superior Subsurface Mooring Array.....	3
2.1.1 Instrumentation .....	7
2.2 Ice Cover Data.....	17
2.2.1 Great Lakes Ice Atlas (GLIA) Datasets .....	17
2.2.2 Ice Mapping System (IMS) Datasets .....	18
2.2.3 Combining the GLIA and IMS ice datasets .....	19
2.3 Meteorological Data .....	22
2.3.1 National Data Buoy Center (NDBC) Database.....	22
2.3.2 Global Historical Climatology Network (GHCN) Database .....	30
2.3.3 North American Regional Reanalysis (NARR) product.....	40
2.3.4 Estimating Winter Wind Velocity at Offshore Locations.....	41
2.4 Bathymetry Data.....	43
2.5 Water Level Data.....	44
2.6 Regional Ocean Modeling System (ROMS) Numerical Model .....	44
2.6.1 Lake Superior Model Description.....	44
2.6.2 Model Forcing.....	45
<b>3.0 Interactions between Ice Cover and Lake Processes.....</b>	<b>57</b>
3.1 Thermal Structure .....	59
3.2 Effect of Ice Cover on Surface Heat Flux.....	63
3.3 Effect of Ice Cover on Surface Currents and Large-Scale Circulation.....	66
3.4 Conclusion.....	76
<b>4.0 Lake Superior Ice Characteristics .....</b>	<b>78</b>
4.1 Ice Drift.....	80
4.2 Ice Keels .....	102
4.3 Conclusion.....	110

<b>5.0 Sensitivity of Great Lakes Ice Cover to Climate .....</b>	<b>113</b>
5.1 Initial analysis.....	114
5.2 Time Sensitivity.....	120
5.2.1 Propagation of Anomalies.....	121
5.2.2 Time Sensitivity by Month .....	127
5.2.3 Time Sensitivity Seasonal Approach .....	134
5.3 The relationship between air temperature and ice-on date .....	142
5.4 Comparison to ice sensitivity in small lakes.....	148
5.5 Numerical Modeling Sensitivity Analyses .....	159
5.6 Conclusion.....	166
<b>6.0 Conclusion .....</b>	<b>168</b>
<b>7.0 Bibliography.....</b>	<b>171</b>

## List of Tables

Table 2.1 – ADCP deployment list.....	16
Table 2.2 – Summary of wind velocity empirical transfer functions.....	43
Table 5.1 – Correlation between seasonal ice cover and air temperature by timeframe.....	137
Table 5.2 – Correlations between ice cover and air temperature.....	141

## List of Figures

Figure 1.1 – Historic air temperature and ice cover.....	1
Figure 2.1 – Conceptual mooring diagram.....	4
Figure 2.2 – Map of Lake Superior mooring array.....	5
Figure 2.3 – Lake Superior mooring array deployment history.....	6
Figure 2.4 – Thermistor depth coverage for the Western, Central, and Eastern Moorings. ....	8
Figure 2.5 – Visualization of thermistor data. ....	10
Figure 2.6 – Determination of pressure sensor depth. ....	13
Figure 2.7– GLIA data example. ....	18
Figure 2.8 – IMS data example.....	19
Figure 2.9 – Comparison of GLIA and IMS datasets. ....	21
Figure 2.10 – NDBC database station locations, Lake Superior.....	23
Figure 2.11 – NDBC database data availability, Lake Superior.....	24
Figure 2.12 – NDBC database station locations, Lake Michigan. ....	25
Figure 2.13 – NDBC database data availability, Lake Michigan. ....	26
Figure 2.14 – NDBC database station locations, Lake Huron. ....	27
Figure 2.15 – NDBC database data availability, Lake Huron.....	28
Figure 2.16 – NDBC database station locations, Lake Erie.....	28
Figure 2.17 – NDBC database data availability, Lake Erie. ....	29
Figure 2.18 – NDBC database station locations, Lake Ontario.....	29
Figure 2.19 – NDBC database data availability, Lake Ontario.....	30
Figure 2.20 – GHCN database station locations, Lake Superior. ....	31
Figure 2.21 – GHCN database data availability, Lake Superior. ....	31
Figure 2.22 – GHCN database station locations, Lake Michigan. ....	32
Figure 2.23 – GHCN database data availability, Lake Michigan. ....	33
Figure 2.24 – GHCN database station locations, Lake Huron. ....	34
Figure 2.25 – GHCN database data availability, Lake Huron. ....	34
Figure 2.26 – GHCN database station locations, Lake Erie. ....	35
Figure 2.27 – GHCN database data availability, Lake Erie.....	35
Figure 2.28 – GHCN database station locations, Lake Ontario. ....	36
Figure 2.29 – GHCN database data availability, Lake Ontario. ....	36
Figure 2.30 – Comparison of NDBC and GHCN air temperature data. ....	38
Figure 2.31 – NARR grid, Great Lakes Region.....	41
Figure 2.32 – ROMS Lake Superior basin grid. ....	45
Figure 2.33 – ROMS test run with unadjusted NARR forcing. ....	47
Figure 2.34 – ROMS test run with NARR net-as-downward shortwave forcing. ....	49
Figure 2.35 – Comparison of NARR air temperature to GHCN observed air temperature. ....	51
Figure 2.36 – Ratio of NARR to observed observed downward shortwave radiation.....	53
Figure 2.37 – ROMS base run. ....	55
Figure 3.1 – Map of relevant locations for Section 3.0 .....	58
Figure 3.2 – Mooring thermistor contour plots, winter 2013-2014. ....	60
Figure 3.3 – Mooring thermistor line plots, winter 2013-2014.....	61

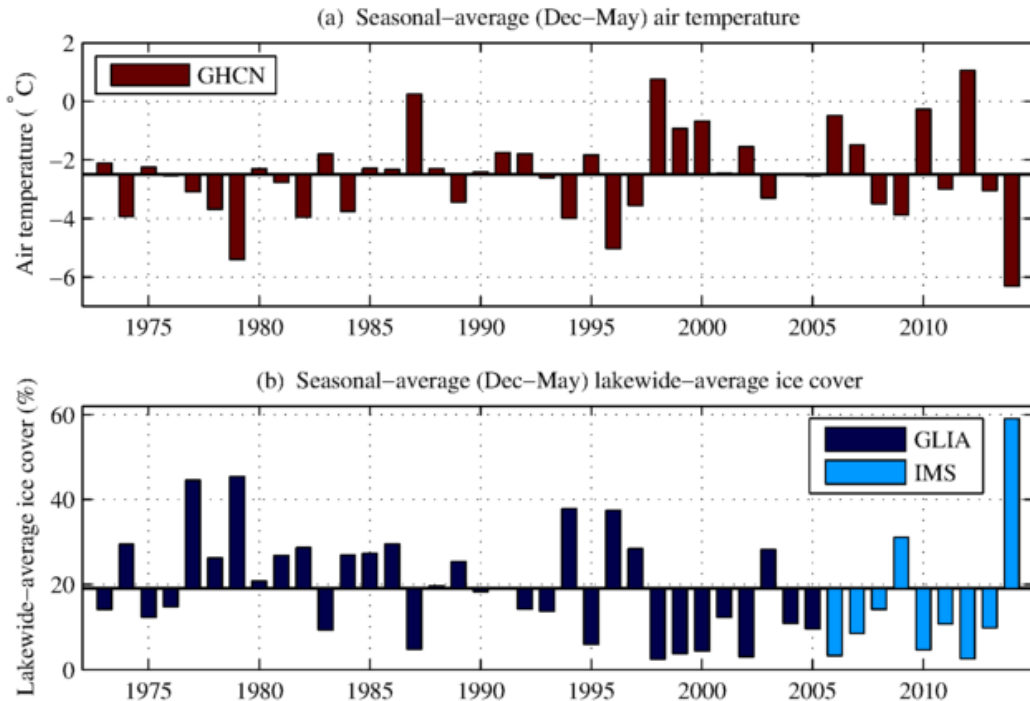
Figure 3.4 – Heat content and ice cover, winter 2013-2014.....	64
Figure 3.5 – Western Mooring water velocity and wind velocity PVD, winter 2013-2014.....	67
Figure 3.6 – Heat redistribution conceptual sketch.....	69
Figure 3.7 – Eastern Mooring water velocity and wind velocity PVD, winter 2013-2014. ....	70
Figure 3.8 – Typical Water current and wind direction.....	72
Figure 3.9 – Lake bathymetry near the Western Mooring. ....	74
Figure 3.10 – Lake bathymetry near the Eastern Mooring. ....	75
Figure 4.1 – Map of relevant locations for Section 4.1 and Section 4.2.....	80
Figure 4.2 – ADCP intensity plots, Winter 2013-2014.....	82
Figure 4.3 – Average ADCP intensity profile, Western Mooring, Winter 2013-2014.....	84
Figure 4.4 – Wind and ice PVDs, Western Mooring, Winter 2013-2014.....	86
Figure 4.5 – Ice speed and wind speed time-series, Winter 2013-2014. ....	88
Figure 4.6 – Determination of linear range of ice speed vs. wind speed. ....	90
Figure 4.7 – Ice speed vs. wind speed relationship.....	92
Figure 4.8 – Ice direction vs. wind direction relationship.....	95
Figure 4.9 – Example of ice locking up, Western Mooring, Februay 2014.....	97
Figure 4.10 – The ratio of ice speed to wind speed as a function of wind direction.....	99
Figure 4.11 – Ice lockup dependency on estimated wind stress and wind direction. ....	100
Figure 4.12 – Western Mooring pressure sensor record, Winter 2013-2014.....	103
Figure 4.13 – Ice keels conceptual diagram.....	105
Figure 4.14 – Central Mooring pressure sensor record, Winter 2013-2014. ....	106
Figure 4.15 – Eastern Mooring pressure sensor record, Winter 2013-2014. ....	107
Figure 4.16 – Profile of deepest Western Mooring ice keel. ....	109
Figure 4.17 – Prevalence of ice keels at the Western Mooring. ....	110
Figure 5.1 – Sensitivity of lakewide average ice cover to air temperature, Lake Superior. ....	115
Figure 5.2 – Sensitivity of lakewide average ice cover to air temperature, Great Lakes.....	117
Figure 5.3 – Seasonally-averaged ice cover relationship with average lake depth.....	119
Figure 5.4 – Ice-cover anomaly ACFs, seasonal timescale, Great Lakes.....	122
Figure 5.5 – Air temperature anomaly ACFs, seasonal timescale, Great Lakes.....	124
Figure 5.6 – CCFs for ice-cover and air temperature, seasonal timescale, Great Lakes.....	126
Figure 5.7 – Correlation ( $r^2$ ) between seasonal ice cover and monthly air temperature. ....	129
Figure 5.8 – Correlation ( $r^2$ ) between ice-on day and monthly air temperature. ....	131
Figure 5.9 – Correlation ( $r^2$ ) between ice-off day and monthly air temperature.....	132
Figure 5.10 – Determination of air temperate most correlated with seasonal-average ice cover.	135
Figure 5.11 – Average (Dec-May) ice cover vs. winter (Dec-Feb) air temperature correlations.	139
Figure 5.12 – Ice-on date vs. December 1 through January 15 air temperature correlations. ....	146
Figure 5.13 – Ice-on date vs. Dec 1-Jan 15 air temperature correlation offset by lake depth.....	147
Figure 5.14 – Spatial variability in ice sensitivity slope, Great Lakes.....	150
Figure 5.15 – Spatial variability in ice sensitivity model accuracy, Great Lakes.....	151
Figure 5.16 – Locations of NSIDC North American lakes with mean depth less than 10 m. ....	153
Figure 5.17 – Portions of the Great Lakes with mean depth less than 10 m.....	154
Figure 5.18 – Ice-air temperature relationship, comparison with small lakes. ....	155
Figure 5.19 – Modeled sensitivity of ice cover to air temperature, 1980-2014 base run.....	160

Figure 5.20 – Ice cover sensitivity analysis with seasonal air temperature.....	162
Figure 5.21 – Ice cover sensitivity analyses with monthly air temperature.....	163
Figure 5.22 – Ice cover sensitivity analysis with lake depth adjustment.....	165

## 1.0 Introduction

The 2013-2014 winter was among the harshest winters on record in the Great Lakes region, producing cold air temperatures in the region and high ice cover on the lakes (Figure 1.1; Clites et al. 2014; Gronewold 2015). This exceptional winter occurred as I was beginning my PhD program, and as subsurface moorings were deployed on Lake Superior (Section 2.1). Data collected from the lake during this cold and icy winter resulted in a unique opportunity to examine ice cover on the Great Lakes in an era characterized by declining ice cover (Wang et al. 2012b; Van Cleave et al. 2014; Wang et al. 2010). In this dissertation, three distinct aspects of ice cover on the Great Lakes are examined:

- The interaction between ice cover and water column processes (Section 3)
- The characteristics of ice during a high-ice cover (Section 4)
- The sensitivity of Great Lakes ice cover to climate variability (Section 5)



**Figure 1.1 – Historic air temperature and ice cover.** Historic seasonal-average values of (a) air temperature and (b) ice cover are plotted relative to their longterm averages. Air temperature data is from the Global Historical Climatology Network (GHCN) datasets (see Section 2.3), and ice cover data is from the Great Lakes Ice Atlas (GLIA) and Ice Mapping System (IMS) datasets (see Section 2.2).

The focus on winter conditions is driven by the lack of winter data from large lakes. This gap in our knowledge of large lakes was discussed in my Masters thesis, the results of which were published as Titze and Austin (2014). In my Masters work, I showed that early-season ice inhibited heat loss from the water column. In Section 3, I expand upon this work and demonstrate that late-season ice delays spring warming. This is a mechanism established empirically by Austin and Colman (2007), but which had not been directly observed. In addition, my Masters work acknowledged the importance of horizontal mixing processes, and I expand upon that work by examining ADCP data alongside thermal structure data. Specifically, I provide evidence that ice-induced shifts in circulation patterns drive large-scale redistribution of heat in the water column.

In Section 4, I examine the characteristics of the ice, itself. I show that ice on Lake Superior is generally free-drifting, even during a high ice year, and that ice keels of greater than 11m depth are present throughout the open water portions of the lake. To my knowledge, these are the first published records of their kind on the Great Lakes. Finally, in Section 5, I examine the relationship between climate and ice cover, and identify interannual variability in air temperature as the main driver of the high degree of interannual ice cover variability observed on the Great Lakes. This dissertation is structured such that each of the aforementioned topics has its own introduction and literature review. After this brief introduction, general methods and data sources are detailed in Section 2, which is intended to serve as a reference for the three subsequent results and discussion sections, and the dissertation ends with a brief conclusion.

## **2.0 Methods and Data Sources**

This section focuses on general methods regarding data collection, including data collected in the field from the Lake Superior mooring array (Section 2.1), as well as data obtained from other sources, including ice cover data (Section 2.2), meteorological data (Section 2.3), bathymetry data (Section 2.4), and water level data (Section 2.5). In addition, the Lake Superior application of the Regional Ocean Modeling System (ROMS) numerical model is discussed, as well as the methods used to calibrate forcing parameters (Section 2.6). This section covers general methods and data sources, while specific to particular analyses are discussed in the sections containing those analyses. Matlab is used for all data analysis in this dissertation. Multi-year analyses are conducted through the year 2014, and any data from the various sources that was collected after 2014 are not considered. Throughout this dissertation, when a particular winter is referred to using a single year, the year corresponds to the portion of the winter from January onward.

### **2.1 Lake Superior Subsurface Mooring Array**

One or more subsurface moorings have been deployed on Lake Superior mooring from fall 2005 through the present (Summer 2016 at the time of this writing). Moorings consist of a cable that is attached at one end to an anchor on the bottom of the lake, and at the other end to a float near the water surface. This results in a cable that spans the water column, to which instruments may be attached at various depths (Figure 2.1). All moorings on the Lake Superior mooring array have been equipped with a series of thermistors, and some have been equipped with additional sensors (see Section 2.1.1 for more about instrumentation).

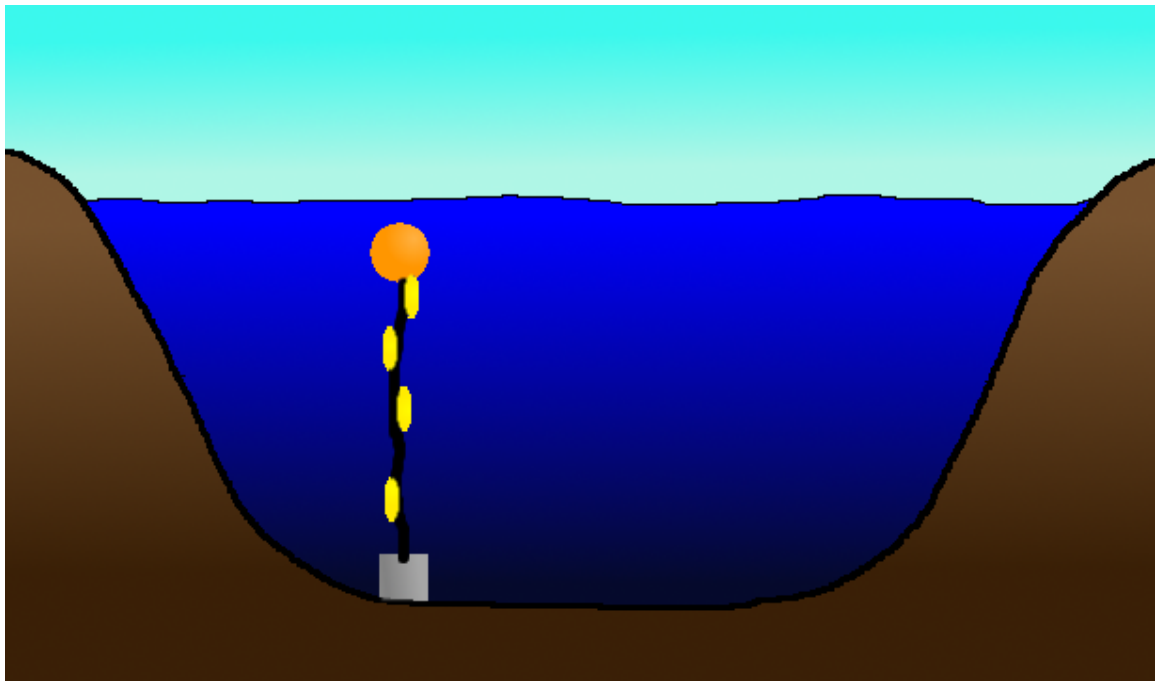


**Figure 2.1 – Conceptual mooring diagram.** This figure depicts a conceptual diagram of a mooring. As shown, moorings consist of a cable that is attached to a top float at one end, anchored to the bottom of the lake at the other, and with instruments attached at various depths along the cable. The diagram is not to scale.

The Lake Superior moorings are deployed at deep, offshore locations, and up to seven moorings have been deployed simultaneously (Figure 2.2). The core mooring array consists of the Western (WM), Central (WM) and Eastern (EM) Moorings, which were deployed within 2 km of the locations of National Data Buoy Center (NDBC) meteorological buoys 45006, 45001, and 45004, respectively (NDBC buoys are discussed in Section 2.3.1). These three core moorings have been supplemented by up to four outer moorings – the Far Western (FWM), Northern (NM), Southern (SM), and Far Eastern (FEM) Moorings – to enhance spatial coverage on the lake. Analyses in this dissertation focus on the core moorings, and especially on the Western and Eastern Moorings.

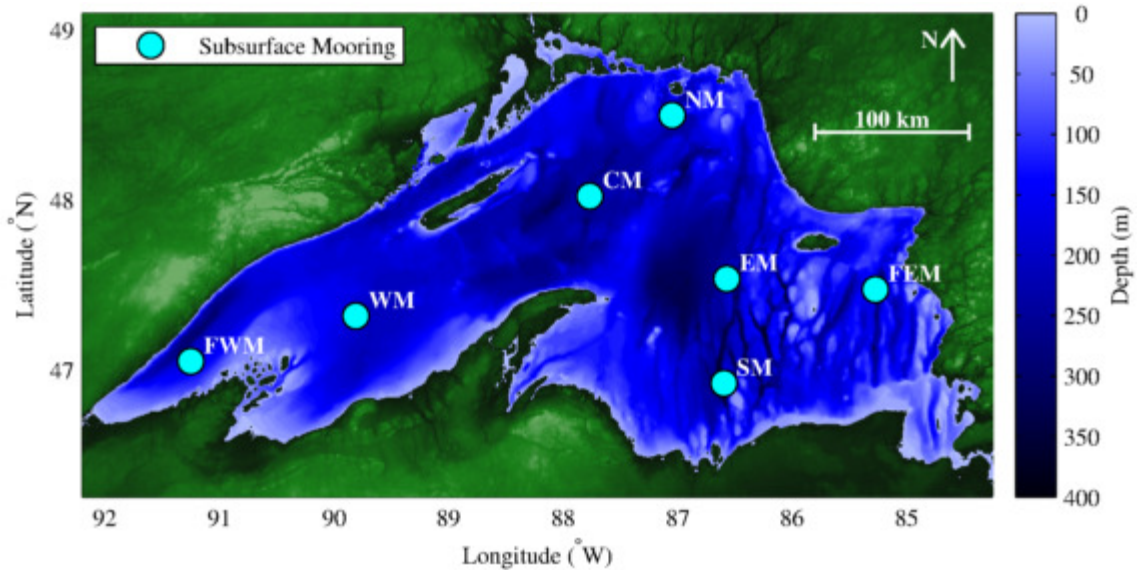


**Figure 2.2 – Map of Lake Superior mooring array.** The locations of subsurface moorings that have comprised the Lake Superior mooring array are shown.

Figure 2.3 shows the deployment history for the Lake Superior mooring array. The Western Mooring was first deployed in fall 2015, with the Central and Eastern Moorings first deployed in spring 2008. Subsequently, the outer moorings were put into service, beginning with the Far Western Mooring in fall 2008, and followed by the Northern, Southern, and Far Eastern Moorings in spring 2009. The four outer moorings were removed from service in spring 2012, while the Central and Eastern Moorings were removed from service in spring 2014. The Western Mooring remains in operation as of summer 2016.

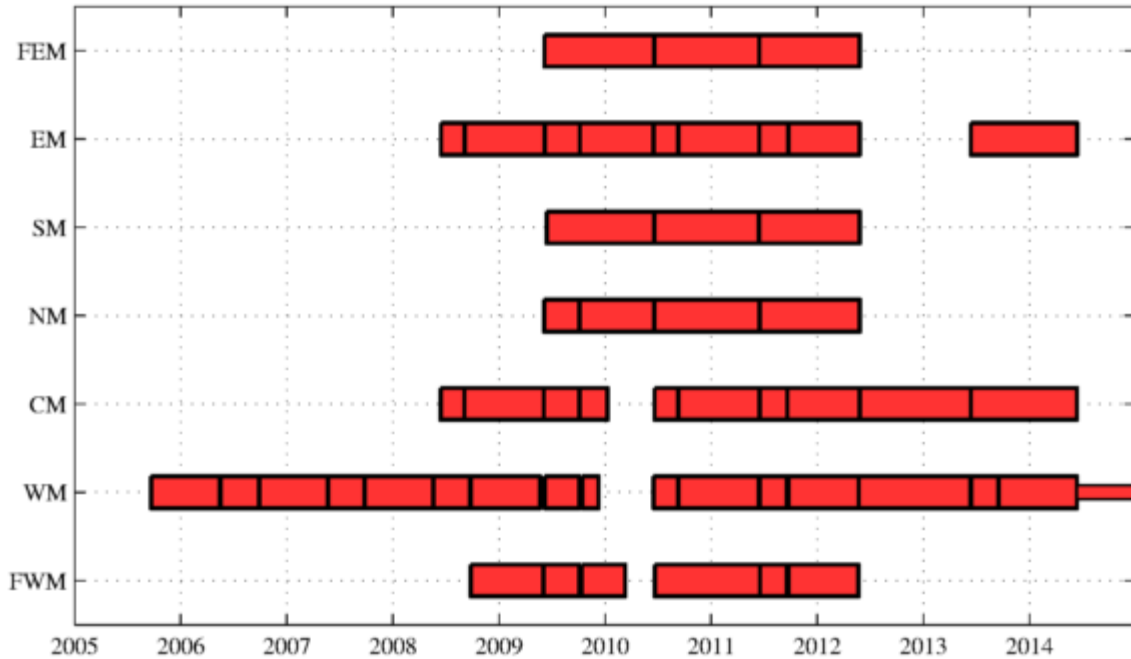


**Figure 2.3 – Lake Superior mooring array deployment history.** The deployment history for the Lake Superior mooring array is shown. Data gaps at FWM, WM, and CM between late 2009 and early 2010, as well as at EM between spring 2012 and spring 2013, are due to failed mooring cables at these locations. The Western Mooring remains in service as of spring 2016.

The short breaks in the data correspond to the brief periods between deployments during which moorings are recovered, necessary maintenance is performed, and moorings are redeployed. Mooring recovery and redeployment occurs in the spring, and sometimes additionally in the fall. These maintenance periods generally span periods of few hours, but may extend up to a couple of days if it is more efficient, in terms of boat time, attend to other moorings in between recovery and redeployment of another mooring.

The longer breaks in data correspond to deployments during which the mooring failed. During the fall 2009 deployment, a faulty batch of mooring cable was used at the Far Western, Western, and Central Moorings, causing them to collapse to the bottom of the lake between late 2009 and early 2010. Instruments connected to these moorings were successfully recovered from the bottom of the lake; however, data collected between the time of cable failure and mooring recovery is not usable. Similarly, a mooring cable corroded through at the Eastern Mooring following the spring 2012 deployment. In this case, most instruments on the mooring could not be recovered, so there is a gap in data at the Eastern Mooring from spring 2012 through spring 2013.

## **2.1.1 Instrumentation**

All moorings have been equipped with thermistors for every deployment, and some have also been equipped Acoustic Doppler Current Profiles (ADCPs), ice profilers, O<sub>2</sub> Sensors, NO<sub>3</sub> sensors, and sediment traps. In addition, each mooring is equipped with two pressure sensors to verify the depth of deployment. I use thermistor data, ADCP data, and pressure sensor data in my analyses, and the operation and configuration of these instruments are discussed in detail in the two subsequent subsections (Section 2.1.1.1 and Section 2.1.1.2).

### **2.1.1.1 *Thermistors and Pressure Sensors***

Each mooring has been equipped with a set of thermistors, which are spaced more closely in the upper portion of the water column, where the strongest temperature gradients occur, and farther apart in the bottom portion of the water column, where temperature gradients are much weaker. A typical mooring configuration includes thermistors at depths of approximately 10 m, 15 m, 20 m, 25 m, 30 m, 40 m, 50 m, 60 m, 80 m, 100 m, and with deeper thermistors spaced 50 m apart down to the lake bottom.

A plot showing the depth coverage of thermistors at the Western, Central, and Eastern Moorings is shown in Figure 2.4. Moorings do not extend to the surface, so that they remain safely below the draft of shipping vessels on the lake. During periods of strong positive stratification in the summer, surface temperatures are available from the nearby NDBC buoys (see Section 2.3.1). During the winter, when NDBC buoys are not in service, the isothermal surface-mixed layer consistently extends significantly deeper than the depth of the uppermost mooring thermistor, as observed from multiple years of data from multiple moorings. This suggests that surface temperature can be adequately estimated from the uppermost thermistor during these periods of weak negative stratification.

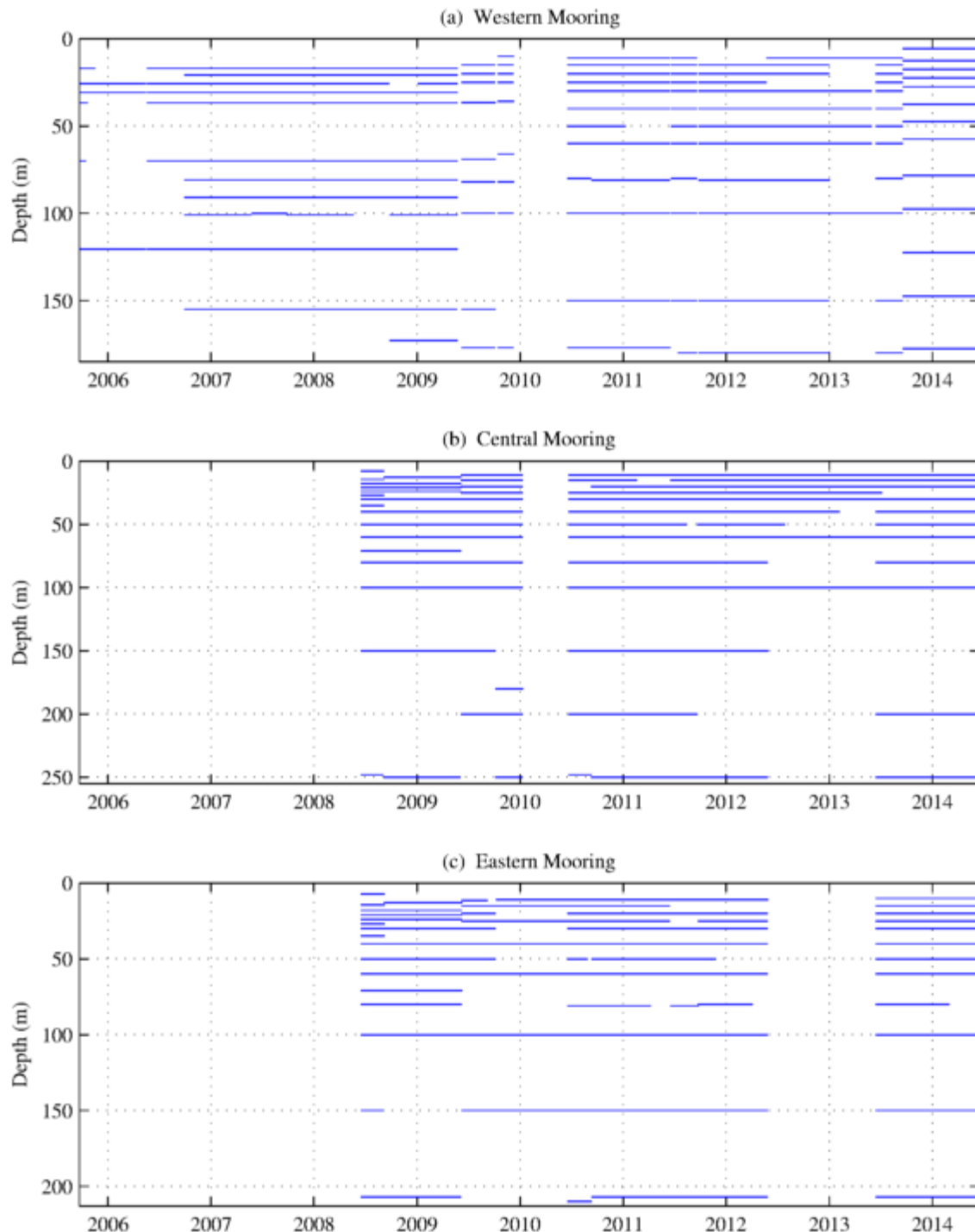


**Figure 2.4 – Thermistor depth coverage for the Western, Central, and Eastern Moorings.** The depths of thermistors are shown for the (a) Western, (b) Central, and (c) Eastern Moorings. Solid lines represent thermistor deployments.

The thermistors used throughout the project have consisted of Brancker Research models TR-1000, TR-1050, TR-1060, TD-2050, and TRsolo, and Seabird Electronics models SBE-39 and SBE-39P. All thermistors were periodically recalibrated, with pre-calibration drifts generally less than 10 mK, and post-calibration accuracy of approximately 2 mK. The TD-2050 and SBE-39P models also contain pressure sensors, and one of these dual temperature-pressure models is used as the 10 m and 100 m sensor on each mooring to verify the depth of the mooring deployment.

The interval at which the thermistors can take measurements over the course of the deployment is limited by their storage capacity and response time. A measurement frequency of 10 min was used for the TR-1000 and SBE sensors, which have response times of several minutes, a measurement frequency of 1 min was used for TR-1050, TR-1060, and TD-2050 sensors, which have response times of approximately 3 s, and a measurement frequency of 10 s was used for TRsolo sensors, which have response times of approximately 1 s. In this thesis, I am looking at season-scale thermal processes, occurring over timescales of days to months, so all temperature data analyzed and presented herein has been binned onto an hourly time grid. This creates a uniform time-grid for all thermistors, which is necessary for some calculations, such as heat content, and reduces file sizes for more efficient computing.

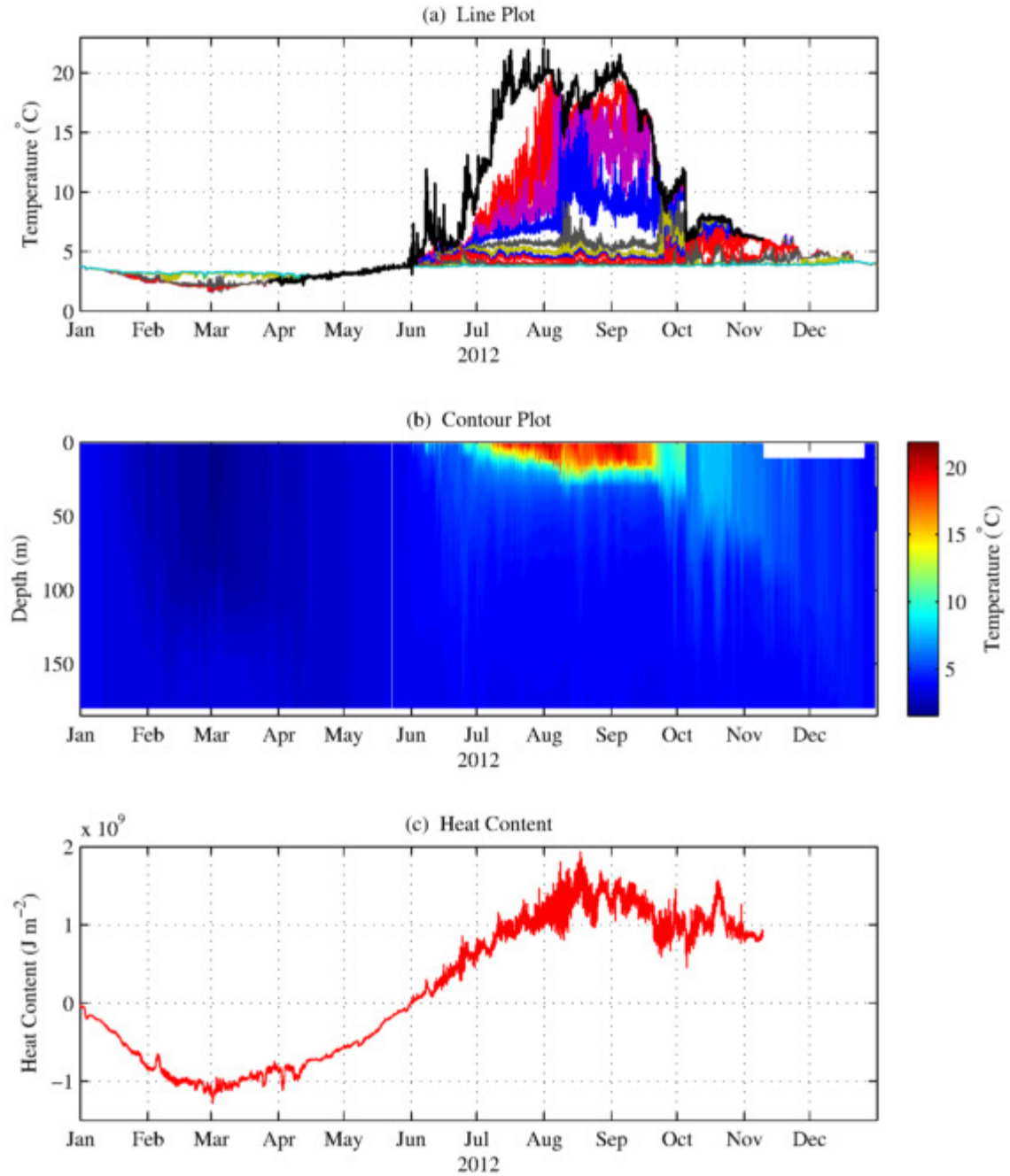


**Figure 2.5 – Visualization of thermistor data.** Data from the Western in 2012 are depicted in three different ways, in conjunction with near-surface data from NDBC buoy 45006. Panel (a) contains a line plot, where raw data from each thermistor is shown as a separate line. No depth legend is included, because individual lines are hard to distinguish. However, the range of temperatures can be accurately read from such a plot. Panel (b) contains a contour plot, where temperature is plotted using color as a third dimension. Panel (c) shows the heat content of the water column, relative to the temperature of maximum density.

Figure 2.5 is included as an example of the data collected by thermistors, and shows three different ways to depict the data. Figure 2.5a shows a line plot, where a time-series from each thermistor is plotted as a separate line. Given the number of themistors, this plot is not intended to be used to read the temperature at a given depth (as such, no legend is included); rather, it is intended to accurately show the range of temperatures in the water column, from which such parameters as surface temperature, bottom temperature, and the relative degree of positive or negative stratification can be inferred. Figure 2.5b shows a contour plot, where temperature is plotted as a function of depth and time. This sort of plot is useful for examining changes in the thermal structure of the water column over time, such as the depth of the thermocline. However, it is difficult to read temperature precisely from a contour plot, because it is plotted using color as a third dimension. Finally, Figure 2.5c shows the heat content of the water column, in which thermistor data is integrated throughout the water column, relative to the pressure-dependent (and therefore depth-dependent) temperature of maximum density, to determine the total heat in the water column relative to that reference:

$$H \approx \rho c_p \sum_{i=1}^n [T_i - T_{MD}(z_i)] \Delta z_i \quad \text{Equation 2.1}$$

Where  $H$  [ $\text{J m}^{-2}$ ] is the heat content,  $\rho$  [ $\text{kg m}^{-3}$ ] is the density of the water,  $c_p$  [ $\text{J kg}^{-1} \text{K}^{-1}$ ] is the specific heat capacity of water,  $T$  [K] is the temperature of the water at depth  $z$  [m].  $T_{MD}$  [K] is the depth-dependent temperature of maximum density, and  $z_i$  [m] is the depth of the thermistor layer defined as having boundaries equidistant between adjacent thermistors.

Sensor depth ( $z_{sensor}$ ) is determined by subtracting the regional atmospheric pressure ( $P_{atm}$ ) from the pressure sensor readings ( $P_{sensor}$ ), and using the hydrostatic equation:

$$z_{sensor} = \frac{P_{sensor} - P_{atm}}{\rho g} \quad \text{Equation 2.2}$$

Where density ( $\rho$ ) is taken to be a constant  $1000 \text{ kg m}^{-3}$ , and gravity ( $g$ ) is  $9.81 \text{ m s}^{-2}$ . The regional air pressure is determined using the data from the ROAM4 NDBC station (see Section 2.3.1).

Figure 2.6 demonstrates the process through which pressure sensor data is corrected to determine the depth of the pressure sensor.

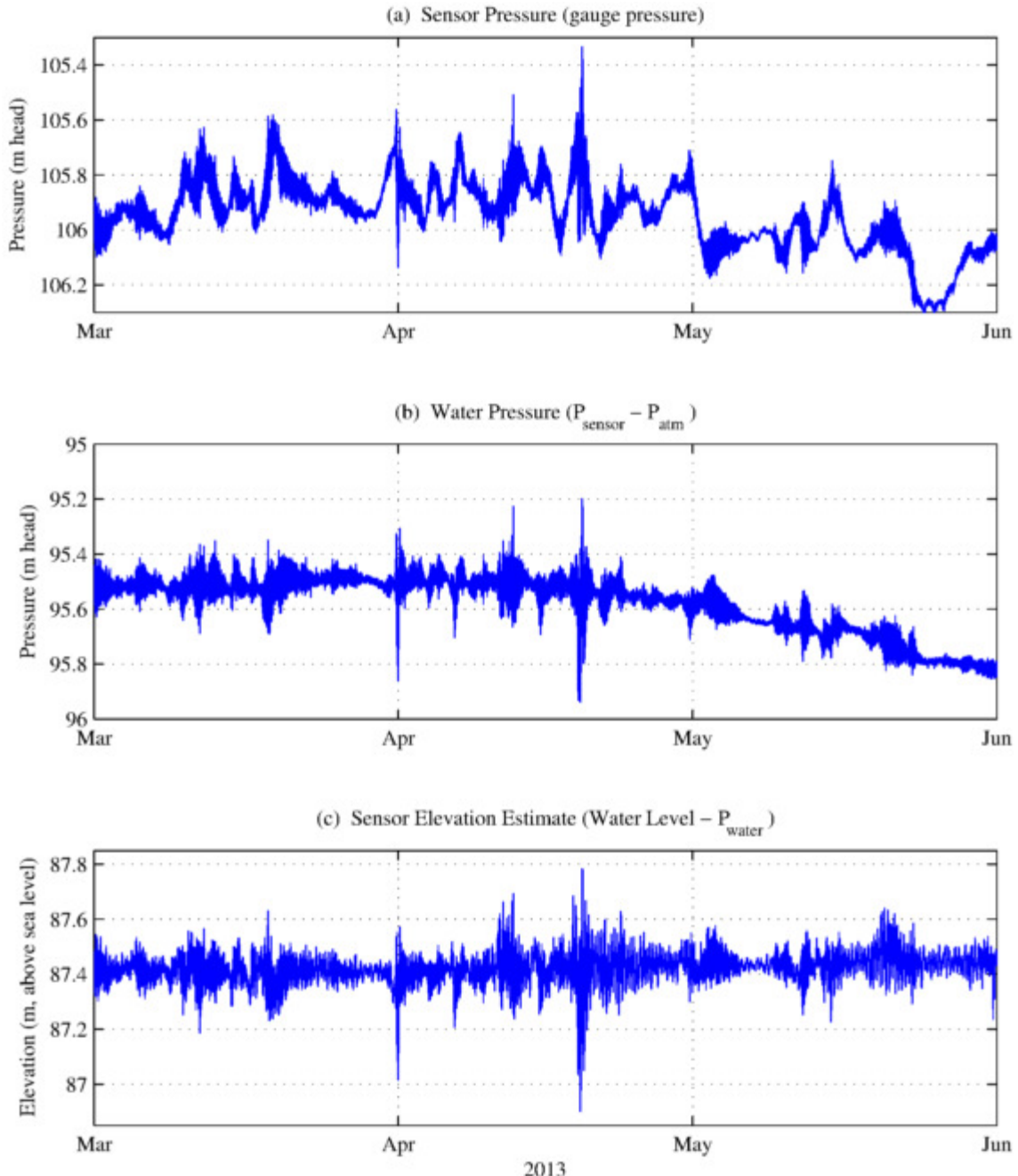


**Figure 2.6 – Determination of pressure sensor depth.** This figure presents pressure sensor data from the Central Mooring in 2013 as an example of how pressure sensor data can be corrected for air pressure to determine sensor depth. Panel (a) shows uncorrected data from the pressure sensor, converted to m head, which can be referred to as gauge pressure. Panel (b) shows the same data after the air pressure signal has been removed, based on data from NDBC station ROAM4, which is representative of sensor depth. Panel (c) shows the data relative to the water level at the Grand Marais, MN station, for which the mean signal is an estimate of sensor elevation.

The pressure readings from the sensor (Figure 2.6a) correspond to the absolute pressure. Because the absolute pressure includes both the pressure signal from the atmosphere and the pressure signal from the water volume, there are significant fluctuations at timescales on the order of days, corresponding to synoptic-scale fluctuations in the atmospheric pressure. Once the atmospheric signal is subtracted, these synoptic-scale fluctuations are removed (Figure 2.6b). High frequency fluctuations remain, on the order of seconds or minutes, which correspond to surface gravity waves, as well as a seasonal-scale trend, which corresponds to seasonal fluctuations in the water level. When pressure readings are additionally corrected for the water level of the lake (Figure 2.6c), in this case based on data from the water level station 9099090, located in Grand Marais, MN (National Oceanographic and Atmospheric Administration Tides and Currents 2015; see Section 2.5), it can be seen that the mean signal remains constant with time, and that only the gravity-wave-induced high frequency variability remains.

### **2.1.1.2      *Acoustic Doppler Current Profilers (ADCPs)***

Acoustic Doppler Current Proilers (ADCPs) are designed to measure water currents. ADCPs operate by producing an acoustic signal outward from each of its multiple beams. In the case of RDI Workhorse ADCPS, there are four beams that are oriented approximately 20° outward in different directions from the ADCP axis. In addition, ADCPs contain a compass, so the cardinal orientation of the beams is known, as well as the pitch and roll of the instrument. After the acoustic signal is produced, scatterers in the water column reflect a portion of the signal back toward the ADCP, and based upon the Doppler shift of this return signal along each of the beam axes of different known orientations, the velocity of the scatterers can be estimated. The velocity of scatters is used as a proxy for the velocity of the water. Additionally, ADCPs contain a thermistor, so that the sound-speed velocity can be determined and used to calculate the distance that the acoustic signals have traveled at different time intervals. By listening for the return signal at different time intervals, the ADCP can estimate water velocity at different distances from the ADCP, thereby producing a profile of water velocity in the direction that the ADCP is looking.

All ADCPs used in the mooring array were 300 kHz or 600 kHz RDI Workhorse models. ADCP deployments associated with the Lake Superior mooring array are listed in Table 2.1, including the configuration of each ADCP. The Western Mooring was deployed approximately 3 m

shallower than designed over the 2013-2014 winter, so the ADCP was positioned at about 77 m depth, with a range of 80 m. This resulted in unintended measurements of ice drift, which are discussed in detail in Section 4.1.

Mooring	Deployment	Direction	Depth (m)	Range (m)	Bin-Size (m)	Meas. Freq. (min)	Data Timespan
Far Western	Fall 2008	Upward	80	82	4	60	Sep 08 – Jun 09
Western	Fall 2008	Upward	80	82	4	60	Sep 08 – Jun 09
Western	Fall 2008	Downward	115	81	2	60	Sep 08 – May 09
Western	Spring 2009	Upward	80	80	2	60	Jun 09 – Oct 09
Western	Spring 2009	Downward	115	80	2	60	Jun 09 – Oct 09
Western	Fall 2009	Upward	80	80	2	60	Oct 09 – Feb 10
Western	Fall 2009	Downward	115	80	2	60	Oct 09 – Jun 10
Western	Spring 2010	Upward	80	80	2	60	Jun 10 – Sep 10
Western	Fall 2010	Upward	80	80	2	60	Sep 10 – Jun 11
Western	Fall 2010	Downward	155	30	1	60	Apr 11 – Jun 11
Western	Spring 2011	Upward	80	80	2	60	Jun 11 – Sep 11
Western	Spring 2012	Upward	80	80	2	20	May 12 – Oct 12
Western	Fall 2013	Upward	77	80	2	20	Sep 13 – Jun 14
Western	Spring 2014	Upward	80	72	1	30	Jun 14 – Nov 14
Central	Spring 2009	Upward	80	80	2	60	Jun 09 – Oct 09
Central	Fall 2010	Upward	80	80	2	60	Sep 10 – Jun 11
Central	Spring 2011	Upward	80	80	2	60	Jun 11 – Sep 11
Northern	Fall 2009	Upward	80	80	2	60	Oct 09 – Jun 10
Eastern	Spring 2008	Upward	80	80	2	60	Jun 08 – Sep 08
Eastern	Fall 2008	Upward	80	80	2	60	Sep 08 – Jun 09
Eastern	Spring 2009	Upward	80	80	2	60	Jun 09 – Oct 09
Eastern	Fall 2009	Upward	80	80	2	60	Oct 09 – Jun 10
Eastern	Spring 2010	Upward	80	80	2	60	Jun 10 – Sep 10
Eastern	Fall 2010	Upward	80	80	2	60	Sep 10 – Dec 10
Eastern	Spring 2011	Upward	80	80	2	60	Jun 11 – Sep 11
Eastern	Spring 2013	Upward	80	80	2	60	Jun 13 – Jun 14
Eastern	Spring 2014	Upward	80	80	2	20	Jun 14 – Jun 15

**Table 2.1 – ADCP deployment list.** All ADCP deployments associated with the Lake Superior mooring array are listed. The table shows which mooring the ADCP was deployed on, the season in which the ADCP was deployed, the direction the ADCP was looking, the depth at which the ADCP was deployed, the range of distance away from the ADCP included in the velocity measurement profile, the bin-size for velocity measurements in the profile, the frequencies at which measurements were taken, and the months during which measurements are available for that ADCP deployment.

## **2.2 Ice Cover Data**

Remotely sensed ice cover data used in this dissertation was obtained from two sources: the Great Lakes Ice Atlas (GLIA) datasets (Assel 2003; Assel 2005; Wang 2012a), and the National Ice Center (NIC) Ice Mapping System (IMS) datasets (National Ice Center 2008). The GLIA data is available on a consistent time grid for the winters of 1973 to 2005, and the IMS data is available for the winters of 2005 to present. These datasets are discussed in the following two subsections.

### **2.2.1 Great Lakes Ice Atlas (GLIA) Datasets**

The GLIA is a compilation of ice data from various sources and is specific to the Great Lakes region. Daily lakewide-average ice cover values are available for the winters of 1973 through 2005 for each of the Great Lakes. In addition to these lakewide averages, spatially-resolved data are available for each lake for the winters of 1973 through 2002. These spatially-resolve data have a grid spacing of approximately 2.5 km, and ice coverage is estimated to the nearest 10% within each grid point. An example of GLIA ice cover data from March 1, 1997 is shown in Figure 2.7.

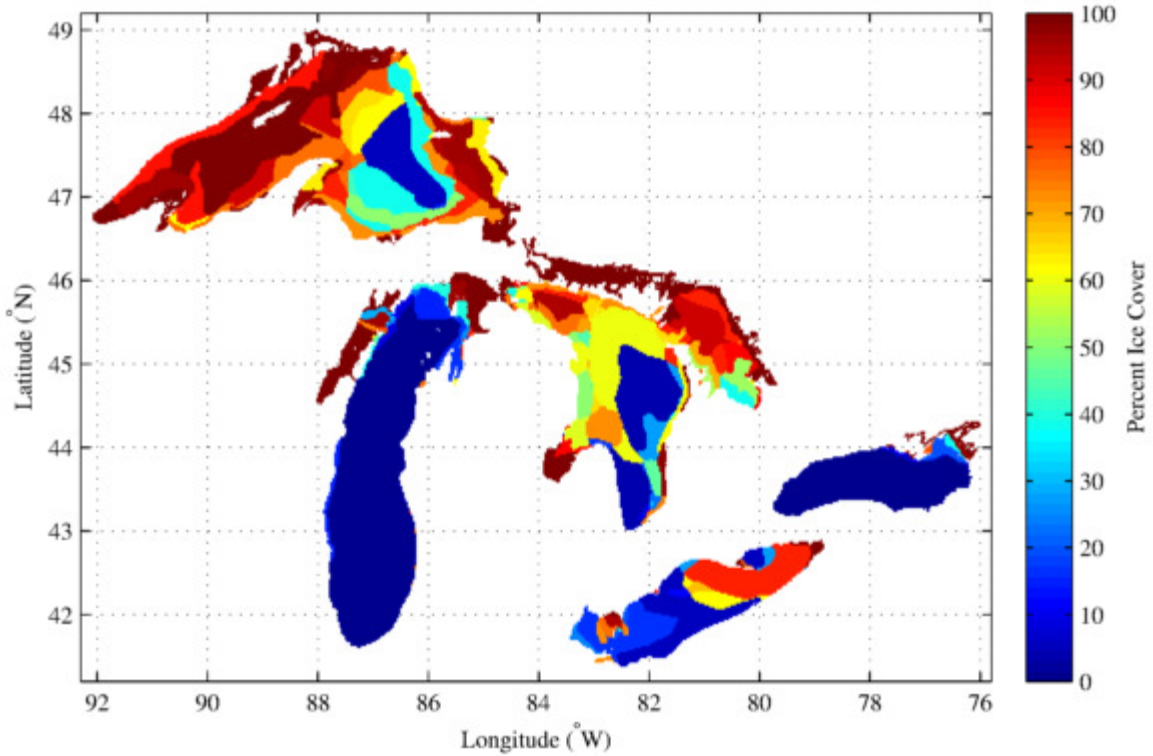


**Figure 2.7– GLIA data example.** This figure shows Great Lakes ice cover data for March 1, 1997 as an example of the type of data available from the GLIA datasets for years for which spatially resolved data are available. For each grid point, the areal ice coverage is estimated to the nearest 10%.

### 2.2.2 Ice Mapping System (IMS) Datasets

The IMS dataset is derived from satellite data, and is available for the entire northern hemisphere. Data are available at nominal 24-km grid spacing from February 1997 to present, at nominal 4-km grid spacing from January 2004 to present, and at nominal 1-km grid spacing from December 2014 to present. In this thesis, I use the 4-km dataset. IMS maps are manually produced by a satellite analyst, using primarily visual imagery, but incorporating microwave imagery and data from previous days when cloud cover is present. The IMS data are binary, indicating only whether ice was present or absent in each grid point, and do not give any information regarding ice thickness or the fraction of ice cover within a grid point. An example of 4-km IMS data for March 1, 2009 is shown in Figure 2.8.

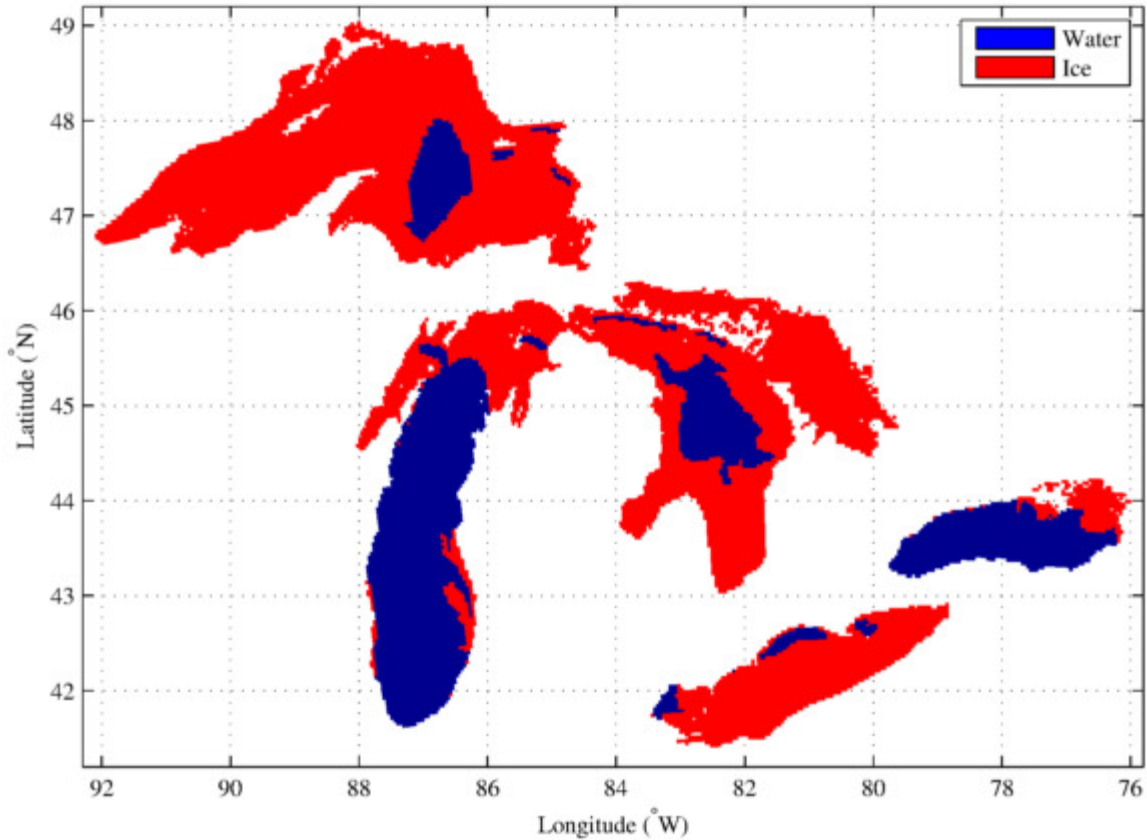


**Figure 2.8 – IMS data example.** This figure shows IMS ice cover data for March 1, 2009 as an example of the type of data available from the IMS datasets. For each grid point, a binary value for the presence ice cover or open water is given.

### 2.2.3 Combining the GLIA and IMS ice datasets

Because the GLIA data is not available for winters after 2005, and the IMS data are not available for winters before 2004 (or before 1998 in the case of the 24-km dataset), the datasets must be combined to form a complete historic record. Such a record is necessary for long-term analyses of interannual ice cover variability, such as those in the ice sensitivity analyses in Section 5.0 . Given that the GLIA and IMS datasets overlap for the winter of 2005, the two datasets can be compared to ensure there is no significant bias associated with the datasets' methods, and that the two datasets can be reasonably combined.

Ice cover data from the GLIA and the IMS are compared in Figure 2.9 for the winter of 2005, which is the only winter for which data is available from both datasets. As can be seen in Figure 2.9, the two datasets are in reasonably good agreement over the 2005 winter. While there are some periods during which the two datasets diverge, they capture the same general trends throughout the season and there does not appear to be any systematic bias between the datasets. As such, it is reasonable to combine the GLIA data for the winters of 1973 through 2005 with the IMS data for the winters of 2006 through 2014 to create a long-term record.

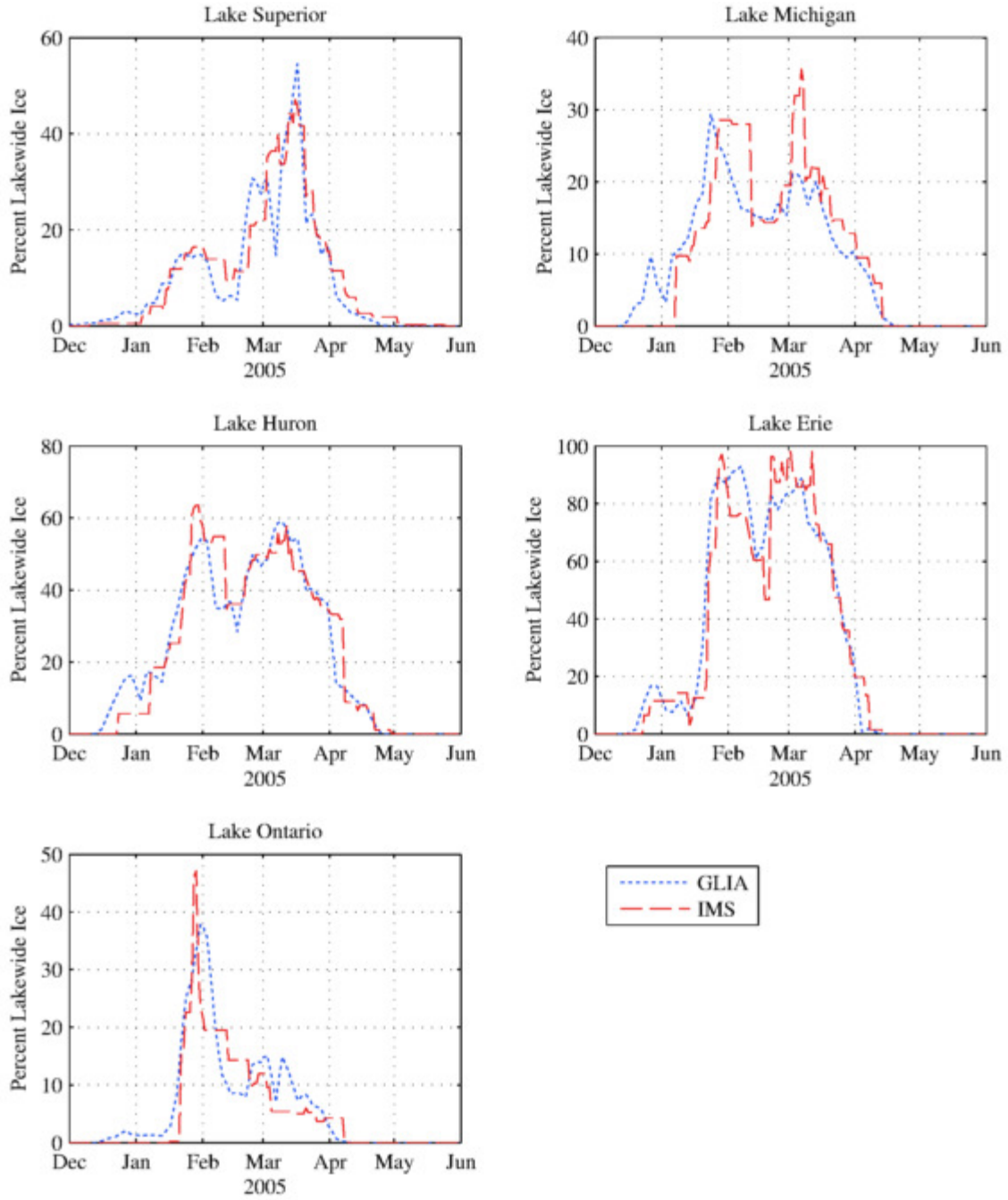


**Figure 2.9 – Comparison of GLIA and IMS datasets.** Ice cover data from the GLIA and the IMS are compared for the winter of 2005, the only year during which data is available from both datasets. Lakewide average ice cover is shown for each of the Great Lakes. The dotted blue line represents GLIA data, and the dashed red line represents IMS Data.

## **2.3 Meteorological Data**

Meteorological data were obtained from multiple different sources for use in different analyses. Meteorological observations were obtained from the National Data Buoy Center (NDBC) database (National Data Buoy Center 2015), and from the Global Historical Climatology Network (GHCN) datasets (National Centers for Environmental Information 2015b). In addition, meteorological reanalysis data was obtained from the North American Regional Reanalysis (NARR) product (National Center for Environmental Prediction 2015). Details regarding these datasets, including the advantages and disadvantages of each, are discussed in Section 2.3.1 (NDBC), Section 2.3.2 (GHCN), and in Section 2.3.3 (NARR).

### **2.3.1 National Data Buoy Center (NDBC) Database**

The NDBC hosts data from a number of meteorological buoys and coastal meteorological stations around the lake (National Data Buoy Center 2015). The stations are owned and operated by the NDBC, the National Oceanic and Atmospheric Administration's National Ocean Service, and the National Weather Service, among others. The Austin lab at the Large Lakes Observatory (LLO) at University of Minnesota Duluth maintains two meteorological buoys as part of the Great Lakes Observing System (GLOS), which are included in the database. Both of these buoys are in the far western arm of Lake Superior, with one of the buoys located near-shore, referred to as LLO1 (NDBC station 45027), and the other located off-shore, referred to as LLO2 (NDBC station 45028).

Data availability within the NDBC database varies by station. Datasets from stations around the Great Lakes extend back as far as 1979 at some stations, with most stations beginning operation in 2005 or later. Hourly measurements of air temperature, wind velocity, and air pressure are available at most stations, and measurements of wave height and surface water temperature are available at select stations. The fact that most stations in the NDBC database do not have winter data prior to 2005 in the Great Lakes Region limit the use of NDBC in longer-term analyses of winter interannual variability. However, the relatively high temporal resolution of the data from more recent years makes these datasets well-suited for analyses where high temporal resolution is important.

The locations of NDBC data stations and their corresponding data availability are shown for Lake Superior (Figure 2.10 and Figure 2.11), Lake Michigan (Figure 2.12 and Figure 2.13), Lake

Huron (Figure 2.14 and Figure 2.15), Lake Erie (Figure 2.16 and Figure 2.17), and Lake Ontario (Figure 2.18 and Figure 2.19).

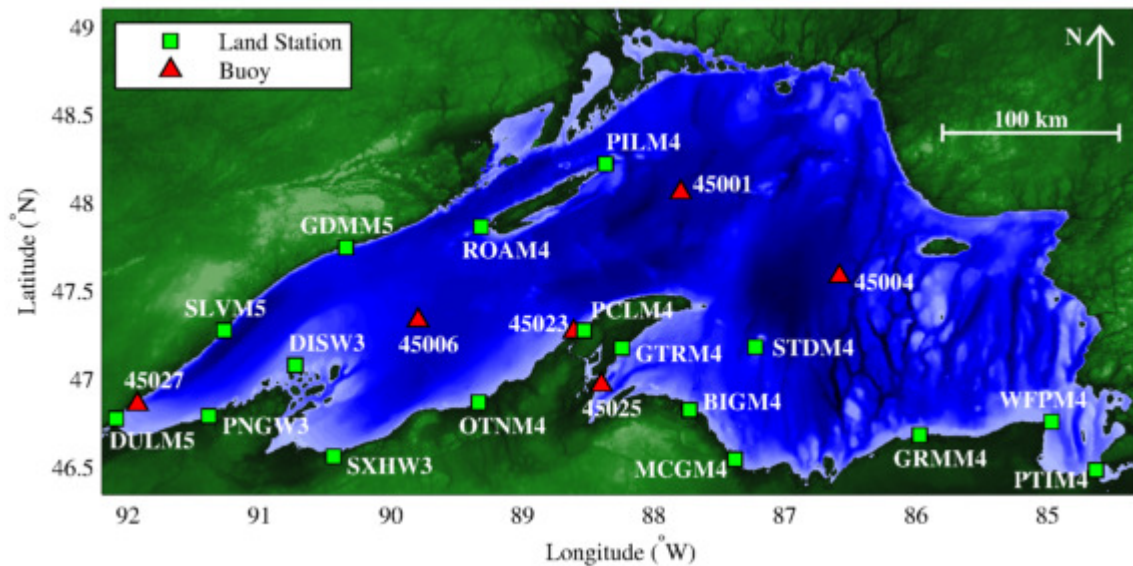


**Figure 2.10 – NDBC database station locations, Lake Superior.** Stations on Lake Superior that are part of the NDBC database are shown. Red triangles represent offshore buoy stations, and green squares represent land-based coastal stations.

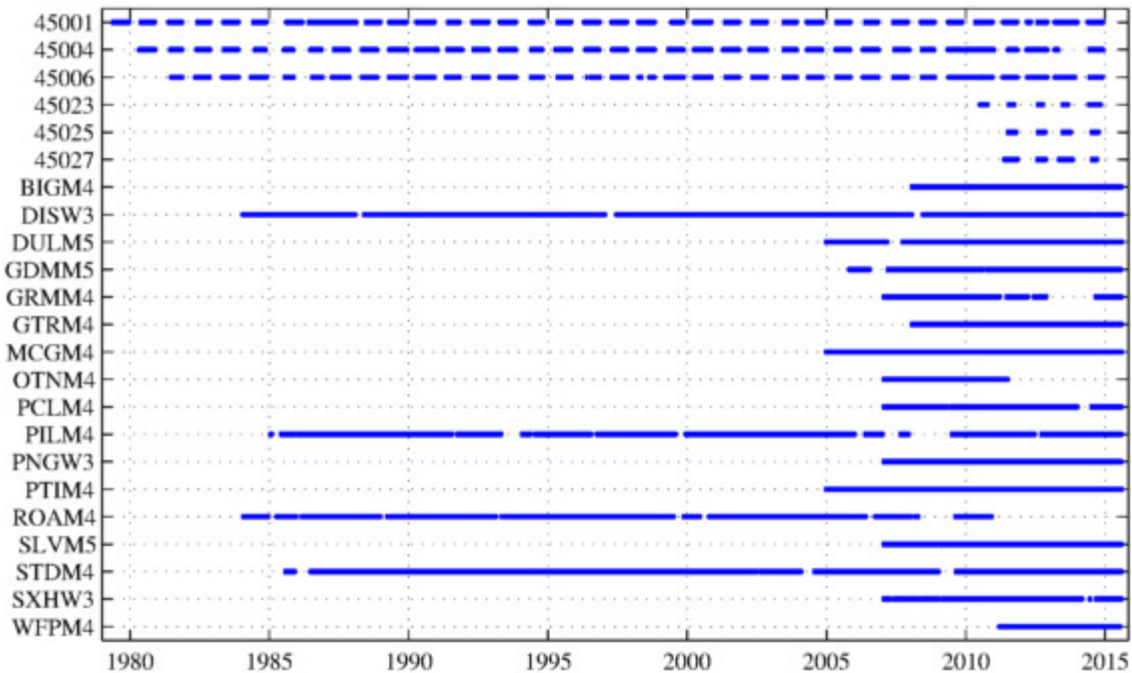


**Figure 2.11 – NDBC database data availability, Lake Superior.** The availability of NDBC database data for stations on Lake Superior is shown. Solid lines represent the times for which data are available at the listed station.

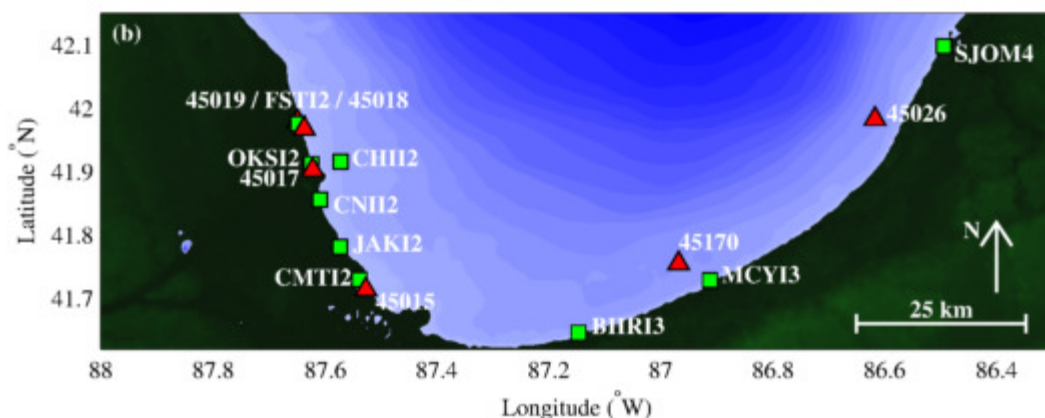
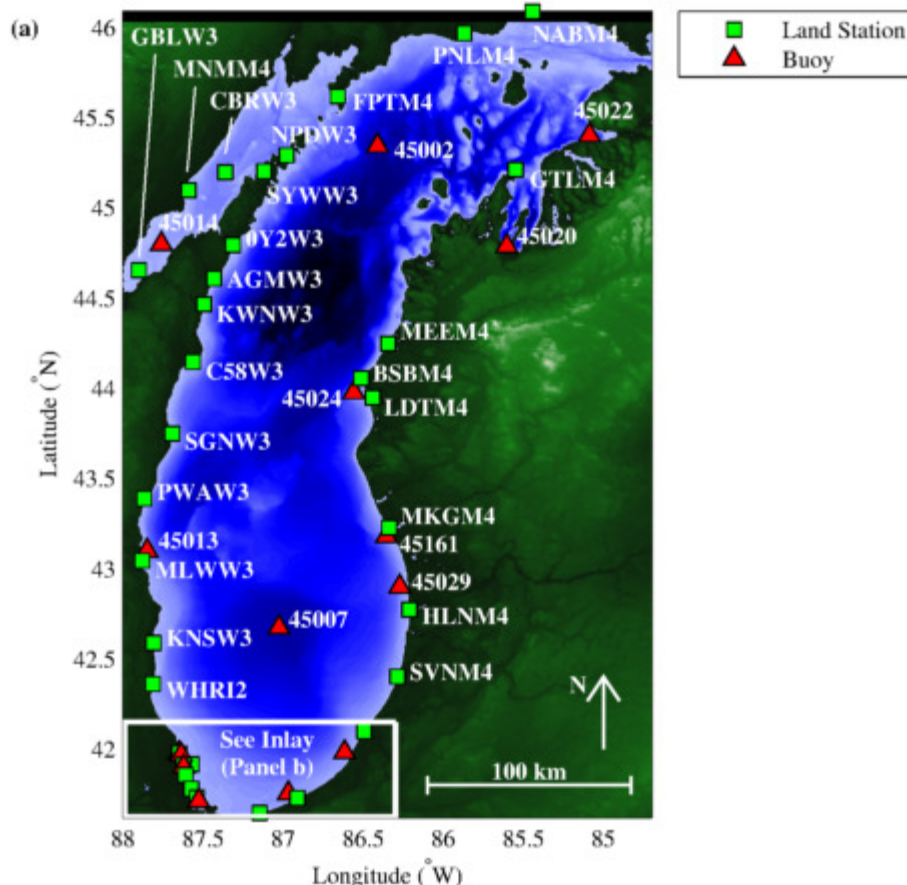


**Figure 2.12 – NDBC database station locations, Lake Michigan.** Stations on Lake Michigan that are part of the NDBC database are shown. Red triangles represent offshore buoy stations, and green squares represent land-based coastal stations. Given the density of stations in the south part of the lake, both (a) an overview of stations on the lake, and (b) an inlay for the southern region of the lake are provided.

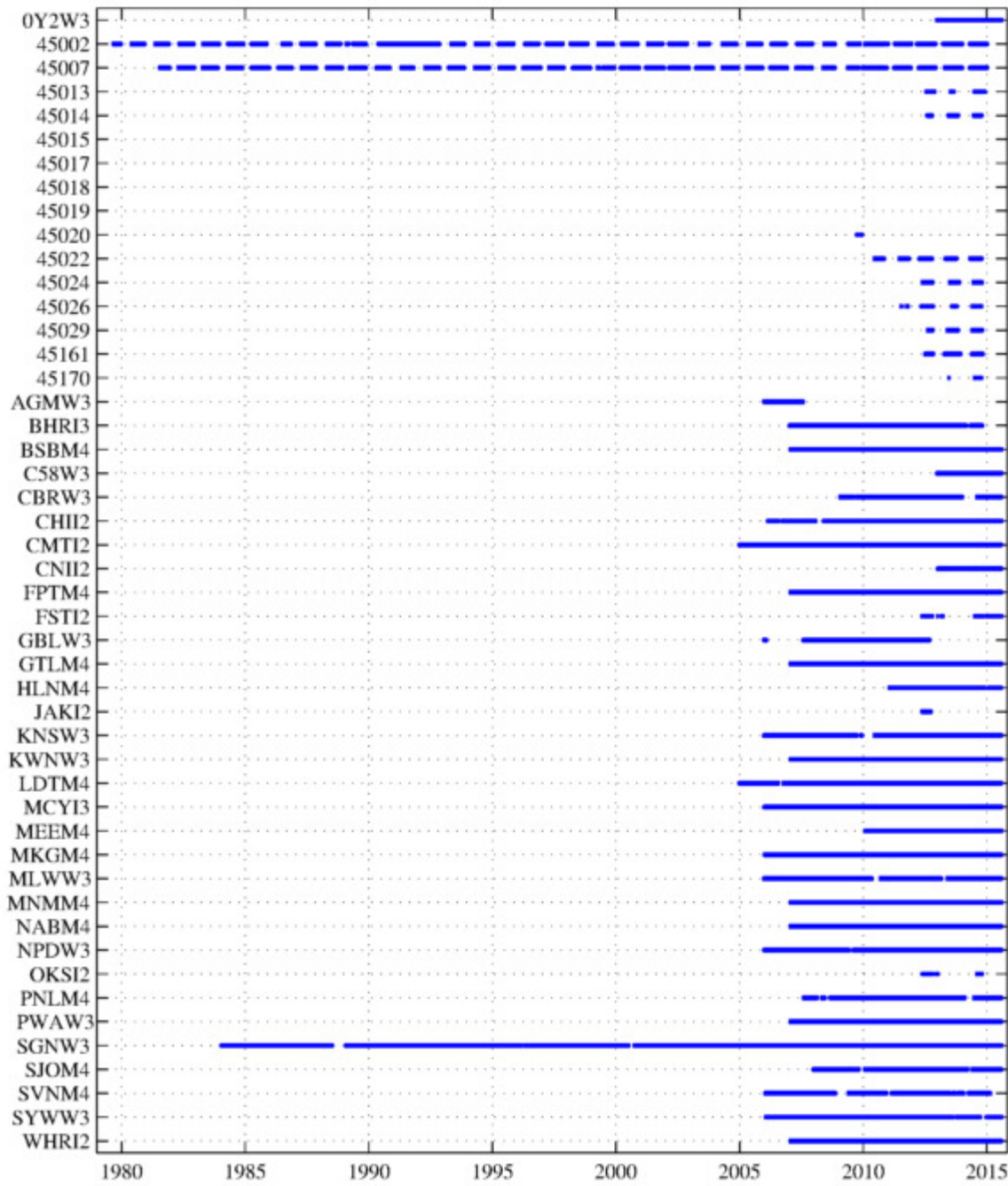


**Figure 2.13 – NDBC database data availability, Lake Michigan.** The availability of NDBC database data for stations on Lake Michigan is shown. Solid lines represent the times for which data are available at the listed station.

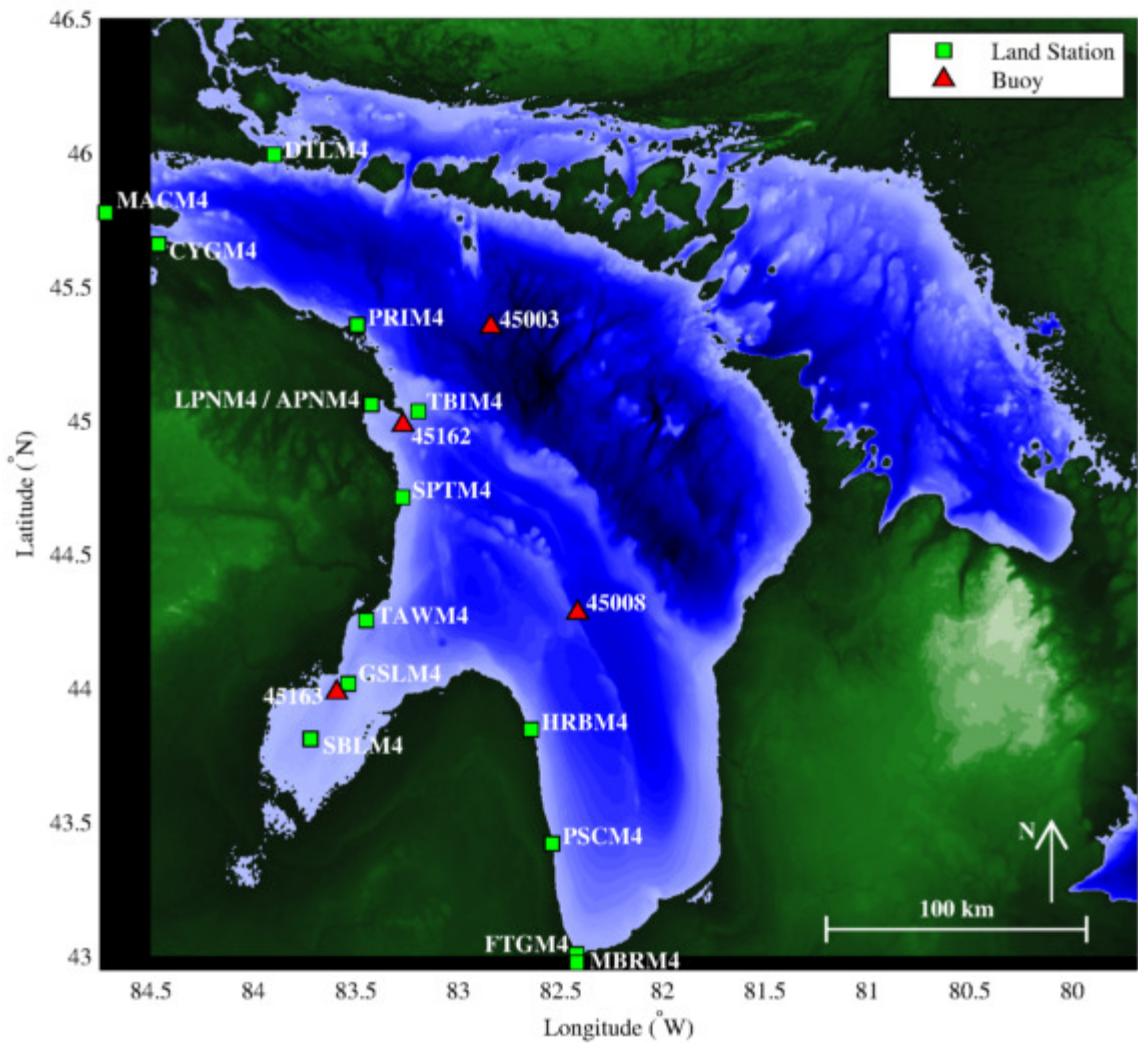


**Figure 2.14 – NDBC database station locations, Lake Huron.** Stations on Lake Huron that are part of the NDBC database are shown. Red triangles represent offshore buoy stations, and green squares represent land-based coastal stations.

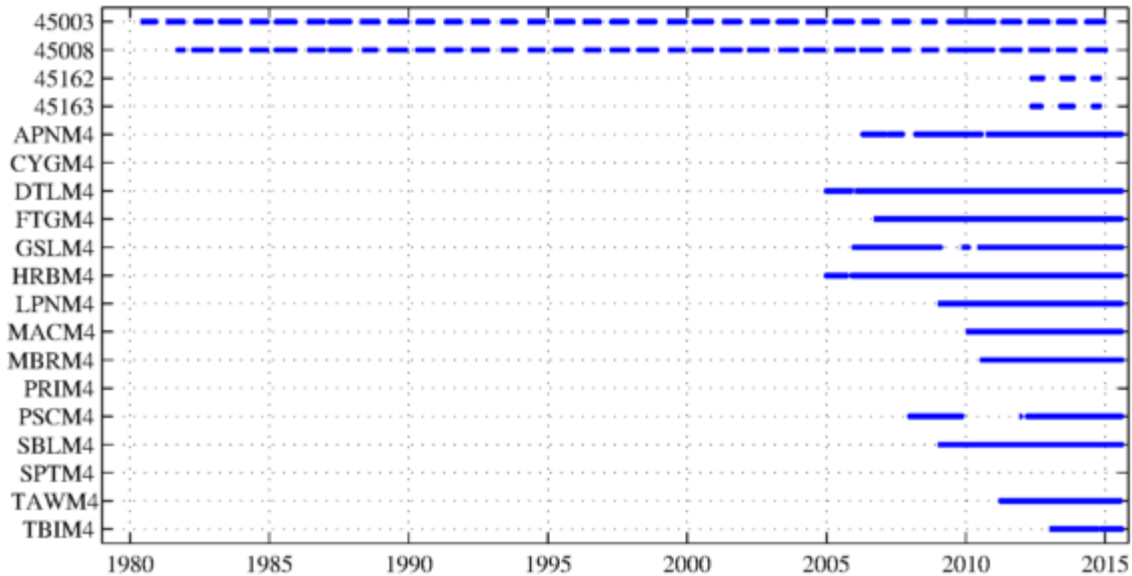


**Figure 2.15 – NDBC database data availability, Lake Huron.** The availability of NDBC database data for stations on Lake Huron is shown. Solid lines represent the times for which data are available at the listed station.

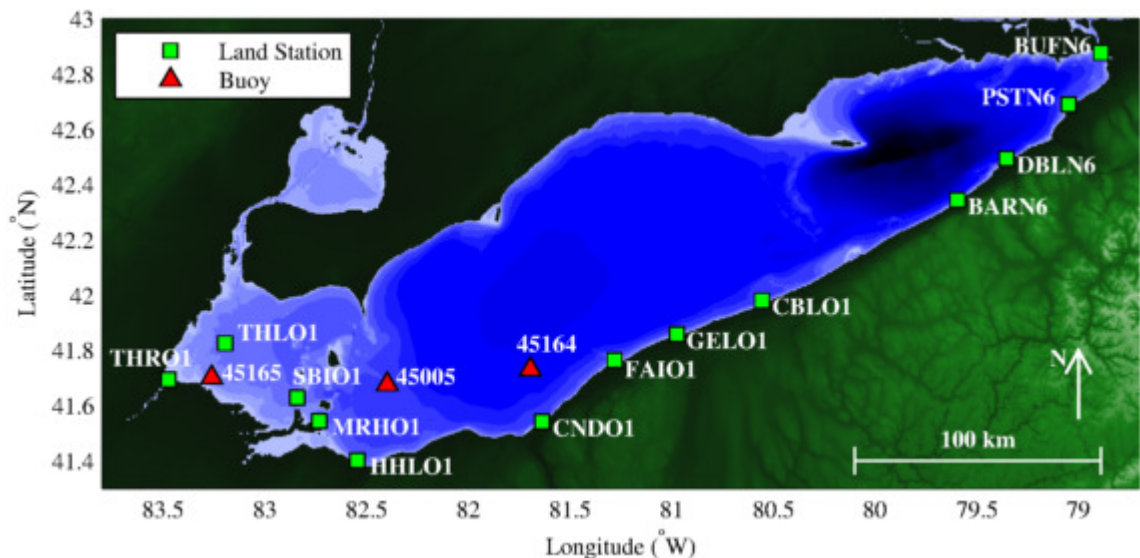


**Figure 2.16 – NDBC database station locations, Lake Erie.** Stations on Lake Erie that are part of the NDBC database are shown. Red triangles represent offshore buoy stations, and green squares represent land-based coastal stations.

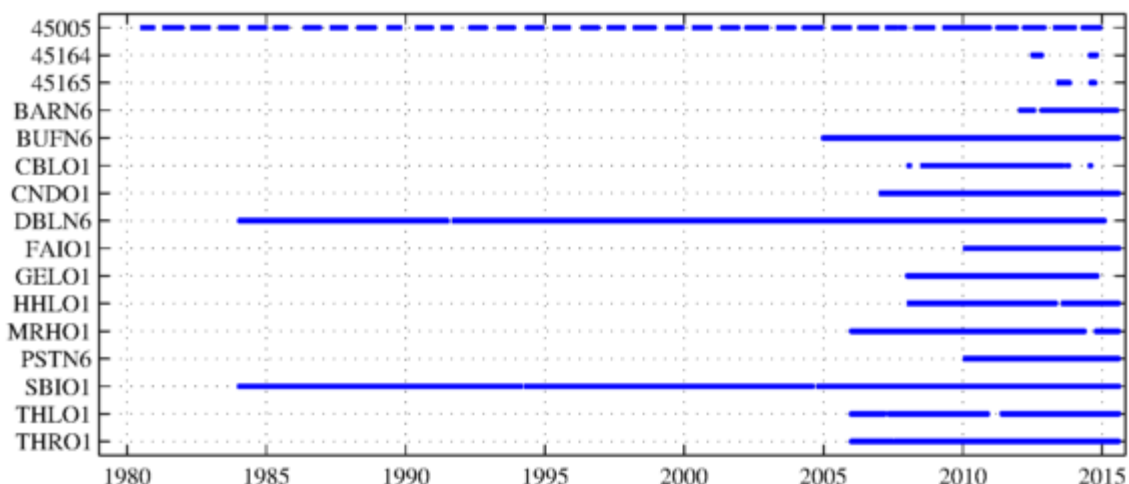


**Figure 2.17 – NDBC database data availability, Lake Erie.** The availability of NDBC database data for stations on Lake Erie is shown. Solid lines represent the times for which data are available at the listed station.

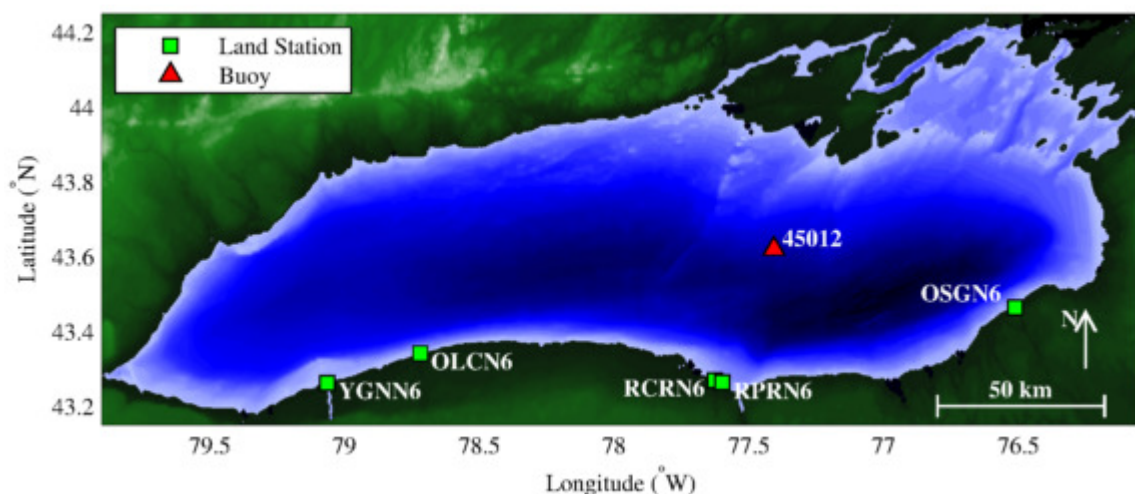


**Figure 2.18 – NDBC database station locations, Lake Ontario.** Stations on Lake Ontario that are part of the NDBC database are shown. Red triangles represent offshore buoy stations, and green squares represent land-based coastal stations.

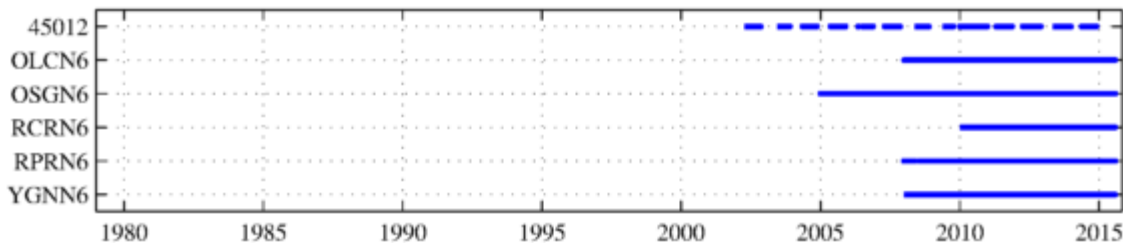


**Figure 2.19 – NDBC database data availability, Lake Ontario.** The availability of NDBC database data for stations on Lake Ontario is shown. Solid lines represent the times for which data are available at the listed station.

### 2.3.2 Global Historical Climatology Network (GHCN) Database

The GHCN is a database of climate records from around the world (National Centers for Environmental Prediction 2015b). Data is available at daily intervals, with wind speed and air temperature measurements dating back over a century at some stations. Unlike the datasets contained in the NDBC database, the GHCN data are not limited to that from coastal stations or buoys. In addition, the GHCN stations have data from Canadian stations, while the NDBC datasets are limited to the United States.

While the GHCN database has the advantage of a wider station distribution and longer temporal coverage, data is available at only daily intervals, and only minimum and maximum air temperatures are reported; average air temperature is not reported. Additionally, only maximum wind gusts are reported, and metrics used to characterize these wind gusts are generally not consistent throughout the longer time-series. Therefore, it is generally not possible to compile a complete long-term historic time-series of any one wind speed parameter, and GHCN wind velocity parameters were not used in any analyses. The long-term nature of the datasets makes them well-suited for analyses relating to interannual variability of air temperature over long-term historic timeframes, such as the ice sensitivity analyses in Section 5.0 . However, the relatively coarse temporal resolution and the imprecise metrics used in GHCN datasets limit their usefulness to analyses at longer timescales, such as seasonal timescales, for which precise characterization of parameters at higher temporal resolution not important.

Subsets of GHCN stations were selected around the Great Lakes to create representative long-term regional-average air temperature datasets for each of the lakes. To the extent possible,

stations were selected such that they are relatively evenly-spaced around each lake, chosen based on the geographical location of the stations, as well as the long-term and complete availability of data at those stations. The locations of GHCN stations and their corresponding data availability are shown for Lake Superior (Figure 2.20 and Figure 2.21), Lake Michigan (Figure 2.22 and Figure 2.23), Lake Huron (Figure 2.24 and Figure 2.25), Lake Erie (Figure 2.26 and Figure 2.27), and Lake Ontario (Figure 2.28 and Figure 2.29).

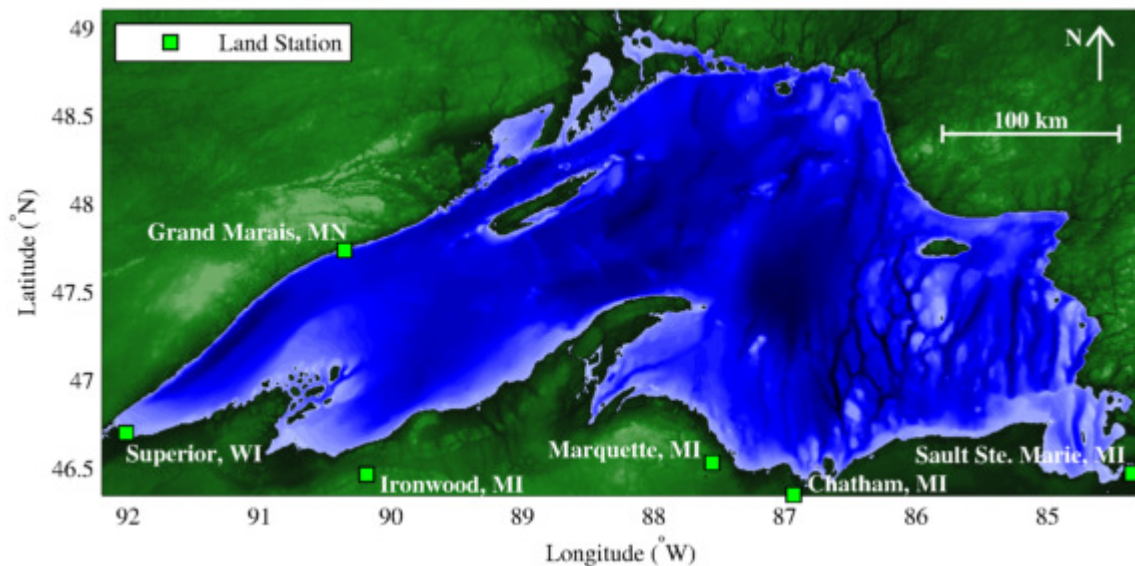


**Figure 2.20 – GHCN database station locations, Lake Superior.** GHCN stations on Lake Superior selected for use in analyses are shown. All GHCN stations shown are land-based stations. Data from Chatham, MI comes from a set of two nearby stations.

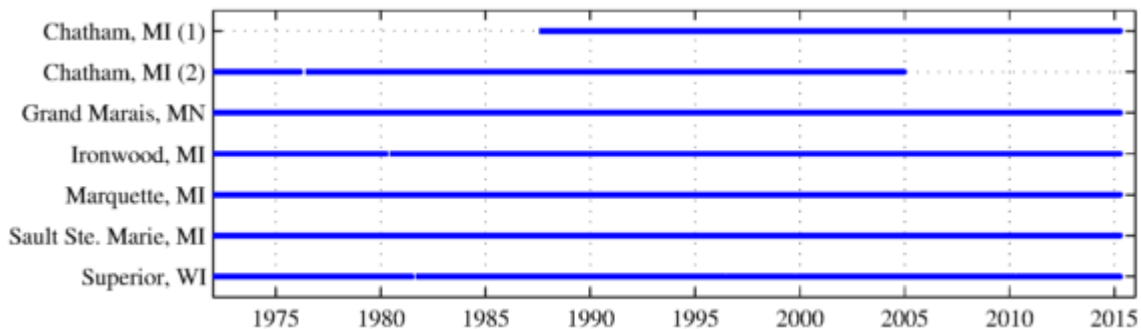


**Figure 2.21 – GHCN database data availability, Lake Superior.** The availability of GHCN stations on Lake Superior selected for use in analyses is shown. Solid lines represent the times for which data are available at the listed station.

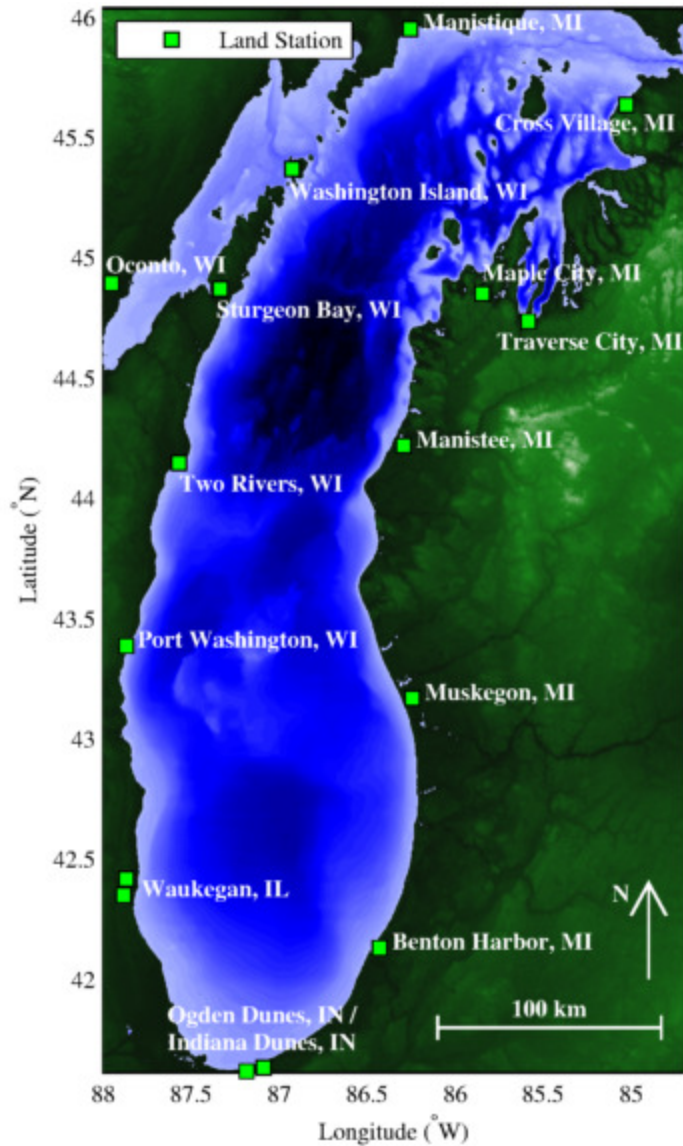


**Figure 2.22 – GHCN database station locations, Lake Michigan.** GHCN stations on Lake Michigan selected for use in analyses are shown. All GHCN stations shown are land-based stations. Data from Waukegan, IL come from a set of two nearby stations.

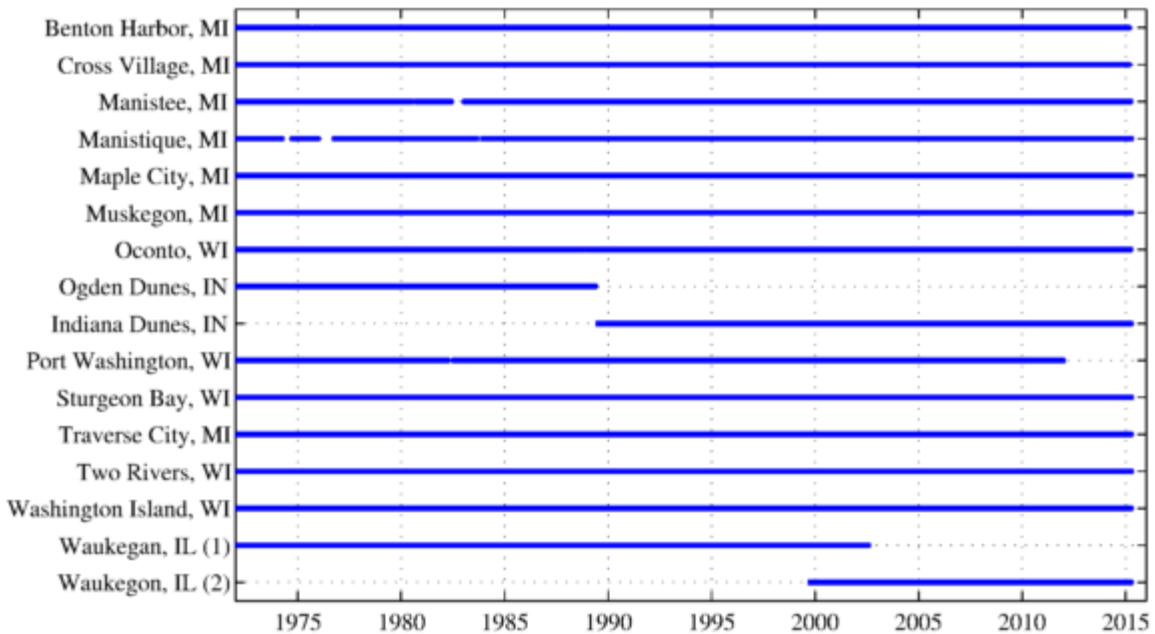


**Figure 2.23 – GHCN database data availability, Lake Michigan.** The availability of GHCN stations on Lake Michigan selected for use in analyses is shown. Solid lines represent the times for which data are available at the listed station.

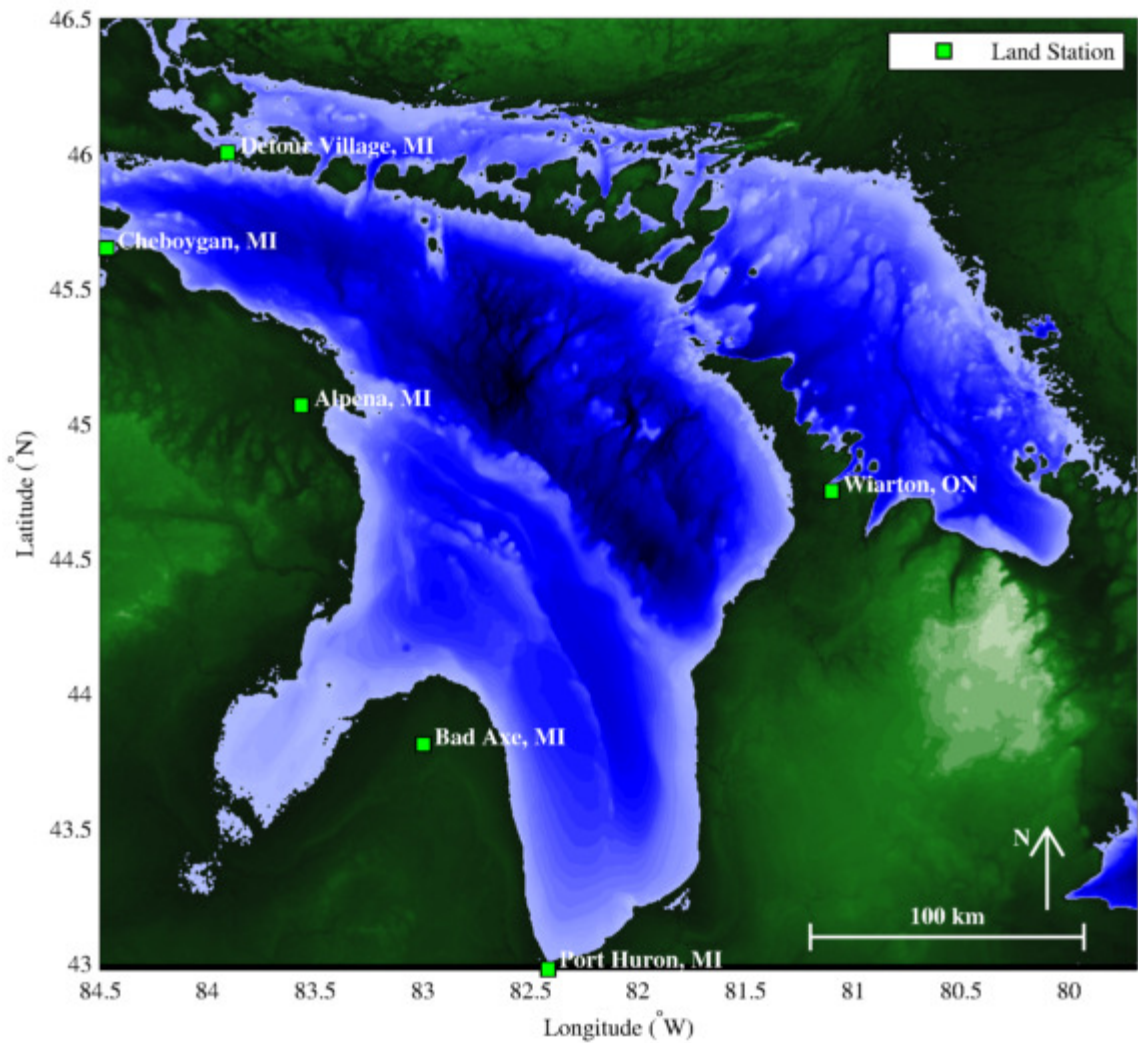


**Figure 2.24 – GHCN database station locations, Lake Huron.** GHCN stations on Lake Huron selected for use in analyses are shown. All GHCN stations shown are land-based stations.

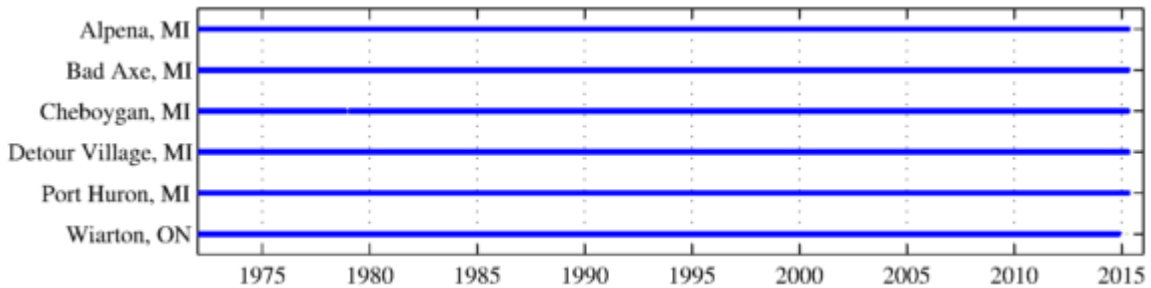


**Figure 2.25 – GHCN database data availability, Lake Huron.** The availability of GHCN stations on Lake Huron selected for use in analyses is shown. Solid lines represent the times for which data are available at the listed station.

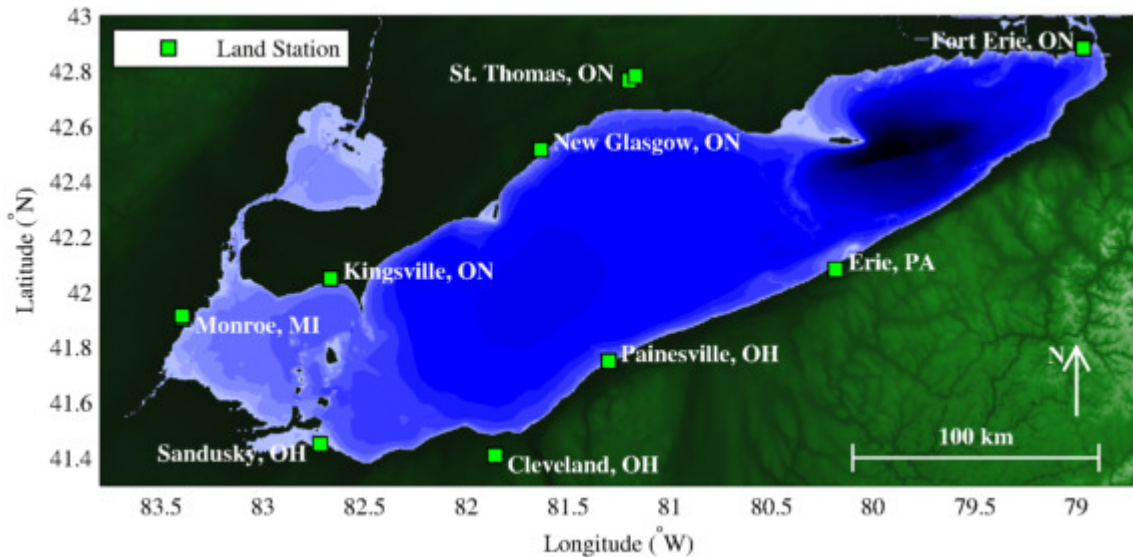


**Figure 2.26 – GHCN database station locations, Lake Erie.** GHCN stations on Lake Erie selected for use in analyses are shown. All GHCN stations shown are land-based stations. Data from Monroe, MI and St. Thomas, ON each come from a set of two nearby stations.

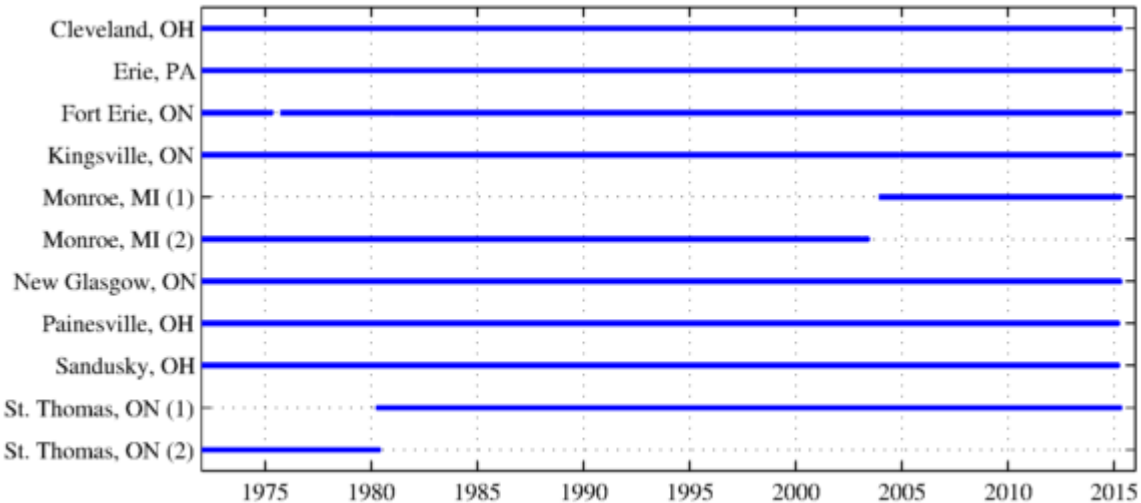


**Figure 2.27 – GHCN database data availability, Lake Erie.** The availability of GHCN stations on Lake Erie selected for use in analyses is shown. Solid lines represent the times for which data are available at the listed station.

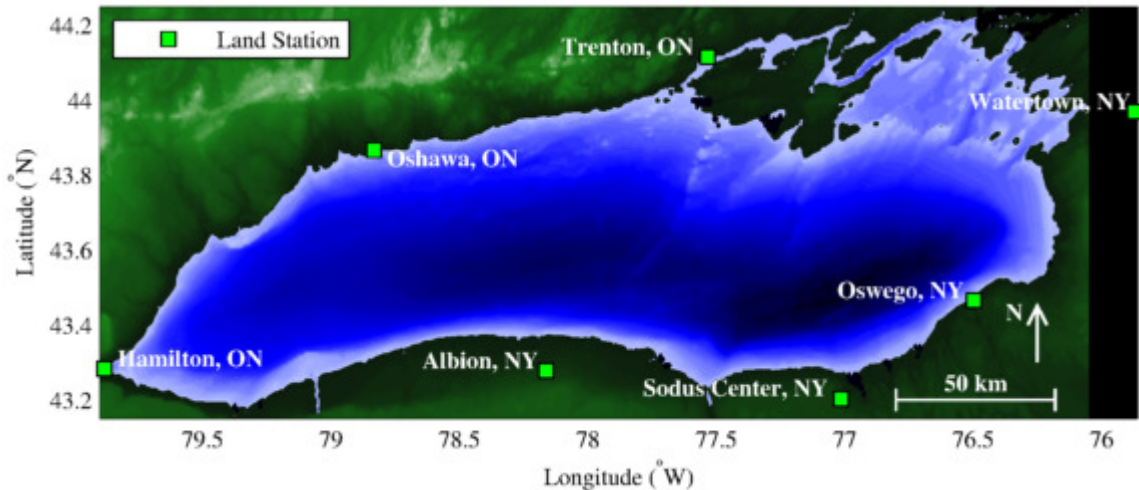


**Figure 2.28 – GHCN database station locations, Lake Ontario.** GHCN stations on Lake Ontario selected for use in analyses are shown. All GHCN stations shown are land-based stations. Data from Hamilton, ON come from a set of two nearby stations.

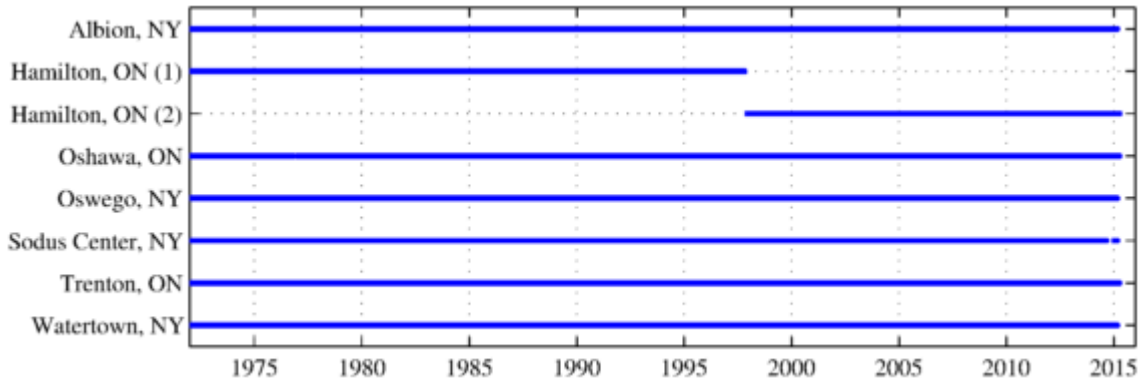


**Figure 2.29 – GHCN database data availability, Lake Ontario.** The availability of GHCN stations on Lake Ontario selected for use in analyses is shown. Solid lines represent the times for which data are available at the listed station.

Air temperatures from GHCN stations around each lake were averaged to estimate a lakewide average air temperature that is representative of the region surrounding the lake. Because GHCN datasets report only the maximum and minimum air temperature each day, the average daily temperature was estimated as the average of the maximum and minimum temperature. In addition, some locations have their records broken up between two nearby stations, one of which has older data and the other of which has more recent data. In such cases, there is often some overlap between the operation of the two stations, and in those cases, overlapping data from the

two stations was first averaged together to create a single air temperature record for the location, and that single record is averaged with data from other locations to calculate the lakewide average air temperature. This is done to prevent biasing the lakewide average with duplicate data from similar locations. The following sets of stations were combined: two Chatham, MI station (Figure 2.20 and Figure 2.21), Ogden Dunes, IN and Indiana Dunes, IN (Figure 2.22 and Figure 2.23), two Waukegan, IL stations (Figure 2.22 and Figure 2.23), two Monroe, MI stations (Figure 2.26 and Figure 2.27), two St. Thomas, ON stations (Figure 2.26 and Figure 2.27), and two Hamilton, ON stations (Figure 2.28 and Figure 2.29).

Given that average lakewide air temperature metrics calculated from GHCN data were estimated using the average of the daily minimum and maximum air temperatures, it is important to check that these metrics are representative of the true average temperature around the lake. This was done by comparing the GHCN lakewide average air temperature metrics to similar metrics derived from the NDBC database data (see Section 2.3.1) for periods in which data is available from both datasets. Hourly NDBC database data were binned onto the daily GHCN grid, and comparisons between the two datasets are shown for each of the Great Lakes in Figure 2.30.

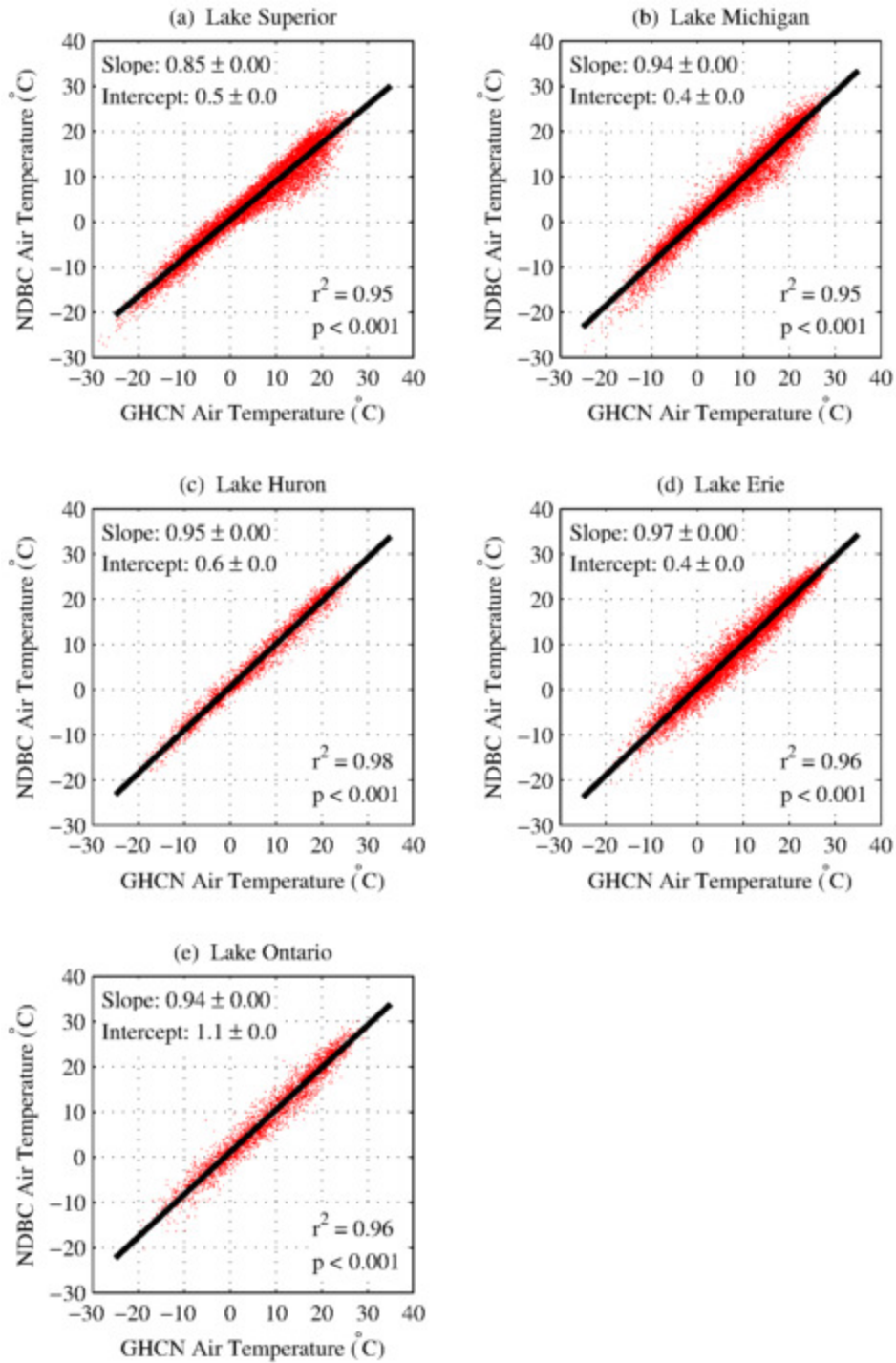


**Figure 2.30 – Comparison of NDBC and GHCN air temperature data.** Comparisons between air temperature data from NDBC database data and GHCN data are shown for (a) Lake Superior, (b) Lake Michigan, (c) Lake Huron, (d) Lake Erie, and (e) Lake Ontario. Confidence intervals for all slope and intercept parameters are zero to the number of significant figures presented.

As can be seen in Figure 2.30, GHCN data are well-correlated with NDBC database data;  $r^2$  values are 0.95 or greater for all five of the Great Lakes. All of the slopes of the best fit lines are slightly below 1 (ranging from 0.85 for Lake Superior to 0.97 for Lake Erie), and all of the intercepts are slightly above zero (ranging from 0.4°C for Lake Michigan to 1.1°C for Lake Ontario). The temperature at which the lakewide average air temperature estimates are statistically equivalent between the NDBC database metric and GHCN metric is informative, and can be determined by finding the point at which the best-fit line intersects the line for a one-to-one correlation. This can be algebraically determined by combining with the equation for the best-fit line (Equation 2.3) with the equation for a one-to-one correlation (Equation 3.3), and rearranging:

$$T_{NDBC} = m T_{GHCN} + b \quad \text{Equation 2.3}$$

$$T_{NDBC} = T_{GHCN} \quad \text{Equation 2.4}$$

Combining Equation 2.3 and Equation 2.4 yields:

$$T_{GHCN} = m T_{GHCN} + b \quad \text{Equation 2.5}$$

Because we are solving for the temperature at which the GHCN air temperature is equal to the NDBC database air temperature, GHCN-derived air temperature ( $T_{GHCN}$ ) can be replaced by the air temperature of equivalency ( $T_{EQ}$ ). After this substitution, Equation 2.5 can be rearranged to produce the result:

$$T_{EQ} = \frac{b}{1 - m} \quad \text{Equation 2.6}$$

Using Equation 2.6 in conjunction with the best-fit parameters shown in Figure 2.30, it can be determined the temperature at which NDBC database and GHCN lakewide average air temperature metrics are equal is 3°C for Lake Superior, 7°C for Lake Michigan, 12°C for Lake Huron, 14°C for Lake Erie, and 19°C for Lake Ontario. The fact that best-fit slopes are slightly below 1 suggests deviations from these air temperatures are estimated as somewhat more moderate in the NDBC database datasets, and somewhat more extreme in the GHCN datasets. This can likely be explained, at least in part, by the fact that NDBC database stations are located

on the coasts of the lakes, where air temperatures would be moderated by the lake, whereas GHCN stations are located farther from the lakes, where such moderating effects would be more minimal.

The lower best-slope for Lake Superior, compared to the other lakes, may be due to the large surface area of the lake, which could enhance the effects of such air temperature moderation. The higher intercept for Lake Ontario, compared to the other lakes, may be due, at least in part, to the fact that there are no NDBC database stations on the colder north side of the lake, while there are GHCN stations north of the lake. However, the same is true for Lake Erie, which does not have a similarly high intercept.

In summary, estimates of air temperature from GHCN stations correlate well to estimates from NDBC database stations. Differences between the metrics can likely be explained, at least in part, by differences in the locations of the stations, with GHCN-derived air temperature having less lake-induced moderation of air temperature than the NDBC datasets. Therefore, the GHCN datasets, despite their less-precise air temperature metrics, produce a representative estimate of air temperature around the lake.

### **2.3.3 North American Regional Reanalysis (NARR) product**

The North American Regional Reanalysis is a reanalysis product, in which historic observations are input into a computer model and reprocessed onto an even spatio-temporal grid that covers the northern hemisphere (National Center for Environmental Prediction 2015). The NARR output is available from 1979 through present at a temporal resolution of 3 hours, with grid spacing of approximately 32 km. NARR datasets includes such parameters as air temperature, wind velocity, air specific, specific humidity, heat flux, and precipitation, among many others. Because the reanalysis product relies on model assumptions to assimilate observations onto the consistent grid, it is inherently less reliable than pure observations. However, the consistent and evenly-spaced nature of the output, as well as the extensive list of available parameters, makes the NARR products appealing for forcing numerical models. A portion of the NARR grid around the Great Lakes is presented in Figure 2.31 to visually demonstrate the spatial resolution of the data.

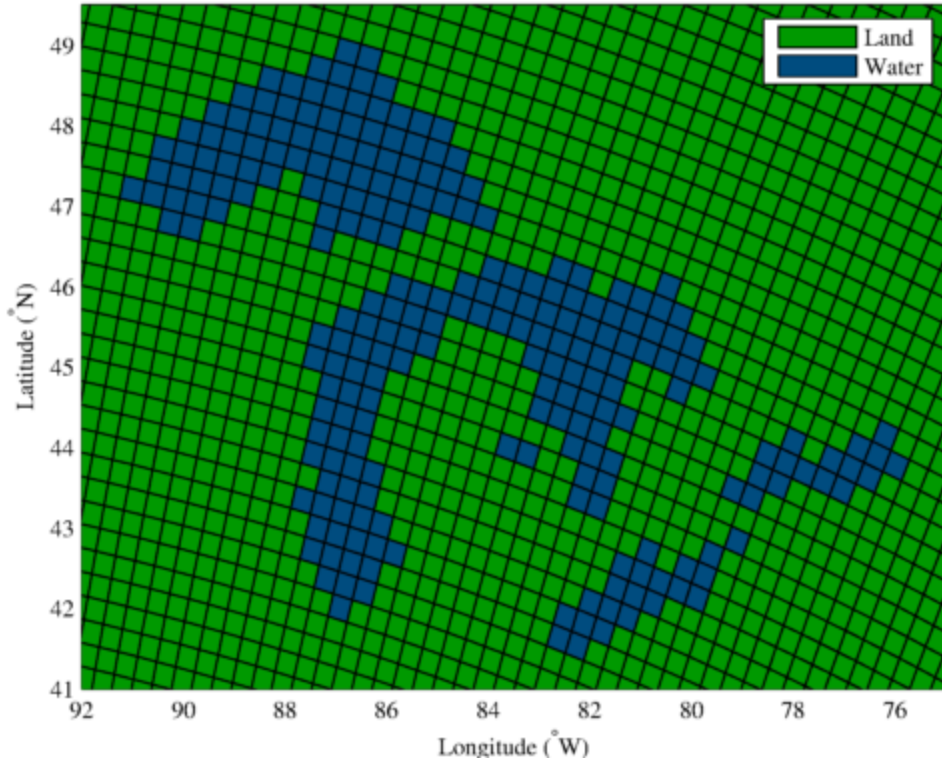


**Figure 2.31 – NARR grid, Great Lakes Region.** The NARR grid for the Great Lakes region is shown. Grid spacing is approximately 32 km. Blue squares represent water and green squares represent land.

### 2.3.4 Estimating Winter Wind Velocity at Offshore Locations

For some analyses, it is necessary to estimate wind velocity at mooring locations (see Section 2.1) during the winter months. Because NDBC buoys (see Section 2.3.1), which are located proximal to the moorings, are not in service during the winter months, a land-based proxy must be used. Wind velocity time-series from these land-based stations were compared to wind velocities at NDBC buoys during periods in which both the land-based and buoy stations are operating simultaneously in order to determine the relationships between wind velocities at the mooring locations and wind velocities measured at the land-based stations. For each combination of a buoy and a land-based station, separate regressions were performed between the two stations for the May 1 through August 31 periods for each of the years spanning 2004 through 2013 for which data from both

stations is available for at least 25% of that summer period. Because the goal of these regressions is to predict offshore wind velocity from the land-based stations, data from the land-based stations were used as the independent variable in the regressions, and data from the buoy stations were used as the dependent variable.

For wind direction relationships, the slopes of the best-fit line were fixed to 1 and only the directional offsets was fit. This method was chosen because there is no reason to expect that the directional relationship between stations would vary linearly with wind direction. Additionally, it was found that, to two significant figures,  $r^2$  values for fits derived using this fixed-slope method are identical to those for fits in which the slope is also fit for all combinations of stations examined. This suggests that no explanatory power of the correlation is lost by fixing the regression slope to 1.

A linear relationship in wind speed is expected between two stations that are at similar locations but different heights (Hsu et al. 1994), and it should logically also be expected that wind speed at the buoy stations would be zero when wind speed at the corresponding land-based stations is zero. However, regressions for all combinations of stations examined show a statistically significant positive intercept was found for all combinations of stations examined. Further, it was found that fixing the intercept to zero and fitting only the slope greatly reduces the  $r^2$  values of the fits, and visual inspection of the data confirms that a line with a positive intercept fits the data better than a line with an intercept fixed to zero. For these reasons, both the slope and the intercept were fit in the empirical relationships for wind speed, although the cause of these intercepts is not clear.

The average of the slopes and intercepts from these regressions was used to develop an empirical transfer function between the land-based station and the mooring locations. In all cases, wind speeds at the land-based stations are significantly higher than wind speeds at the buoy stations. This can be attributed, at least in large part, to the fact that anemometers at land-based are located at higher elevations than those at the buoy stations. However, the adjustment factors derived from these empirical relationships is greater than predicted by the power law described by Hsu et al. (1994). In some cases,

there is a relatively small directional offset between the land-based station and the buoy station. It is not known whether these direction offsets are due to biases in the instrument or whether geophysical factors lead to differences in wind direction between locations.

The relationships used to estimate wind speed are summarized in Table 2.2, below. Similar relationships cannot be developed for the outer moorings, because no meteorological buoys are located at their locations during any part of the year.

Dependent Variable Station (nearby mooring)	Independent Variable Station	Wind Direction Relationship			Wind Speed Relationship		
		Slope	Offset (° CCW)	r <sup>2</sup>	Slope	Intercept (m s <sup>-1</sup> )	r <sup>2</sup>
45006 (WM)	DISW3	1 (fixed)	no offset	0.78	0.57 ± 0.02	1.56 ± 0.09	0.49
45006 (WM)	ROAM4	1 (fixed)	9.2 ± 3.7	0.78	0.37 ± 0.03	1.92 ± 0.14	0.32
45001 (CM)	PILM4	1 (fixed)	8.0 ± 2.9	0.86	0.50 ± 0.03	1.63 ± 0.16	0.39
45004 (EM)	STDM4	1 (fixed)	8.7 ± 4.0	0.85	0.43 ± 0.03	1.17 ± 0.21	0.47
45004 (EM)	BIGM4	1 (fixed)	13.3 ± 1.7	0.70	0.66 ± 0.09	3.03 ± 0.15	0.20

**Table 2.2 – Summary of wind velocity empirical transfer functions.** This table presents a summary of best fit parameters used to estimate wind velocity at offshore mooring locations from land-based stations. Slope, offset/intercept values used to estimate wind direction/speed at the dependent variable stations from the independent variable stations are shown, as well as the corresponding r<sup>2</sup> values for the correlations. The mooring near which the dependent variable stations are located are listed in parentheses. Slope was fixed to 1 for all wind direction correlations. Intervals shown for parameters are 95% confidence intervals.

## 2.4 Bathymetry Data

Bathymetric data were obtained for the Great Lakes from the National Oceanographic and Atmospheric Administration's (NOAA) National Centers for Environmental Information (NCEI) datasets (National Centers for Environmental Information 2015a). These datasets provide bathymetric data for each the Great Lakes at a horizontal resolution of approximately 90 m. In addition to being used in some analyses, such as the analyses of ice sensitivity to depth in Section 5.0 , this bathymetry data is used in many of the geographical figures throughout this thesis.

## 2.5 Water Level Data

Water level data from the Great Lakes are occasionally referenced throughout this thesis, and those data were obtained from the National Oceanographic and Atmospheric Administration's (NOAA) Tides and Currents water level datasets (National Oceanographic Administration Tides and Currents 2015). These datasets contain water level data from a number of stations around the Great Lakes at temporal resolutions of up to 6 minutes. Data used in this thesis were hourly.

## 2.6 Regional Ocean Modeling System (ROMS) Numerical Model

Several sensitivity experiments using numerical models were conducted to supplement the results of observational analyses presented in this thesis. Modeling experiments were setup using the Regional Ocean Modeling System (ROMS) numerical model (Shchepetkin and McWilliams 2005; Moore et al. 2004; Shchepetkin and McWilliams 2003) to model the Lake Superior basin with dynamic lake ice. ROMS is a free-surface hydrodynamic model that driven by fundamental physical equations. It has been widely used in the oceans (Tsumune et al. 2012; Powell et al. 2009; Wilkin et al. 2005) and, to a lesser extent, on large lakes and inland seas, such as the Caspian Sea (Turuncoglu et al. 2013), Lake Kinneret (Shilo et al. 2007), and Lake Superior (White et al. 2012; Matsumoto et al. 2015).

### 2.6.1 Lake Superior Model Description

The application of ROMS to the Lake Superior basin uses the model developed and described by White et al. (2012) and improved by Matsumoto et al. (2015). The model uses 5 km horizontal grid spacing, 20 terrain-following vertical sigma levels, and has realistic bathymetry (Figure 2.32). In the numerical model, Lake Superior is modeled as a closed basin, with no river input or output, salinity is uniformly zero, and a freshwater equation of state is used to improve modeling near the temperature of maximum density (Chen and Milero 1986). Dynamic lake ice is implemented in the model, as described by Hedrstrom (2009) and Budgell (2005), which allows for modeling of the fractional areal ice cover and average ice thickness at each grid point. Heat flux was calculated in the model using bulk formulas and the forcing parameters discussed in the next section (Section 2.6.2). For all runs, initial conditions for the model spin-up period, water temperature in the lake was set uniformly to 3.8°C, which is equivalent to the temperature of maximum density at approximately 100m depth, and water velocity was uniformly set to 0 m s<sup>-1</sup>.

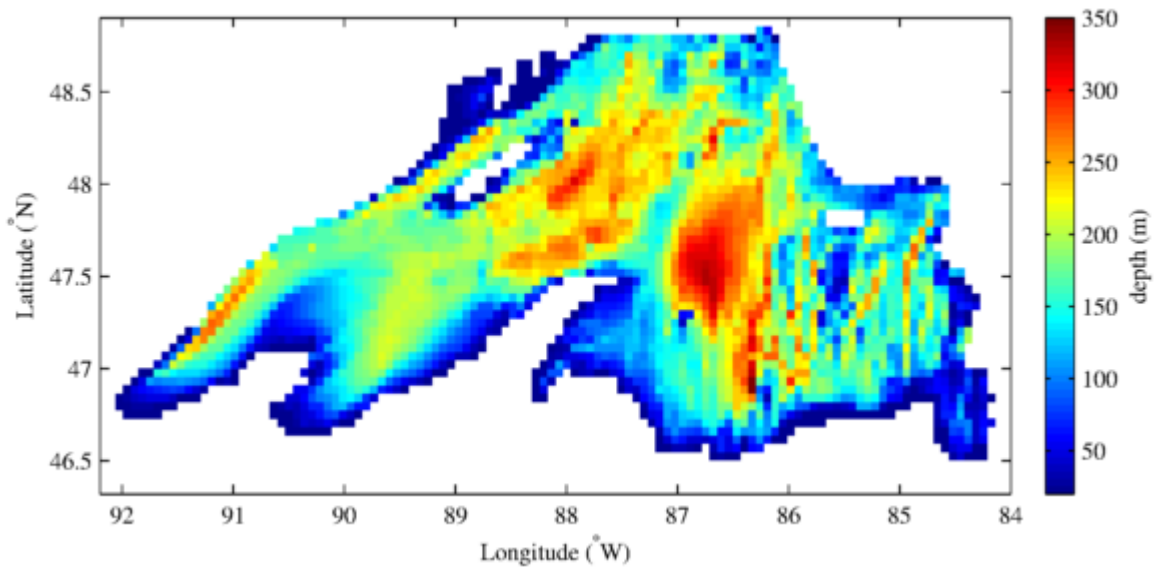


**Figure 2.32 – ROMS Lake Superior basin grid.** The ROMS grid used to model the Lake Superior basin is shown, including bathymetry. The model has 5 km horizontal spacing and is described in White et al. (2012) and Matsumoto et al. (2015).

## 2.6.2 Model Forcing

The NARR climate datasets (see Section 2.3.3) were chosen as the baseline datasets with which to force the model, chosen because of the historic availability of the data and the selection of available climate parameters. The following parameters were used to force the model:

- Air Temperature (calibrated, discussed below)
- Precipitation
- Downward Longwave Radiation (calibrated, discussed below)
- Shortwave Radiation (reduced downward, discussed below)
- Atmospheric Pressure
- Specific Humidity
- Zonal Wind Speed
- Meridional Wind Speed

These parameters setup for the Lake Superior model, using a two-dimensional interpolation scheme to grid the forcing parameters from the NARR grid onto the ROMS 5km-resolution Lake Superior grid. Upward longwave heat flux, sensible heat flux, and latent heat flux are calculated by ROMS using these input parameters with bulk formulas. When the ice model is implemented in the model, as is the case for all of the analyses in this thesis, the model is designed such that downward shortwave radiation is forced, and reflected shortwave is removed based on the dynamic albedo of the lake. However, it was found that when NARR downward shortwave is used as the forcing for the model, lake conditions in the model have a strong warm bias, both under-predicting ice cover and over-predicting water temperature. This is consistent with findings by White et al. (2012) and Matsumoto et al. (2015), and is examined in detail, below.

First, a test run was conducted using unadjusted NARR forcing parameters, as outlined above, for the years of 1980-2014, with the year of 1979 used as a spin-up year. Output from this test model run was compared to observational data, in terms of both seasonal-average ice cover and summer surface water temperatures in order to assess its accuracy and bias. Seasonal-average ice cover was calculated as the average areal lakewide ice cover on the lake from December through May, and was compared to observations of the same metric. Observations were from the GLIA datasets (see Section 2.2.1) for the years of 1980 through 2005, and from the IMS datasets (see Section 2.2.2) for the years of 2006 through 2014. Summer surface water temperature was calculated as the average water temperature from July through September in the uppermost layer of the model at the model grid point closest to the Western Mooring location (see Section 2.1). This was compared to the same July through September surface water metric, based on observations from NDBC buoy 45006 (see Section 2.3.1), which is located proximal to the Western Mooring. Comparisons between model results from the test run and corresponding observational data are presented in Figure 2.33.

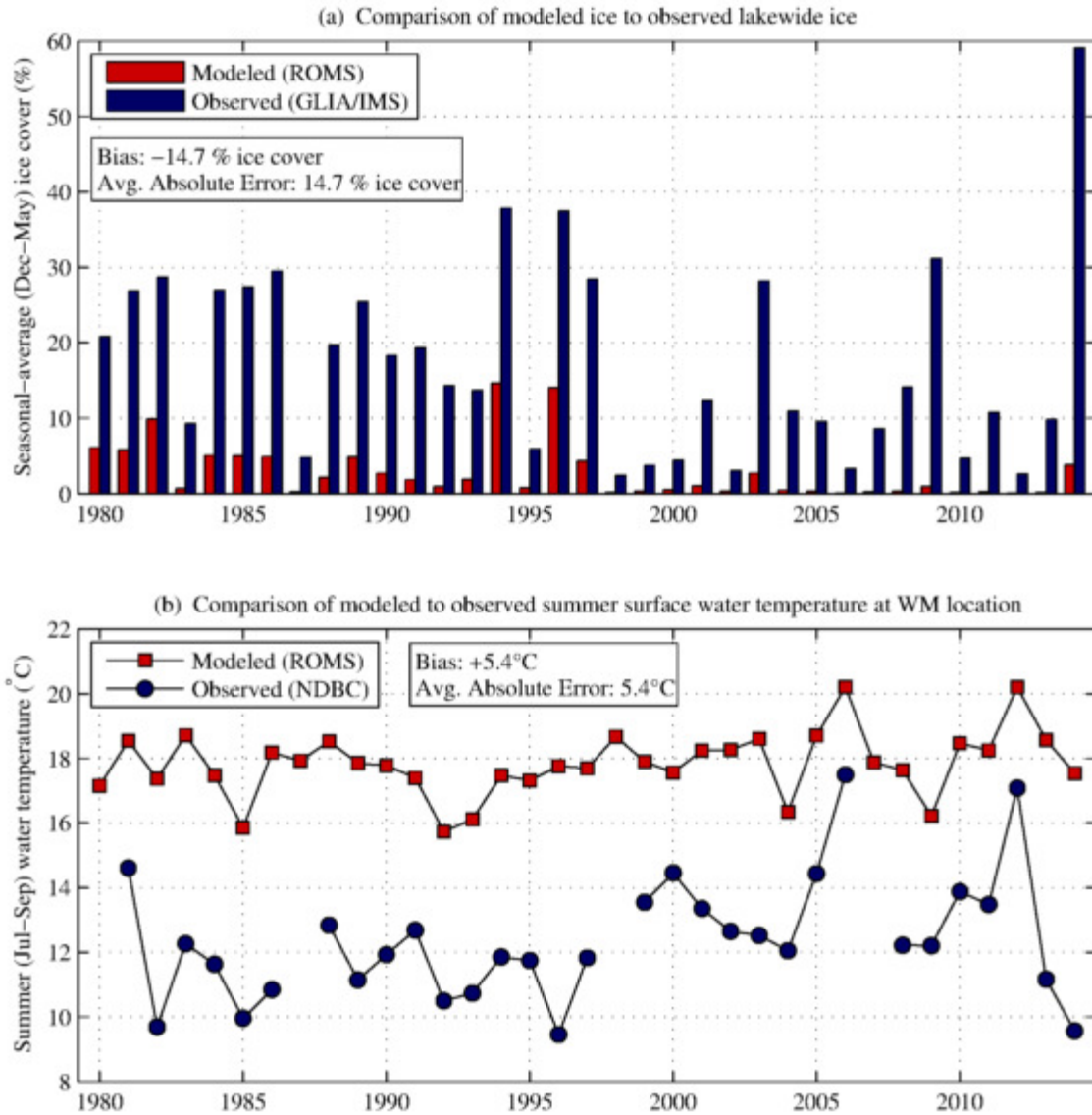


**Figure 2.33 – ROMS test run with unadjusted NARR forcing.** Results from a ROMS test run, using unadjusted NARR forcing for the years of 1980 through 2014, are presented and compared to observational data, for both (a) seasonal-average (Dec-May) lakewide ice cover, and (b) summer (Jul-Sep) surface water temperature at the Western Mooring location. Observational ice cover data is from the GLIA ice datasets for the years of 1980 through 2005, and from IMS datasets for the years of 2006 through 2014. Observational surface water temperature data is from NDBC buoy 45006 for years in which observations are available.

As evident in Figure 2.33, there is a clear warm bias in the model when unadjusted NARR forcing is used. Ice cover is consistently substantially underestimated, with a calculated bias of -14.7% seasonal-average ice cover. This is a very substantial bias, given that average seasonal average ice cover is about 19%. Likewise, summer surface water temperature is consistently

underestimated, with a bias of +5.4°C. This demonstrates that the model is warm, in general, and does not simply under-estimate ice cover.

NARR datasets are reanalysis products and are therefore, themselves, products of numerical modeling. As such, climate parameters provided by the NARR datasets rely heavily on the assumptions of NARR reanalysis model around the Great Lakes, and any bias in these assumptions would be manifest through the NARR datasets. It is likely that some combination of assumptions in the NARR reanalysis model and the ROMS model results in this systematic bias in model results.

Matsumoto et al. (2015) addressed this bias by reducing the amount of incoming shortwave radiation. They did this by using NARR net shortwave forcing as downward shortwave radiation in the model, calculated by subtracting NARR upward shortwave radiation from NARR downward shortwave radiation. As such, under this method, reflected shortwave radiation is removed once based on the values of the NARR reanalysis data and again, subsequently, based on the dynamic albedo of the model. This spatially variable reduction of downward shortwave radiation, using NARR upward shortwave radiation, is akin to an assumption that NARR, ROMS, or both underestimate the amount of shortwave radiation reflected by the Lake Superior surface. Results from model runs using this forcing are compared to observed data in Figure 2.34.

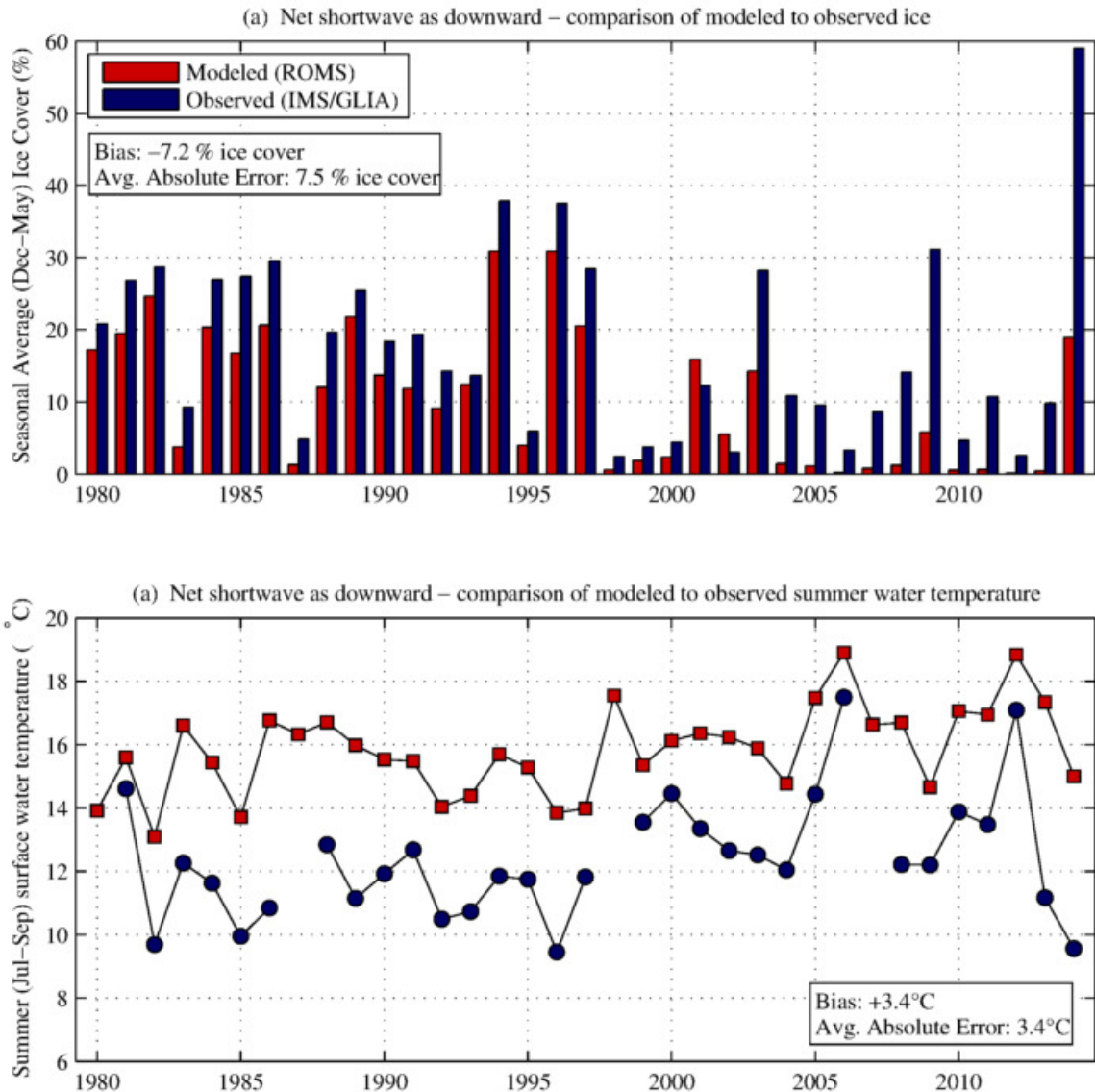


**Figure 2.34 – ROMS test run with NARR net-as-downward shortwave forcing.** Results from a ROMS test run, using NARR net-as-downward forcing for the years of 1980 through 2014, are presented and compared to observational data, for both (a) seasonal-average (Dec–May) lakewide ice cover, and (b) summer (Jul–Sep) surface water temperature at the Western Mooring location. Observational ice cover data is from the GLIA ice datasets for the years of 1980 through 2005, and from IMS datasets for the years of 2006 through 2014. Observational surface water temperature data is from NDBC buoy 45006 for years in which observations are available.

As observed in Figure 2.34, even using this net-as-downward reduced shortwave forcing, the model under-predicts ice by an average of 7.2% seasonal-average ice cover, and has a warm bias in summer water temperature of +3.4°C. While these results are considerably better than those of the unadjusted shortwave scenario (Figure 2.33), the underprediction of ice cover and

overprediction of summer water temperatures demonstrates that, even under this reduced shortwave scenario, there is a warm bias in the model.

Air temperature and shortwave radiation forcing were examined as possible means of improving model results. Values of air temperature from the NARR reanalysis datasets were compared to observed values of air temperature from the GHCN datasets. To make this comparison in an objective way, average daily temperatures from the NARR datasets were determined using the six ROMS grid points that correspond to the six GHCN station locations (Figure 2.20) from which average air temperature was derived. This comparison of air temperatures is presented in Figure 2.35.

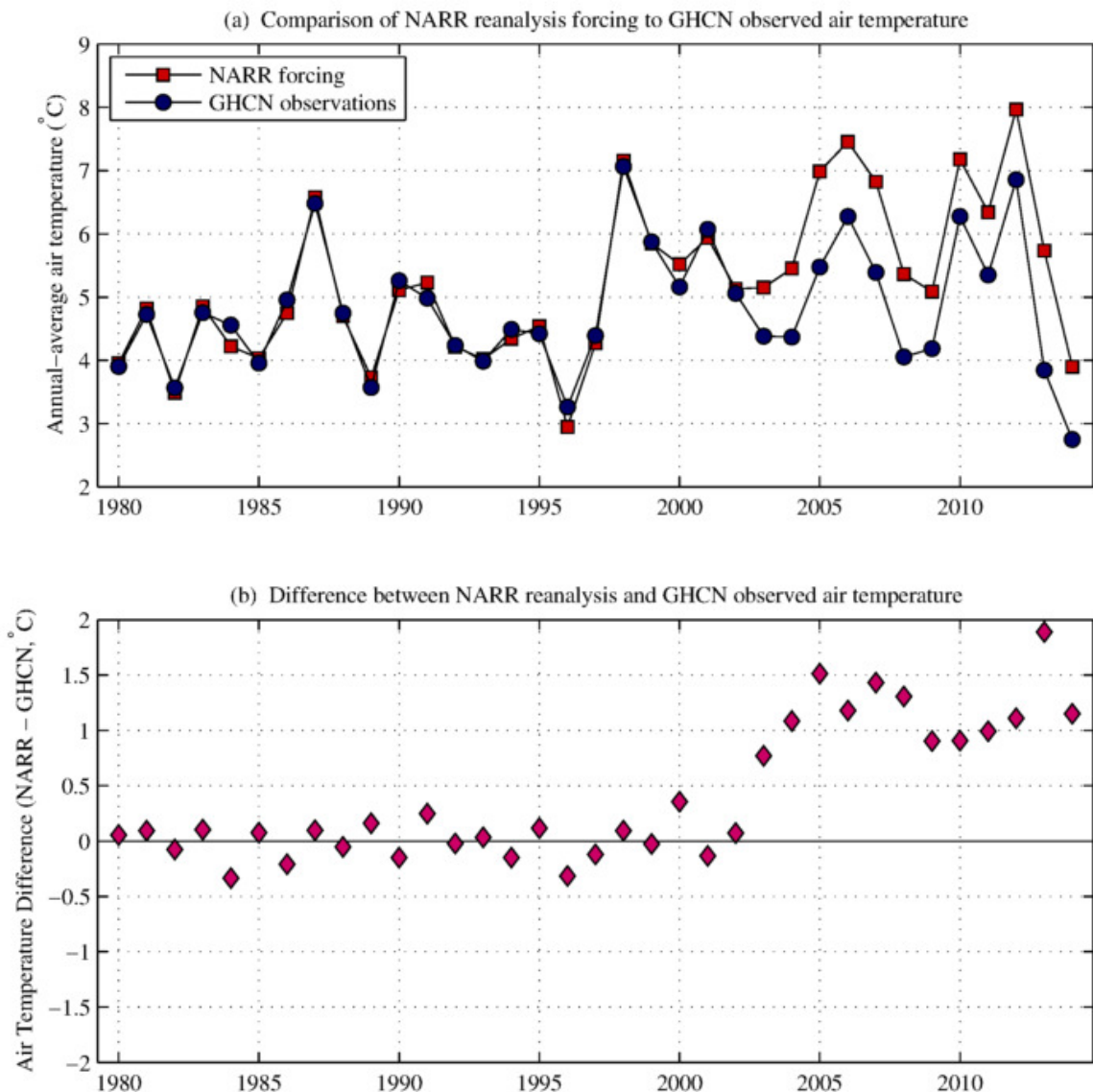


**Figure 2.35 – Comparison of NARR air temperature to GHCN observed air temperature.** (a) Annual average air temperatures are compared between NARR reanalysis air temperature (red squares) and GHCN observed air temperature (blue circles). (b) This difference between these annual average air temperature values is plotted by year.

As shown in Figure 2.35, NARR reanalysis data show a good fit with GHCN observational data for the years of 1980 through 2002, with differences consistently less than 0.5°C, and no clear overall warm or cold bias. However, starting in 2003, there is a significant warm bias in NARR air temperatures, on the order of 1°C to 2°C. A warm bias in NARR air temperature data has been documented by Bennington et al. (2010) and Matsumoto et al. (2015), although they do not

identify the bias as beginning in 2003. The presence of a warm bias in NARR data, beginning around 2003 (Figure 2.35), is consistent with the more substantial under-prediction of ice cover that begins around that time in the net-as-downward shortwave model runs (Figure 2.34). To address this, a hybrid NARR-GHCN air temperature forcing dataset was compiled. To compile this hybrid NARR-GHCN time-series, a spatially uniform adjustment factor was added to NARR air temperature data, on a day-by-day basis, such that the daily-average air temperature NARR air temperature matches the daily average GHCN air temperature. Again, to make this adjustment in an objective way, average daily temperatures from the NARR datasets were determined using the 6 ROMS grid points that correspond to the 6 GHCN station locations (Figure 2.20) from which average air temperature was derived.

In addition, downward longwave radiation was adjusted accordingly, based on the strong relationship between air temperature and longwave radiation. This adjustment was applied based on the relationship described in Austin and Allen (2011):

$$Q_{LW\_DOWN\_ADJ} = Q_{LW\_DOWN} \left( \frac{T_A + \Delta T_A}{T_A} \right)^4 \quad \text{Equation 2.7}$$

Where  $T_A$  is the NARR air temperature prior to the air temperature adjustment (in K), and  $\Delta T_A$  is the magnitude of the applied air temperature adjustment (in K).

Next, available measurements of shortwave radiation were compared to values in the NARR datasets. These shortwave radiation measurements come from the meteorological buoys operated by the University of Minnesota Duluth Large Lakes Observatory (LLO) as part of the Great Lakes Observing System (see Section 2.3). The buoys are located off of McQuade Harbor, near Duluth, MN, and consist of a nearshore buoy (LLO1) and an offshore buoy (LLO2). Daily average values of downward shortwave radiation from these buoys were compared to daily average values of downward shortwave radiation in the NARR datasets at the nearest grid points for the 2013 and 2014 summer seasons, and the ratio of the observed values to NARR values are presented in Figure 2.36.

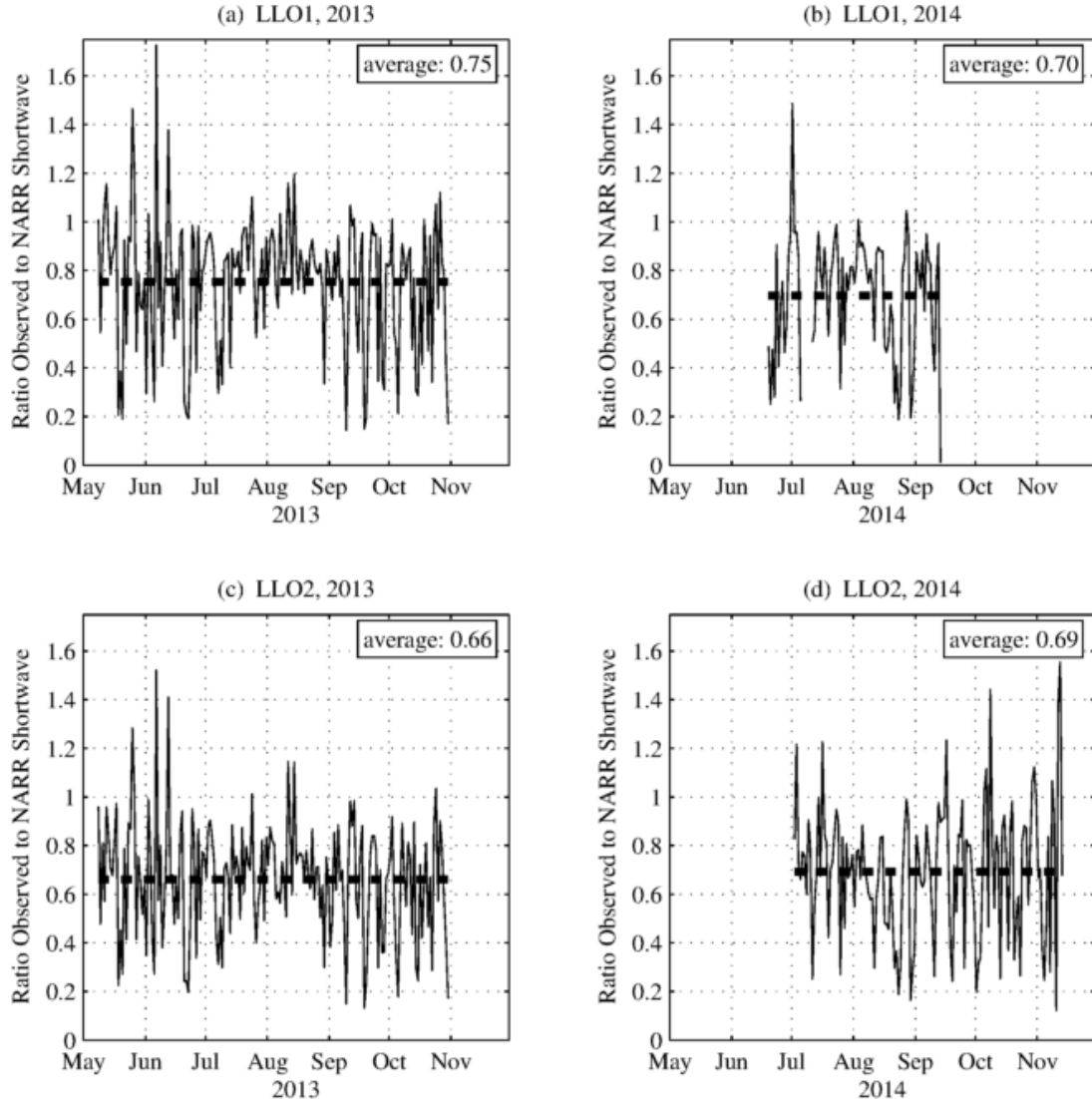


**Figure 2.36 – Ratio of NARR to observed downward shortwave radiation.** Values of downward shortwave radiation from NARR reanalysis datasets were compared to observed values, and the ratio of the observed value to NARR value at the nearest grid point is presented for buoy LLO1 for the years of 2013 and 2014 (a, b, respectively) and for buoy LLO2 for the years of 2013 and 2014 (c, d, respectively). In addition, the average value of the ratio for each buoy and season is shown.

The ratios of observed shortwave radiation to NARR shortwave radiation shows that downward shortwave radiation is overestimated in the NARR datasets. On average, observed shortwave radiation is consistently on the order of 70% that which is observed by the meteorological buoys. Based on this comparison, the NARR incoming shortwave radiation was reduced by 30% when forcing the model.

Based on the results of NARR air temperature and downward shortwave radiation assessments, above, the model was run using hybrid NARR-GHCN air temperature forcing, and 30% reduced NARR downward shortwave radiation forcing. Results of this baseline model run for the winters of 1980 through 2014 using these forcing parameters are shown in Figure 2.37.

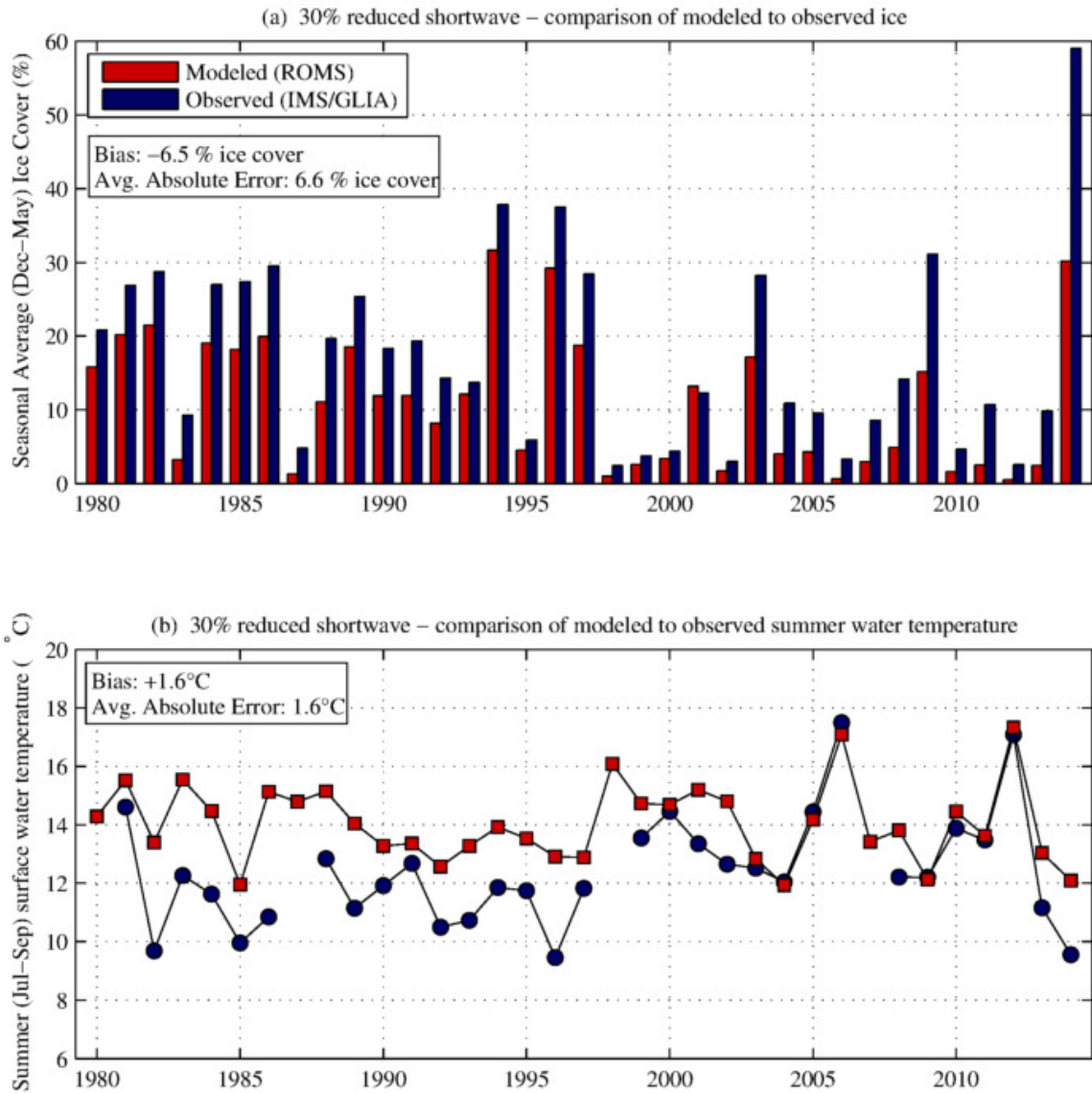


**Figure 2.37 – ROMS base run.** Results from the ROMS base run, using hybrid NARR-GHCN air temperature forcing and 30% reduced NARR downward shortwave radiation forcing for the years of 1980 through 2014, are presented and compared to observational data, for both (a) seasonal-average (Dec-May) lakewide ice cover, and (b) summer (Jul-Sep) surface water temperature at the Western Mooring location. Observational ice cover data is from the GLIA ice datasets for the years of 1980 through 2005, and from IMS datasets for the years of 2006 through 2014. Observational surface water temperature data is from NDBC buoy 45006 for years in which observations are available.

The results shown in Figure 2.37, using hybrid air temperature forcing and 30% reduced shortwave forcing, demonstrate an improvement in the results shown in Figure 2.34, in which net-as-downward shortwave forcing was used. Using these improved forcing parameters, the bias in ice cover was reduced from -7.2% to -6.5% seasonal-average ice cover, and the warm bias in

summer water temperatures was reduced from +3.4°C to +1.6°C. On top of the better agreement between model output results and observational data, these adjustments to forcing are believed to better represent the conditions experienced by the lake. It was found that reducing shortwave radiation by 50%, instead of 30%, further improves estimation of seasonal-average ice cover; however, this reduction leads to a cool bias in summer water temperature of more than 3°C and is not justified by observational data. Based on the improved model results and defensible nature for the forcing adjustments, the hybrid NARR-GHCN air temperature forcing and 30% reduced NARR downward shortwave radiation forcing were used in all model simulations in this dissertation.

It should be noted that White et al. (2012) forced the model with data from observations, as opposed to the NARR reanalysis used here, and that a warm bias was still observed in their model results. This suggests that the warm bias in the model is at least partially due to model parameterization, and cannot be accounted for by adjusting model forcing to observed values, which is the only form of calibration examined in this dissertation. In addition, some of the discrepancy in the air temperature differences may be due to the fact that the comparison is made between a grid cell in the model, which represents an average of a 5km-by-5km area, and a point measurement in the lake. Such a comparison is not necessarily reliable in a quantitative sense, and may account for some of the observed bias in water temperatures that is observed.

### 3.0 Interactions between Ice Cover and Lake Processes

This section focuses on the influence that ice cover has on the water column of the lake, and its influence on lake-climate processes. Ice has been shown to play a role in a variety of fundamental lake-climate processes, including surface heat flux (Titze and Austin 2014; Gerbush et al. 2008), lake-effect precipitation (Cordeira and Laird 2008), evaporation (Blanken et al. 2011), and the onset of summer stratification (Rodgers 1987, Austin and Colman 2007). As ice cover declines in response to climate change, these and other processes will be affected. Here, I specifically examine the influence of ice cover on heat flux and subsurface circulation.

Of the work contained in this thesis, this section follows most directly from the work of the Masters thesis, which was modified and published as Titze and Austin (2014). In Titze and Austin (2014), we examined the influence of ice cover on heat flux in Lake Superior during the winter of 2008-2009, which was characterized by moderate ice cover in a historical context. We found that spatial variability in ice cover led to spatial variability in heat flux, which ultimately affected the timing of summer stratification. These results were largely qualitative, and the problem was viewed in a one-dimensional sense. Specifically, we did not attempt to examine horizontal processes in our winter heat flux analysis, although we did conclude horizontal mixing must be significant during spring warming.

In this section, I expand on this previous work and examine the effects of ice cover on lake processes during the exceptionally cold 2013-2014 winter. The most basic contribution that this makes is the addition of a second year of under-ice observations to our understanding of the influence of ice cover on heat flux. This serves to corroborate the conclusions of Titze and Austin (2014), as well as to help answer some of the questions that could not be answered with a data from a single season of under-ice data. For example, during the winter of 2008-2009, ice cover formed during the early portions of the season, during which the lake was experiencing rapid heat loss. As a result, the icier western basin lost less heat than the relatively ice-free eastern basin, and the western location stratified earlier. We hypothesized that the timing of ice is important, and that late-season ice could have the opposite effect, preventing the lake from warming during times when it would otherwise be rapidly gaining heat in the spring. This would be consistent with the conclusions of Austin and Colman (2007). The 2013-2014 experienced record-late ice cover, which will allow for assessment of this hypothesis.

In addition to adding a second year of observations to the analysis, I consider processes in the context of ADCP water velocity data from the Western and Eastern Moorings (see Section 2.1). The availability of simultaneous measurements of water velocity and thermal structure at two locations results in a rare opportunity to begin to examine the role that advective processes have on heat distribution in the lake. In addition, there is ADCP data available from these mooring locations over multiple previous winters. During most of those winters, there was little to no ice in the vicinity of the moorings. I will examine the water velocity data from the icy 2014-2015 winter in comparison to previous winters with less ice to demonstrate the manner in which ice influences the velocity of water currents in the upper portions of the water column.

A map of locations on Lake Superior relevant to analyses in this section is provided in Figure 3.1. Figure 3.1 includes the locations of moorings (see Section 2.1), the locations of nearby NDBC meteorological buoys (see Section 2.3.1), and the location of coastal meteorological stations from the NDBC database (see Section 2.3.1).

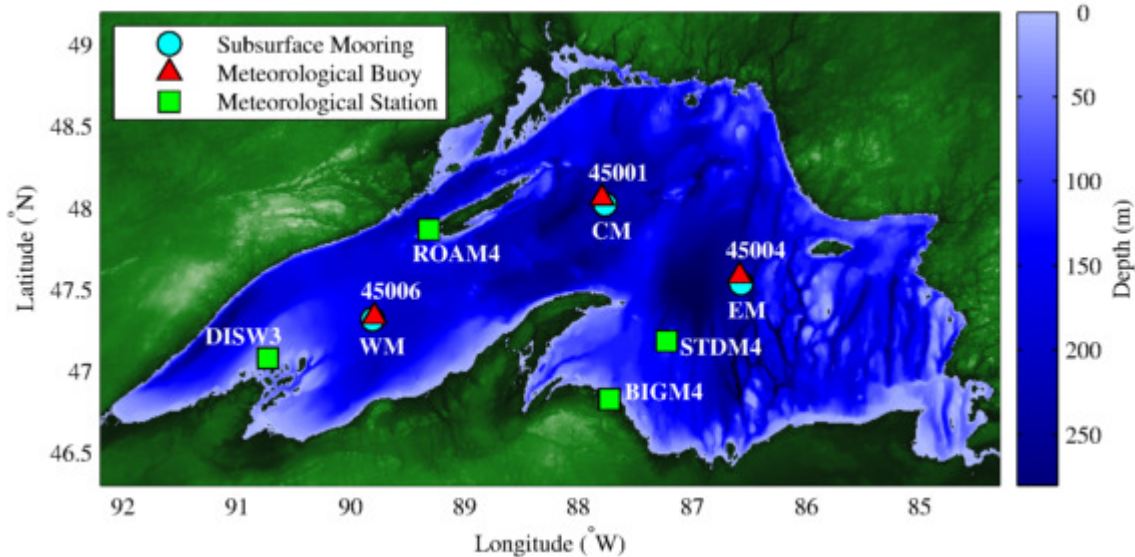


**Figure 3.1 – Map of relevant locations for Section 3.0 .** This map shows locations on Lake Superior that are relevant to this section, including subsurface moorings (blue dots), NDBC meteorological buoy locations (red triangles), and NDBC database coastal meteorological stations (green squares).

### **3.1 Thermal Structure**

The temperature time series from the mooring array provide a detailed look of the thermal structure of the water column throughout the extreme conditions of the 2013-2014 winter season. Figure 3.2 presents the thermal structure data from each of the moorings in contour form, and Figure 3.3 presents the same data in the form of a line plot, where the temperature time-series from each thermistor is plotted. The contour plot is more useful for understanding how the thermal structure evolves throughout the season, while the line plots are useful when it is important to understand more precisely what the temperature is at a given depth. The plots include the onset and offset of local ice cover at each mooring to provide some context for the surface conditions. Local ice cover time-series were compiled from the IMS ice datasets (see Section 2.2.2), and were calculated as the average of the 21 IMS grid points that fall within a 10 km radius of the mooring. Complete time-series of local ice cover are included for each of the moorings during the 2013-2014 winter later, as part of Figure 3.4.

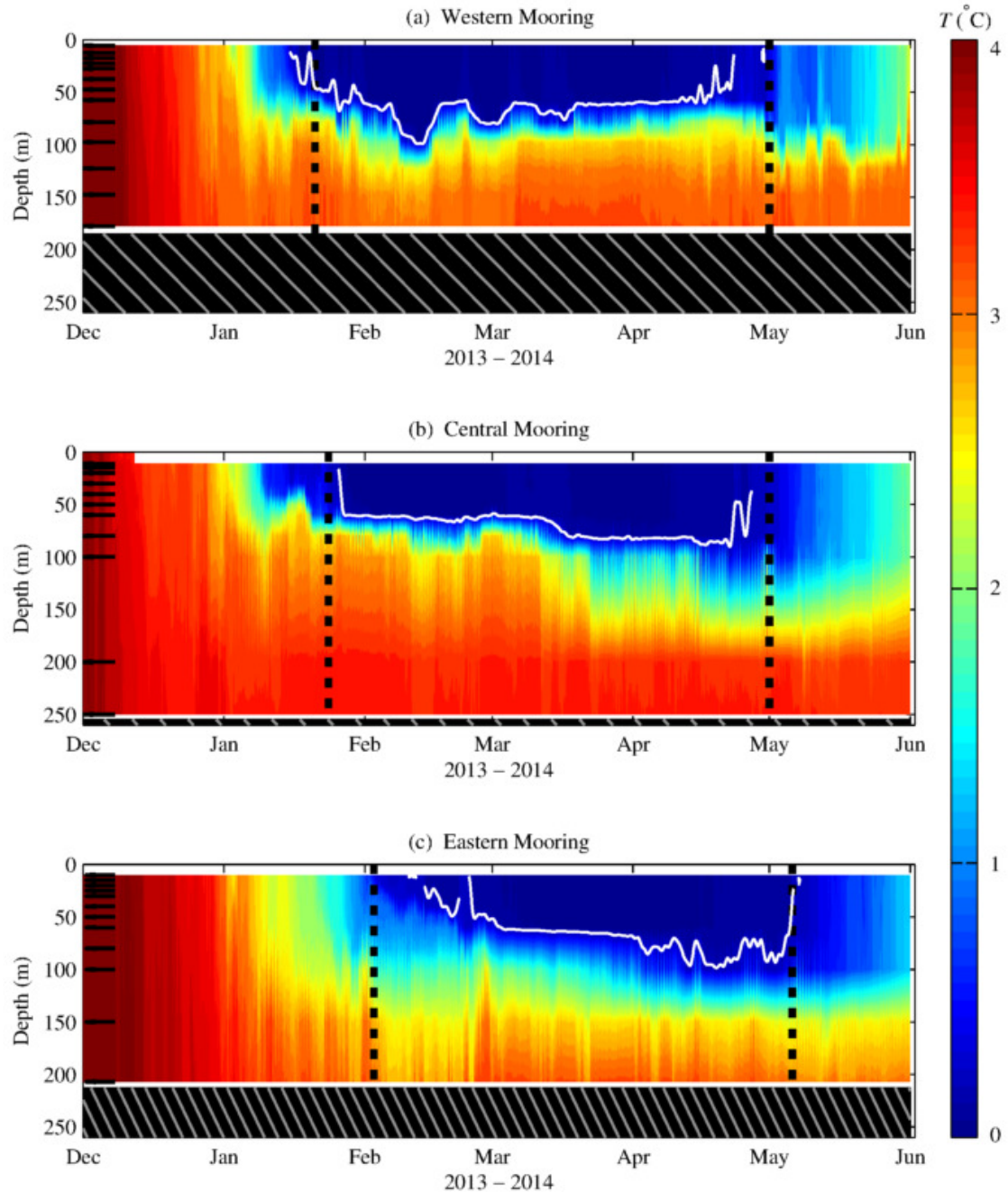


**Figure 3.2 – Mooring thermistor contour plots, winter 2013-2014.** Water temperature is shown as a function of time and depth for the (a) Western Mooring, (b) Central Mooring, and (c) Eastern Mooring during the 2013-2014 winter season. The  $0.2^{\circ}\text{C}$  isotherm is shown by a bold white line, and dashed vertical lines depict the beginning and end of the ice-covered period, as defined by the first and last days of the season for which the IMS dataset shows 100% local ice cover. Black tick marks along the y axes represent the depths of thermistors at each of the moorings.

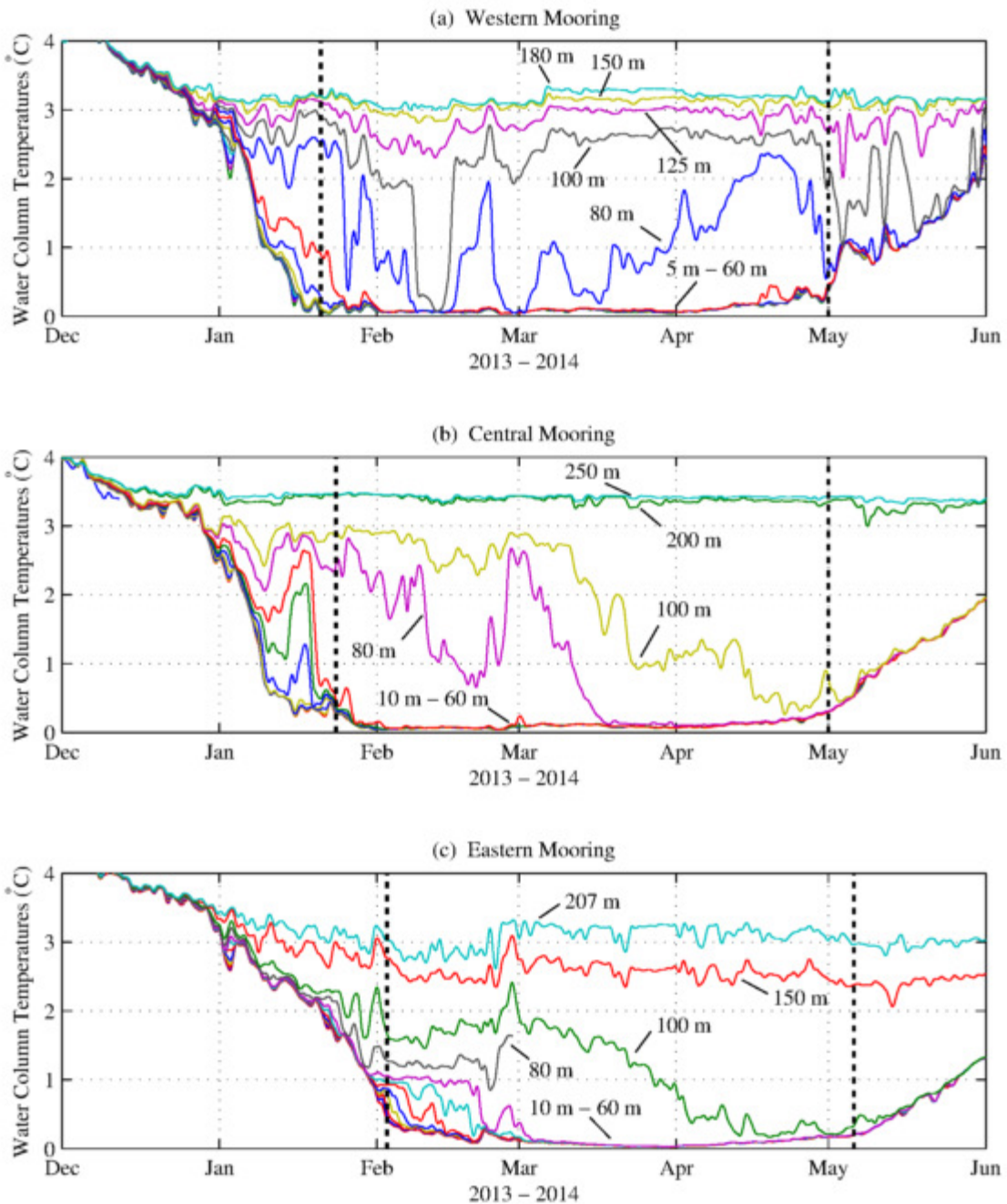


**Figure 3.3 – Mooring thermistor line plots, winter 2013-2014.** Water temperature is shown during the 2013-2014 winter season for the (a) Western Mooring, (b) Central Mooring, and (c) Eastern Mooring. At each of the three moorings, there are 7 thermistors in the 10m to 60m depth range, which could not be labeled separately in the plots because the layer is isothermal through most of the winter season. Dashed vertical lines depict the beginning and end of the ice-covered period, as defined by the first and last days of the season for which the IMS dataset shows 100% local ice cover.

At all three mooring locations, deep surface mixed layers with temperatures just above 0°C persisted throughout most of the winter season. At the Western Mooring, this layer of water with a temperature of approximately 0.1°C was observed from late January through mid April (Figure 3.2a, Figure 3.3a), and the depth of the layer varied throughout the winter season. It extended to depths between 60 and 80 m by the end of January, deepened to depths of greater than 100 m in early February, and rose to between 80 and 100 m deep from late February through mid March, and to between 60 and 80 m from mid March through mid April. Similar deep surface mixed layers with temperatures of approximately 0.1°C were observed at the Central Mooring (Figure 3.2b, Figure 3.3b) and Eastern Mooring (Figure 3.2c, Figure 3.3c). Unlike at the Western Mooring, where the depth of the surface layer was greatest in early February, the cold surface layer deepened throughout the winter at the Central Mooring and the Eastern Mooring. At the Central Mooring, this approximately 0.1°C layer deepened from approximately 60 m in early February to between 80 m and 100 m in early April. As the water column at the Central Mooring began to warm in early May, the surface mixed layer deepened to below 100 m. At the Eastern Mooring, the surface mixed layer extend deeper than 40 m by late February, deeper than 60 m by early March, and deeper than 100 m for most of April. The surface layer was also slightly colder at the Eastern Mooring than at the Western Mooring or the Central Mooring, dropping consistently below 0.05°C from mid March through early April. Bottom temperatures were warmest at the Central Mooring, ranging from approximately 3.3°C to 3.5°C throughout the stratified season (Figure 3.3b), and coldest at the Eastern Mooring during the same period, ranging from approximately 2.6°C to 3.3°C (Figure 3.3c). At the Western Mooring, the bottom temperatures were approximately 2.9°C to 3.4°C (Figure 3.2a).

In addition to the spatial variability in the thermal structure of Lake Superior (Figure 3.2), there is significant interannual variability in thermal structure of the lake. For comparison to the winter of 2014 presented here, data from 2012 (the warmest winter of the deployment) and from 2009 (the only other winter during the deployment history with substantial open lake ice cover) are presented in Titze and Austin (2014). In 2012, thermocline depths were on the order of 50 m deeper than in 2014 at all three moorings, and minimum winter surface temperatures at the Western, Central, and Eastern Moorings were above 1.5°C, 2.2°C, and 2.4°C, respectively. Stratification was also much weaker during 2012, with maximum temperature differences across the water column of approximately 1.6°C, 1.2°C, and 0.8°C at Western, Central, and Eastern Moorings, respectively, during the negatively stratified season.

One noteworthy aspect of the thermal structure under the ice is the fact that the surface mixed layer is deep, uniformly  $<0.1^{\circ}\text{C}$ , and persistent, extending to 60m at all three sites, and extending deeper in other years (Titze and Austin 2014). This is in marked contrast to the behavior of smaller lakes, which tend to form ice soon after the lake cools below the temperature of maximum density, thereby isolating the water column from wind-driven mixing (Bengtsson 2011). In these lakes, the temperature of the bulk of the water column is just below the temperature of maximum density, and a thin molecular sublayer is located just below the bottom of the ice (Ellis et al. 1991, Jonas et al. 2003). Even in Lake Baikal, where the surface water cools to near  $0^{\circ}\text{C}$  before ice formation, significant stratification forms over the course of the season in the meter below the bottom of the ice (Aslamov et al. 2014). The difference in behavior between the large and small lakes is largely due to the difference in fetch and the corresponding wave climate (Kirillin et al. 2012); the difference between Lake Superior and Lake Baikal is largely a consequence of ice Lake Baikal freezing over completely each year (Shimaraev et al. 1994), due to its cold climate, whereas ice on Lake Superior is predominantly drifting (see Section 4.0 ).

### 3.2 Effect of Ice Cover on Surface Heat Flux

The timing of the ice season was examined throughout the IMS record to put the 2013-2014 season in perspective (not shown). For this examination, ice-on was defined as the first day with lakewide-average ice cover greater than 10%, and ice-off was defined as the day after the last day with lakewide-average ice cover above 10%. The 2013-2014 ice-on date of December 19 has some recent precedent, as the date of ice-on was December 23 in 2008-2009 and December 21 in 2009-2010. On the other hand, there are no years in the IMS record with ice occurring nearly as late in the season as in 2013-2014, had an ice off date of May 22. Within the last 10 years, the latest that ice was observed prior to 2013-2014 was in April 23 during the 2012-2013 season, about a month earlier than that of 2014. Therefore, in a temporal sense, while the above-average ice cover in 2013-2014 is a result of an overall longer ice season, but the late-season ice is especially noteworthy.

Plots showing heat content and local ice cover at the three mooring locations during this year characterized by late-season ice are shown in Figure 3.4.

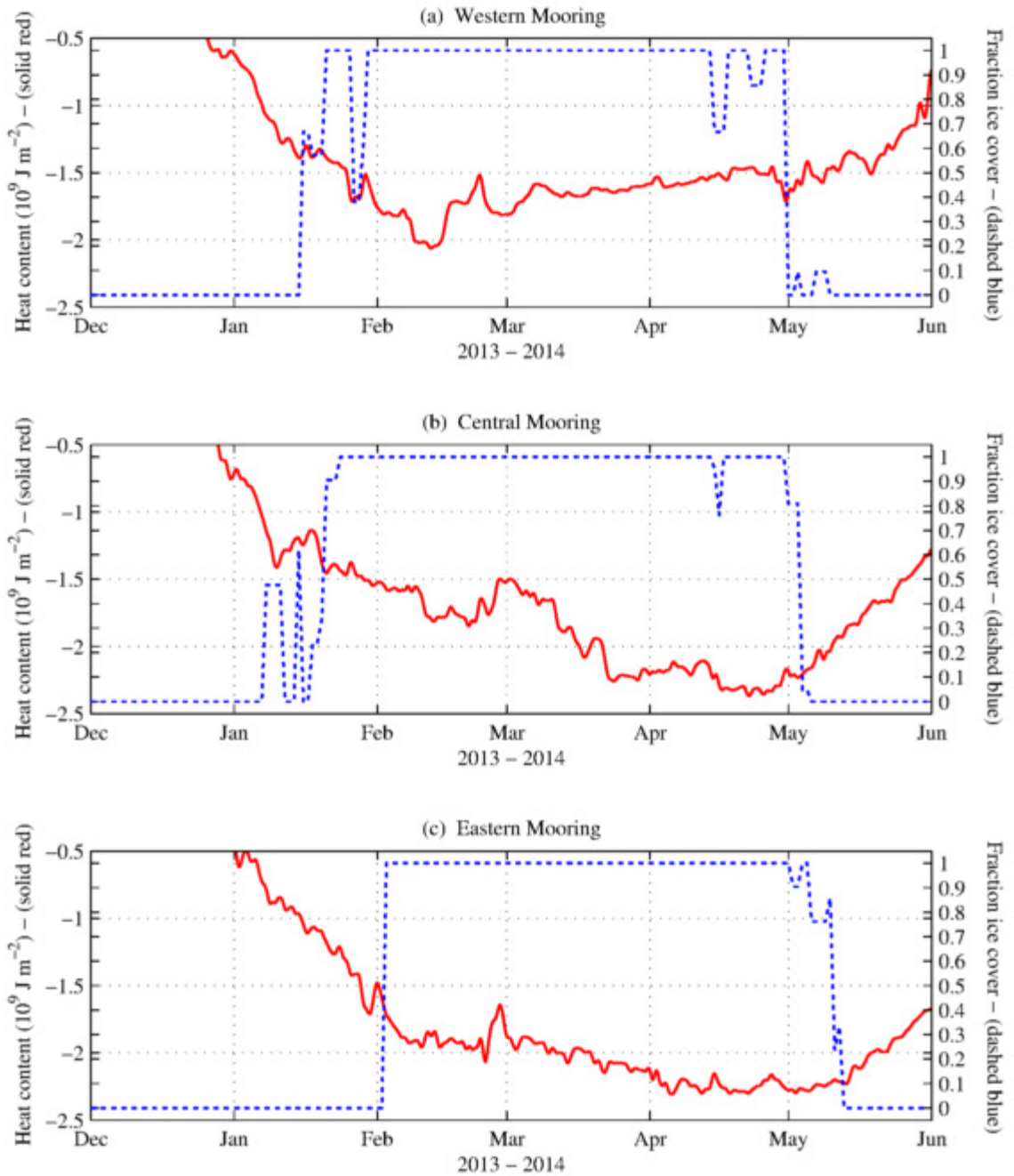


**Figure 3.4 – Heat content and ice cover, winter 2013-2014.** Heat content (solid red line) and local ice cover (dashed blue line) are shown for each of the three mooring locations during the 2013-2014 winter season. Heat content was estimated from mooring thermistor data, and local ice cover was extracted from the IMS ice datasets, calculated as the average of the 21 grid points around each mooring that fall within a 10 km radius of the mooring location.

Although not as marked as the results from the winter of 2009, evidence of reduced heat loss in the presence of ice cover was again observed during the 2013-2014 winter (Figure 3.4). This effect is most noticeable at the Eastern Mooring, where the rate at which heat is being lost from the water column is significantly reduced in early February, coincident with the formation of ice at that location. Additionally, the water column at the Eastern Mooring enters a phase of rapid warming immediately following the offset of local ice. The lake around the Western Mooring and Central Mooring also experience a rapid increase in warming around the time of their local ice-off dates. Ice offset and corresponding warming occur earlier at the Western Mooring and the Central Mooring than at the Eastern Mooring, suggesting that local ice conditions are, at least in part, responsible for spatial variability in the onset of spring warming. This is consistent with the findings of Austin and Colman (2007), though it is the first time direct observations of the phenomenon have been documented on Lake Superior.

At the Central Mooring, there is not as obvious a reduction in heat loss at the time of ice onset, as was observed at the Eastern Mooring. The lake in the vicinity of the Central Mooring continues to lose heat throughout periods of local ice cover, and at rates comparable to pre-ice conditions. Differences in heat content between the moorings are likely due to some combination of differences in advective flux and differences in aspects of local ice cover. Factors such as ice thickness and the percentage of each 4 km by 4 km IMS grid point that is covered, which cannot be resolved in the IMS datasets used, are likely important.

The extent of local ice cover around the Western Mooring fluctuates throughout the second half of January, and the water column continues to rapidly lose heat through mid February. The water column, however, experiences its lowest heat content of the winter in mid February. Heat content then increases at a relatively slow rate until ice offset at the start of May, at which point the water column begins to warm more rapidly. This is the first example throughout the mooring deployment history in which any mooring has been observed to show a warming trend as early as February. Given that the below-average regional air temperatures experienced in 2014 would result in greater heat loss from turbulent and longwave heat fluxes, and that increased albedo from above-average ice cover would reduce shortwave heat flux, the earlier warming cannot be attributed to surface heat flux. Instead, it must be attributed to advective processes. Specifically, as the temperature of the upper and lower layer at the Western Mooring do not change appreciably, almost all of the observed increase in heat content can be attributed to a shallowing of the thermocline.

### 3.3 Effect of Ice Cover on Surface Currents and Circulation

To investigate the processes by which such local warming may have occurred at WM, water velocity data from winter 2014 was examined along with nearby wind velocity data. Water velocity data was from an ADCP (see Section 2.1.1.2) deployed on the Western Mooring, and wind data was obtained from NDBC database datasets (see Section 2.3.1). Because wind data is not available at the offshore Western Mooring location during the winter months, a transfer function was developed to estimate wind velocity at the Western Mooring location using data from the land based Devils Island, WI (DISW3) station (see Section 2.3.4). The ADCP was a 300 kHz RDI Workhorse model, deployed upward looking at a depth of 80 m, with a bin size of 2 m and a measurement frequency of 20 minutes. To examine currents in the surface layer, ADCP water velocity was averaged for bin with depths in the 10 m to 20 m range, which was chosen because it falls safely within the range of the surface mixed layer (Figure 3.2), but is deep enough to minimize interference from surface waves. Results are not sensitive to this choice of depth range.

Progressive vector diagrams (PVDs) were used to visualize the prevailing wind and water velocities around the Western Mooring over the course of the 2014 winter, and these are presented in Figure 3.5. PVDs (Emery and Thomson 2001) represent the cumulative sum of a velocity time-series taken from a single point and represent the path a particle would travel over a given timeframe, and are therefore a Lagrangian representation of an Eulerian observation. They are calculated from discrete data using:

$$\vec{x}_n = \vec{x}_0 + \sum_{i=1}^n \vec{v}_i \Delta t \quad \text{Equation 3.1}$$

Where  $\vec{x}_n$  is the position after  $n$  time-steps,  $\vec{x}_0$  is the initial position (taken to be the axes origin here),  $\vec{v}_i$  are the measured velocities, and  $\Delta t$  is the time step. For the data presented in Figure 3.5, wind velocity has a time-step of 1 hour, and ice velocity has a time step of 20 minutes.

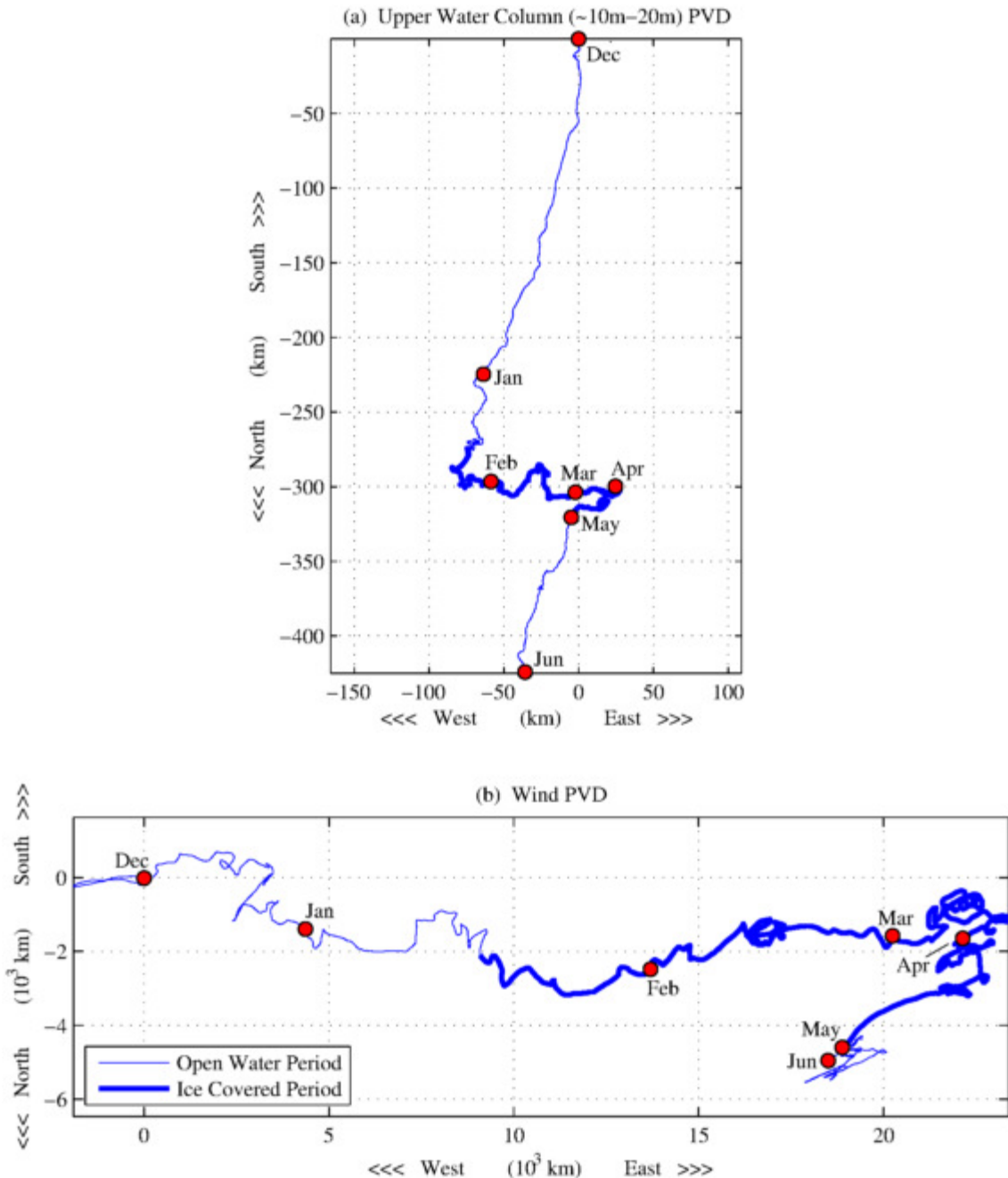


**Figure 3.5 – Western Mooring water velocity and wind velocity PVD, winter 2013-2014.** Progressive vector diagrams are shown for (a) water in the upper water column (~10-20m depth), and (b) estimated winds at the Western Mooring location to show their predominate directions of movement. Dots are shown to represent the beginning of each calendar month, and bold lines indicate the period during which Western Mooring was under ice cover, as determined from the IMS datasets.

Wind velocities were predominantly heading east-southeast from mid December through late January, east-northeast from late January through the end of February, and south-southwest during most of April (Figure 3.5b). Throughout March, wind velocities are highly variable, with no clear predominant direction, and the same is true during May.

The dynamics of water currents in the upper water column shift dramatically in the presence of local ice cover (Figure 3.5a). Prior to the formation of ice around the Western Mooring, currents in the upper water column were predominantly heading south-southwest, and showed no apparent direct response to variations in wind velocity. However, beginning shortly after the onset of ice, and continuing through ice-covered season. Although visual inspection of Figure 3.5a alongside Figure 3.5b suggests that the direction of surface currents is in the same predominant direction as that of the wind, a closer analyses (not shown) demonstrates the two are not directly correlated. At approximately the time of ice offset (May 1), upper water column currents again resume flow in a south-southwest direction.

I will first focus on implications of the shift in near-surface water velocity in the presence of ice cover; however, the predominate south-southwest direction of water velocity during ice free periods will be addressed subsequently. It is not currently known why the flow direction shifts dramatically during periods of heavy ice cover. The shift in flow dynamics cannot be attributed to stratification, because the stratified period at the Western Mooring begins earlier and ends later than the ice covered period (Figure 3.2), and therefore does not correspond with the timing of the observed shift. This leaves ice cover as the only plausible explanation, though the physical role ice plays in driving this shift is not immediately clear.

For the western portions of the lake, a predominantly eastern flow of the upper water column, as was observed at the Western Mooring during February and March (Figure 3.5a), is favorable for upwelling. As cold water in the upper water column moves east, away from the western edge of the basin, there must be a compensating westward flow of warmer bottom water (Figure 3.6). Such upwelling will drive the thermocline upward in the western portion of the lake, as seen at the Western Mooring throughout the winter season (Figure 3.2a). In turn, rising thermoclines during these conditions of negative stratification would locally increase heat content through this advective process. Therefore, the observed shift in upper water column currents at the Western Mooring location is a plausible explanation for the gradual rise in heat content documented at the Western Mooring throughout the ice-covered season (Figure 3.4a).

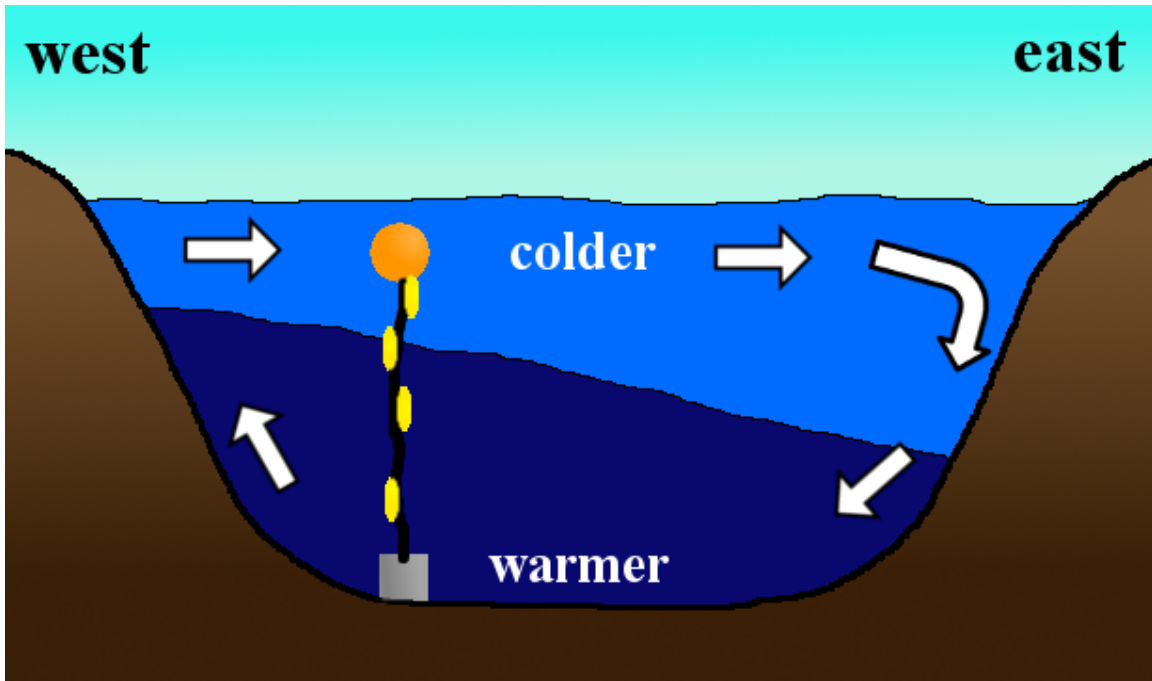


**Figure 3.6 – Heat redistribution conceptual sketch.** This figure conceptually demonstrates how surface currents moving to the east could produce a displacement of the thermocline and corresponding redistribution of heat.

It is difficult to draw any inferences on the size of such heat redistribution circulation patterns, given that the Western Mooring ADCP water current data comes from a single point in space. The Eastern Mooring was equipped with an ADCP, so there is also water velocity data available from one location in the Eastern Basin of the lake during the 2013-2014 winter season. The ADCP at the Eastern Mooring was also a 300 kHz RDI Workhorse model, and was deployed upward looking at a depth of 80 m, with a bin size of 2 m and a measurement frequency of 1 hour. Figure 3.7 presents a PVD for near-surface (~10 m to 20 m depth) water velocities, along with a PVD of estimated wind velocities for context. Wind velocity at the Eastern Mooring during the 2013-2014 winter was estimated from the Stannard Rock, MI (STDM4) station (see Section 2.3.1) using an empirical transfer function (see Section 2.3.4).

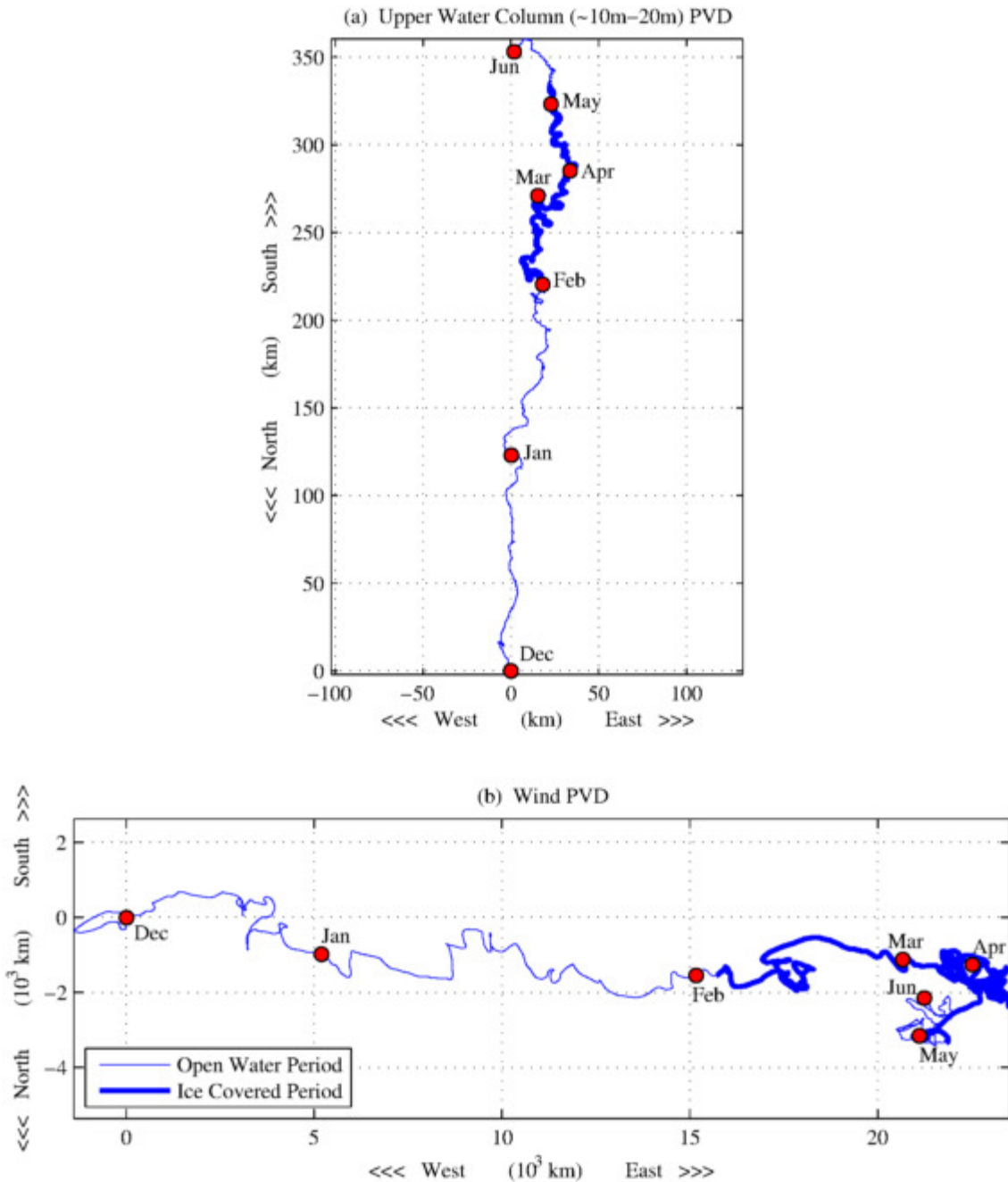


**Figure 3.7 – Eastern Mooring water velocity and wind velocity PVD, winter 2013-2014.** Progressive vector diagrams are shown for (a) water in the upper water column (~10-20m depth), and (b) estimated winds at the Eastern Mooring location to show their predominate directions of movement. Dots are shown to represent the beginning of each calendar month, and bold lines indicate the period during which Eastern Mooring was under ice cover, as determined from the IMS datasets.

The progression of wind velocity over the course of the 2013-2014 winter season at the Eastern Mooring (Figure 3.7b) is similar to that estimated at the Western Mooring (Figure 3.5b). Wind velocity at the Eastern Mooring is predominately to the east throughout the early portions of the winter season, and exhibits no predominate direction through late March and early April, is generally to the southwest in the latter portions of April, and has no predominate direction throughout May. Water velocities in the surface layer at the Eastern Mooring (Figure 3.7a), however, travel nearly due north throughout the 2013-2014 winter. Unlike at the Western Mooring (Figure 3.5a), water currents at the Eastern Mooring show no clear shift in direction during times of ice cover. The northern direction of waters in the surface layer at the Eastern Mooring during both open-water and ice-covered conditions suggests that the shift in water currents and corresponding redistribution of heat inferred from the observations at Western Mooring was not a lakewide phenomenon.

In order to gain a better understanding of the shift in near-surface currents observed at the Western Mooring in the presence of ice cover, and the extent to which the shift can be attributed to the unusually high ice cover observed during the 2013-2014 winter, PVDs were assembled for all years for which data is available from the Western or Eastern Moorings. The Western Mooring has water velocity data from the surface layer for the winters of 2008-2009, 2010-2011, and 2013-2014, while the EasternMooring has data for the winters of 2008-2009, 2009-2010, and 2013-2014. When possible, wind velocity at the Western Mooring was estimated from the Devils Island, WI (DISW3) station; however, wind velocity data was not available from DISW3 during the 2008-2009 winter, and wind velocity was instead estimated from the Rock of Ages, MI station (ROAM4) during that year. Similarly, wind velocity at the Eastern Mooring was estimated from the Stannard Rock, MI (STDM4) when possible, but data was not available from STDM4 during the 2008-2009 winter, and was estimated from the Big Bay, MI (BIGHM4) station instead. The locations and data availability of the NDBC database stations from which wind velocity was estimated are presented in Section 2.3.1, and the development of the empirical transfer functions is presented in Section 2.3.4. PVDs showing water velocity in the surface layer and estimated wind velocity for years in which data is available at each of the mooring locations is presented in Figure 3.8.

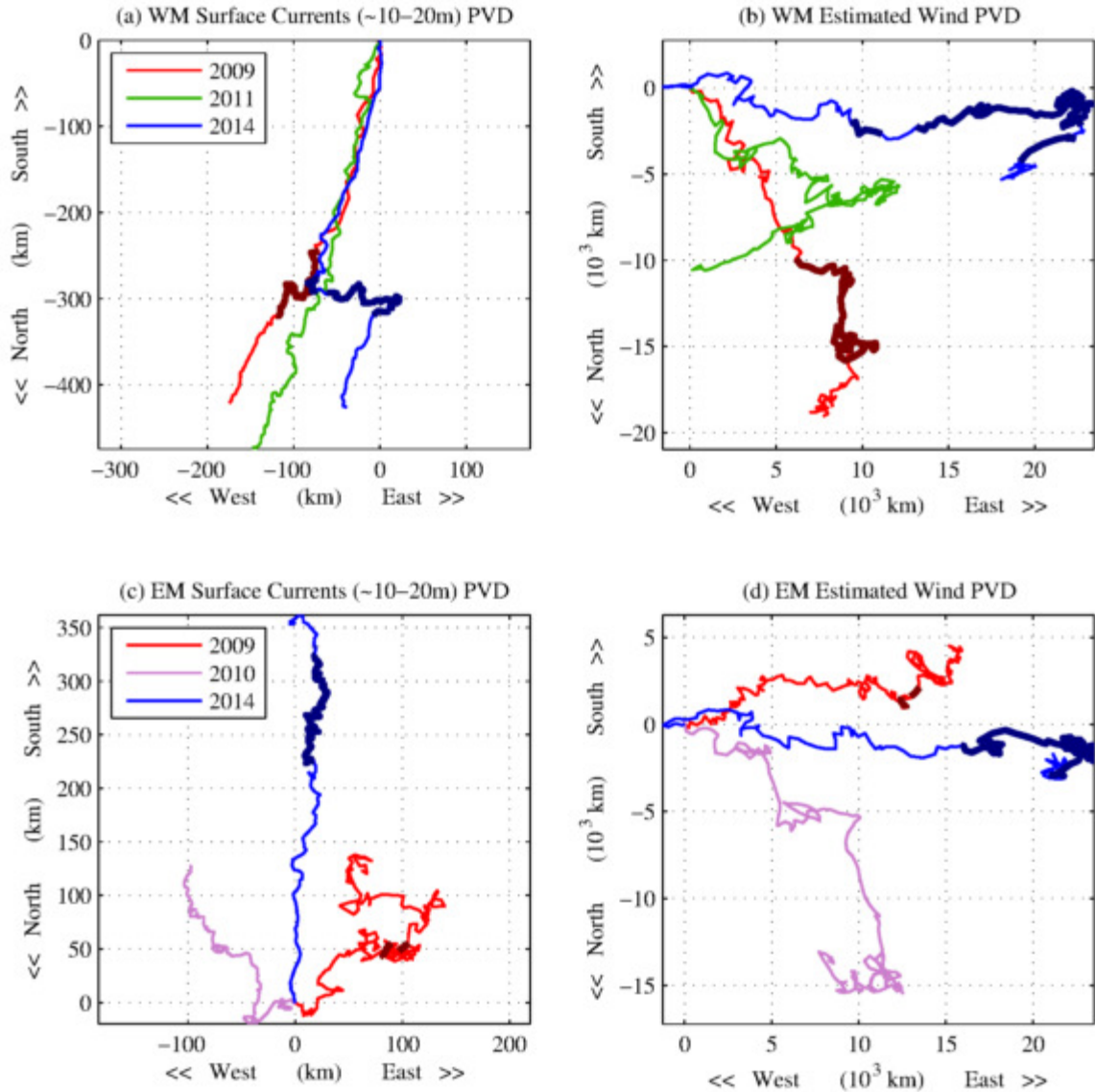


**Figure 3.8 – Typical Water current and wind direction.** Progressive vector diagrams are shown for (a,c) water in the upper water column (~10-20m depth), and (b,d) estimated winds for both the (a,b) Western Mooring and (c,d) Eastern Mooring for years during which data were available. Bold lines indicate the period during which Eastern Mooring was under ice cover, as determined from the IMS datasets.

Neither mooring demonstrates an obvious, direct response of water velocity to wind velocity. Over the years for which data is available, winds at both the Eastern and Western Mooring locations are characterized by a zonal component that is generally to the east, although that component does shift to the west near the end of the winter season during most years. The meridional component of the wind velocity is generally to the south at the Western Mooring, and varies from slightly to the north to significantly to the south at the Eastern Mooring. Water

velocities at the Western Mooring are consistently to the south-southwest at the Western Mooring, except during periods of ice cover. Water velocities at the Eastern Mooring consistently have a northward component, but there is variability in the zonal component between the three years of available data.

The predominate direction of water movement during open-water water periods at both the Western and Eastern Moorings can be better understood in the context of the local bathymetry around each of the moorings. The lake bathymetry in the region surrounding the Western Mooring is shown in Figure 3.9 and the bathymetry surrounding the Eastern Mooring is shown in Figure 3.10, based on data from the NCEI datasets (see Section 2.4). When the near-surface currents shown in Figure 3.5 are examined in the context of the bathymetry shown in Figure 3.9, it is evident that the orientation of the near-surface currents corresponds well to the orientation of isobaths in the vicinity of the Western Mooring. Bennington et al. (2010) show that mean winter currents in the vicinity of the Western Mooring exhibit a general counter-clockwise circulation pattern around the deep basin to the east of the Western Mooring. The south-southwest direction of currents at the Western Mooring during portions of the winter without ice cover is consistent with currents that are part of such a counter-clockwise circulation pattern following the relatively steep ridge on which the Western Mooring is located. Similarly, Bennington et al. (2010) show that mean winter currents flow clockwise around the deep basin the eastern part of Lake Superior, and the Eastern Mooring is located along the eastern edge of that basin (Figure 3.10). While the bathymetry is somewhat uneven around the Eastern Mooring, and the direction of near-surface currents some variability over the years examined (Figure 3.8c), the general northern flow of water observed at the Eastern Mooring is consistent with counter-clockwise flow around the deep basin next to which it is located.

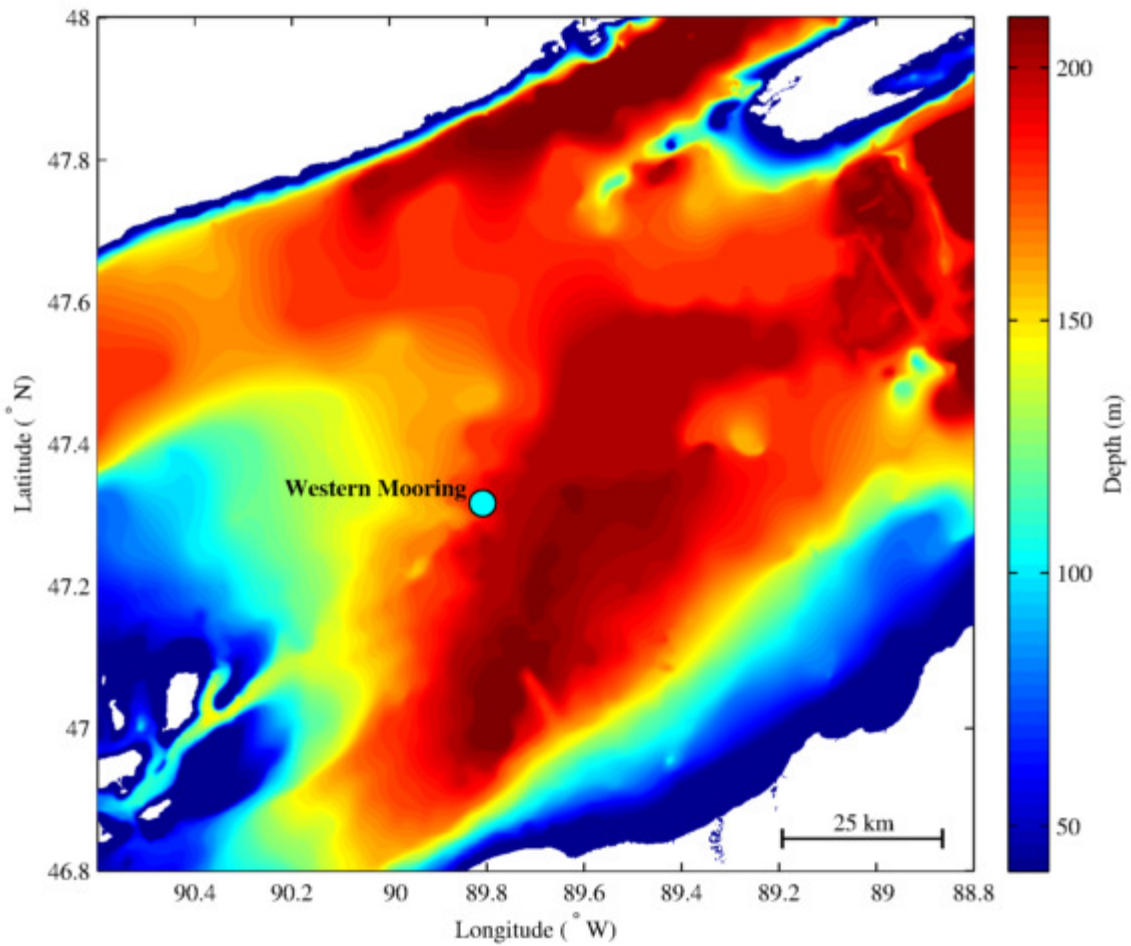


**Figure 3.9 – Lake bathymetry near the Western Mooring.** Lake Superior bathymetry from the NCEI datasets is shown for the region surrounding the Western Mooring.

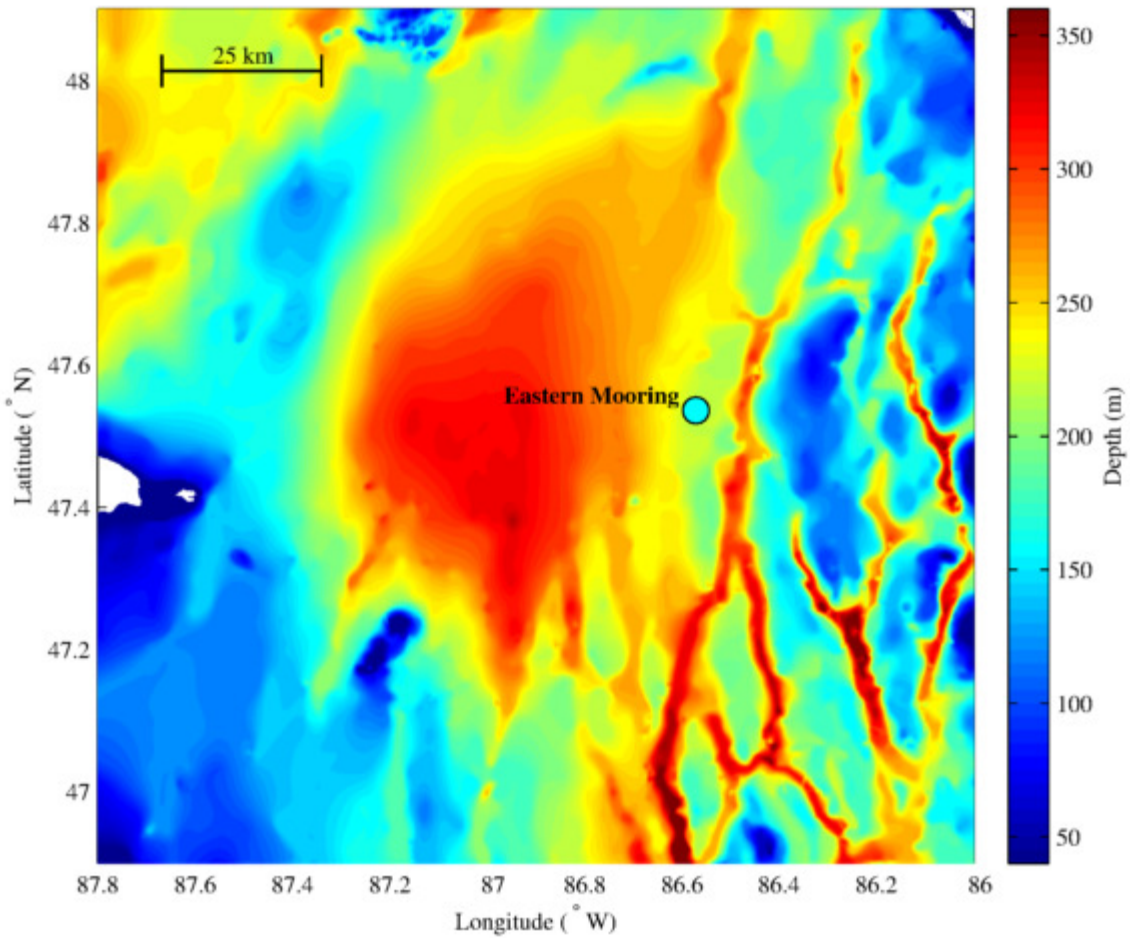


**Figure 3.10 – Lake bathymetry near the Eastern Mooring.** Lake Superior bathymetry from the NCEI datasets is shown for the region surrounding the Eastern Mooring.

While the predominate current direction at each of the two moorings can be largely explained in the context of basin-scale lake gyres (Bennington et al. 2010) and local bathymetry (Figure 3.9; Figure 3.10), the mechanism driving the shift of currents at the Western Mooring when ice is present remains to be determined. Because there is no clear relationship between the direction of currents during times of ice cover and the direction of wind during times of ice cover (Figure 3.8), this mechanism can likely not be established through a local force balance. It is possible that the size or position of basin-scale gyres is affected by the presence of ice, and that the dramatic shift in current direction observed at the Western Mooring is simply a results of its location within the gyre. It is also possible that the ice field in the western portion of the lake, which has been observed to dynamically lock-up (as discussed in Section 4.0 ), shields the lake

from wind stress sufficiently to inhibit gyres from forming. While the clear shift in currents in the presence of ice cover is interesting, additional work is needed to characterize the extent of its influence and the mechanisms by which it occurs.

### 3.4 Conclusion

The results presented in this section expand on the work conducted for my Masters thesis, and later published in Titze and Austin (2014). In the high ice-year of 2013-2014, early-season ice was observed to reduce heat loss in open-water locations on the lake, consistent with the conclusions of Titze and Austin (2014). The persistent late-season ice in 2013-2014 was observed to delay spring warming, which is a relation that was empirically established by Austin and Colman (2007), but that has previously not been directly observed in Lake Superior.

While horizontal redistribution of heat was discussed in Titze and Austin (2014), the work contained in this section takes the next step toward understanding those processes by analyzing ADCP water column current data alongside water column thermal structure data. Heat content at the open-water Western Mooring location rises throughout the winter season, coincident with a shift in the direction of surface-layer currents at that location. The rise in heat content at the Western Mooring is associated with a rise in the thermocline, suggesting that the shift in surface currents resulted in horizontal redistribution of heat, in which colder surface water from the Western Mooring location were blown to the east, and compensate by an influx of warmer bottom water. No evidence of corresponding heat redistribution was observed at the Eastern Mooring, demonstrating that this is not a lakewide circulation pattern.

Surface currents at the Western Mooring were found to have deviated from their predominate south-southwestward direction only during the periods when ice cover was present at the Western Mooring, implicating ice cover in the directional shift of currents. Analysis of current data from previous years show that a similar shift in currents was observed in the presence of ice cover at the Western Mooring during the winter of 2008-2009, and no shift was observed in the ice-free winter of 2010-2011. Similar shifts were not observed at the Eastern Mooring during any of the years examined.

Additional work is needed to characterize the observed shift in currents in the western arm of the lake. This could likely be best accomplished through numerical modeling. The ROMS Lake

Superior model used in this thesis has been unable to reproduce the observed shift in currents to this point. This is likely, in part, due to its general propensity to under-predict ice on the lake (see Section 2.6). As such, any improvement in the ability of the model to predict ice cover on the lake would likely be of use with regard to our understanding of this phenomenon.

Observationally, an array of moorings that is focused in the western arm of the lake would be helpful toward characterizing the scale of these circulation patterns and corresponding redistribution of heat. During the 2013-2014 winters, ADCPs were only deployed on the Western and Eastern Moorings. While this was helpful in discerning that heat redistribution was not occurring on a lakewide scale, a tighter array of moorings may be helpful in narrowing down the scales over which these processes occur in the western arm of the lake.

## 4.0 Lake Superior Ice Characteristics

*Results from this section have been modified into a manuscript, co-authored by Jay Austin, which has been peer reviewed and accepted in the Journal of Great Lakes Research, in press as of September 2016.*

The combination of Lake Superior's size and mid-latitude location places it within a relatively narrow regime of large lakes that form drift ice. The drift of ice, while extensively studied in the world oceans (Leppäranta 2008), has been largely unstudied in large lakes, such as Lake Superior, due in large part to the fact that few lakes are large enough to support drifting ice (Kirillin et al. 2012). While there are some datasets available that describe the areal extent of ice cover on the Great Lakes (see Section 2.2), there is very little data available on the characteristics of that ice. Available measurements are primarily derived from remotely sensed data (Assel 2003; Assel 2005; Wang et al. 2012a; National Ice Center 2015; Leshkevich and Nghiem 2013), with very little in-situ data available. In addition, a decline in ice cover has been observed in water bodies throughout the Northern Hemisphere over the last few decades (Magnuson et al. 2000, Benson et al. 2012) and has been well-documented in Lake Superior (Wang et al. 2012b; Van Cleave et al. 2014; Wang et al. 2010). With fewer high-ice years occurring in recent decades, opportunities to collect data on ice cover in large lakes, as well as role ice plays in influencing various lake-climate processes, are becoming increasingly less common. However, during the 2013-2014 winter, the Great Lakes region experienced unusually cold temperatures and high ice cover (Clites et al. 2014; Gronewold 2015). This resulted in a rare opportunity to study the characteristics and behavior of ice on Lake Superior during a high-ice year.

To put this problem in context, the spectrum of ice dynamics can be described in terms of two extremes. At one extreme, there is free-drifting ice, in which there are no internal stresses in the ice field and the stress of the wind on the ice is balanced by the stress of the water on the ice. An example of such free-drifting ice is an iceberg drifting in the ocean. At the other extreme is landfast ice, where a coherent body of ice forms over all or part of a lake, and does not move or drift. In the last of landfast ice, the wind stress is balanced by internal forces in the ice field and by ice pressing on the shores of the water body. Examples of landfast ice are the solid ice surfaces that form on smaller lakes in mid-latitude or higher regions (Kirillin et al. 2012), as well as large higher-latitude lakes, such as Lake Baikal (Shimarev et al. 1994). The Great Lakes

experience partial ice-cover each year, most of which is not landfast, but which can be present at concentrations upwards of 90% throughout all or most of the lakes during high-ice years (Assel 2003; Assel 2005; Wang et al. 2012a). As such, the Great Lakes fall between these two extremes, and it is not known if ice on the Great Lakes behaves more like free-drifting ocean ice, or if it is significantly restricted by internal stresses.

I use data from this particularly cold and icy to characterize the dynamics of drift ice on a large lake. Specifically, I use ADCP data from the Western Mooring (see Section 2.1) during the 2013-2014 winter, which captured ice-drift, in conjunction with wind velocity data from nearby onshore meteorological stations (see Section 2.3.1). By comparing ice drift velocities with wind velocity, I examine whether the ice is responding to wind stress like free-drifting ice, or whether it is restricted by internal forces. Leppäranta (2008) describes, in detail, the dynamics of free-drifting ice in the oceans, and that text will be used as a basis for this comparison.

In addition, unintended measurements of depths of passing ice keels were also made over the 2013-2014 winter by pressure sensors on the moorings. While these ice keel observations measurements are not representative of general ice thickness on the lake, they provide some insight toward the depths to which ice ridges pile up within the lake. When coupled with ADCP data that shows the speed of the passing ice keel (used in combination with the duration of its passing from the pressure sensor data, I make some approximations as to the horizontal size of the keels. In addition, by looking at the percentage of time that ice keels of various depths were present above the Western Mooring, some estimates can be made as to the extent to which ice is tied up in these deep keels. These ice-keel measurements provide an interesting extra dimension to our understanding of ice characteristics on large lakes.

Given that the Great Lakes represent such large and important systems, and that ice is present on the lake for a significant portion of the year, it is fundamentally important that the characteristics of that ice are understood. Perhaps the most beneficial use of such an understanding would be in improvement in the ability to model ice systems, both dynamically and thermodynamically. As our knowledge of ice on large lake systems is advanced through observations, so too will our ability to develop and improve numerical models that produce accurate and realistic results. With the lack of observations describing ice dynamics on large lakes, these observations will fill an important void in our understanding of lake-ice systems.

## 4.1 Ice Drift

Three moorings subsurface moorings were deployed in Lake Superior over the 2013-2014 winter season (Figure 4.1). Each mooring was equipped with thermistors and pressure sensors, and the Eastern and Western Moorings were equipped with ADCPs. The Lake Superior mooring array is discussed in detail in Section 2.1. ADCPs at the Western and Eastern Moorings were upward-looking 300 kHz RDI Workhorse models, with designed deployment depths of 80 m, and were intended to measure currents in the upper portion of the water column. A bin size of 2 m and a measurement frequency of 20 min were used during this deployment, and the compass of each ADCP was calibrated immediately prior to being deployed.

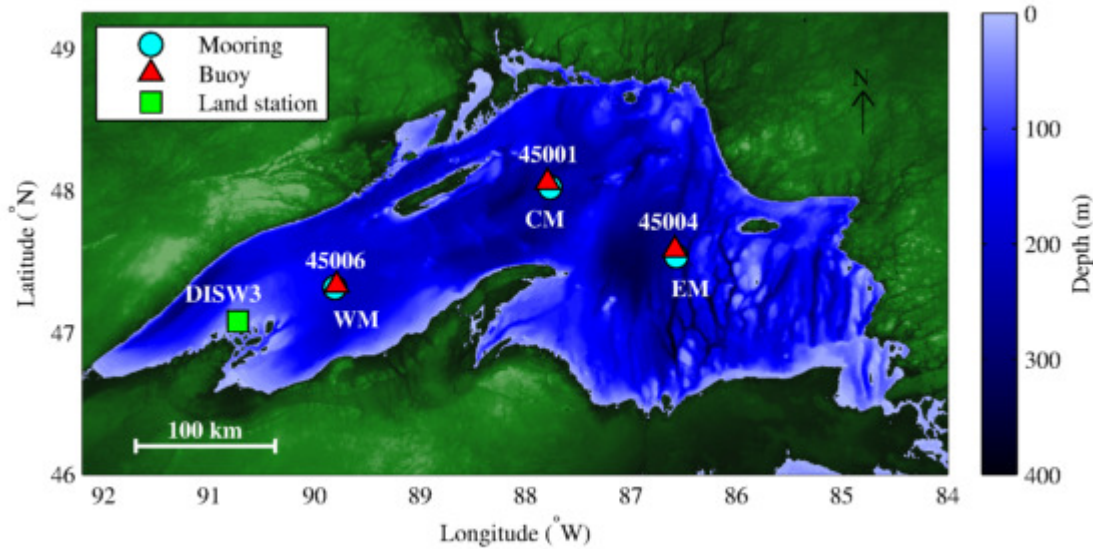


**Figure 4.1 – Map of relevant locations for Section 4.1 and Section 4.2.** This map shows locations on Lake Superior that are relevant to Section 4.1 and Section 4.2, including subsurface moorings (blue circles), NDBC meteorological buoy locations (red triangles), and NDBC database coastal meteorological stations (green squares).

Due to steep gradients in bathymetry in certain regions of the lake, which can make it difficult to deploy moorings at the designed depth, the Western Mooring was deployed approximately 3 meters shallower than intended during the 2013-2014 winter deployment. This resulted in unintentional measurements of ice drift. Typically, near-surface data from ADCPs are not useful because the reflections from waves at the surface interfere with the signals. Given the unreliable nature of the data, and the fact that storage capacity is often a limiting factor in our ADCP operations, near-surface ADCP data have not historically been collected. However, the shallow

deployment of the Western Mooring resulted in the ADCP range overshooting the surface, and during this high ice-cover year, a clear signal was obtained off of the bottom of the ice during periods of ice cover.

Figure 4.2 shows plots of signal return intensity from the Western and Eastern Moorings during the 2013-2014 winter season. A clear peak in signal return intensity is evident in the plot from the Western Mooring (Figure 4.2a), which is indicative of a reflective interfacial boundary. This is in contrast to the plot at the Eastern Mooring (Figure 4.2b), which is representative of a typical upward-looking ADCP deployment for the Lake Superior mooring array, in which the ADCP range extends to slightly below the surface.

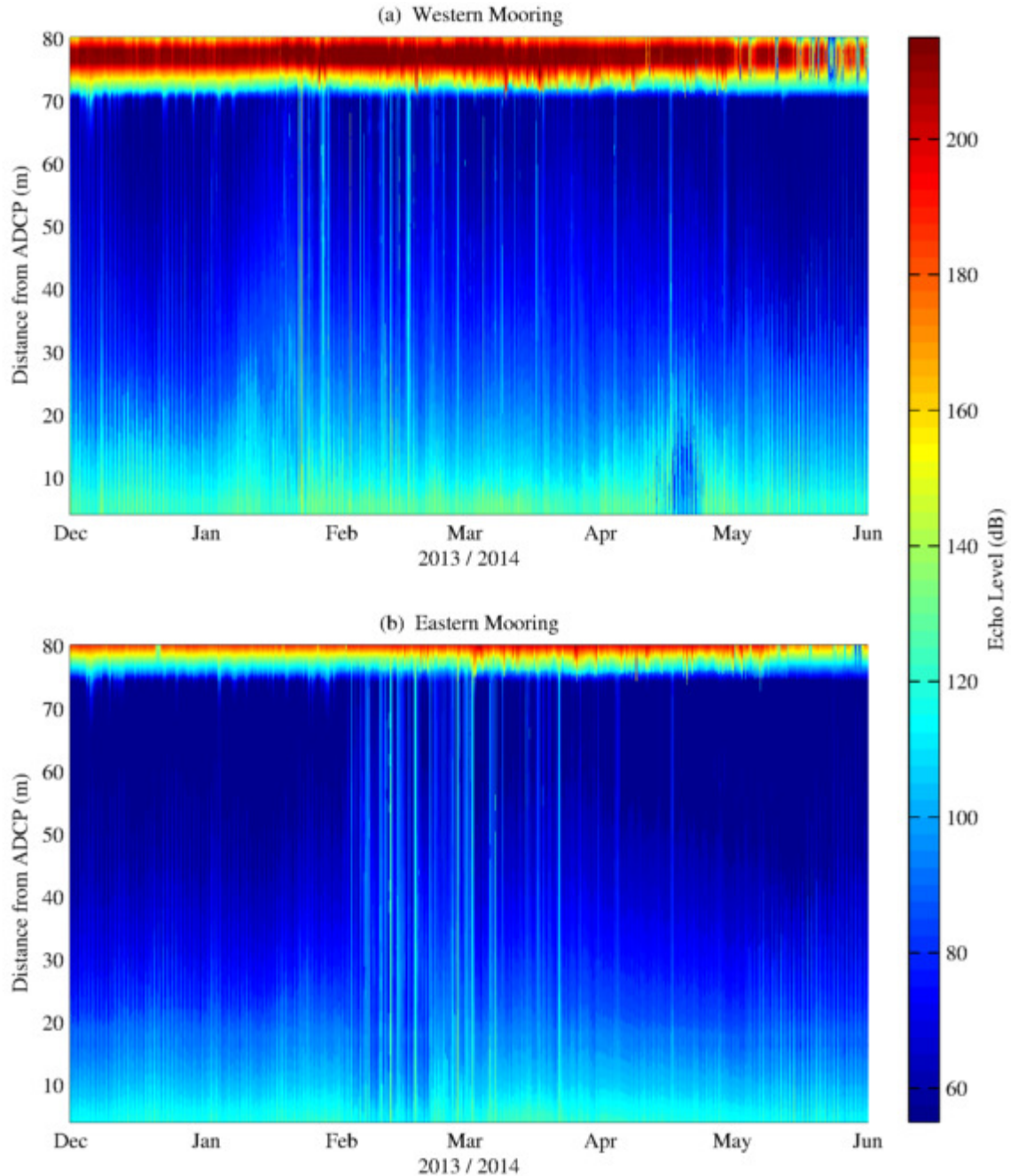


**Figure 4.2 – ADCP intensity plots, Winter 2013-2014.** The intensity of signal return (echo level) is shown for the ADCPs at the (a) Western Mooring and (b) Eastern Mooring during the 2013-2014 winter.

While ADCPs are designed to produce records of water currents, under the proper setup and conditions, it is possible to extract additional signals from the measurements they produce, including estimates of ice drift and ice draft. ADCP ice drift measurements are obtained using

the same principles through which ADCP water velocity measurements are obtained (see Section 2.1.1.2). As the ADCP signal is reflected off the bottom of the ice surface, the velocity of that ice surface can be inferred based off of the doplar shift of the return signal. Ice draft can be estimated using the peak of the intensity curve, because the location of the peak corresponds to the location of the ice-water boundary. Such techniques have been used successfully in the oceanographic community (Belliveau 1990, Shcherbina et al. 2005, Björk 2008). In the case of the Western Mooring ADCP over the 2013-2014 winter, the ADCP collected reliable measurements of ice velocities; however, at 2 m, bin size was unfortunately too coarse to be useful in characterizing ice thickness.

Figure 4.3 shows the average intensity of signal return for each bin during the ice-covered portion of the 2013-2014 winter season. The ice-covered period is defined as the first and last days where the IMS dataset (see Section 2.2.2) shows 100% ice cover in the 10-km region surrounding the Western Mooring. This was found to be January 21, 2014 through April 30, 2014. As shown in Figure 4.3, there are two bins that show near-equal average signal return intensity, suggesting that the ice surface was located at a distance from the ADCP near the middle of these range bins. Ice velocities were calculated using the average of these two 2-m bins.

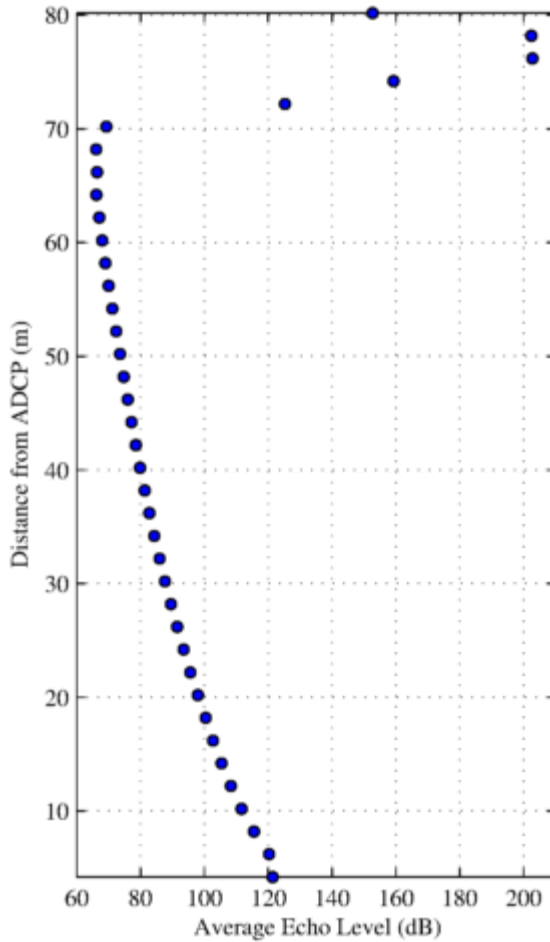


**Figure 4.3 – Average ADCP intensity profile, Western Mooring, Winter 2013-2014.** The time-averaged profile of signal return intensity for the Western Mooring during the ice-covered portion of the 2013-2014 winter. Each point represents the average signal return intensity for a discrete ADCP bin.

These ice drift velocities were examined in the context of wind velocities in order to examine the relationship between ice drift and wind forcing. Because offshore wind velocity data are not available during the winter months, a land-based station must be used to estimate offshore winds. The NDBC Devils Island, WI station (DISW3) was used to estimate winds at the Western Mooring during the 2013-2014 winter. Wind velocities from DISW3 were compared to wind velocities at NDBC Buoy 45006 (located proximal to the Western Mooring) during periods in which both stations are operating simultaneously. No statistically significant directional offset was observed. However, due at least in part to the fact that coastal DISW3 station is located at a much higher elevation than the 45006 buoy, wind speeds measurements are higher at DISW3 than at 45006. An empirical transfer function of  $u_{WM} = 0.57u_{DISW3} + 1.56 \text{ m s}^{-1}$  was found to

best estimate the offshore winds (Table 2.2). Methods used for estimating offshore winds from coastal stations are detailed in Section 2.3.4.

The wind velocity and ice velocity time-series are presented as progressive vector diagrams (PVDs; Emery and Thompson 2001), as described in Section 3.3 by Equation 3.1. These PVDs for wind velocity and ice velocity are shown in Figure 4.4.

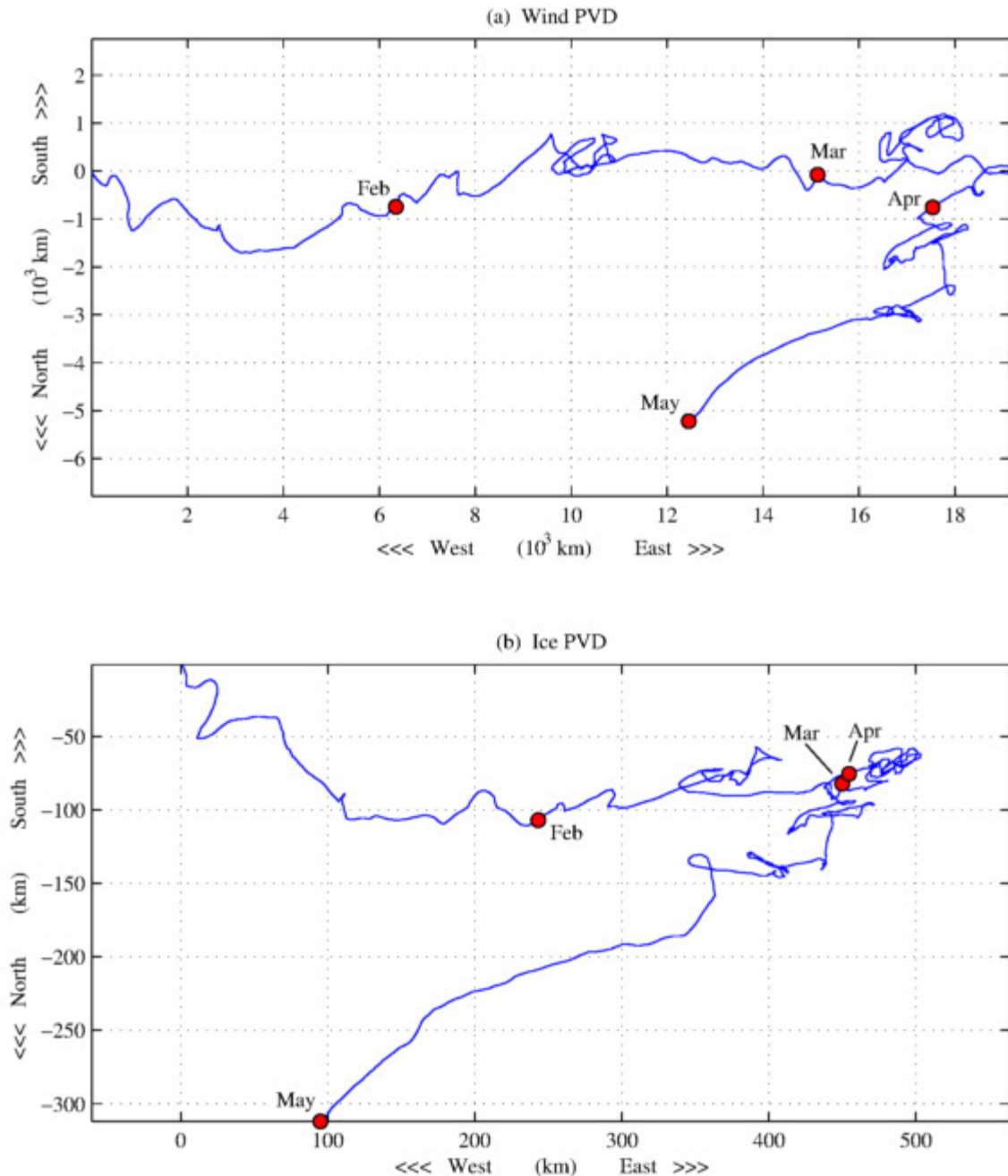


**Figure 4.4 – Wind and ice PVDs, Western Mooring, Winter 2013-2014.** Progressive vector diagrams (PVDs) show the predominant directions of (a) wind and (b) ice at the Western Mooring throughout the 2013-2014 winter season.

Ice velocities are shown to follow the same general patterns as wind velocities (Figure 4.4). From the time of ice formation (January 21) through the beginning of March, ice velocities are in a

predominantly eastern direction, with a slight southern component for most of January, and a slight northern component for most of February. As with wind direction, there is no predominant direction of ice movement throughout March, and ice movement is generally to the south-southwest throughout April. This visually consistent relationship suggests there is, indeed, a coherent relationship between ice velocity and wind velocity, and I will proceed by examining that relationship more closely.

I will begin by more-closely examining the relationship between wind speed and ice speed. Raw wind speed and ice speed time-series are presented in Figure 4.5. While it is difficult to visually pick-out a clear overall relationship from these plots, they are presented to discuss the two ends of the range of ice speeds. First, it is clear from these plots that there are times, such as late February, during which ice speed is stationary or near-stationary while wind speed remains relatively high. This suggests that there are periods in which internal stresses in the ice field likely become important. As such, the relationship between ice speed and wind speed may not hold in cases of high ice concentration or low wind speed. This is further-examined later in this section.

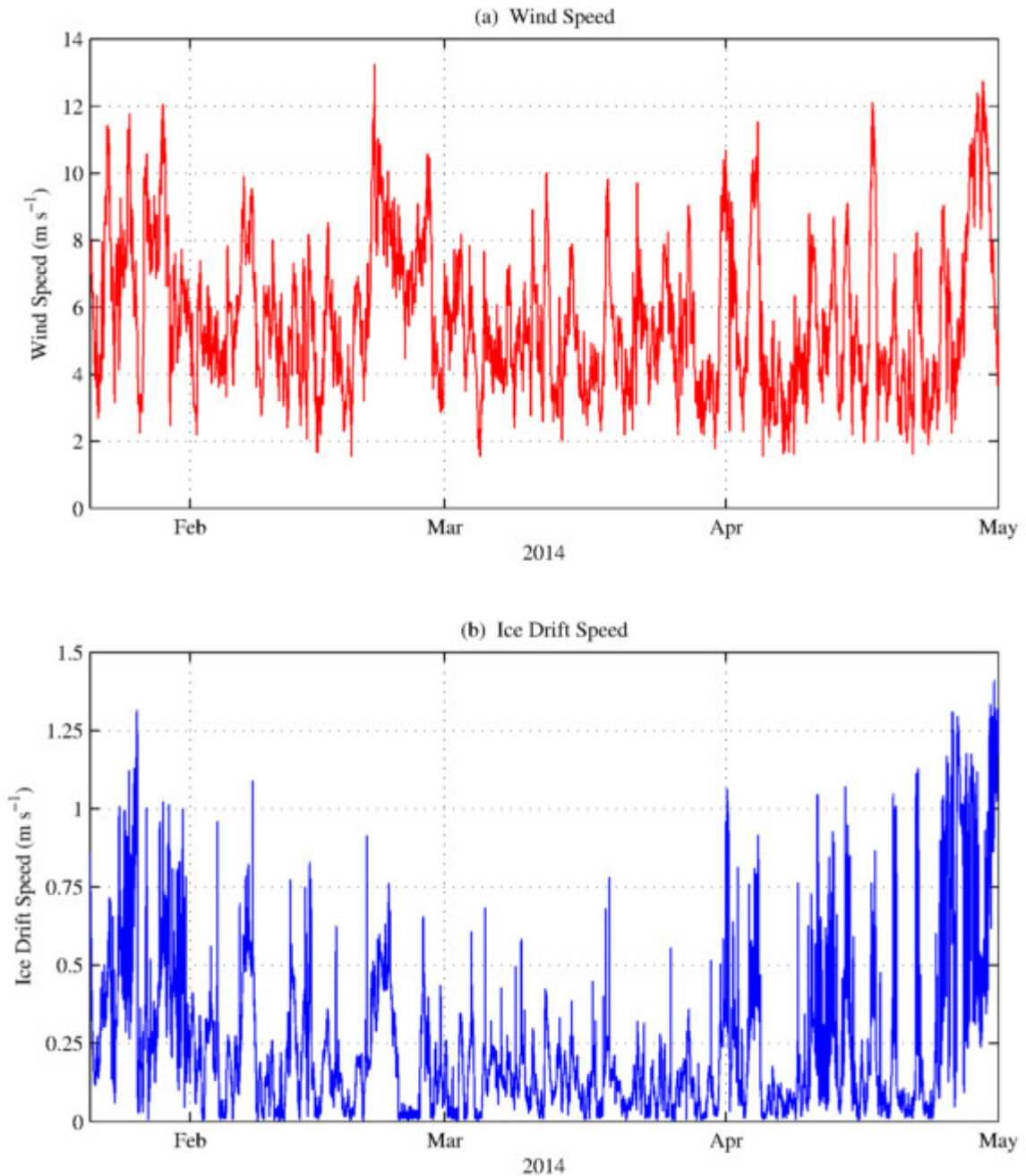


**Figure 4.5 – Ice speed and wind speed time-series, Winter 2013-2014.** Time-series for the 2013-2014 winter of (a) wind speed, and (b) corresponding ice speeds.

Second, there are seemingly unrealistic spikes in the estimates of ice speed throughout the time-series. Ice speeds spike to values of over  $1 \text{ m s}^{-1}$ , and these spikes do not correspond to periods of strong wind speeds. For example, ice speed estimates in mid April are characterized by

frequency spikes of high ice-speed, while wind speeds are generally moderate. These spikes are most likely measurements that occurred during periods of open water and are not believed to be representative of true ice speeds. Given that the IMS dataset used to determine the presence or absence of ice in the region is relatively coarse (4-km resolution), it is not possible to accurately determine exactly which ADCP measurements were taken under ice, and which were taken under patches of open water or under cracks or leads in the ice field. These spikes in ice speed likely correspond to periods during which the region around the Western Mooring is still mostly ice-covered, but the lake surface immediately above the Western Mooring is not. As such, data correspond to the upper range of ice-speed estimates are not believed to be reliable.

In order to determine the range of values for which a relationship exists, 20-minute ice speed data were binned onto the 1-hour wind speed grid, and wind speed and ice speed values were plotted against one-another (Figure 4.6). To create this figure, the hourly datapoints were averaging in range bins separately by wind speed and ice speed, and these binned data are plotted together to gain an understanding of the nature of the relationship between ice speed and wind speed. When these data are binned by wind speed, a clear linear relationship exists for the full range of wind speed values (Figure 4.6a). However, when data are binned by ice speed, it becomes clear that the linear relationship does not hold for the upper and lower range of values. The linear relationship breaks down when ice speed estimates are above approximately  $0.6 \text{ m s}^{-1}$  (Figure 4.6a). As discussed previously in this section, the upper range likely does not represent true estimates of ice speed, and ice speed estimates above  $0.6 \text{ m s}^{-1}$  will be discarded in my ice drift analyses. Also discussed previously, the lowest values of ice speed correspond to periods during which internal stresses in the ice field become important, leading to a fundamentally different dynamical balance between wind stress and ice drift. This shift is, indeed, apparent in the lower range of ice speeds, with the linear relationship between wind speed and ice speed breaking down for values of ice speed below approximately  $0.05 \text{ m s}^{-1}$  (Figure 4.6b).

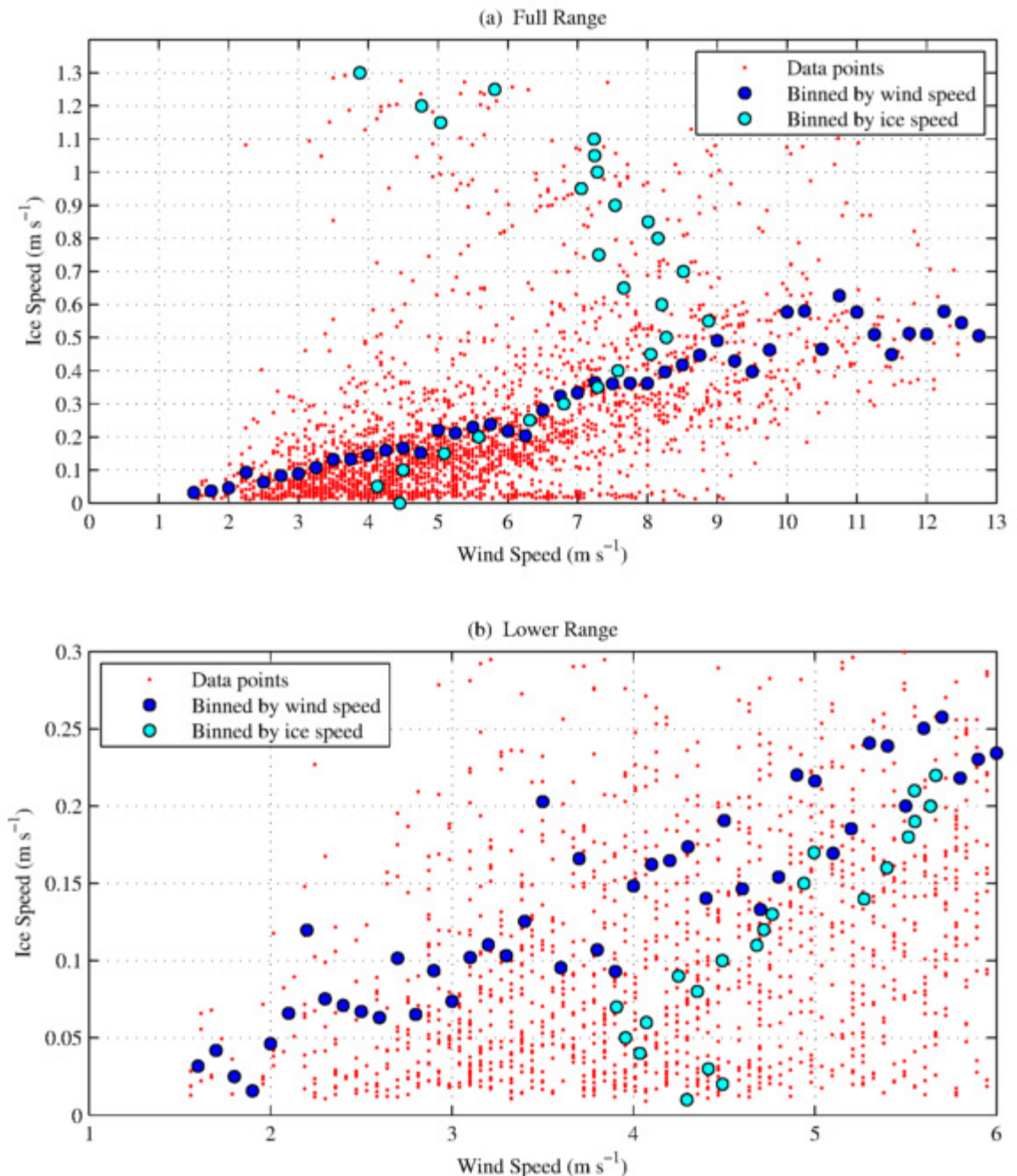


**Figure 4.6 – Determination of linear range of ice speed vs. wind speed.** Ice speed data was plotted against wind speed data in order to determine the range of ice and wind speeds for which a linear relationship exists. The full range of values (a) was used to determine the upper range of ice speed values that should be discarded, with a bin size of  $0.25 \text{ m s}^{-1}$  for wind speed, and a bin size of  $0.025 \text{ m s}^{-1}$  used for ice speed. An inlay of just the lower range (b) was used to determine the lower range of ice speed values that should be discarded, with a bin size of  $0.1 \text{ m s}^{-1}$  used for wind speed and a bin size of  $0.01 \text{ m s}^{-1}$  used for ice speed.

Using these ice speeds as cutoffs, I can categorize data points into three regimes for sake of analyses. The low ice speed regime (ice speeds below  $0.05 \text{ m s}^{-1}$ ), for which internal stress is likely important, the middle ice speed regime (ice speeds at or above  $0.05 \text{ m s}^{-1}$  and below  $0.6 \text{ m s}^{-1}$ ), for which a clear linear relationship between ice speed and wind speed exists, and the high ice speed regime (ice speeds at or above  $0.6 \text{ m s}^{-1}$ ), for which ice velocity measurements are likely associated with open water and are deemed unreliable. During the Western Mooring's 2013-2014 ice-covered season (January 21 through April 30), approximately 20% of data points fall into the low ice speed regime, 71% in the middle ice speed regime, and 9% of points fall in the high regime.

A least-squares linear regression between ice speed and wind speed is presented in Figure 4.7. For this analysis, I use only data points with ice speeds in the  $0.05$  to  $0.6 \text{ m s}^{-1}$  range, because this is the range for which data are believed to be reliably measuring ice drift and for which a linear relationship exists. The slope of the best fit line is  $0.043 \pm 0.002$  and the intercept is  $-0.02 \pm 0.00 \text{ m s}^{-1}$ . In other words, the ice speed is approximately 4% that of the wind. While the  $r^2$ -value, at 0.42, is not particularly high, binning the data visually demonstrates that despite the significant variability in the ice speed signal, the linear model does capture the mean value of the signal quite well. It is worth emphasizing that extrapolation outside the range of values presented here is likely not appropriate, particularly in the lower range, where internal stress in the ice field becomes significant.

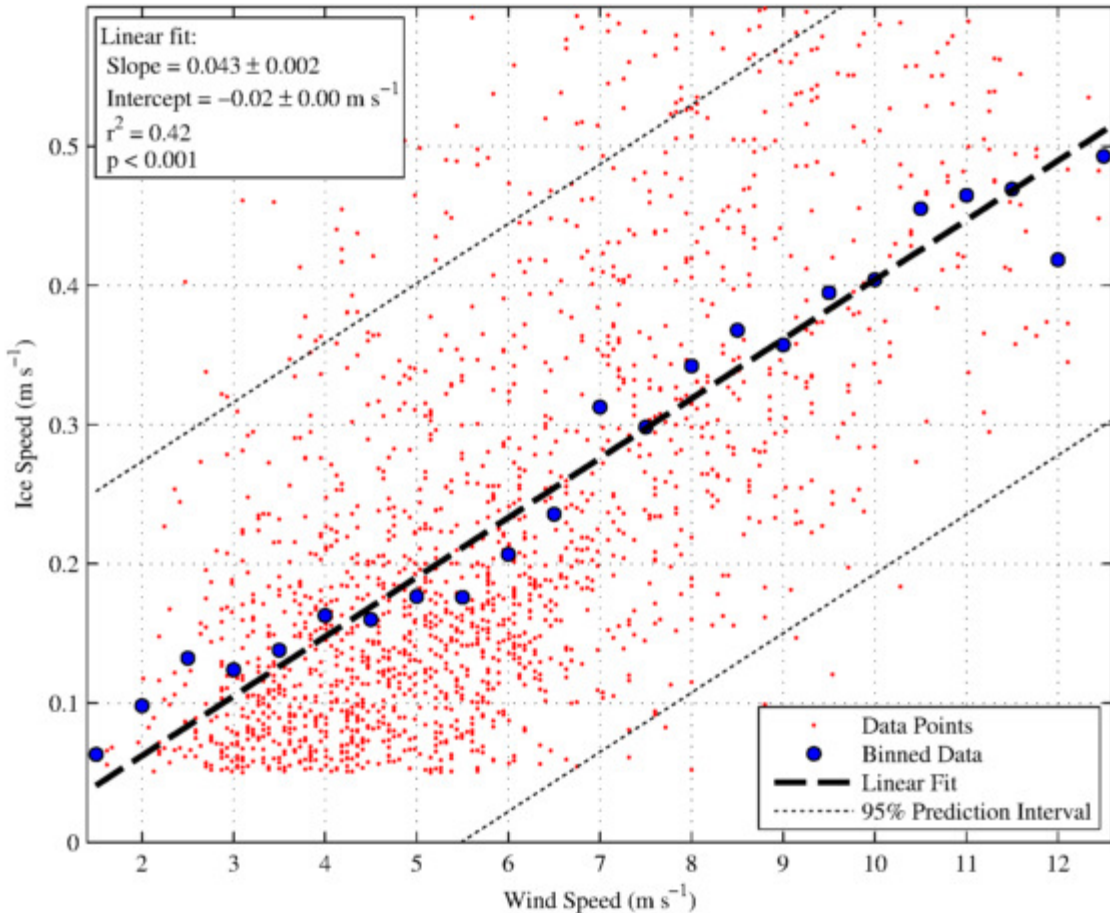


**Figure 4.7 – Ice speed vs. wind speed relationship.** The linear relationship between ice drift speed and wind speed is presented. Data points (dots) were formed by binning the 20-minute ADCP ice data onto the 1-hour NDBC wind time grid. A least-squares linear regression was performed on these data points and is plotted (bold dashed line) along with the 95% prediction interval (dotted lines). Data were also binned into  $0.5 \text{ m s}^{-1}$  bins by wind speed (circles) to demonstrate that the relationship is linear in nature.

In order to assess whether this relationship is representative of free-drifting ice or whether there is some level of restriction, the ratio of ice speed to wind speed can be compared to the ratio one would expect of free-drifting ice. Leppäranta (2008) uses conservation of momentum to derive the free-drift solution for ice movement. Under free-drift conditions, in which no internal stress is present, ice speed is given by:

$$u_{ice} = Na e^{-i\theta_0} u_{wind} + u_{water} \quad \text{Equation 4.1}$$

Where  $u_{ice}$  is the ice speed,  $\theta_0$  is the angle of the ice direction relative to wind direction (also known as the Ekman angle),  $u_{wind}$  is the wind speed,  $u_{water}$  is the speed of the water, and  $Na$  is the Nansen number, defined as:

$$Na = \sqrt{\frac{\rho_a C_a}{\rho_w C_w}} \quad \text{Equation 4.2}$$

Where  $\rho_a$  is the density of air,  $\rho_w$  is the density of water,  $C_a$  is the drag coefficient between the wind and the ice, and  $C_w$  is the drag coefficient between the water and the ice.

Because I am currently examining only the relationship between ice speed and wind speed, the direction of movement is not important to this analysis (it will be examined subsequently in this section), so the complex exponential can be eliminated for these purposes. Additionally, unlike in the oceans, where geostrophic currents can be significant, it is safe to assume that water current velocities in Lake Superior are much smaller than wind and ice velocities. With this assumption, the ratio of ice speed to wind speed is approximated directly by the Nansen number:

$$\frac{u_{ice}}{u_{wind}} \approx Na \quad \text{Equation 4.3}$$

Examining the Nansen number (Equation 4.2), neither the air density nor water density vary significantly at the water surface under a typical range of winter conditions, and it has been found that the ratio of  $C_a$  to  $C_w$  is not very sensitive to ice type (Leppäranta 2008). Therefore, the Nansen number does not vary significantly over a wide range of winter sea-ice conditions. Leppäranta (2008) presents representative values of the Nansen number of approximately 0.025 for ice in the Arctic Ocean, and 0.035 for Antarctic ice.

Therefore, according to the relationship derived in Equation 4.3, under free-drifting conditions, ice drift speeds are predicted to be approximately 3% of the overlying wind speed. This is quite close to the ratio of 4% determined empirically from the 2013-2014 winter data.

Ice direction was compared to wind direction during times when the ice speed was greater than or equal to 0.05 m s<sup>-1</sup> and less than 0.6 m s<sup>-1</sup>, and this relationship is shown in Figure 4.8. A least-squares linear regression produced a slope of  $0.98 \pm 0.01$  and a directional offset of  $-20.3 \pm 3.0^\circ$ , with a negative offset being defined as clockwise. With a slope of approximately 1 and a high

$r^2$ -value (0.93), this linear regression shows that ice was observed to consistently travel approximately  $20^\circ$  clockwise of wind direction. This is consistent with Ekman dynamics, and with previous measurements of this offset in oceanographic settings under free-drifting conditions. Leppäranta (2008) lists a typical offset between ice direction and of  $25^\circ$ , which is close to our measured value of  $20^\circ$ .

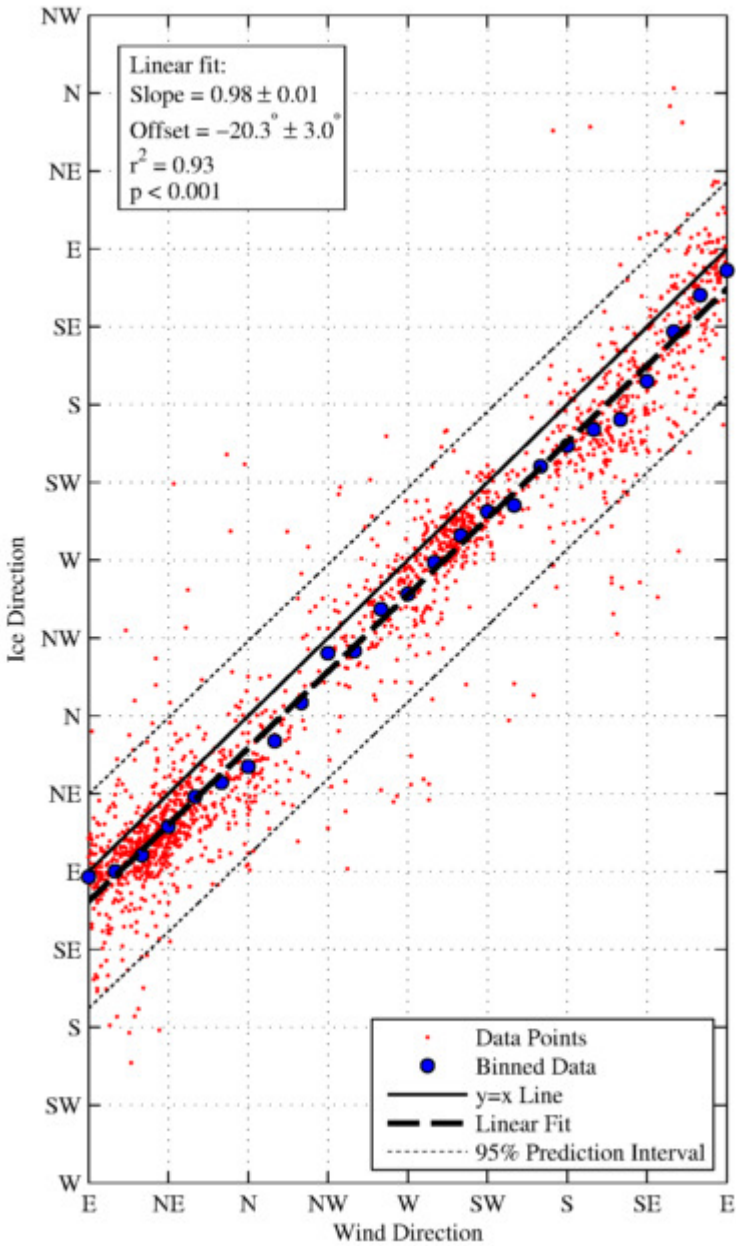


**Figure 4.8 – Ice direction vs. wind direction relationship.** The relationship between the direction of ice drift and the direction of wind speed is shown. Directions on the axes represent the direction in which the ice or wind is headed. Data points (dots) were formed by binning the 20-minute ADCP ice data onto the 1-hour NDBC wind time grid. A least-squares linear regression was performed on these data points and is plotted (bold dashed line) along with the 95% prediction interval (dotted lines). The solid  $y=x$  line is the line points would follow if ice traveled in the same direction as wind. Data were also binned into  $15^\circ$  bins by wind speed (circles) to demonstrate that the relationship is linear in nature.

Our measured ice drift velocities from the 2013-2014 winter are close to values measured under free-drifting ocean conditions, in terms of both speed and direction, demonstrating that ice in the

offshore portion of Lake Superior is characterized, by and large, as free-drifting ice. While there are times during the winter when internal stresses become important, ice velocities during the majority of the ice-covered season fall within this linear regime of values that corresponds to free-drifting ice. If we take the percentage of time that ice speeds are below  $0.05 \text{ m s}^{-1}$  as an order-of-magnitude estimate for the percentage of time that ice movement is significantly restricted, then it can be concluded that ice movement was restricted for only about 20% of the ice-covered season. This is likely to be an overestimate, because some percentage of those low ice speeds can likely be simply attributed to conditions of low wind speed, but where ice is still drifting freely. Given that the 2013-2014 winter, during which these measurements were taken, was characterized by exceptionally high ice cover, it follows that a typical year would be characterized by a less-dense ice field that is even more conducive to free-drifting ice. Therefore, it is safe to conclude that ice in the open-water portions of Lake Superior is predominately free-drifting.

While ice is generally free-drifting, there are periods during which ice speeds at the Western Mooring drop to near-zero for several hours or even days at a time, even in the presence of moderate to strong winds. In these cases, internal stresses in the ice field must be significant in the dynamical balance and therefore represent times when ice movement is restricted, as opposed to free-drifting. Figure 4.9 shows ice speed and wind speed data from the Western Mooring during February 2014, a month which contains several such periods.

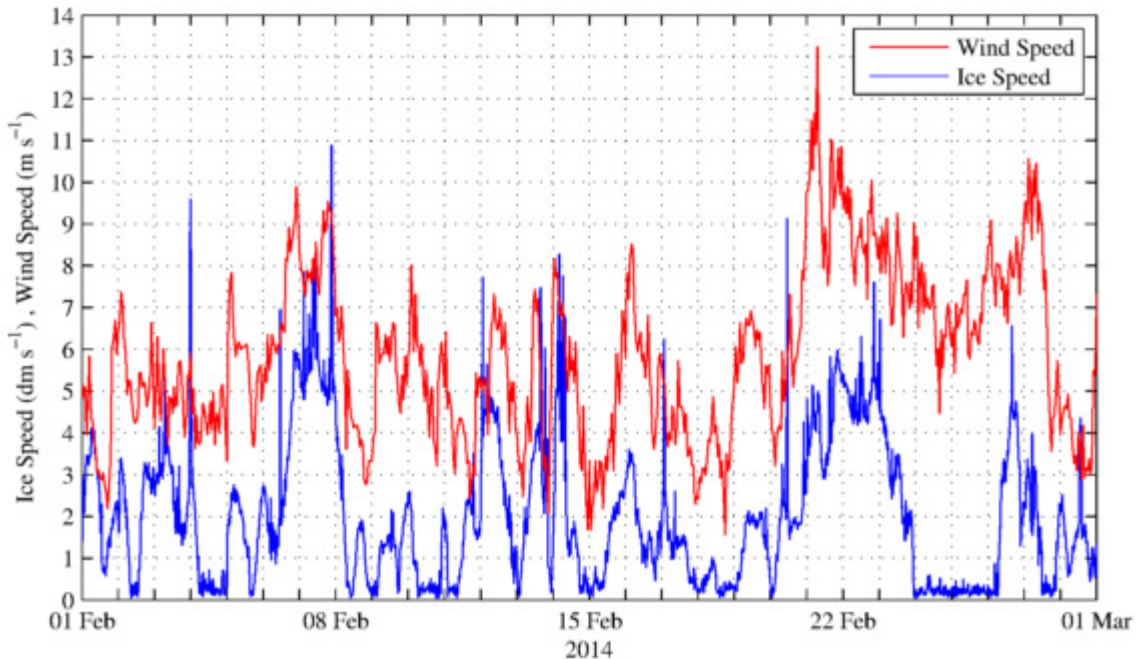


**Figure 4.9 – Example of ice locking up, Western Mooring, Februyay 2014.** Ice speed and wind speed data are presented for the month of February 2014. This month-long period is an example of a window of time with several periods during which the ice locks up, and is not free-drifting.

During these periods of restricted ice movement, the ice speed generally drops quite suddenly to near-zero, remains relatively stationary for hours to days, and then suddenly resumes moving. These periods generally occur when wind speeds are at relative lows. For example, Figure 4.9 shows an extended period of restricted ice movement from approximately February 24-26. While wind speeds during this time period are moderate to high in an absolute sense, they are lower than wind speeds observed during the days preceding and following the period of restricted ice movement. This suggests that internal stresses in the ice field cause the ice field to “lock up” and that there is a threshold wind stress that must be achieved to overcome these internal stresses and force the ice to move.

The wind speeds associated with restricted ice movement on February 24-26 are comparable or higher to wind speeds during other portions of the winter when free-drifting ice was observed. This demonstrates that this threshold wind stress necessary to overcome the internal stresses is not constant. Instead, it likely depends on such factors as ice thickness and ice concentration, which evolve over the course of the season, and which cannot be resolved in our datasets. On average, ice cover on Lake Superior reaches maximum coverage in early March (not shown),

consistent with conditions more likely to result in a restricted ice field, compared to other times in the season.

Figure 4.4 shows that wind moves predominately to the east during the high-ice months of February and March. While ice, too, moves predominately to the east during February, it shows no predominate direction through March. This discrepancy can likely be attributed, at least in large part, to the restricted ice flow dynamics discussed above. The predominate eastern flow of wind at Western Mooring through February and March suggests that over the course of the winter season, ice formed to the west of the Western Mooring may be piling up to the east, along the Keweenaw Peninsula. If the wind continues to blow in a direction where ice is highly concentrated, it follows that it would lead to conditions under which ice movement is restricted, as was observed at the Western Mooring.

To more-closely examine whether winds from a particular direction, the ratio of ice speed to wind speed was plotted as a function of wind direction (Figure 4.10). For this analysis, points with ice speed estimates at or above  $0.6 \text{ m s}^{-1}$  were discarded as unreliable, for reasons discussed earlier, but all other points were retained. This plot shows that the ice speed to wind speed ratio is generally higher when the winds are blowing in the northeast or southwest direction, and the ratio is generally lower when winds are blowing in the northwest or southeast direction. When all points from the NE and SW quadrants are averaged, and all points from the NW and SE quadrants are averaged, the 95% confidence limits of the mean ice speed to wind speed ratio is  $3.7 \pm 0.2\%$  for NE/SW winds, and  $2.9 \pm 0.2\%$  for NW/SE winds.

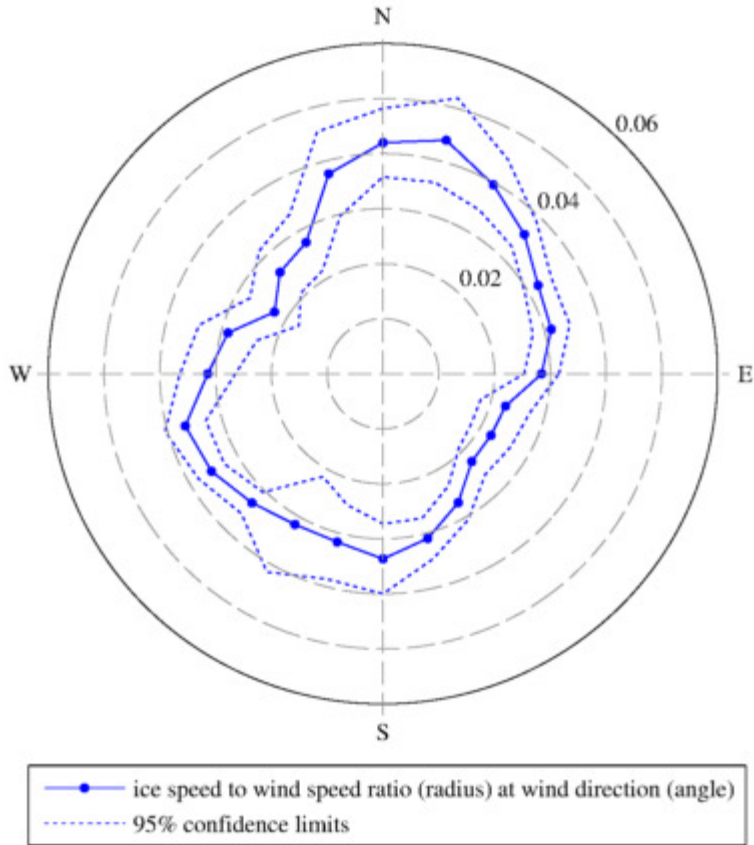


**Figure 4.10 – The ratio of ice speed to wind speed as a function of wind direction.** The ratio of ice speed to wind speed is plotted as a function of wind direction, in polar coordinates. Points were binned into  $15^{\circ}$  bins by wind direction, and are plotted here, connected by lines. In this plot, the angle of the point from the origin represents the direction the wind is headed, and the radial distance from the center represents the ratio of ice speed to wind speed for that wind direction. The concentric circles on the grid correspond to increases of 0.01 in the ratio of ice speed to wind speed.

This statistically significant difference demonstrates that ice is generally less restricted under NE/SW winds than under NW/SE winds. These mean ratios should not be interpreted as distinct persistent dynamical balances under different wind conditions. Rather, the lower ice speed to wind speed ratio under NW/SE winds is more likely attributed to ice being restricted a greater percentage of the time under NW/SE winds than under NE/SW winds, and locking up even when winds are relatively high. This is demonstrated in Figure 4.11, which data points with ice speeds below and above  $0.05 \text{ m s}^{-1}$  are plotted as a function of wind stress and wind direction in order to examine to wind conditions under which low ice speeds are observed. Wind stress was estimated following Smith (1988).

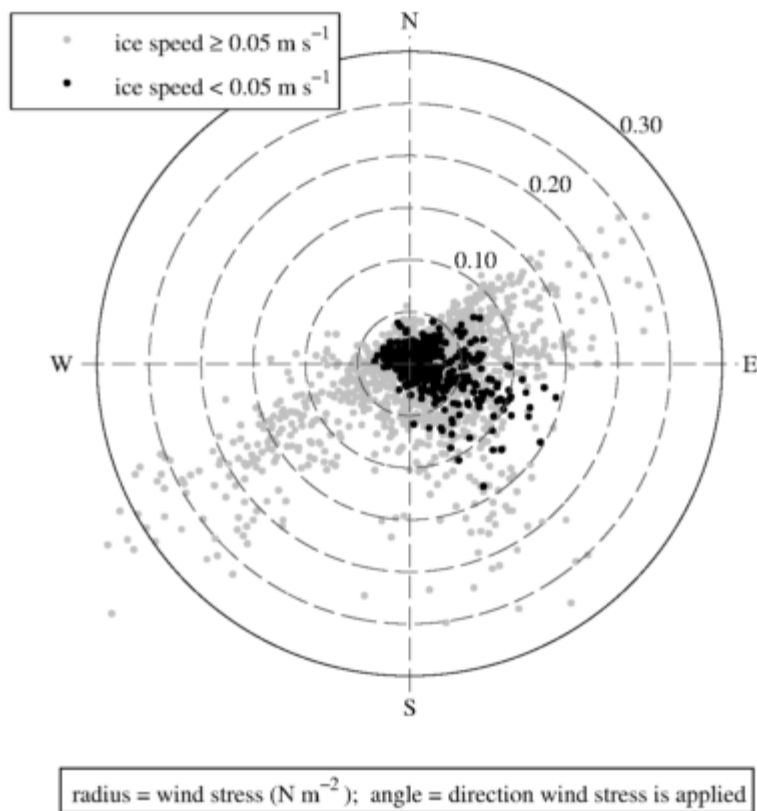


**Figure 4.11 – Ice lockup dependency on estimated wind stress and wind direction.** The wind stress (radius) is plotted as a function of wind direction (angle), in polar coordinates. Light-colored points correspond to times when the ice speed is greater than or equal to  $0.05 \text{ m s}^{-1}$ , while dark-colored points correspond to times when ice speed is less than  $0.05 \text{ m s}^{-1}$ . The concentric circles on the grid correspond to increases of  $0.10 \text{ N m}^{-2}$  in wind stress.

As seen in Figure 4.11, ice speeds are frequently observed to be very low (less than  $0.05 \text{ m s}^{-1}$ ) when winds are blowing to the SE, even when wind stress is relatively high. In contrast, similar low ice speeds are observed when the NE/SW direction only when wind stress is low. Times of high wind stress in the NW direction were not observed during the 2013-2014 winter season. At the Western Mooring location, NE/SW winds can generally be considered along-shore winds, while NW/SE winds can generally be considered cross-shore winds (Figure 4.1). A more restricted ice field under cross-shore winds is consistent with the idea that there are times when the ice field is blown against the shore to the point where it becomes sufficiently concentrated as to restrict further ice movement in the open lake. In this high-ice year, this is true even for at the Western Mooring, located approximately 50 km offshore.

While working with Jay Austin on these analyses, he used a simple scaling involving the yield strength of ice in order to estimate the minimum ice thickness that would be necessary for ice to lock-up under the wind stress conditions observed. I will reproduce that force balance here, as it results in a novel, first-order estimate of ice thickness in the western basin of the lake. The scaling is derived from the following scaling relationship, used to determine the critical point for mechanical breakage of an ice field, from Kirillin et al. (2012):

$$\tau_A L > c_s P^* h \quad \text{Equation 4.4}$$

Where  $\tau_A$  [N m<sup>-2</sup>] is the wind stress,  $L$  [m] is the fetch over which the wind stress is applied,  $c_s$  [ $\sim 1$ ] is a calibration factor,  $P^*$  [ $\sim 3 \times 10^4$  Pa] is the yield strength of ice per unit thickness, and  $h$  [m] is the thickness of ice. The inequality predicts that the ice field will break when the quantity on the left-hand side of Equation 4.4 exceeds the quantity on the right-hand side. This can be rearranged to express the ice thickness necessary for the ice field to lock-up under a given set of conditions:

$$h \geq \frac{\tau_A L}{c_s P^*} \quad \text{Equation 4.5}$$

This states that ice thickness must be greater than or equal to the quantity on the right-hand side of Equation 4.5 in order for the ice field to lock-up. The quantities used in this inequality can be estimated for the Western Mooring location, where ice had been observed to lock-up. The maximum wind stress at which ice was observed to lock-up was approximately 0.15 N m<sup>-2</sup> (Figure 4.11), and the Western Mooring is on the order of 50 km from the nearest shore to the southeast (Figure 4.1). Using these values along with the values for the calibration factor and yield strength given by Kirillin et al. (2012), the minimum ice thickness necessary for ice to lockup is found to be:

$$h \approx \frac{(0.15 \text{ N m}^{-2})(5 \times 10^4 \text{ m})}{(1)(3 \times 10^4 \text{ Pa})} \approx 0.25 \text{ m} \quad \text{Equation 4.6}$$

This shows that ice must be on the order of 0.25 m, at a minimum, in the western arm of Lake Superior in order for the observed lock-up events to occur at the Western Mooring location.

## 4.2 Ice Keels

While the moorings were not purposely equipped with instrumentation designed to monitor ice in 2014, the pressure sensors on the moorings, intended only to verify the depth of deployment, fortuitously captured observations of passing ice formations. As ice keels deeper than the subsurface mooring floats passed over the moorings, these pressure sensors documented the depth to which the top of the mooring was submerged. In particular, due to the inadvertent shallow deployment of the Western Mooring over the 2014 winter, ice keels deeper than about 5 m were detectable, as this was the depth of the top mooring float atop which the upper pressure sensor was fixed.

Figure 4.12 shows the depth of pressure sensors at the Western Mooring during the 2013-2014 winter deployment. Sensor depth was determined using the hydrostatic equation, after subtracting regional air pressure from the raw pressure sensor readings (see Section 2.1.1.1). For this deployment, the Western Mooring was equipped with two TD-2050 sensors, nominally at 5 m and 97m, which collected data at one-minute intervals. The low frequency shift in sensor depths over the course of the season corresponds to seasonal changes in lake level, based on observations from the Grand Marais, Minnesota station (National Oceanic and Atmospheric Administration Tides and Currents 2015). The signal from the upper sensor contains significant ‘symmetric noise’ during times outside of the ice-covered period (January 21 through April 30), which is qualitatively indicative of surface gravity waves (Figure 4.12a). Surface waves are observed into the beginning of the ice-covered period, during which ice is expected to be thinner and patchier. As the season progresses and more cohesive ice forms, this wave-induced noise diminishes, is not present throughout the remainder of the ice-covered period, and is observed again shortly after the offset of ice.

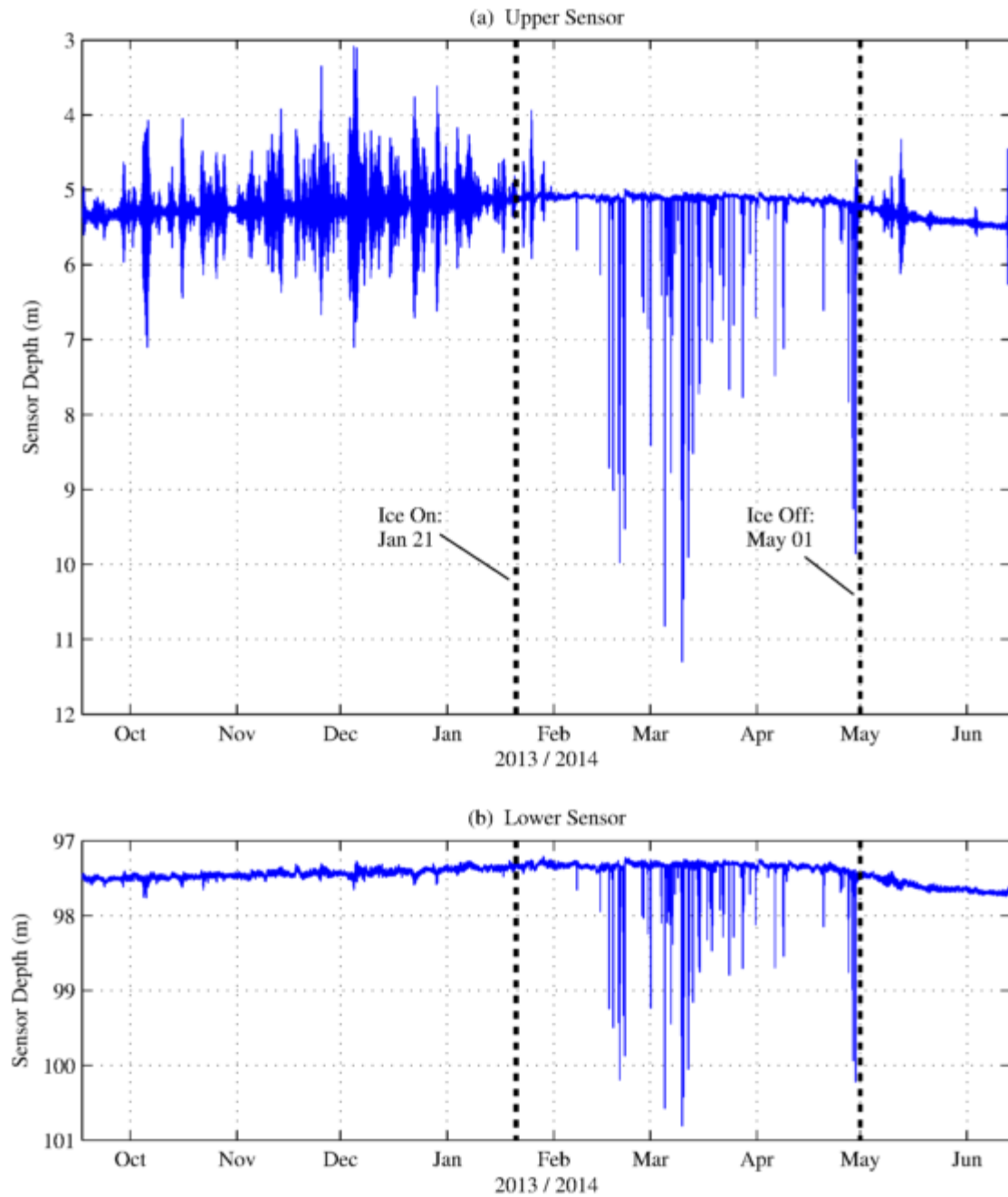


**Figure 4.12 – Western Mooring pressure sensor record, Winter 2013-2014.** The depth of both the (a) upper and (b) lower pressure sensors at the Western Mooring during the winter 2013-2014 deployment is shown.

While the mooring is under ice, frequent quick spikes in pressure readings are observed, going only in the positive (deeper) direction (Figure 4.12a,b). These jumps in sensor depth can be attributed to passing ice keels. As deep ice keels pass through the mooring location, the top float

of the mooring is pulled in the direction of ice movement, generating an angular displacement throughout the mooring cable (Figure 4.13). This angular displacement increases as the ice passes over the mooring, until the top float passes under the ice keel and the mooring returns to its vertical position. The vertical displacement of the sensors that is associated with angular displacement of the cable will be greatest near the surface, and decrease proportionally with depth. Because the lower pressure sensor at the Western Mooring is approximately halfway down the mooring cable, it would be expected that it experienced vertical displacements of about half the magnitude of those experienced by the upper pressure sensor. Indeed, positive spikes in sensor depth are observed in the lower sensor at the same times they are observed in the upper sensor, and displacements are approximately half those of the upper sensor (Figure 4.12). This corroborates the idea that ice keels are, in fact, producing a roughly uniform angular displacement throughout the mooring cable, and that ice keel depth can be reliably obtained from the pressure sensor record.

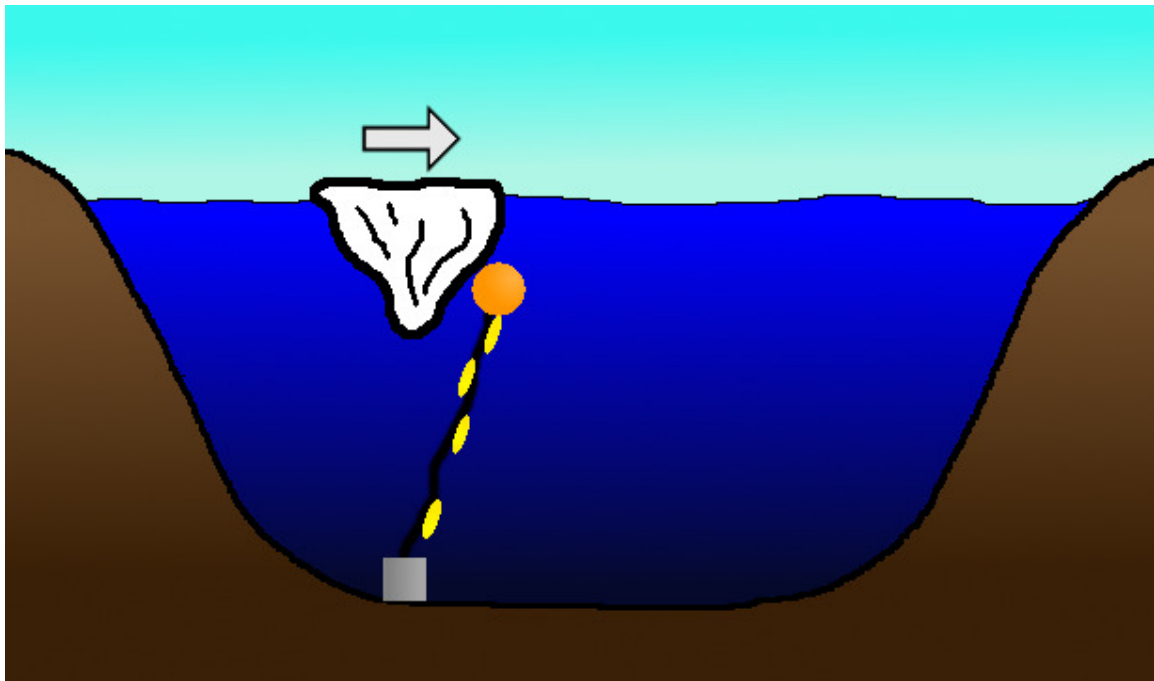


**Figure 4.13 – Ice keels conceptual diagram.** This diagram conceptually demonstrates the displacement of mooring instruments by an ice keel. As the ice keel passes through the mooring, it produces an angular displacement throughout the mooring cable, and a vertical displacement of pressure sensors that is linearly proportional to its distance from the mooring anchor. The diagram is not drawn to scale.

The top floats at the Central and Eastern Moorings were located at about 12 m depth during the 2013-2014 winter, with pressure sensors just below, at 13 m. As such, only very deep ice keels could be detected. A vertical displacement of approximately 1.4 m was observed at the upper sensor at the Central Mooring on March 17 (Figure 4.14), and a vertical displacement of approximately 0.2 m was observed at the Eastern Mooring on March 6 (Figure 4.15), both of which were corroborated by corresponding smaller displacements in the deeper sensors. These displacements correspond to an ice keel deeper than 13 m at the Central Mooring, and an ice keel deeper than 12 m at the Eastern Mooring. The fact that deep ice keels were also observed at the Central and Eastern Moorings demonstrates that this is a lakewide phenomenon, and does not only occur in the western arm of the lake.

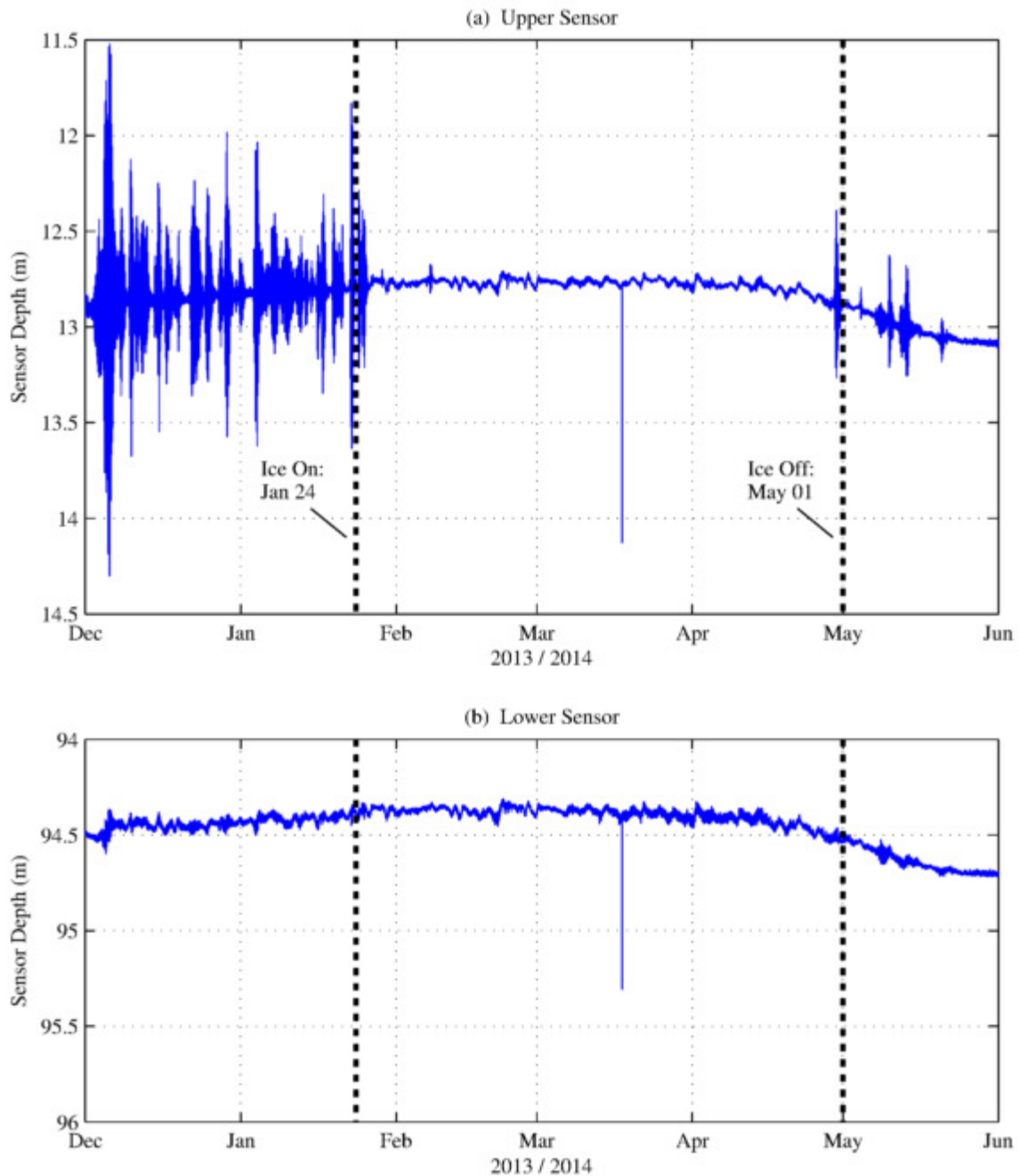


**Figure 4.14 – Central Mooring pressure sensor record, Winter 2013-2014.** The depth of both the (a) upper and (b) lower pressure sensors at the Central Mooring during the winter 2013-2014 deployment is shown.

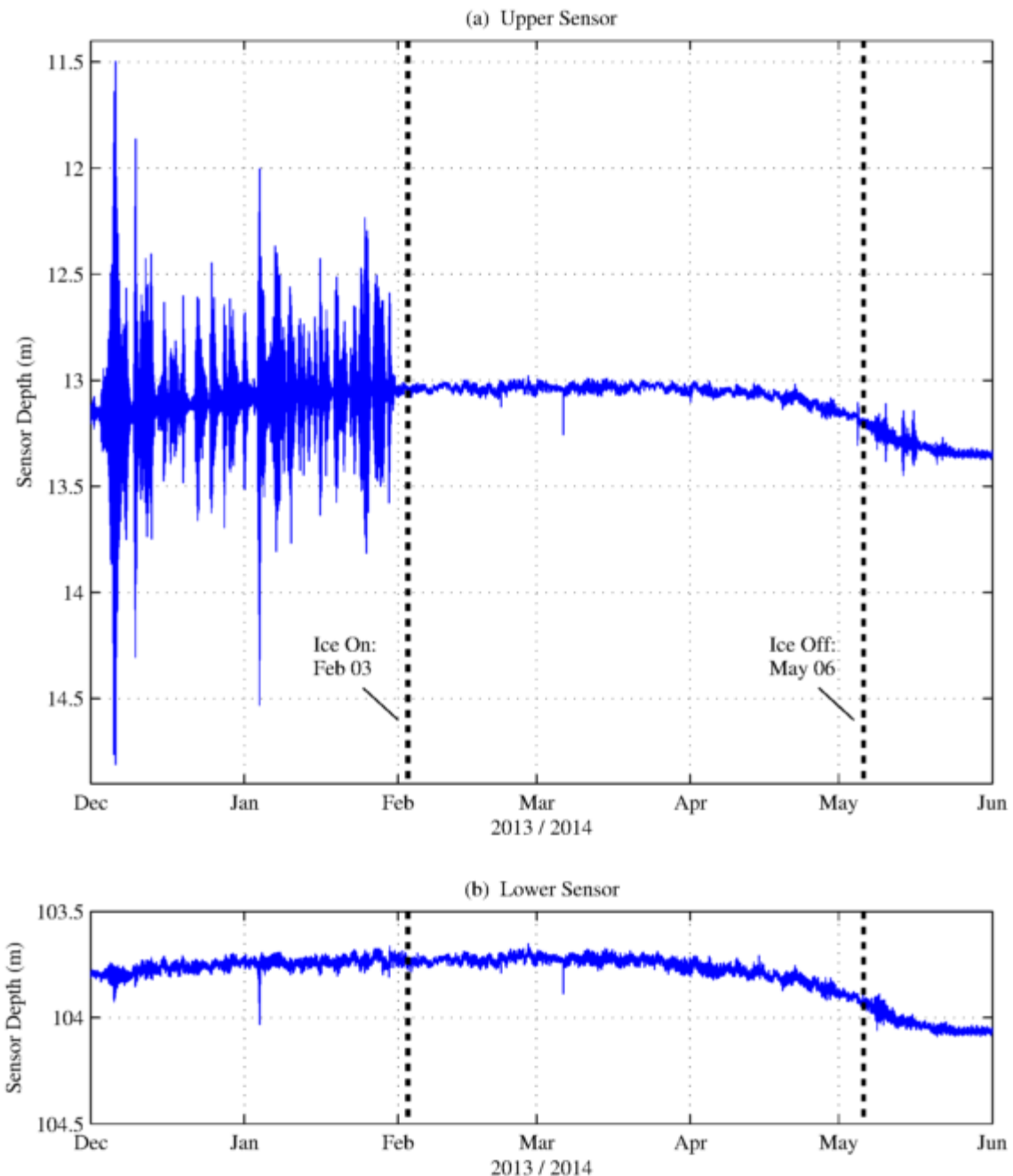


**Figure 4.15 – Eastern Mooring pressure sensor record, Winter 2013-2014.** The depth of both the (a) upper and (b) lower pressure sensors at the Central Mooring during the winter 2013-2014 deployment is shown.

The characteristics of these ice keels will be further characterized using the Western Mooring pressure record (Figure 4.12), because the shallow float depth facilitated the detection of a wider range of ice keel depths. Ice keels of about 5 to 8 m depth occurred frequently at the Western

Mooring throughout the winter 2013-2014 winter season, and that an ice keel of over 11 m was observed in early March. The profile of this deepest ice keel is shown in Figure 4.16. The profile of the ice keel is well-resolved by the 1-minute pressure sensor data, and appears to consist of multiple ridges, presumably formed by convergence of the ice field. Such convergence could occur through converging ice flows in the offshore regions of the lake, or through the convergence of the ice field along the lake shore due to cross-shore winds, as was discussed in Section 4.1.

The width of these ice keels can be estimated using ADCP ice drift velocity data from immediately before and immediately after the ice keel passes, in conjunction with the duration of the displacement. In the case of the deep ice keel observed at the Western Mooring on March 10 (Figure 4.16), ice velocities were approximately  $5 \text{ cm s}^{-1}$  both before and after the mooring was displaced, and the duration of the displacement was approximately 1 hour. While the shape and orientation of the keel relative to its movement would be necessary to accurately characterize its dimensions, these numbers demonstrate an upper limit of approximately 180 m on the width of that deep ice keel.

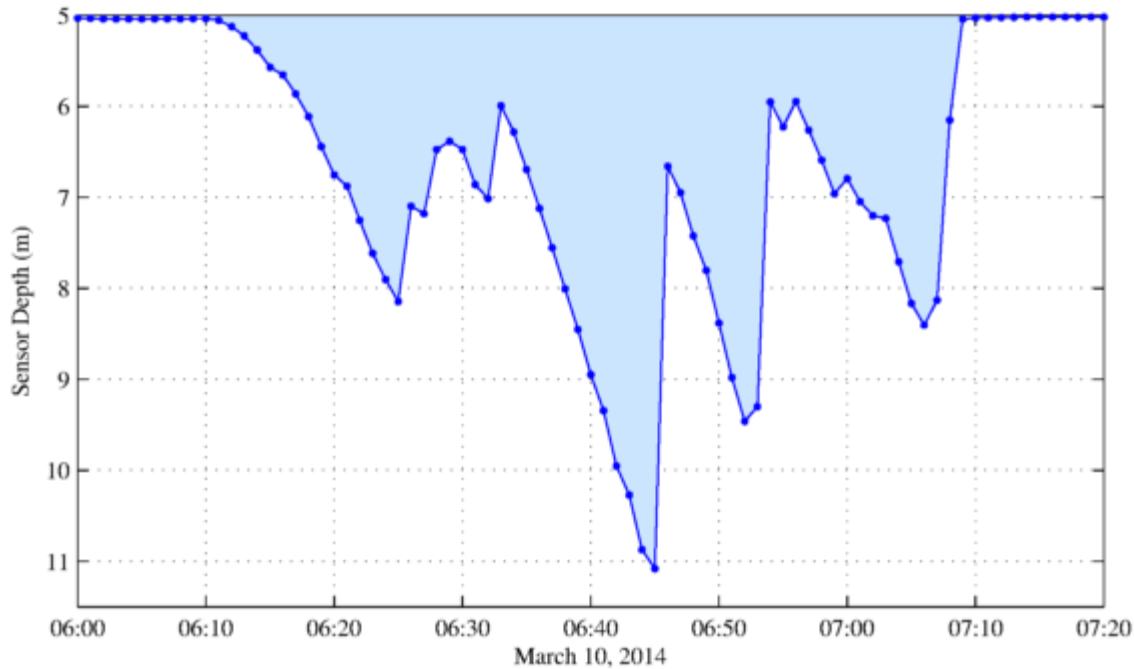


**Figure 4.16 – Profile of deepest Western Mooring ice keel.** The depth of the upper Western Mooring pressure sensor is shown for the period of 0600-0720 GMT on March 10, 2014, depicting the profile of the deepest ice keel observed at the Western Mooring during the 2013-2014 winter. The dots correspond to the discrete pressure sensor readings, taken at 1-minute intervals.

The percentage of time ice keels were present at the Western Mooring during the ice-covered period (January 21 through April 30) was calculated for the range of detectable ice keel depths (Figure 4.17). If we assume, for the sake of an order-of-magnitude estimate, that ice keels are roughly evenly distributed around the lake, then the percentage of time ice keels are present at a given location roughly corresponds to the percentage of the lake over which such ice keels are present. To put the abundance of these keels in perspective, ice keels of 6 m depth or greater were present at the Western Mooring for approximately 0.3% of the ice-covered season. Using the type of order-of-magnitude estimate described above, this would correspond to approximately 250 km<sup>2</sup> of the lake being occupied by ice keels of 6 m depth or greater.

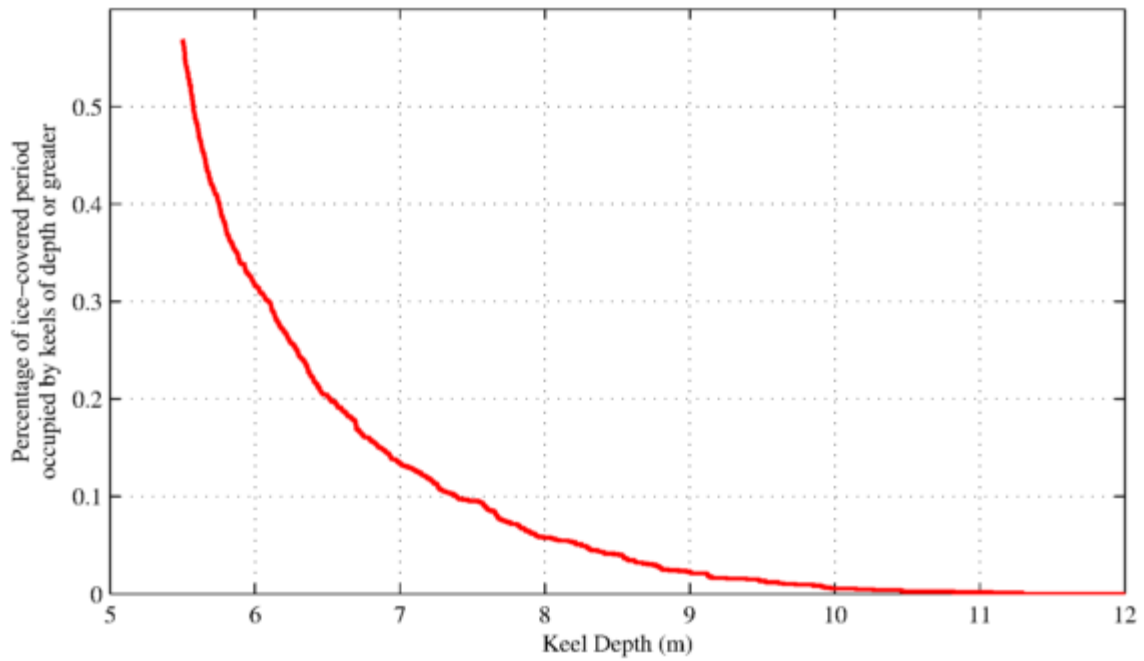


**Figure 4.17 – Prevalence of ice keels at the Western Mooring.** The percentage of the ice-covered period (January 21 through April 30) for which ice keels were present at the Western Mooring is shown for the detectable range of ice keel depths.

Under the same premise, we can integrate the area between the curve shown in Figure 4.17 and the y-axis, and multiply by area of the lake to obtain a rough estimate of the volume of ice associated with ice keels. The calculation yields the result that about 3 billion cubic meters of ice are tied up in ice keels of 5.5 m depth or greater. If spread over a water-body the size of Lake Superior, this would be enough ice to cover the entire lake to a depth of 3 to 4 cm. If we assume that the rest of the lake is covered with ice of thickness 0.25m, based on the rough estimate from Equation 4.6, this would suggest that roughly 15% of the ice volume of the lake is in keels. This is likely an underestimate because it does not take into account keels of less than the detectable 5.5 m thickness, which are likely to be more abundant than thicker keels. Therefore, ice keels are believed to account for a significant fraction of the total volume of ice on the lake.

### 4.3 Conclusion

With the ice-covered season representing a significant and relatively under-studied portion of the year on the Great Lakes, and with ice cover acknowledged to affect a variety of physical, climatic, and biogeochemical lake processes, it is fundamentally important that the dynamics of

lake ice are understood. The observations of ice characteristics presented in this paper work toward that understanding, and are the first of their kind from the Great Lakes. When examined in the context of wind velocity, for most of the season ice drift at WM was shown to move at approximately 4% of the wind speed and about 20° clockwise of wind direction, which is consistent with measurements of free-drifting ice in the oceans. These observations are especially significant because they demonstrate that even during the 2013-2014 winter, which was characterized by record-high ice cover, ice in the open-water portions of the lake was predominately free-drifting. However, under certain wind conditions, there were periods on the order of a couple days when the ice field did, in fact, become sufficiently concentrated to lock up at least 50 km out from the shore, demonstrating that internal stresses in the ice field at times dominate the dynamical balance. A simple scaling using the yield strength of ice along with estimated wind stress facilitates a novel first-order estimate of ice thickness, and suggests that the minimum ice thickness would need to be on the order of 0.25m for these lockup events to occur.

Data from pressure sensors at WM, CM, and EM demonstrate that surface waves are suppressed in the open water portions of Lake Superior in the presence of ice cover, and keels with depths upwards of 11 m were observed to displace the top floats of the moorings. Deep keels were observed at all three open water locations on the lake, and are believed to account for a significant portion of the total ice volume on the lake, likely more than 15%. ADCP data show that there are sporadic periods in which acoustic reflectivity is high throughout the water column, at least to the depth of the ADCP (~80m), and it is believed that this high reflectivity can be attributed to ice crystals saturating the water column. Such events have been observed in other Great Lakes and in the oceans, and while the significance of these ice crystals is not immediately clear, their apparent existence in a wide variety of systems, as well as the lack of attention paid to such events in published literature, suggests that additional focus on these events is warranted.

Given the limitations of remotely sensed data, from which the vast majority of our knowledge of ice on the Great Lakes is derived, the results discussed herein begin to fill the large gap in our understanding of the ice cover on the Great Lakes. In particular, the observations of ice movement demonstrate that ice dynamics on Lake Superior fall within a regime that is characterized by a balance between free-drifting conditions and conditions in which internal stresses in the ice field dominate. As such, in order to understand and accurately model this balance, a careful and thorough characterization of ice cover on the Great Lakes is critical. We believe the observations presented in this paper represent an important step toward that

understanding, and hope they are of immediate use to those studying and modeling these systems. Because the observations used to characterize ice drift and ice keels were obtained through unintended measurements, as discussed previously, the setup of instruments on the mooring was not optimized with these experiments in mind. Using these methods and results as a baseline, our understanding of ice characteristics would further benefit from additional, more focused observational campaigns that build upon these important results.

## 5.0 Sensitivity of Great Lakes Ice Cover to Climate

The sensitivity of lake systems to variability in climate is a topic of much scientific and public interest, due largely to the climate change signal being imposed on lake systems throughout the world. In lakes at higher latitudes, variations in ice cover are an important component of a lake's response to climate change. Ice cover on the Great Lakes, in particular, is characterized by a high degree of interannual variability (Figure 1.1), which has been well-documented through remote sensing (Assel 2003; Assel 2005; Wang 2012a; National Ice Center 2015). Despite the relatively large amount of historic ice cover and meteorological data available from the Great Lakes region, few recent studies have worked toward establishing direct links between variability in Great Lakes ice cover and variability in climatic parameters in the region.

Recent interannual studies on water temperature in large lakes have focused largely on longerterm trends, including in the Great Lakes (McCormick and Fahnenstiel 1999; Austin and Colman 2007), Lake Baikal (Hampton et al. 2008; Izmest'eva et al. 2016), Lake Tanganyika (Verberg et al. 2003), and in lakes throughout the western United States (Coats et al. 2006; Schneider et al. 2010). Similarly, longterm trends in ice cover have been examined, both on the Great Lakes (Wang 2012b; Van Cleave et al. 2014) and in lakes and rivers throughout the northern hemisphere (Magnuson et al. 2000; Benson et al. 2012). Studies in ice cover variability on the Great Lakes have largely been conducted in the context of notable extreme events (Clites et al. 2014; Wang 2010) and their regional climatic significance (Gronewold et al. 2015).

Several older studies have provided evidence of a link between cumulative freezing-degree-days and ice cover in the Great Lakes (Richards 1964; Rodgers 1976; Assel 1991); however, datasets used in these studies were comparably limited, and relationships relied on basin-specific empirically calibrated parameters. Another older study by Assel (1976) examined the relationship between ice thickness and air temperature in Lake Superior, but looked exclusively at nearshore regions of the lake. A more robust analysis was conducted in Lake Baikal, which demonstrated a relationship between air temperatures and ice breakup date, based on data from over 60 ice-covered seasons (Livingstone 1999). In addition, a nonlinear relationship between the timing of ice breakup and air temperature has been established in smaller northern Swedish lakes (Weyhenmeyer et al. 2004), which was expanded to include relationships with the ice on, ice off, and ice duration in lakes throughout the northern hemisphere (Weyhenmeyer et al. 2011). One finding of Weyhenmeyer et al. (2004) and Weyhenmeyer et al. (2011) is that the relationship

between air temperature and ice cover can vary nonlinearly between latitudinal regimes, and such spatial variability in the relationship between air temperature and ice cover is also discussed by Walsh et al. (1998). The evidence of a regional dependence in ice-climate relationships demonstrates the necessity of a focused study in the Great Lakes region.

Much of the work in recent decades on Great Lakes interactions with climate has focused on modeling. An empirical model was established by Piccolroaz et al. (2013) and Piccolroaz et al. (2015) that dynamically estimates Lake Superior water temperature using only air temperature; however, simplifying assumptions were made to account for ice formation. A complex one-dimensional model was developed by Croley and Assel (1994), using bulk-flux parameters and empirically calibrated parameters to model ice cover on the Great Lakes. More recently, an application of the ROMS three-dimensional hydrodynamic model (Section 2.6) has been used to model dynamically ice cover on Lake Superior (White et al. 2012; Matsumoto et al. 2015).

As discussed in Section 4.0 , the combination of the depth and latitudinal position of the Great Lakes places them in a regime in which they form partial ice cover each year, but do not freeze over completely. As such, the extent to which ice forms on the lakes in a given season is naturally dependent on the meteorological conditions experienced by the lakes during that season. In this section, I will use both observational data and three-dimensional numerical modeling to examine the sensitivity to ice cover on the Great Lakes to climate variability. Understanding how lakewide ice has responded to historic variability in climate is essential toward understanding how the Great Lakes will respond to climate change.

## 5.1 Initial analysis

An initial analysis was conducted by simply plotting the available historic values of seasonally-averaged ice cover (Figure 1.1b) against corresponding values of seasonally-averaged air temperature (Figure 1.1a). An averaging period of December through May was used for both air temperature and ice cover in this initial analysis. The resulting plot is shown in Figure 5.1.

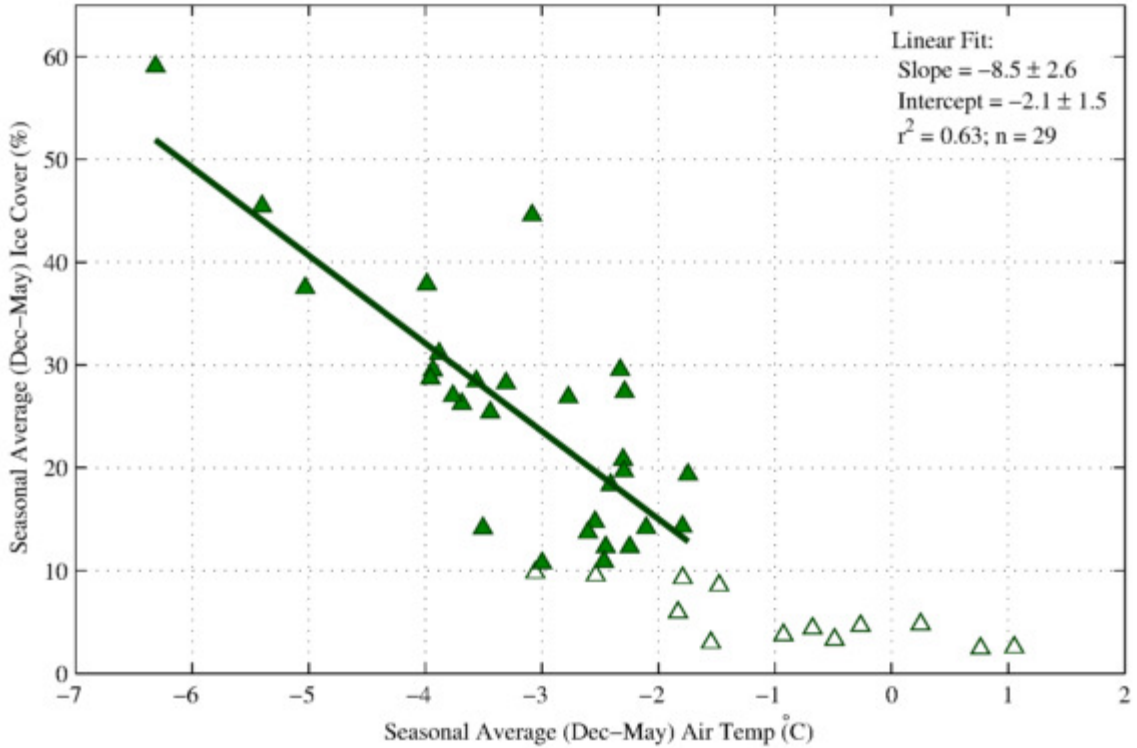


**Figure 5.1 – Sensitivity of lakewide average ice cover to air temperature, Lake Superior.** Seasonally-averaged ice cover is plotted against seasonally-averaged air temperature for Lake Superior. A linear regression is presented for points that have seasonally-averaged ice cover above 10% (filled points) with 95% confidence intervals, and points with ice cover below 10% (open points) were not included in the regression. Both ice cover and air temperature were averaged over the interval of December 1 through May 31 to calculate seasonally-averaged metrics. Ice cover data is from the GLIA datasets for the winters of 1973 through 2005, and from the IMS datasets for the winters of 2006 through 2014. Air temperature data is from GHCN datasets for all years.

As evidenced in Figure 5.1, the relationship between air temperature and ice cover is roughly linear over a certain range of values. A linear trend was fit to data points with seasonally-averaged ice cover greater than 10%. While this threshold of 10% is ultimately arbitrary, a threshold is necessary when examining this linear relationship between air temperature and ice cover, because the relationship does not hold at higher air temperatures. In years of higher air temperature, ice still forms, but only a small amount, in a lakewide sense. The small amount of ice cover that forms in years with high seasonally-averaged air temperature is attributable to shallow bays and coastal regions of the lake, particularly the northern bays, for which a combination of shallower depth, more restricted wave field, and lower temperatures associated with higher latitude remains conducive to ice formation, even when lakewide-average air temperature is exceptionally high in a historical context.

The slope of the linear portion of the air temperature-ice cover relationship is  $-8.5\text{ \% }^{\circ}\text{C}^{-1}$ , which can be interpreted to mean that over this linear range of values, each  $1^{\circ}\text{C}$  increase in air temperature corresponds to a  $-8.5\%$  decrease in seasonally averaged ice cover. As seen in Figure 5.1, based on the distribution of points, a typical year on Lake Superior has seasonally-averaged ice cover in the range of roughly 10% to 30%. As such, the 8% to 9% decrease in seasonally-averaged ice cover that is associated with just a  $1^{\circ}\text{C}$  increase in air temperature is significant relative to the typical amount of ice cover that forms on the lake.

Ice cover was plotted against air temperature in the five remaining Great Lakes, also with linear trends plotted for data points with values of seasonally-averaged ice cover greater than 10%. These relationships are presented in Figure 5.2.

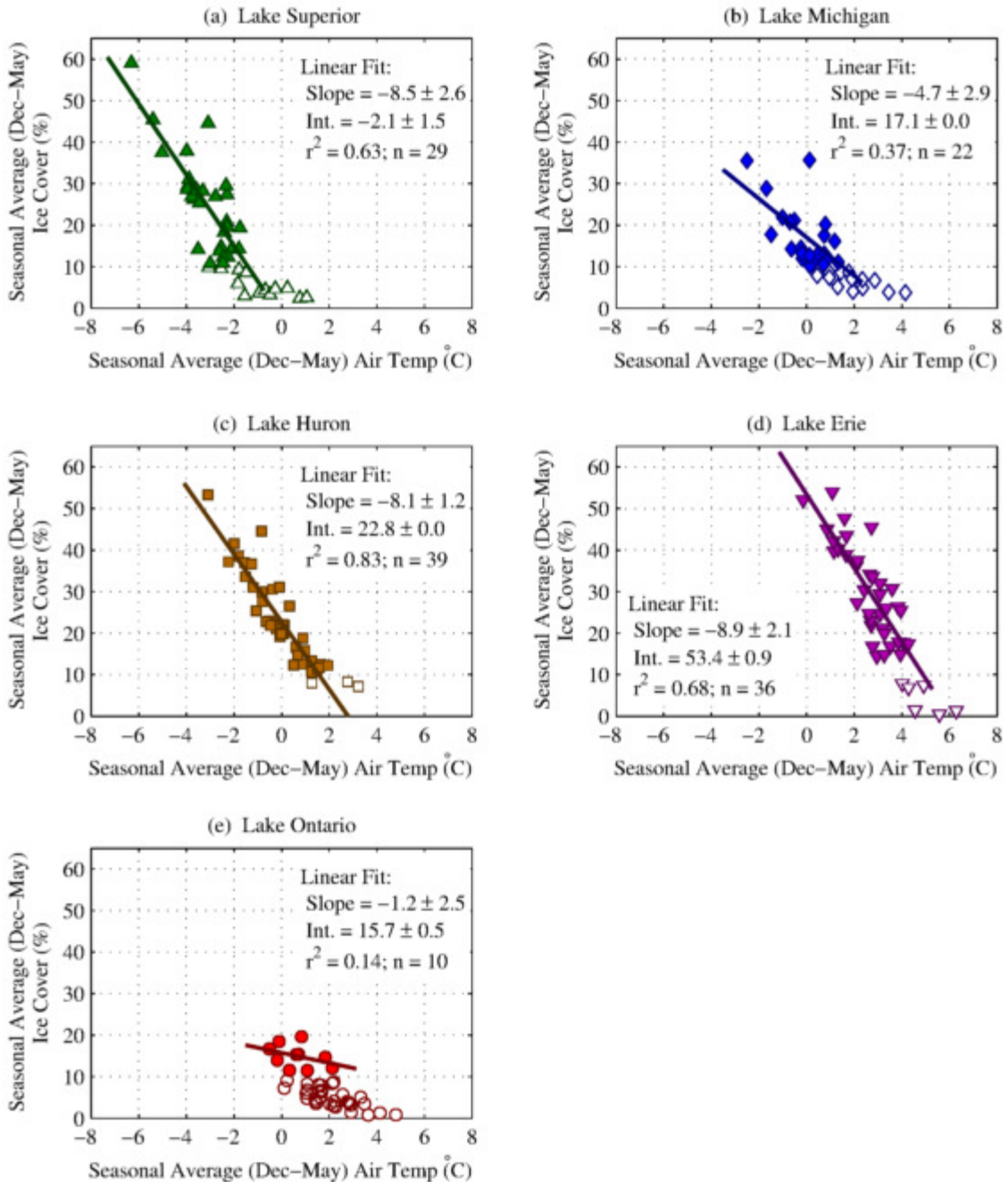


**Figure 5.2 – Sensitivity of lakewide average ice cover to air temperature, Great Lakes.** Seasonally-averaged ice cover is plotted against seasonally-averaged air temperature for each of the Great Lakes. A linear regression is presented for points that have seasonally-averaged ice cover above 10% (filled points), while points with ice cover below 10% (open points) were not included in the regressions. Intervals listed for the linear regression are 95% confidence intervals. Both ice cover and air temperature were averaged over the interval of December 1 through May 31 to calculate seasonally-averaged metrics. Ice cover data is from the GLIA datasets for the winters of 1973 through 2005, and from the IMS datasets for the winters of 2006 through 2014. Air temperature data is from GHCN datasets for all years.

The slopes of the best-fit lines in both Lake Huron ( $-8.1 \text{ \% } ^\circ\text{C}^{-1}$ , Figure 5.2c) and Lake Erie ( $-8.9 \text{ \% } ^\circ\text{C}^{-1}$ , Figure 5.2d) are quite similar to the slope of the best-fit line for Lake Superior ( $-8.5 \text{ \% } ^\circ\text{C}^{-1}$ , Figure 5.2a). Given the differences in size, depth, and latitude of these three lakes, it is noteworthy that they exhibit such similar sensitivity of ice cover to air temperature. The estimated slope of the best-fit line for Lake Michigan ( $-4.7 \text{ \% } ^\circ\text{C}^{-1}$ , Figure 5.2b) is smaller than that of those three lakes; however, its 95% confidence interval ( $-4.7 \pm 2.9 \text{ \% } ^\circ\text{C}^{-1}$ ) does overlap those of Lake Superior ( $-8.5 \pm 2.6 \text{ \% } ^\circ\text{C}^{-1}$ ), Lake Huron ( $-8.1 \pm 1.2 \text{ \% } ^\circ\text{C}^{-1}$ ), and Lake Erie ( $-8.9 \pm 2.1 \text{ \% } ^\circ\text{C}^{-1}$ ). Lake Ontario, which has low values of seasonally-averaged ice cover relative to the other four Great Lakes, does not exhibit a statistically significant trend in the sensitivity of ice cover to air temperature at the 95% confidence level, based on these metrics (slope =  $-1.2 \pm 2.5 \text{ \% } ^\circ\text{C}^{-1}$ , Figure 5.2e).

Next, the linear trends from the different lakes are examined together in order to examine the difference in the trends, as it relates to average lake depth. First, the best-fit lines were plotted together (Figure 5.3a), with boundaries on the air temperature axis for each line that correspond to the range of seasonally-averaged air temperatures from years in which seasonally-averaged ice cover above 10% has been observed in that lake. While there are some differences in slopes between lakes and the lakes do not experience the same ranges of temperature, by looking at the offsets of the lines, it can be qualitatively concluded from Figure 5.3a that shallower lakes form more ice than deeper lakes. For a given temperature, Lake Erie (average depth of 19 m) tends to form the most ice, and Lake Superior (average depth of 147 m) tends to form the least ice. Likewise, Lake Huron (average depth of 59 m) tends to form more ice than Lake Michigan (average depth of 85 m). Lake Ontario (average depth of 86 m), for which the trend between air temperature and ice cover is not significant, forms, in general, similar amounts of ice to Lake Michigan and Lake Huron over its observed range of seasonally-averaged air temperatures.

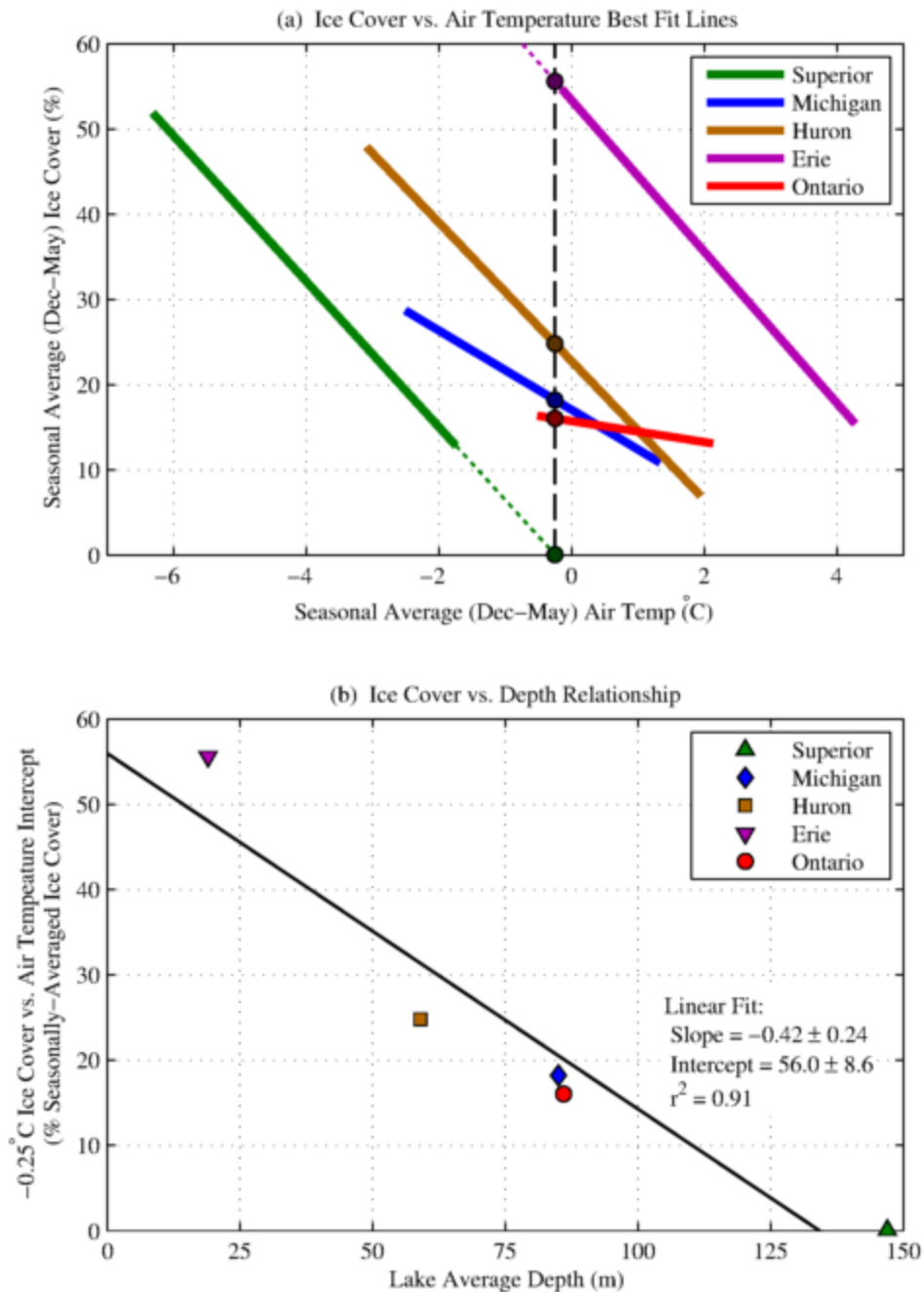


**Figure 5.3 – Seasonally-averaged ice cover relationship with average lake depth.** (a) Best fit lines for the relationship between seasonally-averaged ice cover and seasonally-averaged air temperature, as presented separately in Figure 5.2, are plotted together for each of the Great Lakes. The  $-0.25^{\circ}\text{C}$  intercept is shown for each lake with a dot. The Horizontal (air temperature) boundaries of solid line represent the range of seasonally-averaged air temperatures in years for which seasonally-averaged ice cover was greater than 10%. Best fit lines for Lake Superior and Lake Erie were extrapolated to determine the  $-0.25^{\circ}\text{C}$  intercept. (b) The  $-0.25^{\circ}\text{C}$  intercept is plotted against average lake depth for each of the five Great Lakes, and a linear regression is presented for the relationship between predicted ice cover at  $-0.25^{\circ}\text{C}$  and average lake depth.

In order to quantify the relationship between the offset of the ice cover vs. air temperature trend, the -0.25°C intercept of the best fit lines were plotted against average lake depth, and a linear regression was performed on those data points (Figure 5.3b). There is no one air temperature that falls within the observed range in all five of the Great Lakes, so the -0.25°C intercept was chosen as the metric for quantifying the offset of trend lines because it required minimal extrapolation outside of the range of observed air temperature values and did not produce negative ice cover values. -0.25°C is within the observed range of values for Lake Michigan, Lake Huron, and Lake Ontario, is approximately 1.5°C out of the range of values for Lake Superior, and approximately 0.1°C outside the range of values for Lake Erie. Because the slopes of the best fit lines are not equal, results of this offset analysis are somewhat sensitive to the choice of intercept. However, the relationship remains statistically significant at the 95% confidence level for all choices of intercept between -2°C and +2°C, which cover the ranges of seasonal-average air temperature that are experienced most commonly throughout the Great Lakes System.

As shown in Figure 5.3b, the offset, as defined by the -0.25°C intercept, is well-correlated with average lake depth ( $r^2 = 0.91$ ), and the linear trend is significant at the 95% confidence level. The slope of the line is  $-0.42\text{ \% m}^{-1}$ , which can be interpreted to mean that each 10 m increase in average lake depth will result in 4.2% less seasonal-average ice cover. The strong linear correlation between both air temperature (Figure 5.2) and average lake depth (Figure 5.3), especially in Lake Superior, Lake Huron, Lake Erie, and to a lesser extent, Lake Michigan, suggests that most of the variability in seasonal-average ice cover can be explained by these two metrics.

## 5.2 Time Sensitivity

The December through May period over which air temperature was averaged in the above analysis was chosen to be consistent with the time period used to compute seasonal averages for ice cover. Given that December through May encompasses the entire ice season in most years, it is an unbiased metric for assessing interannual variability in ice cover; however, it is ultimately an arbitrary choice when examining variability in air temperature. This section examines the sensitivity of ice cover to air temperature at different times of year in order to assess the times of year for which variability in air temperature has the greatest impact on the variability in ice cover.

### **5.2.1 Propagation of Anomalies**

In order to properly interpret the results of this section, it is first important to understand the extent to which ice cover and air temperature anomalies propagate through time. In other words, it is necessary to determine to what extent anomalies at a given time are correlated with anomalies at previous times. This was examined by calculating auto-correlation functions (ACFs) for both ice cover (Section 5.2.1.1) and air temperature (Section 5.2.1.2). ACFs are functions by which a given data from a given time-series are regressed against data from the same time-series that are offset by a given time lag (Shumway and Stoffer 2011). This allows for examination of the extent to which observations in that time-series are correlated with observations from that time-series that are set apart by a consistent amount of time. The computation of an ACF requires that time-series do not have missing values and that they have a constant time-step. Additionally, because examining the correlation between observations from the past and future is equivalent to examining the correlation between observations at the future and past, ACFs are necessarily symmetric about the zero-lag axis.

#### **5.2.1.1 Ice Cover ACFs**

A time-series of ice cover anomalies was developed for each of the Great Lakes by subtracting the average annual signal from the ice cover time-series. The average annual signal was determined by averaging 42 years of ice cover data on each calendar day of the year in order to determine the average annual ice cover on that day. This day-by-day approach to determining the average annual ice cover signal is necessary, because ice cover on the Great Lakes does not follow a regular periodic function, such as a sinusoid. Because GLIA datasets have ice cover data for only the months of December through May and because the ACF analyses require continuous time-series with a constant time-step, lakewide average ice cover was assumed to be zero from June through November for years in which ice-cover data from the GLIA was used. This is a reasonable assumption, because ice is generally not observed on the lakes during those months. ACFs for each of the Great Lakes are presented in Figure 5.4.

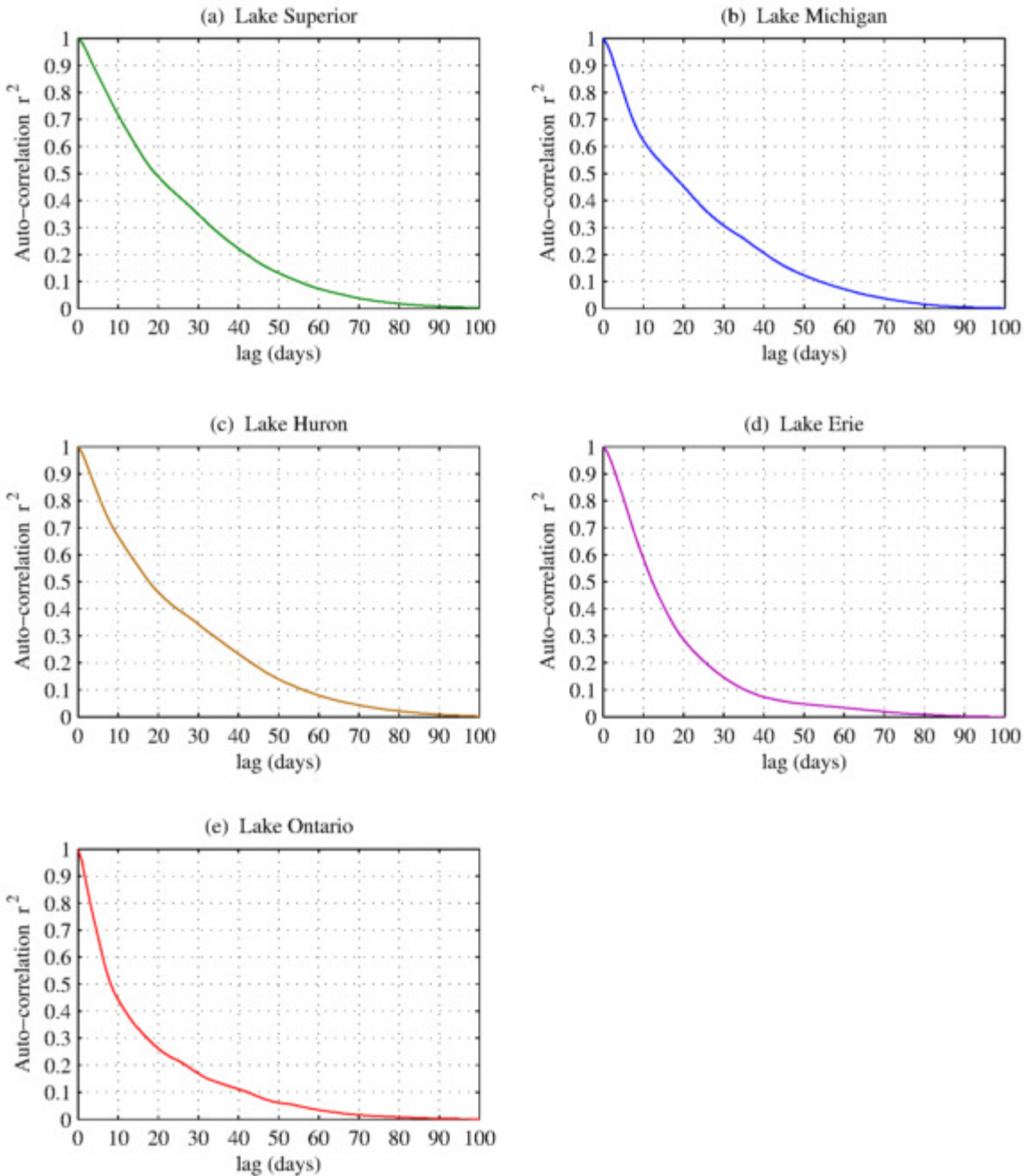


**Figure 5.4 – Ice-cover anomaly ACFs, seasonal timescale, Great Lakes.** The figure presents ACFs of ice-cover anomalies for each of the Great Lakes, and shows the ACF for lags representative of seasonal timescales.

At the seasonal scale, ACFs show similar patterns among all of the lakes (Figure 5.4). The ACFs for Lake Erie (Figure 5.4d) and Lake Ontario (Figure 5.4e) decay faster than those for Lake Superior (Figure 5.4a), Lake Michigan (Figure 5.4b), and Lake Huron (Figure 5.4c). However

the same general conclusion can be drawn for all of the lakes, which is that ice cover anomalies persist in the ice cover record for scales on the order of weeks. It is somewhat intuitive that ice cover anomalies persist at seasonal timescales, due to the ice albedo feedback mechanism. Once ice forms, it increases the albedo of the lake, and reduces the amount of shortwave radiation that is absorbed into the lake, thereby reducing a heat source into the lake. As such low ice conditions are generally less conducive to ice formation and high ice conditions are generally more conducive to sustained ice.

### **5.2.1.2      *Air Temperature ACFs***

Air temperature anomaly time-series were developed using the same methods used to construct the ice cover anomaly time-series in the previous section. As was done with the ice-cover data, the average annual air temperature signal was determined by averaging 42 years of air temperature data on each calendar day of the year. While air temperature does follow a regular sinusoidal pattern, this day-by-day approach to determining the average annual air temperature signal was chosen so as to be consistent with the methods use for ice cover. Air temperature anomaly ACFs for each of the Great Lakes are presented in Figure 5.5.

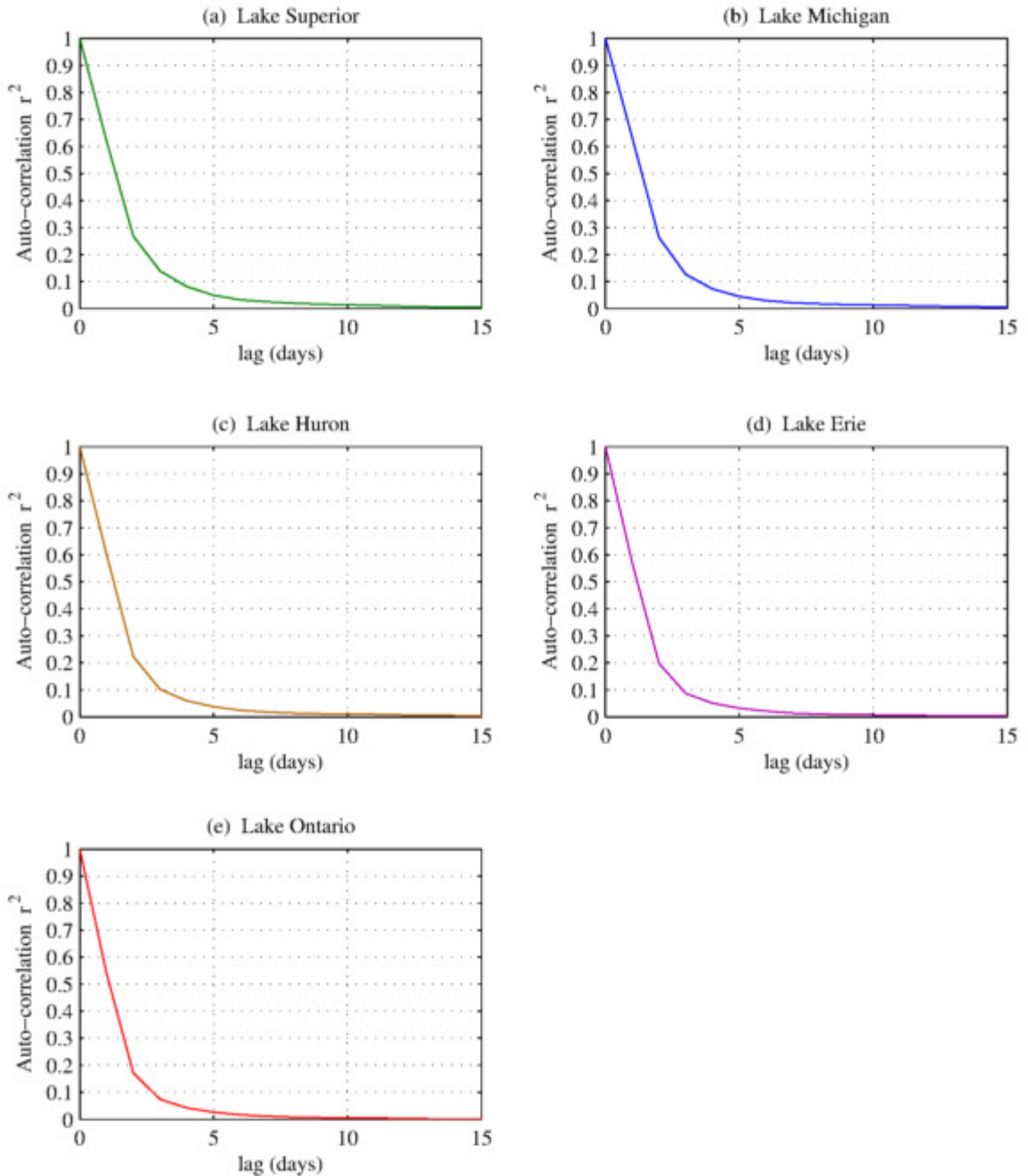


**Figure 5.5 – Air temperature anomaly ACFs, seasonal timescale, Great Lakes.** The figure presents ACFs of air temperature anomalies for each of the Great Lakes, and shows the ACF for lags representative of seasonal timescales.

Air temperature ACFs for all lakes decay at scales on the order of days, with air temperature anomalies in all lakes showing less than 10% correlation with anomalies more than three days

later (Figure 5.5). The decay of air temperature anomalies on the scale of a few days is consistent with the passing of synoptic-scale weather patterns (Woo 2008).

### **5.2.1.3      *Cross Correlation***

Cross-correlation functions (CCFs) were also computed for the relationship between ice cover anomalies and air temperature anomalies on the Great Lakes. CCFs are similar to ACFs, except instead of comparing observations within the same time-series at different offsets, observations from two different time-series are regressed against one another at a series of different lags (Shumway and Stoffer 2011). This is useful for identifying whether a parameter has a lagged effect on another, and to what extent, which might not be discernible if only simultaneous observations are compared. Similar to ACFs, the calculation of CCFs require that both time-series contain no missing values and have an identical constant time-step between observations. Unlike ACFs, CCFs are not necessarily symmetrical about the zero-lag axis, because observations from a given time-series do not necessarily have the same correlation with past values of the other time-series as they do with future values of the other time series.

CCFs between air temperature and ice cover for each of the Great Lakes are presented in Figure 5.6. The convention used for these CCFs is that positive lags correspond to the ice cover time-series lagging the air temperature time-series, and negative lags correspond to the air temperature time-series lagging the ice cover time-series.

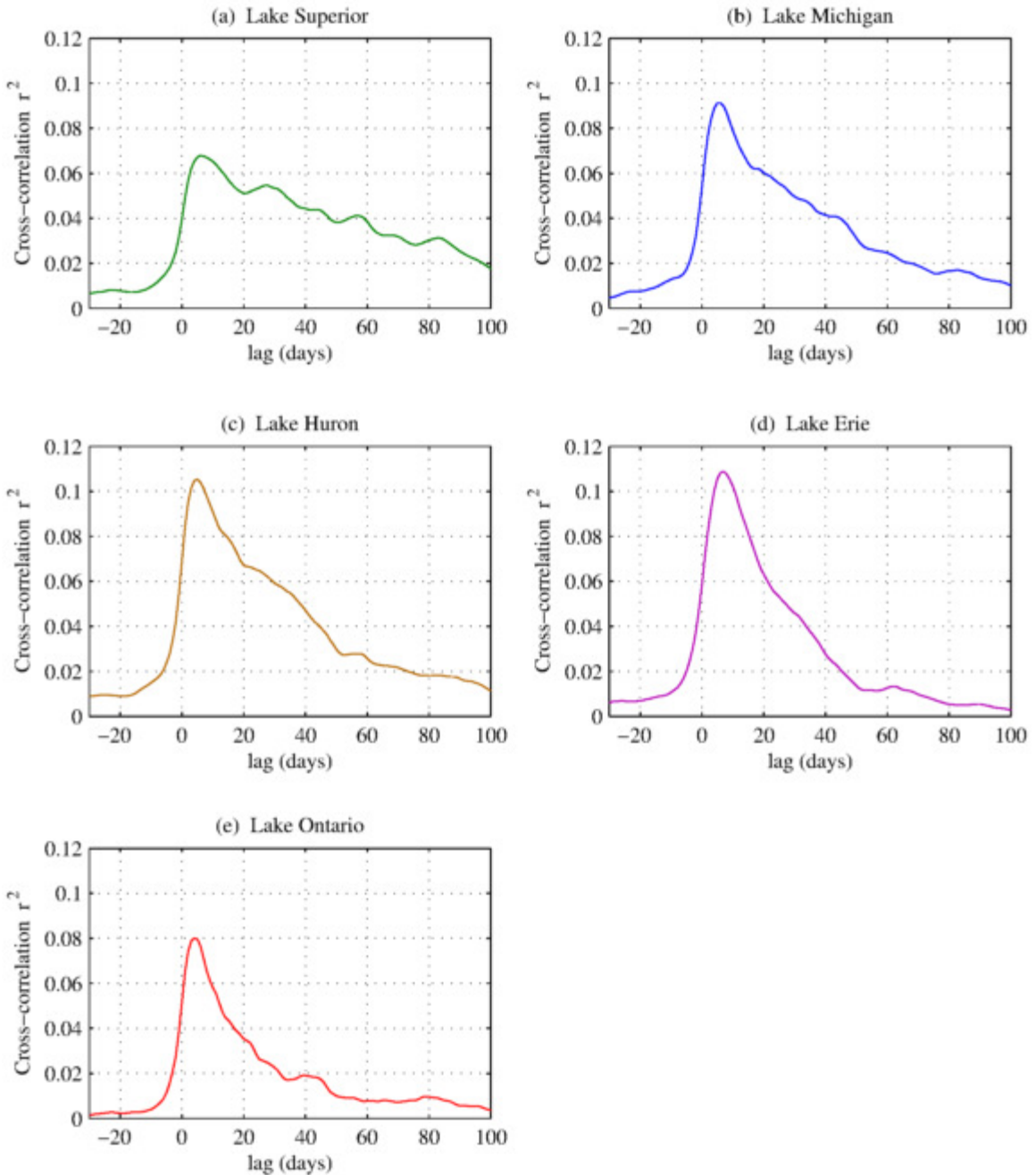


**Figure 5.6 – CCFs for ice-cover and air temperature, seasonal timescale, Great Lakes.** The figure presents the CCFs for ice-cover anomaly and air temperature anomaly for each of the Great Lakes, and shows the CCFs for lags representative of seasonal timescales. Positive lags are associated with ice cover time series lagging the air temperature time-series, while negative lags are associated with the air temperature time-series lagging the air temperature time-series. Ice cover data are from the GLIA datasets for the winters of 1973 through 2005, and from the IMS datasets for the winters of 2006 through 2014. Air temperature data are from GHCN datasets.

One clear aspect of the CCF at lags nearer to zero is that the correlations are stronger for positive lags than for negative lags. This is logical, because it demonstrates that air temperature is a better forward predictor of ice cover than ice cover is of air temperature. However, the correlation between air temperature and ice cover is quite small even at small lags. The maximum  $r^2$  value in any of the CCFs is 0.11 in Lake Huron, at a lag of 5 days. The lag at which the maximum  $r^2$  value occurs ranges from 4 days in Lake Ontario to 7 days in Lake Erie.

The few-day lag in the correlation may be associated with strong synoptic-scale weather patterns. Air temperature anomalies were shown in the previous section (Section 5.2.1.2) to dissipate over the course of a few days. It may be that large air temperature anomalies, associated with strong synoptic-scale weather patterns, result in a compounding formation of ice over the course of the several days that it takes the system to pass through the region, and that the corresponding peak in ice cover occurs at the trailing end of that synoptic system. The fact that all  $r^2$  values are quite small does not directly contradict the results of Section 5.1, which showed that seasonal-average ice cover is well correlated with seasonal-average air temperature. Instead, these CCFs suggest that an air temperature anomaly on any given day is not a great predictor of ice cover at any point in time relative to that anomaly. Air temperatures must be anomalies must be considered over longer timescales in order to be useful predictors of ice cover.

## 5.2.2 Time Sensitivity by Month

In Section 5.1, it was shown that seasonal ice cover is sensitive to variability in seasonal air temperature. On the other end of the spectrum, it was shown in Section 5.2.1 that air temperature anomalies persist over relatively short timescales, and that air temperature on any given day are not a great predictor of ice cover on any subsequent day. As such, longer time periods must be considered when examining the influence of air temperature on ice cover. In this section, the effect that variability in air temperature at monthly timescales has on ice cover. To do this, 42-year-long ensembles of monthly air temperature were compiled for each month of the year for the seasons of 1972-1973 through 2013-2014, and were regressed against ice cover metrics from the same years.

Figure 5.7 shows the results of linear regressions between seasonal-average ice cover and monthly-average air temperature for each of the Great Lakes. A separate linear regression was performed for each month of the year, comparing the ensemble of monthly average air

temperature values to the seasonal ice cover parameter being examined. For these analyses, air temperatures for the months of December through May correspond to the ice season for a given year, and the months of June through November correspond to the months leading up to that season. Correlations that are statistically significant at the 95% confidence level are shaded.

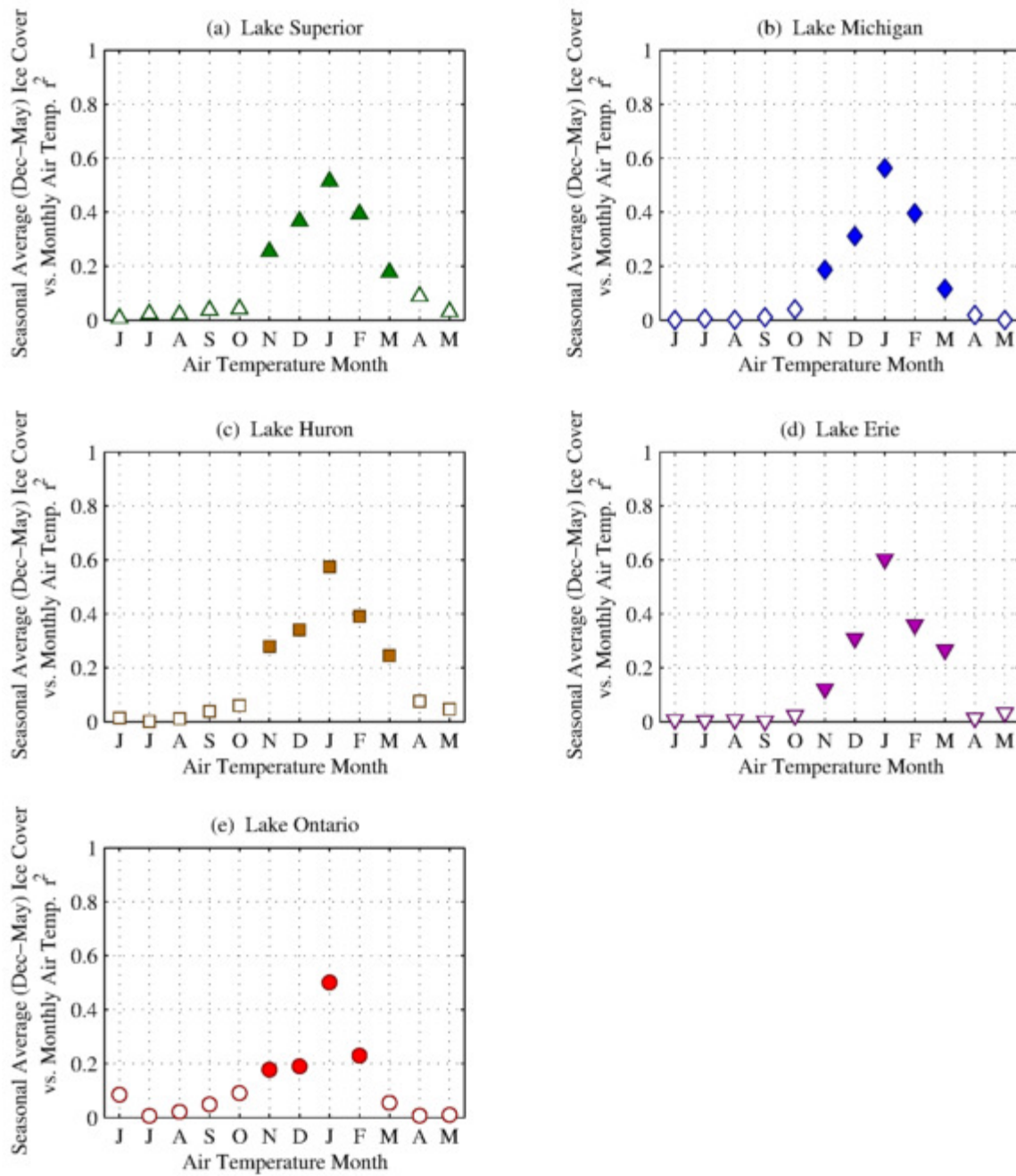


**Figure 5.7 – Correlation ( $r^2$ ) between seasonal ice cover and monthly air temperature.** Seasonally-averaged (Dec-May) ice covers were regressed against ensembles of monthly average air temperature on each of the Great Lakes, based on data from the 1972-1973 season through the 2013-2014 season. The  $r^2$  value for the correlation between seasonally-averaged ice cover and monthly air temperature is presented here for each month of the year for which monthly air temperature was examined. Months with significant trends at the 95% level are shown by filled points. Monthly air temperatures in December through May correspond to the same months over which ice-cover was averaged, and the months of June through November correspond to the months leading up to that period. Air temperature data is from GHCN datasets, while ice-cover data is from GLIA datasets for the winters of 1973 through 2005 and from IMS datasets for the winters of 2006 through 2014.

The months with statistically significant trends and higher  $r^2$  values are months occurring during or soon before the ice-covered season, including November through March. In all five Great Lakes, monthly air temperatures show statistically significant trends with seasonally-averaged ice cover for the months of November through February (Figure 5.7). Lake Ontario is the only Great Lake that does not also show a statistically significant trend between March air temperature and seasonally-averaged ice cover. For all five of the Great Lakes, January air temperature shows the best correlation with seasonal-average ice cover, with an  $r^2$  value of 0.51 in Lake Superior, 0.56 in Lake Michigan, 0.57 in Lake Huron, 0.60 in Lake Erie, and 0.50 in Lake Ontario. This shows that January is the best monthly predictor of the overall amount of ice cover that will form in a given season on the Great Lakes.

The phenology of the ice covered season is often of interest, and it is therefore important to separate the differences between climate effects that condition the lakes for ice formation and those that are important toward ice breakup of ice. To examine this, the same ensembles of monthly-average air temperature were compared against ice on dates and ice off dates for each of the Great Lakes. Both of these processes are integrated into the seasonal-average ice cover analysis presented above; however, ice-on and ice-off are distinct phenological phenomena and warrant compartmentalized analyses. Ice-on and ice-off date are not straight-forward to define on the Great Lakes, where ice cover is primarily drifting (see Section 4.0 for more about ice characteristics). For the sake of these analyses, ice-on date was defined as the first day of the season with lakewide-average ice cover greater than 10%, and ice-off date is defined as the day after the last day of the season with ice cover greater than 10%. This 10% threshold roughly corresponds to the point at which ice formation progresses beyond shallow bays and coastal regions and begins to form in the open-water portions of the lakes. Because, using these metrics, ice-on and ice-off dates are not defined for years in which lakewide-average ice cover does not surpass 10%, only years for which lakewide-average ice cover does form above this threshold are included in these regressions. This threshold was not reached during only one year on Lake Superior and Lake Erie, and during three years on Lake Ontario; it was reached during all years on Lake Michigan and Lake Huron.

Correlations between monthly air temperature and ice-on date are presented in Figure 5.8, and correlations between monthly air temperature and ice-off date are presented in Figure 5.9. Again, correlations that are statistically significant at the 95% confidence level are shaded.

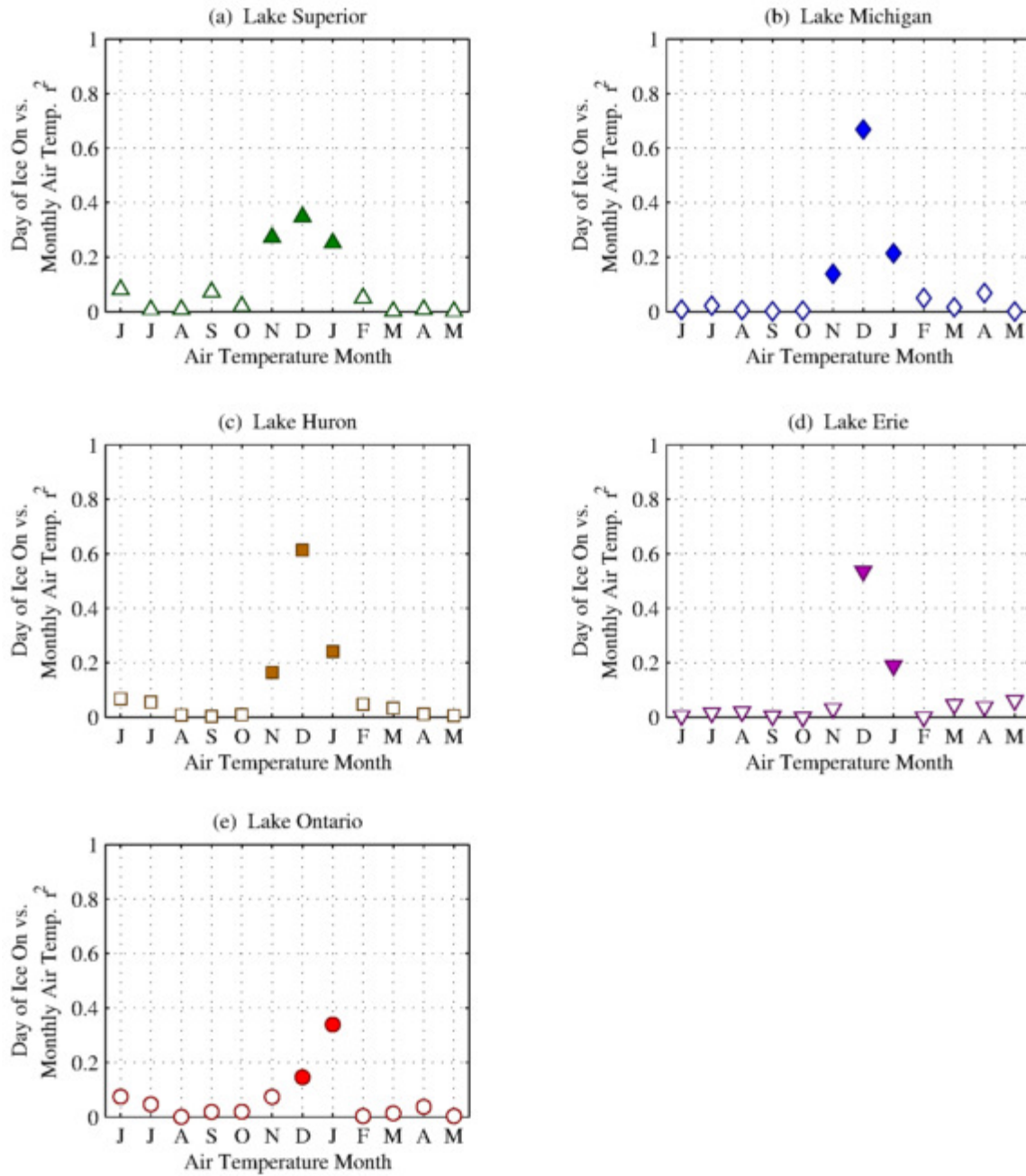


**Figure 5.8 – Correlation ( $r^2$ ) between ice-on day and monthly air temperature.** The yearly day of ice-on, defined as first day with lakewide ice cover greater than 10%, was regressed against ensembles of monthly average air temperature on each of the Great Lakes, based on data from the 1972-1973 season through the 2013-2014 season. The  $r^2$  value for the correlation between ice-on day and monthly air temperature is presented here for each month of the year for which monthly air temperature was examined. Months with significant trends at the 95% level are shown by filled points. Monthly air temperatures in December through May correspond to the winter/spring ice-covered season being considered, and the months of June through November correspond to the months leading up to that period. Air temperature data is from GHCN datasets, while ice-cover data is from GLIA datasets for the winters of 1973 through 2005 and from IMS datasets for the winters of 2006 through 2014.

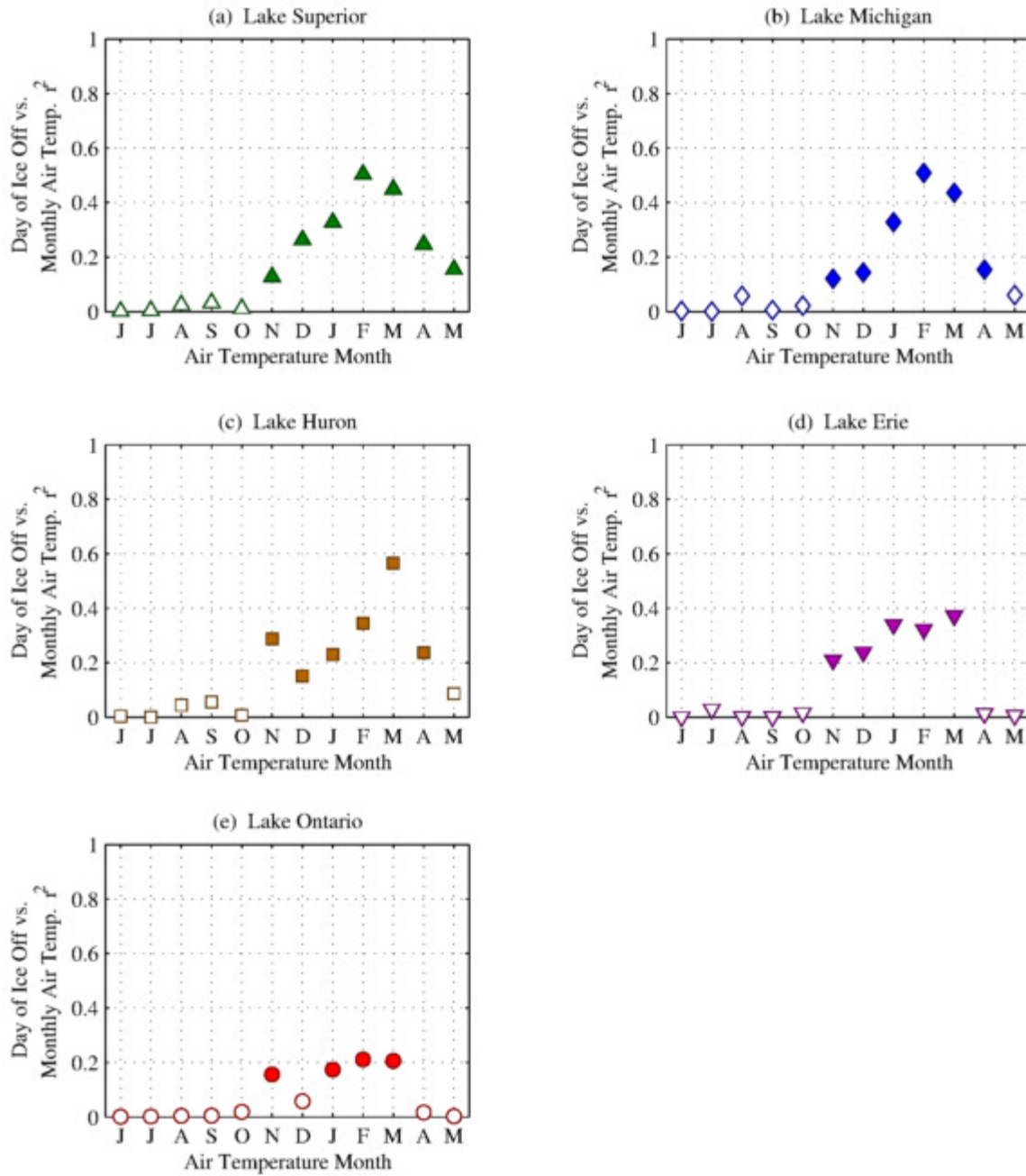


**Figure 5.9 – Correlation ( $r^2$ ) between ice-off day and monthly air temperature.** The yearly day of ice-off, defined as the day after the last day with lakewide ice cover greater than 10%, was regressed against ensembles of monthly average air temperature on each of the Great Lakes, based on data from the 1972-1973 season through the 2013-2014 season. The  $r^2$  value of the correlation between ice-off day and monthly air temperature is presented here for each month of the year for which monthly air temperature was examined. Months with significant trends at the 95% level are shown by filled points. Monthly air temperatures in December through May correspond to the winter/spring ice-covered season being considered, and the months of June through November correspond to the months leading up to that period. Air temperature data is from GHCN datasets, while ice-cover data is from GLIA datasets for the winters of 1973 through 2005 and from IMS datasets for the winters of 2006 through 2014.

In all five Great Lakes, the months of December and January exhibit statistically significant trends between monthly average air temperature and the date of ice-on (Figure 5.8). In addition, Lake Superior, Lake Michigan, and Lake Huron show statistically significant trends between November air temperature and the timing of ice on. The month with the best correlation between monthly average air temperature and the date of ice on is December for Lake Superior ( $r^2=0.35$ ), Lake Michigan ( $r^2=0.67$ ), Lake Huron ( $r^2=0.61$ ), and Lake Erie ( $r^2=0.54$ ), and is January for Lake Ontario ( $r^2=0.34$ ). The fact that only the months of November, December, or January have statistically significant relationships with the timing of ice on shows, perhaps unsurprisingly, that variability in air temperature during the early portion of the winter season, around the time of ice-on dates, best explains variability in ice-on date.

As shown in Figure 5.9, air temperatures from most of the ice season and the months leading up to it are important in determining the timing of ice-off. The months of November, January, February, and March show statistically significant correlations between monthly-average air temperature and ice-off date in all five of the Great Lakes, and Lake Ontario is the only Great Lake that does not additionally show a statistically significant correlation between December air temperature and ice-off date. Lake Superior, Lake Michigan and Lake Huron all show statistically significant correlations between April air temperature and ice-off date, and Lake Superior is the only month to have a statistically significant correlation between May air temperature and ice off. The month with the best-correlation between air temperature and ice-off varies from lake to lake, with February showing the best correlation in Lake Superior ( $r^2=0.50$ ), Lake Michigan ( $r^2=0.51$ ), and Lake Ontario ( $r^2=0.21$ ), and March showing the best correlation in Lake Huron ( $r^2=0.57$ ) and Lake Erie ( $r^2=0.37$ ).

The main takeaway from these monthly regressions is that the date of ice off is influenced by temperatures from throughout the winter season (Figure 5.9). This is in contrast to the relationship between monthly air temperature and ice-on, which only show statistically significant correlations with the months in the early portions of the winter season (Figure 5.8). Seasonal-average (Dec-May) ice cover depends more on air temperatures early in the ice season, or even preceding the ice season, than those late in the ice season (Figure 5.7).

### 5.2.3 Time Sensitivity Seasonal Approach

In Section 5.2.2, it was shown that air temperatures from a variety of different months have statistically significant relationships with ice cover. This was useful in assessing the general times of year for which air temperature is important in influencing ice cover. However, analyzing the relationship by calendar month is ultimately arbitrary. In this section, I examine the same question of the sensitivity of ice cover to variations in air temperature at difference times of year, but this time from a seasonal perspective, rather than a monthly perspective. More specifically, I use an objective algorithm to determine the seasonal timeframe over which average air temperature is best-correlated with ice cover.

To do this, the start day and end day used to calculate the seasonal average air temperature were varied, and the corresponding average air temperature was compared to seasonal-average ice cover, ice-on date, and ice-off date. For each pair of start day and end day values, a 42-year-long ensemble of historic air temperature values corresponding to that time range was assembled for the seasons of 1972-1973 through 2013-2014. These 42-year-long records of air temperature averaged over different timeframes were regressed against the same 42-year-long records of seasonally-averaged (Dec-May) ice cover, ice-on date, and ice-off date used in the previous monthly analyses.

As an example, the resulting plots from analyses for seasonal-average ice cover are shown for each of the Great Lakes in Figure 5.10. In these plots, the  $r^2$  values for relationships that are statistically significant at the 95% confidence level are shown as a function of the start day and end day of the air temepature average, along with the ranges for which air temperatures are best-correlated with ice cover.

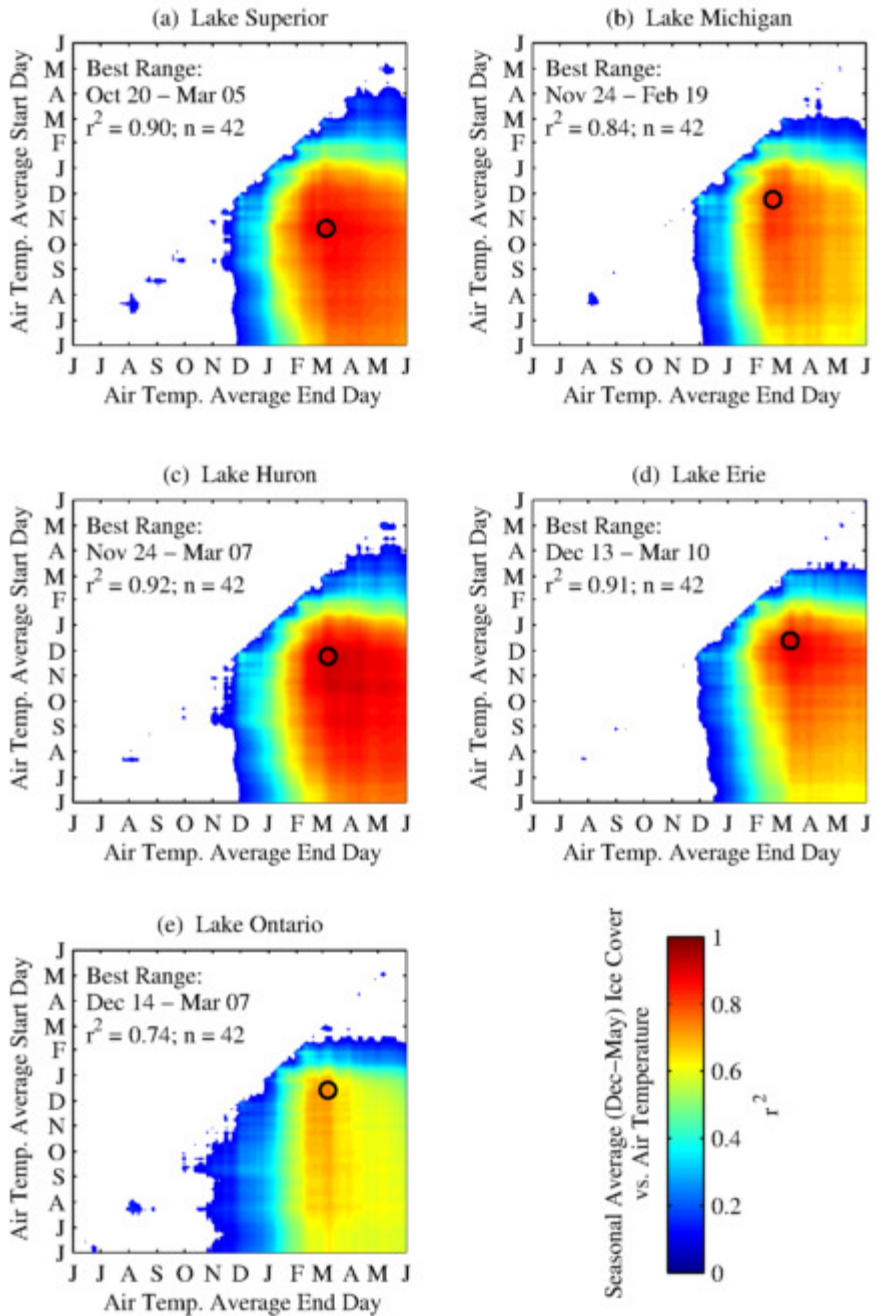


**Figure 5.10 – Determination of air temperate most correlated with seasonal-average ice cover.** A series of linear regressions was performed, comparing seasonally-averaged ice cover with seasonally-averaged air temperature for each of the Great Lakes, using an array of different time periods for the air temperature average. Ensembles used in correlations consisted ice cover and air temperature from the 1973-1973 season through the 2013-2014 season. Ice cover was averaged from December through May for all correlations, while the period used for air temperature was varied.  $r^2$  values for the “start day-end day” pair used to average air temperature are shown on the color axis for correlations that are statistically significant at the 95% confidence level, and the date range with the maximum  $r^2$  value is listed for each lake. Months of December through May correspond to the winter/spring ice-covered season being considered, and the months of June through November correspond to the months leading up to that period.

Figure 5.10 shows that, from this integrated seasonal perspective, air temperatures throughout the early portion of the winter are most important for explaining variability in seasonally-averaged ice cover. The range of air temperature that is best-correlated with seasonally-averaged ice cover is October 20 through March 5 in Lake Superior ( $r^2=0.90$ ), is November 24 through February 19 in Lake Michigan ( $r^2=0.84$ ), is November 24 through March 7 in Lake Huron ( $r^2=0.92$ ), is December 13 through March 10 in Lake Erie ( $r^2=0.91$ ), and is December 14 through March 7 in Lake Ontario ( $r^2=0.74$ ). These time periods are generally consistent with the months found to have statistically significant correlations in Section 5.2.2. The  $r^2$  values for these seasonal relationships are quite high, and show that when air temperature is averaged over an appropriate timeframe, upwards of 90% of interannual variability in ice cover in Lake Superior, Lake Huron, and Lake Erie can be explained in terms of air temperature alone, more than 70% of variability can be explained in Lake Ontario, and more than 80% in Lake Michigan.

While the plots in Figure 5.10 are useful for exploring the sensitivity of ice cover to air temperature over a variety of timeframes, it is difficult to read correlations for exact date pairs. Correlations between lakes for a variety of consistent time periods are summarized in Table 5.1.

	Lake Superior	Lake Michigan	Lake Huron	Lake Erie	Lake Ontario
Oct – Jan	0.74	0.68	0.71	0.60	0.58
Oct – Feb	0.85	0.78	0.85	0.73	0.68
Oct – Mar	0.86	0.74	0.89	0.79	0.64
Nov – Jan	0.74	0.68	0.73	0.64	0.56
Nov – Feb	0.86	0.80	0.89	0.80	0.70
Nov – Mar	0.85	0.74	0.89	0.83	0.61
Dec – Jan	0.69	0.68	0.70	0.70	0.55
Dec – Feb	0.82	0.81	0.89	0.85	0.71
Dec – Mar	0.80	0.73	0.89	0.88	0.62
Jan	0.51	0.56	0.57	0.60	0.50
Jan – Feb	0.67	0.69	0.75	0.71	0.63
Jan – Mar	0.65	0.61	0.77	0.77	0.54

**Table 5.1 – Correlation between seasonal ice cover and air temperature by timeframe.**  $r^2$  values are presented for the linear correlation between air temperature, averaged of the listed timeframe, and seasonally-averaged (Dec-May) ice cover. Months listed for averaging timeframes represent the entirety of that calendar month. All correlations shown in this table are statistically significant at the 95% confidence level. Ensembles used in correlations consisted of seasonally-averaged ice cover and air temperature from the 1973-1973 season through the 2013-2014 season.

Of the time periods list in Table 5.1, air temperatures averaged over meteorological winter (December through February) are consistently well-correlated with seasonally-averaged ice cover values, with an  $r^2$  value of 0.82 in Lake Superior, an  $r^2$  value of 0.81 in Lake Michigan, an  $r^2$  value of 0.89 in Lake Huron, an  $r^2$  value of 0.85 in Lake Erie, and an  $r^2$  value of 0.71 in Lake Ontario. The correlation increases marginally in Lake Huron and Lake Erie when March air temperatures are included in the average, and also increases marginally in Lake Superior when November or November and March air temperatures are included in the average. However, the values presented in Table 5.1 demonstrate that most of the variability in seasonally-averaged ice cover in most of the Great Lakes can be explained in terms of just the air temperatures from December through February.

To visually demonstrate the extent to which ice cover parameters are correlated with air temperature when an appropriate air temperature range is used and examine those linear relationships, correlations between air temperature and seasonally-averaged (Dec-May) ice cover, the correlation between seasonally-averaged ice cover and winter (Dec-Feb) air temperature is shown in Figure 5.11.

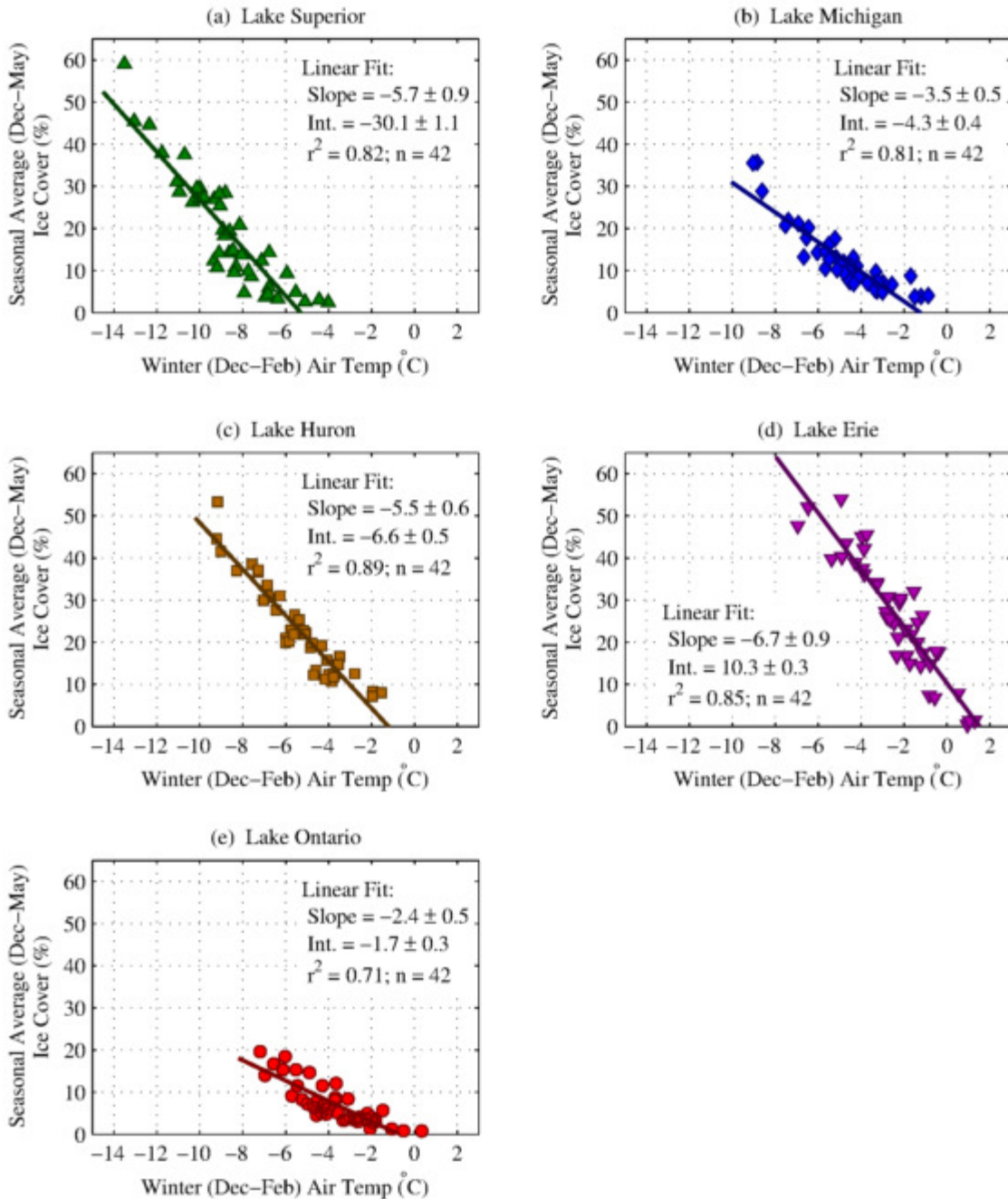


**Figure 5.11 – Average (Dec-May) ice cover vs. winter (Dec-Feb) air temperature correlations.**  
 Seasonally-averaged (Dec-May) ice cover is plotted against winter (Dec-Feb) air temperature for each of the Great Lakes. There is a data point for each winter from 1973 through 2014. A linear regression was performed on data points from each lake, and the results of those regressions are presented with 95% confidence intervals. Ice cover data is from the GLIA datasets for the winters of 1973 through 2005, and from the IMS datasets for the winters of 2006 through 2014. Air temperature data is from GHCN datasets for all years.

The regressions between seasonally-averaged (Dec-May) ice cover and winter (Dec-Feb) air temperature demonstrate that when Dec-Feb as the averaging timeframe for air temperature, air temperature is well-correlated with seasonally-averaged ice cover over the entirety of the ice cover range (Figure 5.11). This is in contrast to the correlation between seasonally-averaged ice cover and air temperature when Dec-May is used as the air temperature averaging interval (Figure 5.2), for which the linear relationship only held in higher-ice seasons. In addition, the  $r^2$  values for the correlations between ice cover and Dec-Feb air temperature for all winters 1973-2014 (Figure 5.11) are consistently higher than the  $r^2$  values between ice cover and Dec-May air temperatures for a subset of colder years (Figure 5.2). This demonstrates that variability in Dec-Feb air temperature can better explain variability in seasonally-averaged ice cover over the entire spectrum of observed winter conditions than can variability in Dec-May air temperature.

Similar analyses were conducted for the timing of ice-on and ice-off. For the sake of brevity, these are not shown or discussed in detail. However, time periods over which air temperature was found to be most consistently best-correlated with these parameters are listed in Table 5.2, along with corresponding  $r^2$  values.

	Lake Superior	Lake Michigan	Lake Huron	Lake Erie	Lake Ontario
Avg. (Dec–May) Ice vs. Air Temperature (Dec – Feb)	0.82	0.81	0.89	0.85	0.71
Ice-On Day vs. Air Temperature (Dec – Jan 15)	0.50	0.77	0.75	0.65	0.41
Ice-Off Day vs. Air Temperature (Dec – Apr)	0.89	0.78	0.76	0.71	0.52

**Table 5.2 – Correlations between ice cover and air temperature.**  $r^2$  values are presented for the linear correlation between air temperature, averaged of the listed timeframe, and the listed ice cover metrics. All correlations shown are statistically significant at the 95% confidence level. Ensembles used in correlations consisted of ice-off and air temperature from the 1973–1973 season through the 2013–2014 season.

The timeframes shown in Table 5.2 are consistent with the results of the monthly analyses discussed in Section 5.2.2. Seasonal-average ice cover is most consistently well-correlated with air temperature during roughly the portion of the winter season when ice is forming, from December through February. The timing of ice-on is most-consistently well-correlated with air temperatures from the beginning of December through the middle of January, which is around the timing of ice-on. Ice-off is most-consistently well-correlated with air temperatures from December through April, demonstrating that ice-off depends on conditions from throughout the winter season. An interesting aspect of these conclusions is that considering air temperatures from before the beginning of the ice season does not generally improve the ability to predict or explain the extent of ice cover and, in fact, often results in slightly weaker correlations.

The reason that air temperature anomalies have a greater influence during the time of the year when ice is forming can be explained in terms of feedback mechanisms. There is a negative feedback mechanism associated with cooling the lake, and a positive feedback mechanism associated with ice formation. Equilibrative heat flux components, including turbulent (sensible and latent) fluxes and net longwave radiative heat flux, are strong functions of the air-water temperature difference. The equilibrative nature of these fluxes means that as the lake is cooled toward the temperature of the air, the magnitude of fluxes decrease. This can be thought of as a

negative feedback mechanism. Ice formation, on the other hand, increases the albedo of the lake surface, thereby reducing net shortwave radiative flux, which is a heat source to the lake. This can be thought of as a positive feedback mechanism.

### 5.3 The relationship between air temperature and ice-on date

In the previous section it was shown that the impact air temperature anomalies will have on ice cover depends on the time of year in which they occur. This emphasizes that the relationship between air temperature and ice cover cannot be explained in terms of a simple thermodynamic scaling, and that phenological factors must be considered. The lake experiences different phases over the course of the year, from heating and cooling to ice formation and ice melt. The equilibrative nature of heat flux, as described above, is a mechanism by which the residual impact of climatic anomalies diminishes over time. The timing of air temperature anomalies found to be important, and understood through the positive and negative feedback mechanisms described above suggest, imply that air temperature anomalies occurring during the time of ice formation are especially important in determining the amount of ice cover that will form in that season. With that in mind, an important step toward understanding the relationship between air temperature and ice cover is understanding the mechanisms driving the time when that ice formation period begins.

In order for ice to form on the lake, the following conditions, at a minimum, must be true:

- Air temperature must be below  $0^{\circ}\text{C}$
- The water column must have cooled to a point where ice will form

The annual air temperature signal can be fit to a sinusoidal function:

$$X = \mu + A \cos[f(YD - \phi)] \quad \text{Equation 5.1}$$

Where  $X$  is the fit value of the annual signal on year-day  $YD$ ,  $\mu$  is the fitted signal average,  $A$  is fitted signal amplitude,  $f$  is the signal frequency ( $2\pi \text{ yr}^{-1}$ ), and  $\phi$  is the phase shift of the signal (the year-day when the signal is at a maximum).

From a phenological perspective, an air temperature anomaly can be thought of phenological time shift in the air temperature signal, such that the lake is experiencing conditions that typically

occur slightly earlier or later in the year. This perceived time shift will occur inversely proportionally to the time derivative of the air temperature signal, evaluated around the time when air temperature anomaly occurs. In this case, that is around the time when air temperature drops below freezing.

The time at which air temperature will reach 0°C can be determined by rearranging Equation 5.1:

$$YD_0 = \frac{\arccos\left(\frac{-\mu_a}{A_a}\right)}{f} + \phi_a \quad \text{Equation 5.2}$$

The time derivative of the air temperature signal (Equation 5.1) is given by:

$$\frac{dAT}{dYD} = -A_a f \sin(f(YD - \phi_a)) \quad \text{Equation 5.3}$$

By taking the inverse of Equation 5.3, substituting the expression from Equation 5.2, and simplifying, the equivalent phenological time shift per degree air temperature anomaly is given by:

$$\frac{dYD}{dAT} = \frac{1}{-A_a f \sin\left(\arccos\left(\frac{-\mu_a}{A_a}\right)\right)} \quad \text{Equation 5.4}$$

Representative values of these parameters were calculated for the Great Lakes region (not shown), and it was found that a typical air temperature signal in the region has an amplitude of 13.0°C and a mean value of 7.7°C. By using these values in Equation 5.4, this time shift is found to be:

$$\frac{1}{-(13.0^\circ C) \left(\frac{2\pi}{365 \text{ day}}\right) \sin\left(\arccos\left(\frac{-(7.7^\circ C)}{(13.0^\circ C)}\right)\right)} = -5.5 \frac{\text{day}}{^\circ C} \quad \text{Equation 5.5}$$

This implies that each 1°C increase in air temperature corresponds to a phenological time shift of 5.5 days.

Next, water column conditions can be examined. Given that lakes stratify, it is the depth of the thermocline that is thermodynamically important throughout the stratified ice season. However, leading up to stratification, the total depth of the water column is important during the isothermal cooling period. It follows that lake depth would be an important parameter in predicting the timing of ice formation, because it describes the amount of water that must be cooled until the water column reaches a point when the water column will stratify and ice will form. Several years of moored thermistor from Lake Superior have shown that the water column does not begin to negatively stratify when it reaches the temperature of maximum density. As discussed in Section 3.1, this is in contrast to small lakes, which will begin to form ice atop a thin stratified surface layer once the water column reaches about 4°C. In fact, these several years of mooring data show that the water column on lake superior begins to stratify when it reaches a temperature closer to 3°C (Titze and Austin 2014; Figure 3.3). As such, after the water column reaches a temperature near 4°C in the fall and mixes, the entire water column must cool by on the order of 1°C before it will begin to stratify.

This can be examined in terms of the thermodynamic temperature change equation:

$$\frac{dT}{dt} = \frac{Q}{\rho c_p z} \quad \text{Equation 5.6}$$

Where  $Q$  is the heat flux into the water column,  $\rho$  is the density of water,  $z$  is the depth of the water column. In order to estimate the time it takes to cool the water column by 1°C, the equation can be discretized and rearranged:

$$\frac{\Delta t}{z} = \frac{\rho c_p \Delta T}{Q} \quad \text{Equation 5.7}$$

This can be estimated for the Great Lakes using a representative value for winter heat flux of 200 W m⁻² (Lofgren and Zhu 2000):

$$\frac{\Delta t}{z} = \frac{\left(1000 \frac{kg}{m^3}\right) \left(4180 \frac{J}{kg \cdot ^\circ C}\right) (1^\circ C)}{\left(200 \frac{W}{m^2}\right)} = 0.24 \frac{day}{m} \quad \text{Equation 5.8}$$

This suggests that for each additional meter of lake depth, it will take on the order of 0.24 days longer to cool to the point where it will stratify.

These scaling can be compared to the observed ice-on relationships in the Great Lakes. Relationships between air temperature and ice-on for each of the Great Lakes are shown in Figure 5.12, and their offsets are plotted as a function of average lake depth in Figure 5.13.

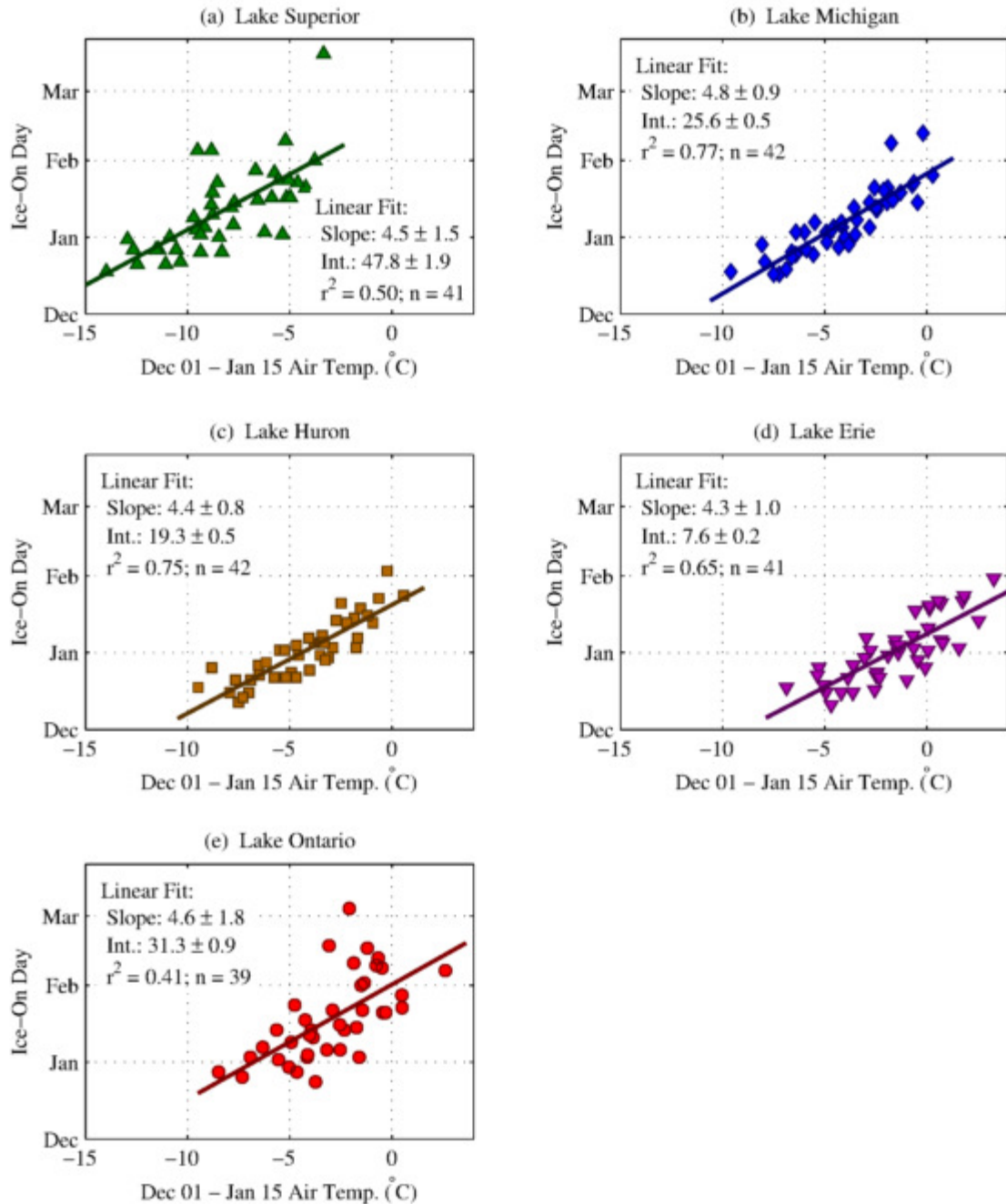


**Figure 5.12 – Ice-on date vs. December 1 through January 15 air temperature correlations.** The date of ice-on is plotted against December 1 through January 15 air temperature for each of the Great Lakes. Ice-on is defined as the first day of the season for which lakewide-average ice cover was at or above 10%, and there is a data point for all years in which lakewide-average ice cover surpassed that threshold from 1973 through 2014. A linear regression was performed on data points from each lake, and the results of those regressions are presented with 95% confidence intervals. Ice cover data is from the GLIA datasets for the winters of 1973 through 2005, and from the IMS datasets for the winters of 2006 through 2014. Air temperature data is from GHCN datasets for all years.

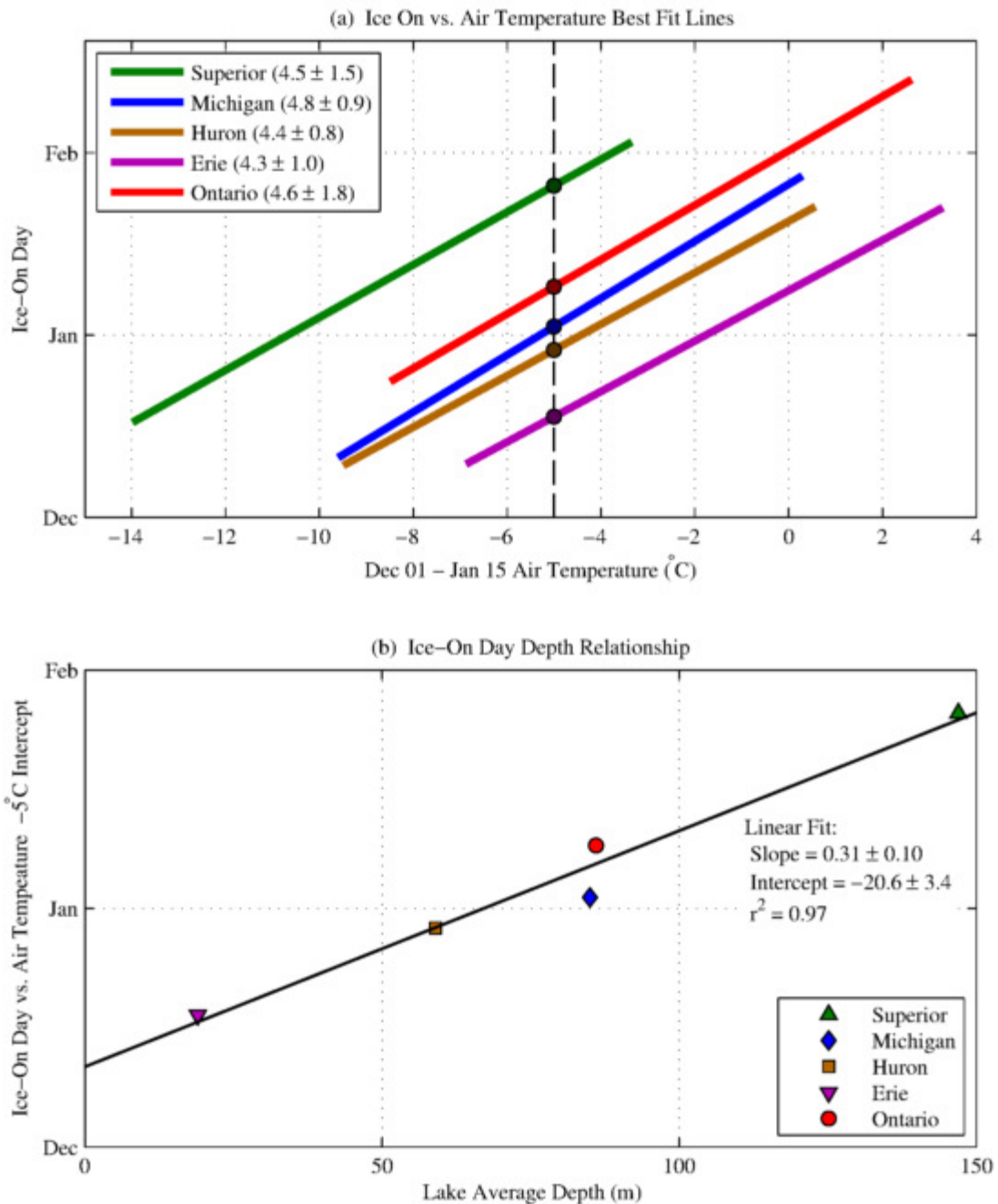


**Figure 5.13 – Ice-on date vs. Dec 1-Jan 15 air temperature correlation offset by lake depth.** (a) Best fit lines for the relationship between ice-on date and December 1 through January 15 air temperature, as presented separately in Figure 5.12, are plotted together for each of the Great Lakes. The  $-5^{\circ}\text{C}$  intercept is shown for each lake with a dot. The Horizontal (air temperature) boundaries of solid line represent the range of Dec 1-Jan 15 air temperatures observed in that lake. (b) The  $-5^{\circ}\text{C}$  intercept is plotted against average lake depth for each of the five Great Lakes, and a linear regression is presented for the relationship between predicted ice-on day at  $-5^{\circ}\text{C}$  and average lake depth.

The slopes of the least-squares fits between ice-on date and Dec 1-Jan 15 air temperature are remarkably similar, ranging from 4.3 day  $^{\circ}\text{C}^{-1}$  in Lake Erie to 4.8 day  $^{\circ}\text{C}^{-1}$  in Lake Michigan (Figure 5.12). These observed slopes are close to the sensitivity of 5.5 day  $^{\circ}\text{C}^{-1}$  predicted by Equation 5.5, suggesting that ice on dates can be largely explained in terms of air temperature phenology. In addition, the offsets of the best-fit lines show a very strong relationship with average lake depth ( $r^2=0.97$ ), with a slope of 0.31 day  $\text{m}^{-1}$ . This depth sensitivity is on the same order as the sensitivity predicted by Equation 5.8, suggesting that the depth-dependent duration of isothermal cooling is, in fact, a factor in dictating the timing of ice onset.

It is important to note that even after the lake begins to stratify, not all heat loss will go into ice formation. In Section 3.1, it was shown that a deep near- $0^{\circ}\text{C}$  surface mixed layer formed on Lake Superior during the high-ice winter of 2013-2014, and a similar deep, cold surface layer was observed during the moderate-ice winter of 2008-2009 (Titze and Austin 2014). This suggests that, in addition to the entire water column cooling to about  $3^{\circ}\text{C}$  and beginning to stratify, the surface will cool to near  $0^{\circ}\text{C}$  before ice cover forms. The depth of the thermocline can vary significantly from location to location in a lake (Figure 3.2), as well as from year to year (Titze and Austin 2014), and is therefore difficult to predict. The relationship between ice-on and air temperature is more consistent between the Great Lakes (Figure 5.12) than is the relationship between seasonal-average ice cover and air temperature (Figure 5.11) or the relationship between ice-off date and air temperature (not shown). One of the reasons for the more consistent relationship between ice-on and air temperature is likely that, given ice-on is defined here at the time that lakewide ice cover reaches 10%, ice-on depends mostly on ice conditions in the shallower, nearshore regions of the lakes, because that is where ice tends to form first. These regions of the lake will generally be sufficiently shallow in depth so as not to stratify, and therefore thermocline depth does not factor into the relationships. In contrast, seasonal-average ice cover and the timing of ice off are both influenced by the total amount of ice that forms throughout the lake, which would be influenced by thermocline depth.

## 5.4 Comparison to ice sensitivity in small lakes

So far in this section, I have examined the trend between ice cover and air temperature in a lakewide sense. Due to spatial heterogeneities in thermal structure within large lakes, it is generally not possible to treat the Great Lakes as monolithic entities, and one-dimensional

thermodynamic modeling on a lakewide scale is generally not appropriate. However, it may be possible to divide the lake into sections that can be modeled one-dimensionally and combine those models to estimate lakewide conditions. Specifically, if ice cover could accurately be modeled as a function of air temperature and water column depth, then it may be possible to model lakewide ice cover as a linear combination of separate one-dimensional models, based on the bathymetric curve of the lake.

To begin examining this idea, spatial variability in the sensitivity of ice cover to air temperature on the Great Lakes is examined, and compared the sensitivity relationships on smaller lakes. Smaller lakes have more spatially homogenous thermal structure, and can therefore be more accurately modeled one-dimensionally. This comparison is intended to examine whether shallow portions of the Great Lakes behave similarly to smaller inland lakes of similar depth, or whether those shallow Great Lakes regions behave fundamentally differently, due to influences from deeper, offshore portions of the lake.

I examine spatial variability in the sensitivity of ice cover to air temperature on the Great Lakes using the spatially resolved GLIA ice cover datasets (see Section 2.2.1). Separate linear regressions were performed with data from each individual 2.5-km GLIA grid point. Ensembles used for these regressions consisted of seasonal-average (Dec-May) ice cover at each GLIA grid point for the winters of 1973 through 2002, each regressed against the ensemble of winter (Dec-Feb) lakewide-average air temperature from the GHCN datasets (see Section 2.3.2). This results in a distinct linear best fit line between air temperature and ice cover for each grid point on the lakes. The slopes of these lines are shown in Figure 5.14, and the standard errors for the linear models are shown in Figure 5.15. A metric of ice-days is used to express ice cover at each point on the lake, which is an integrated metric expressing a point's average ice cover in terms of the equivalent number of 100% ice-covered days. For example, 8 days of 50% ice cover at a point would be expressed as 4 ice-days.

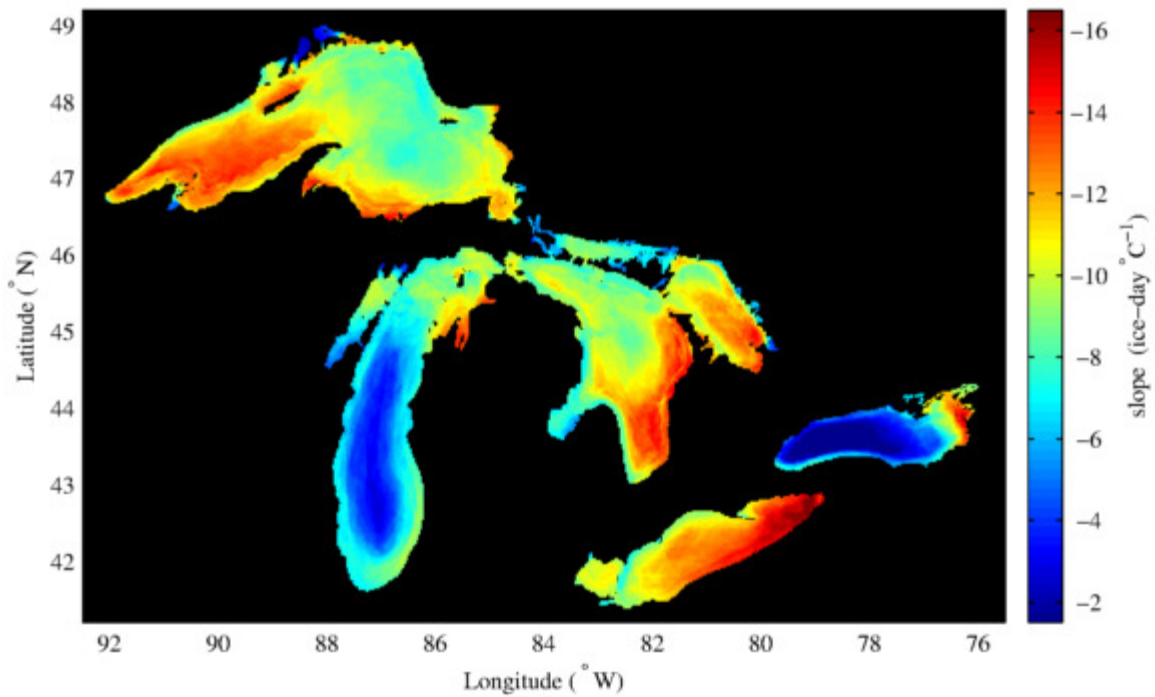


**Figure 5.14 – Spatial variability in ice sensitivity slope, Great Lakes.** Linear regressions between seasonal (Dec-May) ice cover and winter (Dec-Feb) air temperatures were performed separately for each grid points on the GLIA grid over the winters of 1973 through 2002 for each of the Great Lakes. The slopes of these regressions are shown for each grid point in the Great Lakes system. Ice cover is from the GLIA datasets and seasonal ice cover is expressed in terms of ice-days, which was calculated by integrating fractional ice cover over the December through May season. Air temperature data for corresponding years is from GHCN datasets.

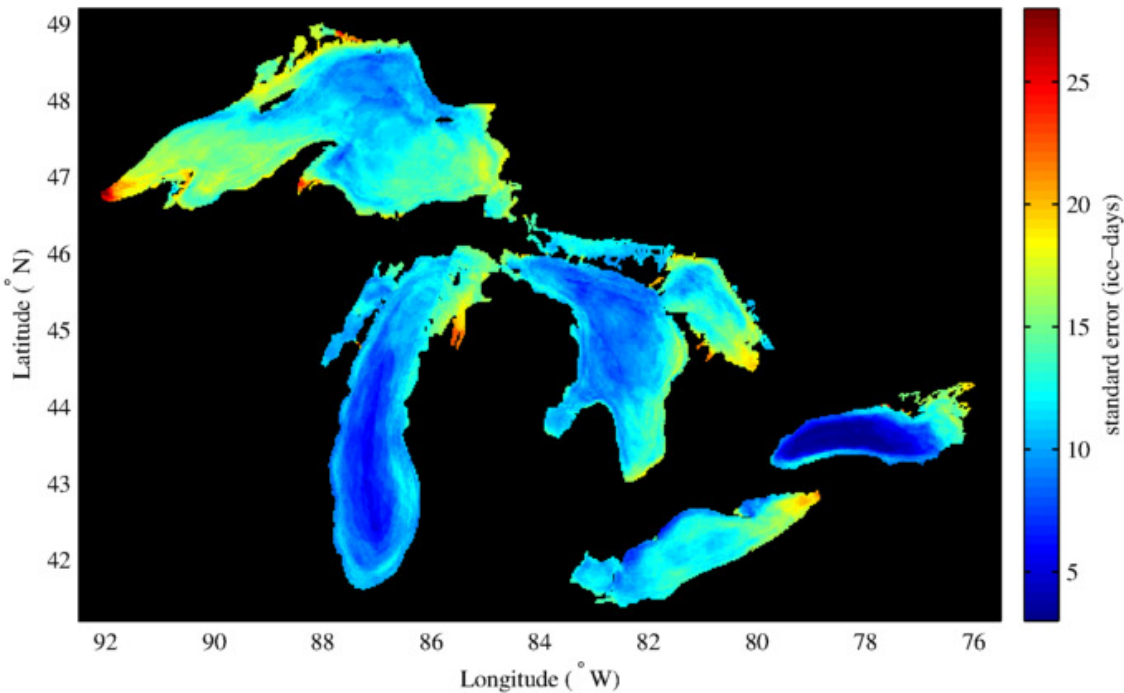


**Figure 5.15 – Spatial variability in ice sensitivity model accuracy, Great Lakes.** Linear regressions between seasonal (Dec-May) ice cover and winter (Dec-Feb) air temperatures were performed separately for each grid points on the GLIA grid over the winters of 1973 through 2002 for each of the Great Lakes. The accuracy (expressed in terms of standard error) of these regressions is shown for each grid point in the Great Lakes system. Ice cover is from the GLIA datasets and seasonal ice cover is expressed in terms of ice-days, which was calculated by integrating fractional ice cover over the December through May season. Air temperature data for corresponding years is from GHCN datasets.

The sensitivity of ice cover to air temperature in the Great Lakes (Figure 5.14) is qualitatively higher in areas experiencing higher annual-average ice cover throughout the Great Lakes System. This is true both in an inter-lake sense, with Lake Michigan and Lake Ontario showing lower sensitivity than Lake Superior, Lake Huron, and especially Lake Erie, and it is also true in an intra-lake sense, with higher-sensitivity regions in each lake generally corresponding to higher-ice regions. For example, the eastern basin of Lake Superior, which receives less ice than the western basin of the lake, shows lower sensitivity to air temperature than the western basin of the lake. Similarly, deeper, offshore portions of the lakes, which tend to form less ice, generally show lower sensitivities than shallower, near-shore regions. An exception to this is the particularly high sensitivity observed in the eastern portion of Lake Erie, which tends to be less icy than the western basin of the lake.

The standard error of the relationships (Figure 5.15) is generally higher in the longitudinal extremities of the lakes, in particular the eastern extremities of the lakes. An exception to this is on Lake Superior, for which the highest standard error is observed in the western extremities of the lake. It is likely that these difficult to predict areas are regions into where ice is commonly advected throughout the season. If that is the case, ice cover would also depend heavily on wind direction and therefore could not be accurately understood in terms of air temperature, alone.

This point-by-point regression method was used to compare the response of the shallow portions of the Great Lakes to comparably shallow smaller lakes. Ice phenology data for these smaller lakes was obtained from the National Snow and Ice Data Center (NSIDC) Global Lake and River Ice Phenology datasets (National Snow and Ice Data Center 2016), which contains ice-on and ice-dates for 865 lakes and rivers around the world. Lakes used in this analysis were limited to those in North America, because this allows for use of algorithmic determination of air temperature around the lake using the NARR reanalysis datasets (see Section 2.3.3). Air temperature was determined as the average December through February air temperature from the NARR monthly-average datasets using a two-dimensional interpolation scheme with the lake's listed longitude and latitude. The lakes were assumed to be 100% ice-covered between the date of ice-on and the date of ice-off, which is generally a reasonable assumption in smaller lakes, such as these (Kirillin et al. 2012). Under this assumption, ice duration is equivalent to ice-days on these smaller lakes.

Only lakes for which average lake depth was listed and was less than or equal to 10m were included, thereby controlling for depth. In all, 67 lakes were included in this analysis, and the locations of these lakes are shown in Figure 5.16. The lakes included in the analyses happen to be located at similar latitudes to the Great Lakes, and in relatively close proximity, which is simply a result of data availability. An ensemble of data points was assembled for each year of ice cover data available on each of the small lakes from the winters of 1980 through 2014, which are the years for which NARR reanalysis data is available. Ice cover was plotted against air temperature for this collection of data points and a linear regression was performed to determine the sensitivity of seasonal ice cover to winter air temperature on these smaller, shallow lakes.

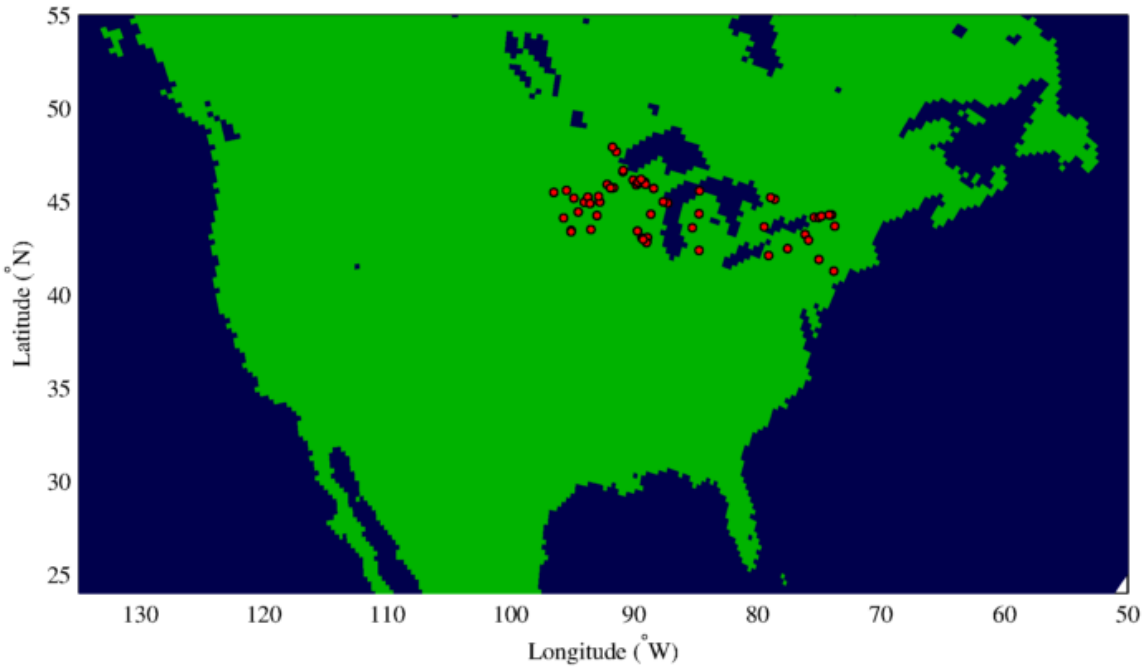


**Figure 5.16 – Locations of NSIDC North American lakes with mean depth less than 10 m.** North American lakes with mean depths less than or equal to 10m that have NSIDC ice phenology data available are shown.

For comparison to the relationship developed for these smaller lakes, seasonal ice cover vs. winter air temperature curves were developed for comparably shallow ( $\leq 10\text{m}$ ) regions on each of the Great Lakes. These relationships were developed by averaging the calculated slopes and intercepts of points with depths less than or equal to 10m, as determined by gridding the NCEI Great Lakes Bathymetry data (see Section 2.4) onto the GLIA ice grid. These shallow portions of the Great Lakes are highlighted in Figure 5.17. The regression for the small lakes, as well as the regions for shallow portions of the Great Lakes, are plotted together in Figure 5.18.

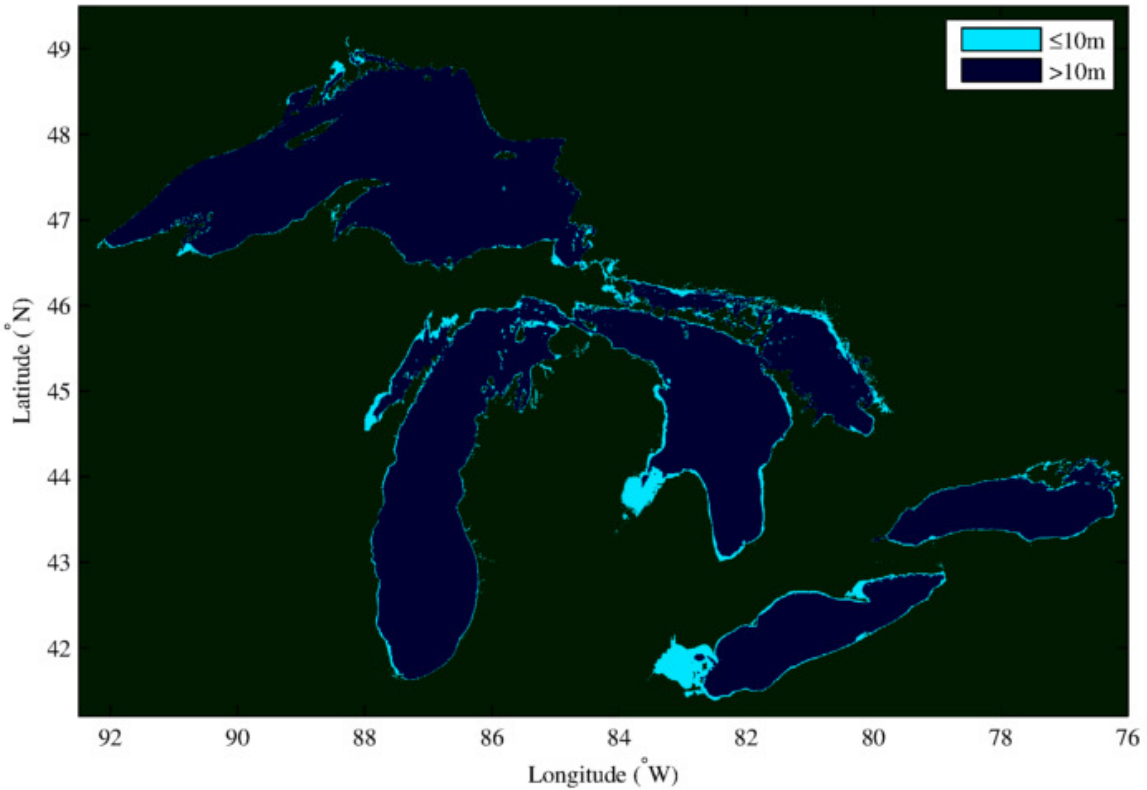


**Figure 5.17 – Portions of the Great Lakes with mean depth less than 10 m.** Portions of the Great Lakes with depths less than or equal to 10m are shown, based on data from the NCEI Great Lakes Bathymetry datasets.

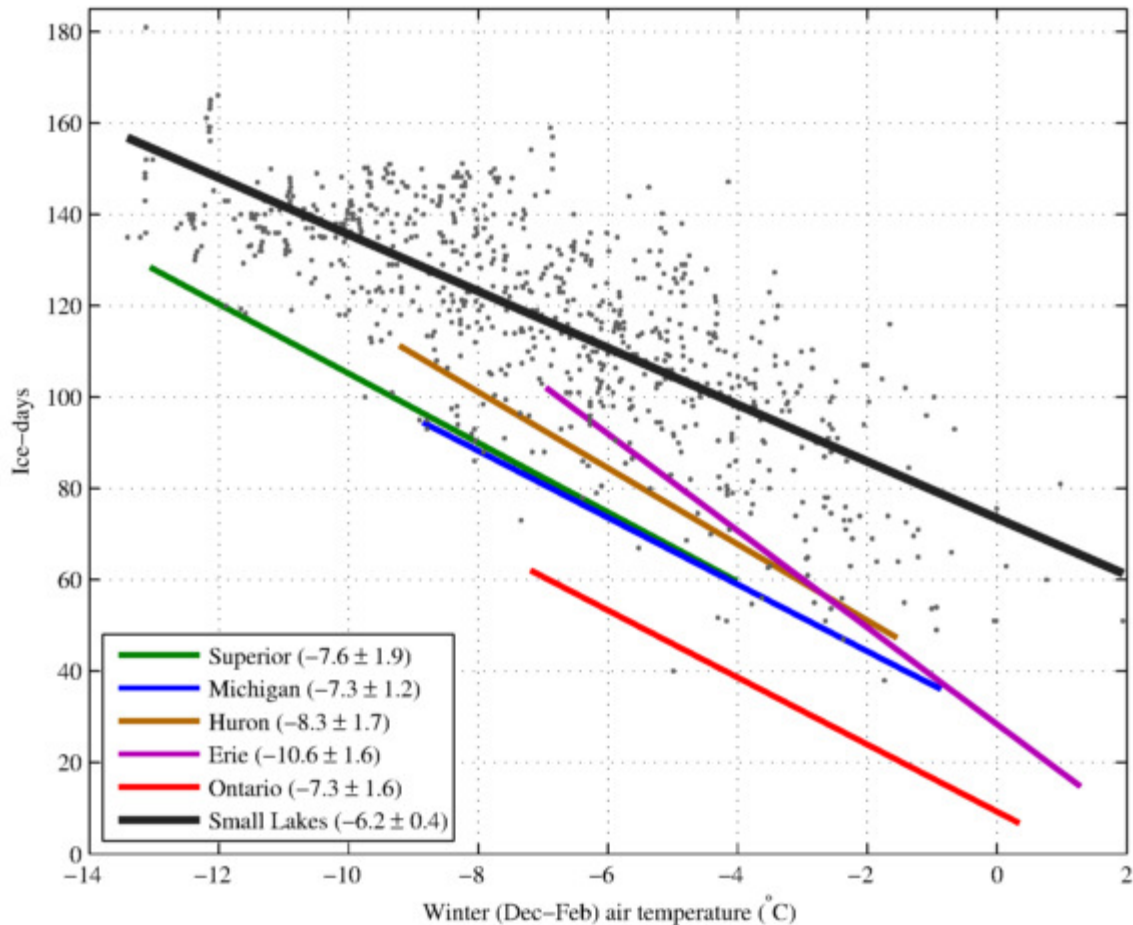


**Figure 5.18 – Ice-air temperature relationship, comparison with small lakes.** A curve showing the sensitivity of ice cover to winter (Dec-Feb) air temperature on a collection of small lakes ( $\leq 10\text{m}$  average depth) around North America is presented, and compared to the sensitivity relationship in shallow regions ( $\leq 10\text{m}$  depth) of the Great Lakes. Ice cover is expressed in terms of ice-days, which was calculated by integrating fractional ice cover over the December through May season in the Great Lakes for points with depths less than 10m, and was calculated as the number of days between ice-on and ice-off in small lakes. Slope are listed in units of ice-days  $^\circ\text{C}^{-1}$ . Great Lakes ice cover data is from GLIA datasets, small lakes ice cover data is the NSIDC Global Lake and River Ice phenology datasets, Great Lakes air temperature is from GHCN datasets, and small lakes air temperature was interpolated from NARR reanalysis datasets.

The sensitivity of seasonal ice cover to winter air temperature is similar in small lakes as it is in the Great Lakes, which demonstrates that ice cover in shallow regions of the Great Lakes responds similarly to air temperature as does ice cover in smaller, shallow lakes. There is a substantial offset between the curve for small lakes and the curves for the Great Lakes, indicating that while the sensitivity to air temperature is comparable in small lakes, those small lakes will generally experience more ice cover than regions on the Great Lakes of comparable depth. This is likely due to the fact that the Great Lakes form deep, near- $0^\circ\text{C}$  surface mixed layers prior to ice

formation (see Section 3.1), while on small lakes, ice tends to form over short time-scales when conditions are calm and cold, and the majority of the water column remains near the approximately 4°C temperature of maximum density (Jonas et al. 2003; Ellis et al. 1991).

Applying this idea to the principles discussed in Section 5.3, an estimate of the delay this additional local water column cooling would have on the ice season can be estimated by rearranging Equation 5.7:

$$\Delta t = \frac{\rho c_p \Delta T z}{Q} \quad \text{Equation 5.9}$$

If we use a representative value for winter heat flux in the Great Lakes region of 200 W m<sup>-2</sup> (Lofgren and Zhu 2000), and assume that the coastal regions of the Great Lakes must cool by an additional 4°C (from TMD to freezing) over the 10m water column:

$$\Delta t = \frac{\left(1000 \frac{kg}{m^3}\right) \left(4180 \frac{J}{kg \cdot ^\circ C}\right) (4^\circ C) (10m)}{\left(200 \frac{W}{m^2}\right)} \approx 10 \text{ day} \quad \text{Equation 5.10}$$

Equation 5.10 shows that a delay in the ice season on the order of 10 days could be explained by local cooling of the water column. Although on the same order of magnitude, the offset in the number of ice-days show in Figure 5.18 is actually on the order of a month, indicating that this mechanism does not completely account for the offset.

The remainder of the offset may be accounted for by a couple of factors. First of all, this delay only seeks to explain the delay in the onset of the ice season. Due to the ice-albedo feedback mechanism, high-ice conditions are conducive to sustained ice cover. As such, a delay in the onset of the ice season would be expected to have a compounding effect throughout the ice season, which is not accounted for in the scaling shown in Equation 5.10. Second, due to horizontal mixing, a portion of the negative surface heat flux occurring in the shallow regions of the Great Lakes would be expected to contribute to the cooling of deeper surrounding regions, which cool more slowly. This would result in a lower local cooling rate than the rate predicted by Equation 5.9, which does not account for advective processes. The extent to which influence from offshore regions affects cooling rates in shallow coastal regions would be determined by both the depth of those offshore regions, and the degree of horizontal interaction between

offshore regions and shallow coastal regions. Horizontal mixing processes in the Great Lakes are not well characterized, and the scales at which such mixing processes are important remain largely unknown.

Influence from offshore regions of the lake may also help explain, at least qualitatively, the offset in best-fit lines observed between shallow portions of the individual Great Lakes (Figure 5.18). In addition to the depth of those offshore regions, the influence that offshore regions of the lake will have on shallower coastal regions will depend on how well-connected those coastal regions are to the offshore regions on the lake. Specifically, more restricted shallow regions, such as embayments, would be expected to experience less influence from offshore regions than other coastal regions. Of the Great Lakes, shallow regions of Lake Erie tend to form more ice than shallow regions on the other lake. As shown in Figure 5.17, a large percentage of shallow points in Lake Erie are contained in the western basin on the lake, which is hydrologically somewhat restricted from the rest of the lake. Likewise, a large percentage of shallow points on Lake Huron are contained within the Saginaw Bay, which may help to explain why shallow regions of Lake Huron are shown to form more ice than shallow regions of Lake Superior, Lake Michigan, or Lake Ontario. Lake Superior has a smaller percentage of shallow points in Nipigon Bay, Black Bay, and Chequamegon Bay, and Lake Michigan has a smaller percentage of shallow points in Green Bay. Lake Ontario, which forms the least amount of ice in shallow regions, does not have any notable shallow embayments.

Advection of ice may also influence these relationships. In lakes that tend to form more offshore ice, such as Lake Erie, more offshore ice may be advected toward these shallow coastal regions than in lakes like Lake Michigan and especially Lake Ontario, which form relatively little offshore ice. This may play a role in the offsets observed in Figure 5.18, but probably not a dominant role, given the relatively low offset observed in Lake Superior and relatively high amount of lakewide ice that it forms (Figure 5.11). The fact that offshore regions of Lake Superior are much deeper than offshore regions of the other Great Lakes is likely at least partly responsible for its lower offset, based on the principles discussed above.

Ice advection may also be responsible for the higher sensitivity of ice cover to air temperature in shallow regions of Lake Erie than in shallow regions of the other Great Lakes or in smaller, shallow lakes (Figure 5.18). As noted above, much of the shallow portion of Lake Erie is contained in the somewhat restricted western basin. Given its shallow and restricted nature, this

tends to be the iciest region of Lake Erie (not shown). During higher ice years, associated with lower air temperatures, Lake Erie will be largely ice covered, possibly inhibiting advection due to a more restricted ice field. However, during lower ice years, associated with higher air temperatures, more advection of ice from the icy western basin to other parts of the lake may occur as a result of the less-restricted ice field. If this is the case, higher air temperatures could be implicated in a reduction of ice in the shallow western basin, both through decreased ice formation and through increased advection, and vice-versa for lower air temperatures. Such a feedback mechanism would result in an increased sensitivity to air temperature, as observed in (Figure 5.18). A similar feedback mechanism in Saginaw Bay may be responsible for the somewhat higher sensitivity to ice cover to air temperature in shallow regions of Lake Huron (Figure 5.18).

An important takeaway from this analysis is that ice cover in small, shallow lakes shows similar sensitivity to air temperature in shallow, coastal regions of the Great Lakes. While the absolute amount of ice that forms is different amongst lakes, the consistent sensitivity relationships between ice cover and air temperature is a promising step toward establishing a common mechanistic link between air temperature and ice cover that is applicable to all lake systems. Much of the difficulty involved in establishing such a relationship for the Great Lakes and much of the largely speculative discussion, above, speaks to the point that the Great Lakes cannot be treated as monolithic entities. The uncertainty associated with the horizontal processes speculatively toward above would likely be accounted for if a linear combination of points were analyzed in the Great Lakes. That is, ice cover in shallower coastal regions may be thermodynamically overestimated by ignoring the influence of the offshore portions of the lake, but ice in those offshore portions would be correspondingly underestimated by ignoring the influence of shallow regions.

However, although a linear combination method may account for uncertainty in horizontal advective processes, uncertainty in vertical thermal structure remains an issue. The reason that relationships between air temperature and ice cover are so consistent in shallow regions is likely due to the fact that the water column in these shallow regions remains isothermal throughout the winter. Thermal structure in offshore regions is more difficult to model, because of the deep, cold surface layers of variable depth that have been shown to form during the winter season (Figure 3.2; Titze and Austin 2014). The amount of heat loss necessary to cool these deep, cold layers is a non-negligible component of the heat budget that is not well-characterized, and is a

fundamental difference between small lakes and large lakes. The depth to which the thermoline forms likely depends on some combination of morphological and climatological parameters, and must be better characterized before offshore portions of the Great Lakes can be accurately modeled in a one-dimensional sense.

## 5.5 Numerical Modeling Sensitivity Analyses

Ice sensitivity modeling was conducted using the Lake Superior application of the ROMS three-dimensional hydrodynamic numerical model as a supplement to the observational ice sensitivity analyses. This application of the ROMS model was developed by White et al. (2012) and improved upon by Matsumoto et al. (2015). This model, including the baseline forcing parameters used, is discussed in Section 2.6. These modeling exercises are a useful addition to the data-driven analyses presented throughout this section, because they provide a prognostic assessment of the sensitivity of ice cover to air temperature. This is distinct from observational studies, which take a diagnostic approach to the question, and must rely on the assumption that variability in air temperature, for example, is reasonably independent from other influences on ice cover. Modeling allows for a more controlled approach, in which a single forcing parameter can be modified, such as air temperature or depth, while holding all other factors constant.

Modeled ice cover from the 1980-2014 baseline run (Figure 2.37a) was plotted against air temperature forcing to understand the extent to which the empirical relationships between ice cover and air temperature found earlier in this section are reproduced by the model. First, comparisons are made between seasonal-average (Dec-May) air temperature and seasonal-average (Dec-May) ice cover for the years in which observed GLIA/IMS ice cover was greater than 10% (as in Figure 5.1), and these model results are shown in Figure 5.19a. Second, comparisons are made between winter-average (Dec-Feb) air temperature and seasonal-average (Dec-May) ice cover for all years 1980-2014 (as in Figure 5.11a), and these model results are shown in Figure 5.19b.

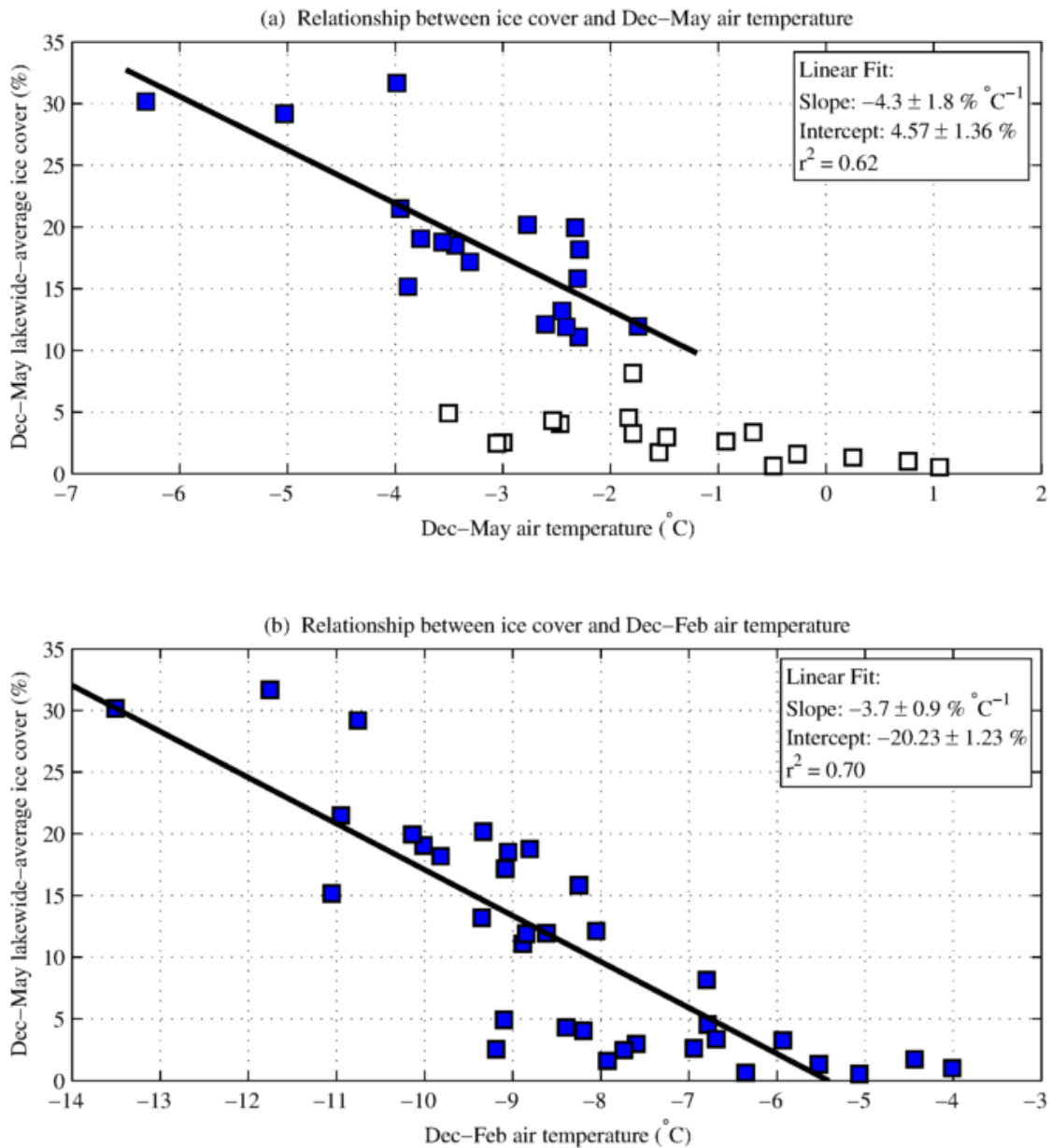


**Figure 5.19 – Modeled sensitivity of ice cover to air temperature, 1980-2014 base run.** Seasonal-average (Dec-May) ice cover are regressed against (a) Dec-May forced air temperature for points with season-average ice cover greater than 10% (as in Figure 5.1), and (b) Dec-Feb air temperatures for all points (as in Figure 5.11).

The model shows lower sensitivity of ice cover to air temperature than do the observational empirical relationships, based on the both the relationship between Dec-May air temperature (Figure 5.1 compared to Figure 5.19a) and between Dec-Feb air temperature (Figure 5.11a compared to Figure 5.19b). It is possible that there is a positive feedback mechanism between air

temperature and other meteorological factors conducive to increased ice formation that is experienced by the lake but controlled for in the model; however, it is more likely that this lower sensitivity is simply associated with the model's tendency to underpredict ice cover (Figure 2.37). Teasing apart and quantifying any such feedback mechanisms should be an important component of future modeling work, as the model's capability to predict ice is improved. However, given the current performance of the model, these baseline results suggest that it is best to treat the results of the sensitivity simulations presented in this section as qualitative.

A seasonal sensitivity analysis was conducted, in which air temperatures from the August through July period surrounding the winter season were adjusted by amounts ranging from -10°C to +10°C in 1°C intervals in order to examine the effects of seasonal air temperature anomalies on seasonal-average ice cover. In each case, a spin-up period of January 1979 through July 1984 was used, and the August through July adjustment was applied over the 1984-1985 season, holding other all other forcing parameters, except longwave radiation, constant. The well-characterized relationship between air temperature and longwave radiation was accounted for, following Equation 2.7 (Austin and Allen 2011). The 1984-1985 season was chosen for these sensitivity analyses because it is a moderate ice-cover year that shows reasonably good agreement with observed data. Results of this seasonal sensitivity analysis are presented in Figure 5.20.

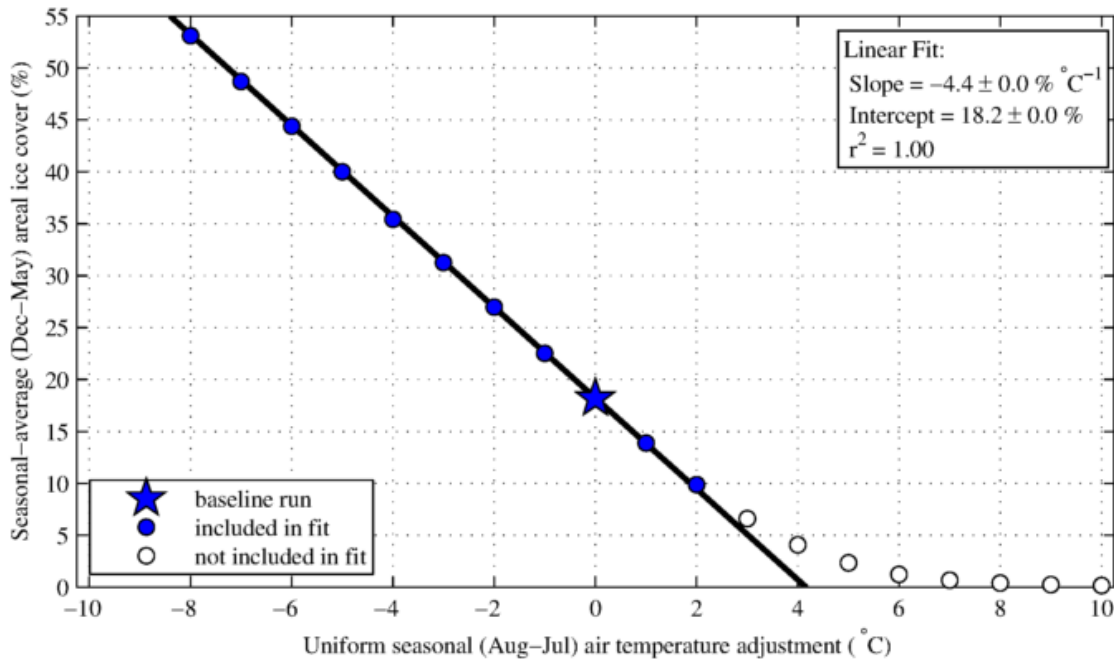


**Figure 5.20 – Ice cover sensitivity analysis with seasonal air temperature.** Modeled ice cover is plotted as a function of the magnitude of the seasonal (Aug-Jul) air temperature adjustment applied. A linear best fit line for the points visually determined to fall within the linear regime of conditions is presented.

The sensitivity analysis shown in Figure 5.20 shows a very clear linear response of ice cover to air temperature over a wide range of conditions. As discussed above, it is not believed to be appropriate to quantitatively analyze this results; however, the clear linear relationship demonstrates that there is a deterministic linear relationship between air temperature and ice cover on Lake Superior. This is consistent with the strong linear correlation between air temepature and ice cover in observational data (Figure 5.11).

Next, a sensitivity analysis was conducted to examine the sensitivity of seasonal average ice cover to air temperature anomalies at different times of the year. Air temperatures for each month of the year were varied by amounts of  $-4^{\circ}\text{C}$ ,  $-2^{\circ}\text{C}$ ,  $-1^{\circ}\text{C}$ ,  $+1^{\circ}\text{C}$ ,  $+2^{\circ}\text{C}$ , and  $+4^{\circ}\text{C}$ , starting in July in the year leading up to the ice season and ending with the June following the ice season. Again, a spin-up period of January 1979 through July 1984 was used, and all other forcing parameters were held constant, except longwave radiation, which was adjusted according to Equation 2.7. Seasonal-average (Dec-May) areal ice cover was calculated for each of these runs to determine the months in which ice cover anomalies have the greatest effect on seasonal-average ice cover. These results are presented in Figure 5.21.

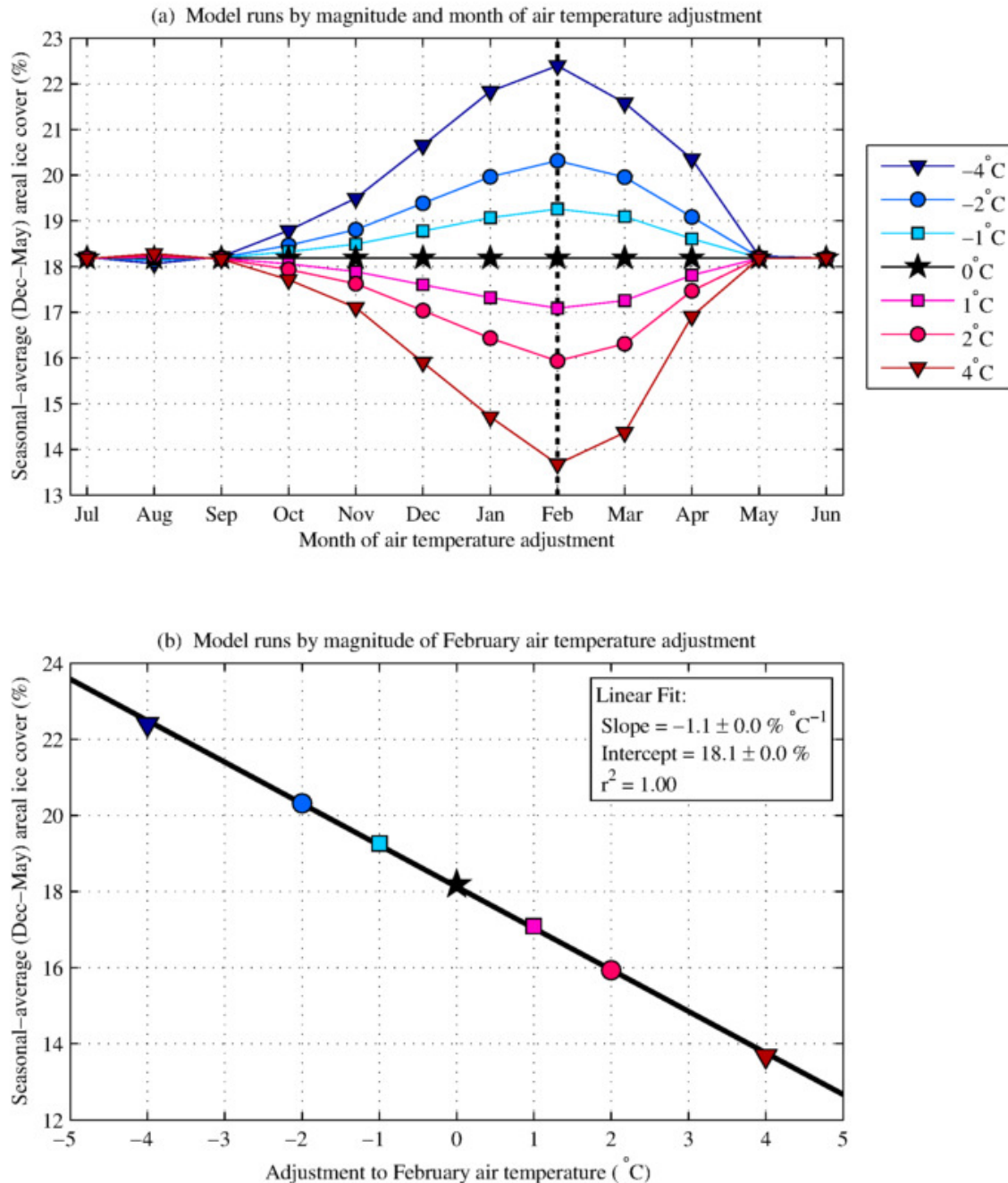


**Figure 5.21 – Ice cover sensitivity analyses with monthly air temperature.** (a) Modeled ice cover is plotted as a function of the month in which a monthly air temperature adjustment was applied, and separate lines are shown for different magnitudes of monthly air temperature adjustments. Air temperature adjustments were applied for each month of the year, beginning with July leading up to ice season and ending with June following the ice season. (b) Modeled ice cover is plotted as a function of the February monthly air temperature adjustment, and a linear best fit relationship is shown.

The results of the sensitivity analysis shown in Figure 5.21a demonstrate that monthly air temperature anomalies applied in February have the greatest impact on the amount of seasonal-average ice cover that forms. Air temperature anomalies in January and March are also shown to have a large influence on seasonal-average ice cover, and the influence of air temperature anomalies in other months declines as anomalies occur farther outside of this range. Air temperature anomalies occurring in September or earlier, as well as those occurring in May or later, are shown to have essentially no impact on the amount of seasonal-average ice cover that forms. These results are largely consistent with the empirical analyses conducted in Section 5.2, although the months shown to be important in the model (January through March) are skewed approximately a month later from the months found to be important through observational data (December through February). This may be due to the fact that model, in addition to underpredicting ice, tends to produce a somewhat delayed ice signal from that observed in the GLIA and IMS datasets (not shown). A delayed ice signal in the model has been previously acknowledged, and is likely due, at least in part, to the fact that the model was originally developed and calibrated to better model summer conditions in the lake (Katsumi Mastumoto, personal communication).

Modeled ice cover was plotted as a function of the February air temperature adjustment (Figure 5.21b) to examine the ice sensitivity to air temperature during the month shown to have the greatest impact on seasonal-average ice cover. Similar to the seasonal sensitivity analysis (Figure 5.20), seasonal-average ice cover shows a clear linear response to February air temperature. Based on the magnitude of slopes shown in Figure 5.20 and Figure 5.21b, about 25% of the impact that a longer-term seasonal air temperature anomaly has on ice cover can be generated by adjusting February air temperature, alone.

Finally, a sensitivity analyses was conducted to examine the influence of lake depth on the amount of seasonal average ice cover that forms. For this analysis, lake depth at every point on the ROMS grid was adjusted by a constant multiplication factor. Multiplication factors of  $2^{-1}$ ,  $1.5^{-1}$ ,  $1.25^{-1}$ ,  $1.1^{-1}$ , 1.1, 1.25, 1.5, and 2 were used. In each case, a spin-up period of 1979 through 1984 was used with the depth-adjustment factor applied throughout that spin-up period, and baseline model forcing was used in all runs. Seasonal-average ice cover was examined over the 1984-1985 winter season for each of the depth adjustment runs, and results of this analysis are presented in Figure 5.22.

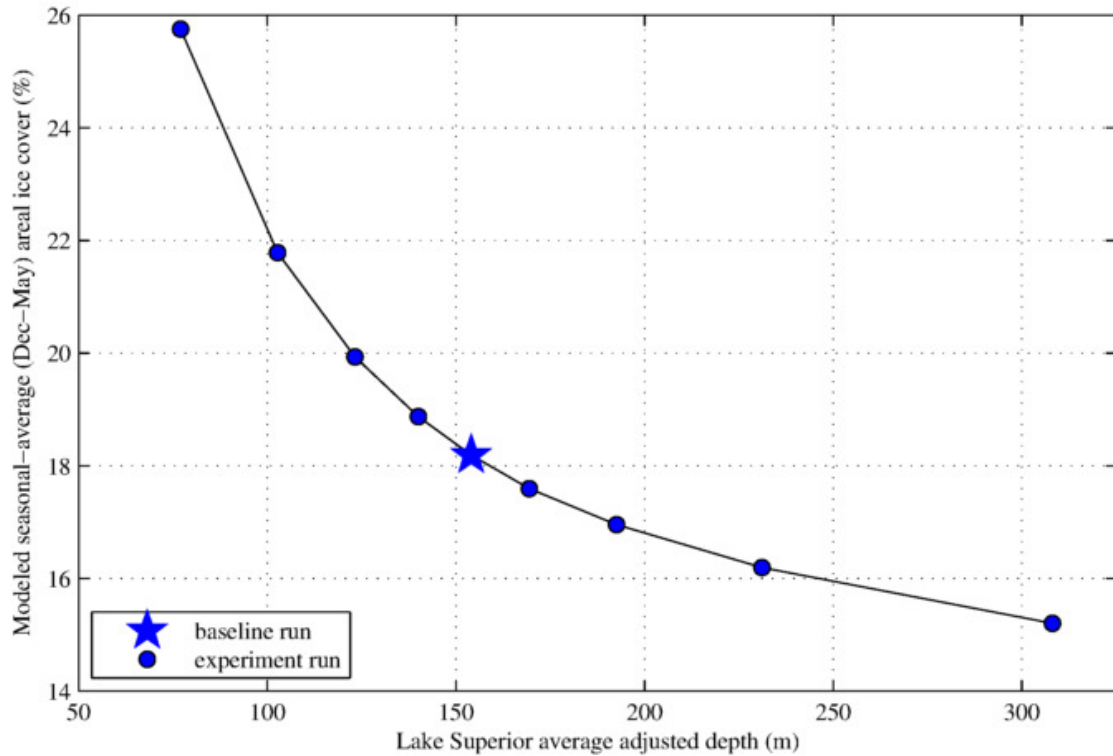


**Figure 5.22 – Ice cover sensitivity analysis with lake depth adjustment.** The amount of seasonal-average (Dec-May) ice cover is plotted as a function of average lake depth. Average lake depth was varied by stretching the depth of the Lake Superior grid by a constant multiplication factor for these runs.

The results of the depth adjustment runs show a non-linear relationship between lake depth and ice cover. This nonlinear relationship is such that as the lake becomes deeper, adjustments to depth have less of an impact on ice formation than adjustments made to lakes of smaller depth. This would follow from the idea that as the depth of the lake increases, the depth of the thermocline does not increase proportionally. As discussed previously, thermal structure in Lake Superior is such that the entire water column generally cools to a temperature near 3°C, and then the surface mixed layer cools to a temperature near 0°C and ice forms. In shallow regions of the lake, which are of comparable or shallower depth than the depth of the thermocline, a depth adjustment will affect both the depth of the water column that will cool to 3°C and the depth of the water column that will cool to 0°C. Meanwhile, in deeper regions of the lake, a depth adjustment will affect only the depth of the water column that will cool to 3°C. Because, throughout the lake, the entire water column cools to near 3°C, the portion of the water column that must cool to 3°C increases proportionally with average lake depth. However, the portion of the water column that cools to near 0°C depends on the bathymetry of the lake, specifically with

regard to the volume of water associated with regions of depths comparable or shallower to the thermocline. This could lead to this nonlinear response of ice cover to adjustments in overall lake depth.

## 5.6 Conclusion

While the results of this section are not tied together by a central narrative, many important conclusions are reached, which can likely be expanded upon in future analyses. Ice cover is shown to exhibit a strong linear sensitivity to air temperature. Upwards of 70% of ice cover variability on all of the Great Lakes can be explained in terms of air temperature, alone, and nearly 90% of ice cover variability can be explained in some lakes (Figure 5.11). In addition, the sensitivity to air temperature is shown to be quite high, and the difference in seasonally-averaged (Dec-May) air temperature between a low ice year and a moderate to high ice year is on the order of a couple degrees Celsius, particularly on Lake Superior, Lake Huron, and Lake Erie (Figure 5.2).

The total amount of ice that forms in during the winter was found to be most influenced by air temperatures during the period contemporaneous with ice formation, from about December through February (Figure 5.7; Figure 5.10; Table 5.2). Air temperature conditions during the pre-winter conditioning period and during the spring melting period were found to have less of an impact on seasonal-average ice cover (Figure 5.7). This is likely due to the fact that there is a negative feedback mechanism when heat loss goes toward cooling the lake, but a positive feedback mechanism when heat loss goes toward ice formation. Ice-on date is best correlated with air temperatures from early in the ice season, from about December 1 through January 15 (Figure 5.8; Table 5.2). These relationships between air temperature and ice on were found to be remarkably consistent in all of the Great Lakes (Figure 5.13), and it was shown that the relationships can be explained mechanistically through air temperature phenology and average lake depth.

Ice cover sensitivity relationships were compared between shallow coastal regions of the Great Lakes and similarly shallow smaller, inland lakes. It was found that the sensitivity to air temperature was quite similar between these coastal regions and smaller lakes, but that the absolute amount of ice that forms varies significantly between small lakes and the Great Lakes, and amongst the Great Lakes, themselves. The similarity in sensitivity relationships between

such vastly different systems is seen as a promising step toward a unified mechanistic framework linking air temperature to ice cover; however, the significant differences in absolute ice formation remains to be explained. Many possible mechanisms for these differences are speculated upon, and it is believed that a better understanding of the factors influencing thermocline depth and temperature are necessary before lakewide ice cover can be accurately modeled using a simplistic one-dimensional framework.

A next step toward this understanding should begin with a closer look at the available mooring data from the outer moorings (see Section 2.1), particularly from the moderate ice-cover year of 2008-2009, to gain a better understanding of the spatial variability in thermocline depth and the factors that may drive it. In addition, using this mooring data to calibrate and validate a hydrodynamic model that accurately reproduces and predicts conditions on Lake Superior would be help in examining this problem in a more highly-resolved and controlled sense. A first step toward an improved model could focus on understanding why ice cover is underpredicted on the lake by the current application of the ROMS model, despite calibrating forcing parameters to observed values.

Finally, the application of the ROMS three-dimensional hydrodynamic numerical model on Lake Superior (White et al. 2012; Matsumoto et al. 2015) was used to examine ice sensitivity. The model verifies a deterministic linear relationship between air temperature and ice cover, which is strongest around the timespan of ice formation. When the Lake Superior bathymetry is vertically stretched, average lake depth is shown to have a nonlinear relationship with seasonal-average ice cover, and this nonlinearity may be associated with a nonlinear increase in the lakewide volume of the suface mixed layer when the lake is streched.

## 6.0 Conclusion

This dissertation makes progress toward our understanding of a variety of aspects of ice cover on the Great Lakes, including the influence of ice cover on surface and subsurface lake processes, the characteristics and dynamics the ice cover, and the sensitivity of Great Lakes ice to climate. Ice cover, and winter conditions in general, remain under-represented topics in large lakes research, despite ice being a defining characteristic of these Great Lakes systems.

Ice cover was shown to influence surface currents in the western arm of Lake Superior, which is a phenomenon that has previously not been discussed in Great Lakes literature, but may be an important driver of heat redistribution in the lake. This assertion is based on simultaneous measurements of currents and thermal structure at the Western Mooring during the 2013-2014 winter, where there was a gradual rise in the thermocline throughout the winter season, coincident with a shift in currents observed at the time of ice formation. The mechanism driving this shift in currents, as well as the extent of its influence, cannot be resolved with available data. It is suggested that these questions would best be resolved through a focused mooring array in the western arm of lake superior and/or through hydrodynamic modeling. The application of the ROMS model used in this dissertation under-predicts ice cover and does not reproduce the shift in currents observed during the 2014-2015 winter. As such, improvement in the model's ability to accurately model ice cover on the lake will be essential toward modeling this phenomenon.

In Section 5.0 , measurements of ice drift and deep ice keels were presented from Lake Superior, which are the first observations of their kind in the Great Lakes. Ice drift measurements help put the ice regime of Lake Superior in perspective, showing that even during the record-high ice year of 2013-2014, ice on Lake Superior was predominately free-drifting. This demonstrates that ice cover on Lake Superior, broadly speaking, has more in common with free drifting ice in the oceans than is does with ice cover on smaller, inland lakes. Remarkably deep ice keels of over 11m depth were observed throughout the lake, and these ice keels are believed to comprise a significant percentage of the total lakewide ice cover, based upon the temporal frequency at which they are observed. The presence and prevalence of these ice keels will likely be of interest to entities involved with lake navigation, and are likely a non-negligible component of the lakewide heat budget. Due to the methods used, only deep ice keels could be detected, and further characterization of these ice keels is warranted, either through use of ice profiling sonars, or through intentional shallow deployment of pressure sensors. Lagrangian measurements of ice

drift are technically difficult to obtain, but would also be useful toward understanding the movement patterns of these keels.

Lastly, ice cover sensitivity relationships were examined in Section 66.0 . The impact that seemingly small changes in air temperature can have on the Great Lakes is put into perspective by demonstrating that a difference in seasonal-average air temperature on the order of 1 or 2 °C can be the difference between a winter with moderate to high ice cover and a winter with very low ice. In addition, it was found the air temperatures during December through February, which roughly corresponds to the interval of ice formation, have the greatest impact in seasonal ice cover. Air temperatures leading up to the winter and those during the ice melting phase have much less impact on ice extent. Ice-on dates were found to be influenced by air temperatures during the very early portion of the ice season, while ice off dates depending on temperatures throughout the whole winter. Modeling sensitivity analyses confirm a linear deterministic relationship between air temperature and ice cover, and corroborate the ice formation period as the time of year when air temperatures have the most influence on seasonal ice cover.

Ice cover in shallow portions of the Great Lakes is shown to have similar sentivity to ice in smaller shallow, inland lakes, which is seen as a promising result toward establishing a unified mechanistic framework linking air temperature to ice cover. However, offshore portions of the Great Lakes remain difficult to model, largely to due uncertainties in the factors dictating thermocline depth. Deep, near-0°C surface layers are observed in open water portions of the lake during seasons when ice cover forms, which represent a non-negligible component of the heat budget. In order to estimate the portion of the heat budget that is available for ice formation, the portion of the heat budget that goes toward cooling the surface layer must be better characterized. A starting point for such further analysis should start with a closer look at Lake Superior mooring data from years when all seven moorings were deployed to better understand spatial variability in thermocline depths within the lake. Improved hydrodynamic modeling, including validating the model with mooring data and determining how to better reproduce ice conditions, would also be useful toward this goal.

In summary, the observations of ice-induced shift in currents and corresponding redistribution heat depict an aspect of ice cover that is not addressed within the Great Lakes community, and which could have important biogeochemical implications, such as the distribution of oxygen or nutrients. The observations of deep ice keels on the Great Lakes help illustrate the remarkable

scale of ice processes on Lake Superior, while observations of ice drifts help emphasize the ice regime of Lake Superior, showing that even in the iciest of years, the lake does not “freeze over” in the sense that smaller lakes do. Finally, analyses of ice cover and air temperature demonstrate just how sensitivity the Great Lakes are to small variations in climate, and a comparison to ice cover on smaller lakes provides evidence that the mechanisms driving this sensitivity are mechanistically similar between a wide variety of lake systems. Many of the observations discussed within this dissertation cannot yet be fully explained, and while much additional work on these topics remain, the results presented and discussed herein represent several important steps toward our understanding of very complex nature of ice cover on the Great Lakes.

## 7.0 Bibliography

- Aslamov, I. A., V. V. Kozlov, G. B. Kirillin, I. B. Mizandrontsev, K. M. Kucher, M. M. Makarov, A. Yu Gornov, and N. G. Granin. 2014. Ice–water heat exchange during ice growth in Lake Baikal. *Journal of Great Lakes Research* 40(3): 599-607.
- Assel, R. A. 1976. Great Lakes ice thickness prediction. *Journal of Great Lakes Research* 2(2): 248-255.
- Assel, R. A. 1991. Implications of CO<sub>2</sub> global warming on Great Lakes ice cover. *Climatic Change* 18(4): 377-395.
- Assel, R.A. 2003. An Electronic Atlas of Great Lakes Ice Cover. NOAA Great Lakes Ice Atlas, Great Lakes Environmental Research Laboratory, Ann Arbor, Michigan 48105.
- Assel, R. A. 2005. Great Lakes ice cover climatology update: Winters 2003, 2004, and 2005. NOAA Technical Memorandum GLERL-135. NOAA Great Lakes Environmental Research Laboratory. [http://www.glerl.noaa.gov/ftp/publications/tech\\_reports/glerl-135/](http://www.glerl.noaa.gov/ftp/publications/tech_reports/glerl-135/)
- Austin, J. A., and J. Allen. 2011. Sensitivity of summer Lake Superior thermal structure to meteorological forcing. *Limnology and Oceanography* 56(3): 1141-1154.
- Austin, J. A., and S. M. Colman. 2007. Lake Superior summer water temperatures are increasing more rapidly than regional air temperatures: A positive ice-albedo feedback. *Geophysical Research Letters* 34(6).
- Banks, C. J., M. A. Brandon, and P. H. Garthwaite. 2006. Measurement of sea-ice draft using upward-looking ADCP on an autonomous underwater vehicle. *Annals of Glaciology* 44(1): 211-216.
- Belliveau, D. J., G. L. Bugden, B. M. Eid, and C. J. Calnan. 1990. Sea ice velocity measurements by upward-looking Doppler current profilers. *Journal of Atmospheric and Oceanic Technology* 7(4): 596-602.
- Bengtsson, L. 2011. Ice-covered lakes: environment and climate- required research. *Hydrological Processes* 25: 2767-2769.
- Bennington, V., G. A. McKinley, N. Kimura, C. H. Wu. 2010. The general circulation of Lake Superior: mean, variability, and trends from 1979–2006. *Journal of Geophysical Research* 115(C12).
- Benson, B. J., J. J. Magnuson, O. P. Jensen, V. M. Card, G. Hodgkins, J. Korhonen, D. M. Livingstone, K. M. Stewart, G. A. Weyhenmeyer, and N. G. Granin. 2012.

- Extreme events, trends, and variability in Northern Hemisphere lake-ice phenology (1855–2005). *Climatic Change* 112(2): 299-323.
- Björk, G., C. Nohr, B. G. Gustafsson, and A. E. Lindberg. 2008. Ice dynamics in the Bothnian Bay inferred from ADCP measurements. *Tellus A* 60(1): 178-188.
- Blanken, P. D., C. Spence, N. Hedstrom, and J. D. Lenters. 2011. Evaporation from Lake Superior: 1. Physical controls and processes. *Journal of Great Lakes Research* 37(4): 707-716.
- Budgell, W. P. 2005. Numerical simulation of ice-ocean variability in the Barents Sea region. *Ocean Dynamics* 55(3-4): 370-387.
- Chapman, R. P., and H. D. Scott. 1964a. Surface backscattering strengths measured over an extended range of frequencies and grazing angles. *The Journal of the Acoustical Society of America* 36(9): 1735-1737.
- Chapman, R. P., and H. D. Scott. 1964b. Backscattering strength of young sea ice. *The Journal of the Acoustical Society of America* 36(12): 2417-2418.
- Chen, C. T. A., and F. J. Millero. 1986. Thermodynamic properties for natural waters covering only the limnological range. *Limnology and Oceanography* 31(3): 657-662.
- Clites, A. H., J. Wang, K.B. Campbell, A. D. Gronewold, R. A. Assel, X. Bai, and G. A. Leshkevich. 2014. Cold Water and High Ice Cover on Great Lakes in Spring 2014. *Eos Transactions AGU* 95: 305-306.
- Coats, R., Perez-Losada, J., Schladow, G., Richards, R. and C. Goldman. 2006. The warming of lake Tahoe. *Climatic Change*, 76(1-2): 121-148.
- Cordeira, J. M., and N. F. Laird. 2008. The influence of ice cover on two lake-effect snow events over Lake Erie. *Monthly Weather Review* 136(7): 2747-2763.
- Cox, C., and W. Munk. 1954. Measurement of the roughness of the sea surface from photographs of the sun's glitter. *Journal of the Optical Society of America* 44(11): 838-850.
- Croley, T. E., & Assel, R. A. 1994. A one-dimensional ice thermodynamics model for the Laurentian Great Lakes. *Water resources research* 30(3): 625-639.
- Ellis, C. R., H. G. Stefan, and R. Gu. 1991. Water temperature dynamics and heat transfer beneath the ice cover of a lake. *Limnology and Oceanography* 36(2): 324-334.
- Emery, W.J., and R.E. Thomson. 2001. Data analysis methods in physical oceanography. Elsevier Science Ltd.

- Fujisaki, A., J. Wang, H. Hu, D. J. Schwab, N. Hawley, and Y. R. Rao. 2012. A modeling study of ice–water processes for Lake Erie applying coupled ice-circulation models. *Journal of Great Lakes Research* 38(4): 585-599.
- Gerbush, M. R., D. A. Kristovich, and N. F. Laird. 2008. Mesoscale boundary layer and heat flux variations over pack ice-covered Lake Erie. *Journal of Applied Meteorology and Climatology* 47(2): 668-682.
- Giordano, N. J. 2012. College Physics, Volume 1, Second Edition. Brooks Cole.
- Glover, D.M., W. J. Jenkins, and S.C. Doney. 2011. Modeling Methods for Marine Science. Cambridge University Press.
- Google Earth. 2015. Google Earth World Image, Data: SIO, NOAA, U.S. Navy, NGA, GEBCO, Image: Landsat, Image: IBCAO. <https://www.google.com/earth/>
- Gordon, R. L. 1996. Acoustic Doppler Current Profilers Principles of Operation: A Practical Primer. RD Instruments.
- Gronewold, D. 2015. Impacts of extreme 2013-2014 winter conditions on Lake Michigan's fall heat content, surface temperature, and evaporation. *Geophysical Research Letters* 42: 3364-3370.
- Hampton, S. E., Izmest, E., Lyubov, R., Moore, M. V., Katz, S. L., Dennis, B., and E. A Silow. 2008. Sixty years of environmental change in the world's largest freshwater lake—Lake Baikal, Siberia. *Global Change Biology*, 14(8), 1947-1958.
- Hastenrath, S. L. 1968. Estimates of the latent and sensible heat flux for the Caribbean Sea and the Gulf of Mexico. *Limnology and Oceanography* 13(2): 322-331.
- Hedström, K.S. 2009. Technical manual for a coupled sea–ice/ocean circulation model (version 3). OCS Study MMS 2009–062.
- Hsu, S. A., E. A. Meindl, and D. B. Gilhousen. 1994. Determining the power-law wind-profile exponent under near-neutral stability conditions at sea. *Journal of Applied Meteorology* 33(6): 757-765.
- Izmost'eva, L.R., Moore, M.V., Hampton, S.E., Ferwerda, C.J., Gray, D.K., Woo, K.H., Pislegina, H.V., Krashchuk, L.S., Shimaraeva, S.V, and E.A. Silow. 2016. Lake-wide physical and biological trends associated with warming in Lake Baikal. *Journal of Great Lakes Research* 42(1): 6-17.

- Jonas, T., A. Y. Terzhevik, D. V. Mironov, and A. Wüest. 2003. Radiatively driven convection in an ice-covered lake investigated by using temperature microstructure technique. *Journal of Geophysical Research: Oceans* 108(C6).
- Kirillin, G., M. Leppäranta, A. Terzhevik, N. Granin, J. Bernhardt, C. Engelhardt, T. Efremova, S. Golosov, N. Palshin, P. Sherstyankin, and G. Zdrovovenova. 2012. Physics of seasonally ice-covered lakes: a review. *Aquatic sciences* 74(4): 659-682.
- Leppäranta, M. 2008. The drift of sea ice. Springer-Verlag.
- Leshkevich, G., and S. V. Nghiem. 2013. Great Lakes ice classification using satellite C-band SAR multi-polarization data. *Journal of Great Lakes Research* 39: 55-64.
- Lewis Jr., W. M. 1983. A revised classification of lakes based on mixing. *Canadian Journal of Fisheries and Aquatic Sciences* 40(10): 1779-1787.
- Livingstone, D. M. 1999. Ice break-up on southern Lake Baikal and its relationship to local and regional air temperatures in Siberia and to the North Atlantic Oscillation. *Limnology and Oceanography* 44(6): 1486-1497.
- Lofgren, B. M., and Zhu, Y. 2000. Surface energy fluxes on the Great Lakes based on satellite-observed surface temperatures 1992 to 1995. *Journal of Great Lakes Research* 26(3): 305-314.
- Macpherson, J. D. 1963. The effect of ice on long range underwater sound propagation. *Radio and Electronic Engineer* 26(4): 293-297.
- Magnuson, J. J., D. M. Robertson, B. J. Benson, R. H. Wynne, D. M. Livingstone, T. Arai, R. A. Assel, R. G. Barry, V. Card, E. Kuusisto, and N. G. Granin. 2000. Historical trends in lake and river ice cover in the Northern Hemisphere. *Science* 289(5485): 1743-1746.
- Matsumoto, K., K. S. Tokos, and C. Gregory. 2015. Ventilation and dissolved oxygen cycle in Lake Superior: Insights from a numerical model. *Geochemistry, Geophysics, Geosystems* 16(9): 3097-3110.
- McCormick, M.J., and G.L. Fahnenstiel. 1999. Recent climatic trends in nearshore water temperatures in the St. Lawrence Great Lakes. *Limnology and Oceanography* 44(3): 530-540.
- Moore, A. M., H. G. Arango, A. J. Miller, B. D. Cornuelle, E. Di Lorenzo, and D. J. Neilson. 2004. A Comprehensive Ocean Prediction and Analysis System Based on the Tangent Linear and Adjoint Components of a Regional Ocean Model. *Ocean Modelling* 7: 227-258.

- National Aeronautics and Space Administration (NASA) Moderate Resolution Imaging Spectroradiometer (MODIS). 2015. Great Lakes Image, October 10, 2015, 16:50 GMT. <http://modis.gsfc.nasa.gov/>
- National Centers for Environmental Information (NCEI). 2015a. Great Lakes Bathymetry. <https://www.ngdc.noaa.gov/mgg/greatlakes/greatlakes.html>
- National Centers for Environmental Information (NCEI). 2015b. Global Historical Climatology Network. <http://www.ncdc.noaa.gov/cdo-web/search>
- National Center for Environmental Prediction (NCEP). 2015. North American Regional Reanalysis (NARR). <http://www.esrl.noaa.gov/psd/data/gridded/data.narr.html>
- National Data Buoy Center (NDBC). 2015. Historical Meteorological Data. <http://www.ndbc.noaa.gov/hmd.shtml>
- National Ice Center (NIC). 2015. Great Lakes Ice Analysis Products. [http://www.natice.noaa.gov/products/great\\_lakes.html](http://www.natice.noaa.gov/products/great_lakes.html)
- National Oceanographic and Atmospheric Administration (NOAA) Tides and Currents. 2015. Water Levels. <https://tidesandcurrents.noaa.gov/stations.html?type=Water+Levels>
- National Snow and Ice Data Center. 2016. Global Lake and River Ice Phenology. [http://nsidc.org/data/lake\\_river\\_ice/index.html](http://nsidc.org/data/lake_river_ice/index.html)
- Piccolroaz, S., Toffolon, M., and B. Majone. 2013. A simple lumped model to convert air temperature into surface water temperature in lakes. *Hydrology and Earth System Sciences* 17(8): 3323-3338.
- Piccolroaz, S., Toffolon, M., and B. Majone. 2015. The role of stratification on lakes' thermal response: The case of Lake Superior. *Water Resources Research* 51(10): 7878-7894.
- Powell, B. S., A. M. Moore, H. G. Arango, E. Di Lorenzo, R. F. Milliff, and R. R. Leben. 2009. Near real-time ocean circulation assimilation and prediction in the Intra-Americas Sea with ROMS. *Dynamics of Atmospheres and Oceans* 48(1): 46-68.
- Richards, T. L. 1964. The meteorological aspects of ice cover on the Great Lakes. *Monthly Weather Review* 92: 297-302.
- Rogers, J. C. 1976. Long-range forecasting of maximum ice extent on the Great Lakes. US Department of Commerce, National Oceanic and Atmospheric Administration, Environmental Research Laboratories, Great Lakes Environmental Research Laboratory.

- Rodgers, G. K. 1987. Time of onset of full thermal stratification in Lake Ontario in relation to lake temperatures in winter. Canadian Journal of Fisheries and Aquatic Sciences 44(12): 2225-2229.
- Roll, H. U. 1965. Physics of the Marine Atmosphere. Academic Press.
- Schneider, P., Hook, S. J., Radocinski, R. G., Corlett, G. K., Hulley, G. C., Schladow, S. G., and T.E. Steissberg. 2009. Satellite observations indicate rapid warming trend for lakes in California and Nevada. Geophysical Research Letters, 36(22).
- Shchepetkin, A. F., and J. C. McWilliams. 2003. A method for computing horizontal pressure-gradient force in an oceanic model with a nonaligned vertical coordinate, Journal of Geophysical Research 108(C3): 3090.
- Shchepetkin, A. F., and J. C. McWilliams. 2005. The Regional Ocean Modeling System: A split-explicit, free-surface, topography following coordinates ocean model, Ocean Modelling 9: 347-404.
- Sheherbina, A. Y., D. L. Rudnick, and L. D. Talley. 2005. Ice-draft profiling from bottom-mounted ADCP data. Journal of Atmospheric and Oceanic Technology 22: 1249-1266.
- Shilo, E., Y. Ashkenazy, A. Rimmer, S. Assouline, P. Katsafados, and Y. Mahrer. 2007. Effect of wind variability on topographic waves: Lake Kinneret case. Journal of Geophysical Research: Oceans 112(C12).
- Shimaraev, M.N., V.I. Verbolov, N.G. Granin, and P.P. Sherstyankin. 1994. Physical Limnology of Lake Baikal: a review. Baikal International Center for Ecological Research.
- Shokr, M., and N. Sinha. 2015. Sea Ice: Physics and Remote Sensing (Geophysical Monograph Series). American Geophysical Union.
- Shumway, R. H., and D. S. Stoffer. 2011. Time Series Analysis and Its Applications: With R Examples. Springer.
- Smith, S. D. (1988). Coefficients for sea surface wind stress, heat flux, and wind profiles as a function of wind speed and temperature. Journal of Geophysical Research: Oceans 93(C12): 15467-15472.
- Talley, L. D., G. L. Pickard, W. J. Emery, and J. H. Swift. 2011. Descriptive Physics Oceanography, Sixth Edition: An Introduction. Academic Press.
- Titze, D. J., and J. A. Austin. 2014. Winter thermal structure of Lake Superior. Limnology and Oceanography 59: 1336-1348.

- Tsumune, D., T. Tsubono, M. Aoyama, and K. Hirose. 2012. Distribution of oceanic  $^{137}\text{Cs}$  from the Fukushima Dai-ichi Nuclear Power Plant simulated numerically by a regional ocean model. *Journal of environmental radioactivity* 111: 100-108.
- Turuncoglu, U. U., G. Giuliani, N. Elguindi, and F. Giorgi. 2013. Modelling the Caspian Sea and its catchment area using a coupled regional atmosphere-ocean model (RegCM4-ROMS): model design and preliminary results. *Geoscientific Model Development* 6(2): 283-299.
- Van Cleave, K., J. D. Lenters, J. Wang, E. M. Verhamme. 2014. A regime shift in Lake Superior ice cover, evaporation, and water temperature following the warm El Niño winter of 1997-1998. *Limnology and Oceanography* 59: 1889-1898.
- Verburg, P., Hecky, R.E., and H. Kling. Ecological consequences of a century of warming in Lake Tanganyika. *Science* 301(5632): 505-507.
- Walsh, S. E., Vavrus, S. J., Foley, J. A., Fisher, V. A., Wynne, R. H., and J.D. Lenters. 1998. Global patterns of lake ice phenology and climate: Model simulations and observations. *Journal of Geophysical Research: Atmospheres* 103(D22): 28825-28837.
- Wang, J., X. Bai, G. Leshkevich, M. Colton, A. Clites, and B. Lofgren. 2010. Severe ice cover on Great Lakes during winter 2008–2009. *Eos* 91(5): 41-42.
- Wang, J., R. A. Assel, S. Walterscheid, A. H. Clites, and X. Bai. 2012a. Great Lakes ice climatology update: Winter 2006 – 2011 description of the digital ice cover dataset. National Oceanic and Atmospheric Administration (NOAA) Technical Memorandum GLERL-155. NOAA Great Lakes Environmental Research Laboratory. [http://www.glerl.noaa.gov/ftp/publications/tech\\_reports/glerl-155/tm-155.pdf](http://www.glerl.noaa.gov/ftp/publications/tech_reports/glerl-155/tm-155.pdf)
- Wang, J., X. Bai, H. Hu, A. Clites, M. Colton, and B. Lofgren. 2012b. Temporal and Spatial variability of Great Lakes ice cover, 1973-2010. *Journal of Climate* 25: 1318-1329.
- Wetzel, R.G. 2001. Limnology, Third Edition: Lake and River Ecosystems. Academic Press.
- Weyhenmeyer, G. A., Meili, M., and D.M. Livingstone. 2004. Nonlinear temperature response of lake ice breakup. *Geophysical Research Letters* 31(7).
- Weyhenmeyer, G. A., Livingstone, D. M., Meili, M., Jensen, O., Benson, B., and J.J. Magnuson. 2011. Large geographical differences in the sensitivity of ice-covered lakes and rivers in the Northern Hemisphere to temperature changes. *Global Change Biology* 17(1): 268-275.
- White, B., J. Austin, and K. Matsumoto. 2012. A three-dimensional model of Lake Superior with ice and biogeochemistry. *Journal of Great Lakes Research* 38(1): 61-71.

Wilkin, J. L., H. G. Arango, D. B. Haidvogel, C. S. Lichtenwalner, S. M. Glenn, and K. S. Hedström. 2005. A regional ocean modeling system for the Long-term Ecosystem Observatory, *Journal of Geophysical Research* 110(C6).

Woo, M. 2008. Cold Region Atmospheric and Hydrologic Studies. The Mackenzie GEWEX Experience: Volume 2: Hydrologic Processes. Springer.